



An Experimental Study on Evaporation, Puffing, Micro-explosion, and Secondary Breakup of Multi-fuel Blend Droplet

A thesis submitted for the degree of Doctor of Philosophy

By

Donghe Sun

Department of Mechanical and Aerospace Engineering

College of Engineering, Design and Physical Sciences

Brunel University London, Uxbridge

United Kingdom

Abstract

To mitigate the significant impact of CO₂ and other GHG on global warming and climate change, it is crucial to target one of the major sources of these emissions—fossil fuel-powered vehicles. These vehicles include cars, trucks, and buses, relying on internal combustion engines and are significant contributors to CO₂ emissions within the transportation sector. Although these vehicles are gradually being replaced by renewable energy and hybrid alternatives, they still hold a significant share of the market and vehicle fleet, making it essential to improve their efficiency and reduce emissions during this transition. Supported by advanced strategies, such as injection techniques—CRDI, PI and VIT, combustion technologies—HCCI, PCCI, LTC and DF, after treatment systems—SCR, DPF and EGR, conventional diesel fuel continues to be widely utilized due to its high energy density and superior fuel efficiency with ICEs. Blending diesel with alternative biofuels such as biodiesel and bio-alcohols, presents a promising approach for enhancing engine performance and reducing emissions. The study critically examines the potential of these alternative biofuels usability in ICEs, to enhance fuel atomization and address the challenges related to their integration into existing engine technologies.

The study investigates the transient behaviours of microdroplets in alternative multi-fuel blends for ICEs with a focus on biodiesel and bio-alcohol blends to explore these behaviours impact on fuel-air mixing. Experiments were conducted through introducing single fuel, binary, and ternary fuel blend droplets in various environmental temperature using LDBOS. These experiments were performed at three high temperatures: LLPT, MLPT and HLPT. The experimental fuels included diesel, biodiesel, HVO, bio-alcohols (methanol, ethanol, and octanol), and their blends. The transient behaviours of these fuel droplets were recorded using DBIMP technique, capturing key phenomena such as evaporation, nucleation, puffing, micro-explosion, secondary breakup, and combustion. Key findings of the study include

- The evaporation rate of diesel-biodiesel blends was slightly lower than that of diesel-HVO blends, with pure diesel demonstrating the fastest evaporation rate.

- The addition of biodiesel and HVO significantly reduced soot formation during combustion.
- Blends with a high diesel content are prone to ignite at high temperatures.
- In diesel-water emulsions, droplets exhibited more reactive behaviour, including rapid expansion and deformation at high temperatures.
- Blends of diesel/biodiesel/HVO with alcohols (methanol, ethanol, and octanol) showed enhanced puffing and micro-explosion phenomena intend to improve fuel-air mixing.
- The inclusion of water with more than 35% volume fraction, further intensified puffing and micro-explosion effects, particularly at higher temperatures.
- Aerated diesel showed shorter evaporation times with longer aeration durations, highlighting the influence of aeration on evaporation behaviour.

Overall, the study suggests that heating temperature has the most significant impact on fuel evaporation, puffing, micro-explosion, and combustion phenomena, followed by fuel composition and blending ratio. These findings provide important guidance for optimizing fuel formulations to enhance fuel atomization and fuel-air mixing, presenting a promising strategy for improving the performance of alternative multi-fuel blends in ICEs.

Acknowledgements

I would like to express my deepest respect and gratitude to my esteemed supervisory team: Professor Lionel Ganippa, Professor Athanasios Megaritis, and Professor Bin Wang. Their unwavering encouragement, support, and guidance throughout my PhD journey have been invaluable. Their expertise and mentorship have profoundly shaped my research and academic growth.

I am deeply thankful to Technician Eamon Wyse for his consistent assistance in procuring essential parts and components, which greatly facilitated the progress of my work. I would also like to extend my appreciation to Technicians Andy Selway and Gopa for their patience and support during my experimental work. Their expertise and cooperation were instrumental in ensuring the smooth execution of my experiments.

My sincere gratitude goes to Dr Aniket for his invaluable help and guidance throughout my experimental work. His expertise and willingness to support me were crucial in overcoming challenges and achieving meaningful results. I am also thankful to Mr. Rahul for his valuable support and suggestions in maintaining the experiments, as well as Mr. Mohamed for generously sharing his knowledge on fuel and combustion engines.

Lastly, I would like to convey my heartfelt thanks to my parents and family members for their unconditional love, unwavering support, and sacrifices throughout my academic journey. Their constant encouragement and belief in my abilities have been a source of strength and motivation.

I am deeply grateful to everyone mentioned above, as well as all those who have contributed to my growth and success, for their invaluable contributions and unwavering support.

Declaration

I hereby declare no portion of the work referred to in the dissertation has been submitted in support of an application for another degree or qualification of this or any other university or other institute of learning.

Contents

Abstract.....	I
Acknowledgements.....	III
Declaration.....	IV
Contents.....	V
Nomenclature	IX
List of Tables	XI
List of Figures	XII
Chapter 1 Introduction	- 1 -
1.1 Background	- 1 -
1.2 Project Aim and Objectives.....	- 2 -
1.3 Thesis Structure	- 4 -
Chapter 2 Fuel and Fuel Atomization	- 6 -
2.1 Fuels and Multi-Fuel Blends.....	- 6 -
2.1.1 Diesel.....	- 6 -
2.1.2 Biodiesel.....	- 8 -
2.1.3 HVO	- 13 -
2.1.4 Methanol.....	- 16 -
2.1.5 Ethanol	- 19 -
2.1.6 Diesel-methanol-octanol blend	- 22 -
2.1.7 Diesel-biodiesel-ethanol blend	- 24 -
2.1.8 Biodiesel-ethanol blend	- 26 -
2.1.9 Biodiesel-methanol-octanol blend	- 27 -
2.1.10 Summary	- 29 -
2.2 Fuel Atomization	- 32 -
2.2.1 Evaporation.....	- 32 -
2.2.2 Puffing	- 38 -
2.2.3 Micro-explosion	- 40 -

2.2.4	Secondary breakup	- 41 -
2.2.5	Auto-ignition	- 44 -
2.2.6	Summary	- 44 -
2.3	Evaporation, Puffing, Micro-explosion and Secondary Breakup Impact Factors ..	- 47 -
2.3.1	Temperature gradient impact.....	- 47 -
2.3.2	Fuel composition impact.....	- 48 -
2.3.3	Water and gas additives impact	- 49 -
2.4	Summary	- 54 -
Chapter 3	Experimental Techniques and Methodologies	- 56 -
3.1	Experiment Equipment	- 56 -
3.1.1	Fuel droplet heating module	- 58 -
3.1.2	Fuel droplet observation module	- 59 -
3.1.3	Fuel droplet generation module.....	- 59 -
3.1.4	Fuel droplet transportation module	- 60 -
3.2	Experiment Subjects and Materials	- 60 -
3.2.1	Experiment test fuel and properties.....	- 60 -
3.2.2	Experiment test fuel mixing process.....	- 62 -
3.3	Experiment Methodology	- 64 -
3.4	Experiment Condition	- 65 -
3.4.1	Experiment test temperature setting	- 65 -
3.4.2	Fuel droplet size setting.....	- 66 -
3.4.3	Limitations of experiment condition	- 66 -
3.5	Experiment Procedure	- 67 -
3.6	Experimental and Parametric Study of Droplet Delivery Variable	- 69 -
3.6.1	Overview	- 69 -
3.6.2	Design and process of experiment	- 70 -
3.6.3	Result and discussion	- 71 -
Chapter 4	Diesel and Biodiesel Blends Droplet Behaviour at Ambient Temperatures..	- 77 -

4.1	Introduction	- 77 -
4.2	Diesel, D-W Emulsion, D-BD and D-HVO Droplet Behaviour at LLPT	- 77 -
4.3	Diesel, D-W Emulsion, D-BD and D-HVO Droplet Behaviour at MLPT.....	- 83 -
4.4	Diesel, D-W Emulsion, D-BD and D-HVO Droplet Behaviour at HLPT.....	- 86 -
4.5	Diesel with Gas Injection Droplet Behaviour at MLPT.....	- 93 -
4.6	Conclusion.....	- 96 -
Chapter 5	Diesel and Alcohol Blends Droplet Behaviour at Ambient Temperatures	- 98 -
5.1	Introduction	- 98 -
5.2	D-M-O, D-BD-E, D-M-U Droplet Behaviour at LLPT	- 98 -
5.3	D-M-O, D-BD-E, D-M-U Droplet Behaviour at MLPT	- 104 -
5.4	D-M-O, D-BD-E, D-M-U Droplet Behaviour at HLPT	- 109 -
5.5	Temperature and Blending Ratio Impact on Puffing and Micro-explosion. -	- 115 -
5.5.1	D-M-O blend	- 117 -
5.5.2	D-BD-E blend.....	- 122 -
5.6	D-M-O(with 10%, 20%, 50% water) Droplet Behaviour at HLPT	- 126 -
5.6.1	D70M15O15 with 10%, 20%, 50% water	- 127 -
5.6.2	D50M25O25 with 10%, 20%, 50% water	- 130 -
5.6.3	D20M40O40 with 10%, 20%, 50% water	- 134 -
5.7	Conclusion.....	- 137 -
Chapter 6	Biodiesel/HVO and Alcohol Blends Droplet Behaviour at Ambient Temperatures	- 139 -
6.1	Introduction	- 139 -
6.2	BD-E, HVO-M-O Droplet Behaviour at LLPT	- 139 -
6.3	BD-E, HVO-M-O Droplet Behaviour at MLPT	- 143 -
6.4	BD-E, HVO-M-O Droplet Behaviour at HLPT	- 147 -
6.5	Temperature and Blending Ratio Impact on Puffing and Micro-explosion. -	- 152 -
6.5.1	BD-E blend.....	- 152 -
6.5.2	HVO-M-O blend	- 160 -
6.6	Conclusion.....	- 165 -

Chapter 7	Numerical Modelling of Droplet Behaviour.....	- 167 -
7.1	Introduction	- 167 -
7.2	Thermodynamic System	- 167 -
7.2.1	Conduction heat.....	- 167 -
7.2.2	Convection heat.....	- 168 -
7.2.3	Radiation heat.....	- 168 -
7.2.4	Complex coupled thermodynamic system	- 169 -
7.2.5	Conclusion.....	- 169 -
7.3	Droplet Behaviour.....	- 169 -
7.3.1	Evaporation phase	- 170 -
7.3.2	Combustion phase	- 170 -
7.3.3	Breakup phase	- 171 -
7.3.4	Conclusion.....	- 173 -
7.4	Droplet Behaviour in Thermodynamic System.....	- 174 -
7.4.1	Temperature field	- 174 -
7.4.2	Droplet behaviour	- 175 -
7.4.3	Droplet in thermodynamic system	- 175 -
7.4.4	Numerical method for coupled solution	- 176 -
7.5	Conclusion.....	- 177 -
Chapter 8	Conclusions and Recommendations.....	- 178 -
8.1	Summary of Findings.....	- 178 -
8.2	Recommendations for Future Work.....	- 181 -
Reference	- 183 -
Appendix A	MATLAB image processing code	- 199 -
Appendix B	Image processing	- 204 -
Appendix C	Droplet behaviour numerical calculation code	- 206 -
Appendix D	Numerical calculations of evaporation, breakup and combustion.....	- 208 -

Nomenclature

BD	Biodiesel
BSEC	Brake Specific Energy Consumption
BSFC	Brake Specific Fuel Consumption
BTDC	Before Top Dead Centre
BTE	Brake Thermal Efficiency
CA	BTDC Crank Angle
CAPF	Centre of Advanced Powertrain and Fuel
CO	Carbon Monoxide
CO ₂	Carbon Dioxide
CRDI	Common Rail Direct Injection
CVC	Constant Volume Combustor
D	Diesel
DBI	Diffused Back-Illumination
DEE	Diethyl Ether
DF	Dual Fuel
DI	Direct Injection
DMCC	Diesel Methanol Compound Combustion system
DoE	Department of Energy
DPF	Diesel Particulate Filter
E	Ethanol
EGR	Exhaust Gas Recirculation
FPS	Frames Per Second
GHG	Greenhouse Gas
GS	Gas Chromatography
HC	Hydrocarbons
HCB	Hydro Catalytic Biodiesel
HCCI	Homogeneous Charge Compression Ignition
HLB	Hydrophile-Lipophile Balance
HLPT	High Liquid Penetration Temperature
HNB	Hydrogen nanobubbles
HRR	Heat Release Rate
HVO	Hydrotreated Vegetable Oil
ICEs	Internal Combustion Engines
IPA	Isopropyl Alcohol
JB	Jatropha Biodiesel
LDBOS	Liquid Droplet Behaviour Observation System
LDPA	Laser Diffraction Particle Size Analyzer
LH ₂	Liquid Hydrogen

LSD	Low Sulphur Diesel
LLPT	Low Liquid Penetration Temperature
LTC	Low Temperature Combustion
M	Methanol
MB	Microbubble
MIT	Main Injection Timing
MLPT	Medium Liquid Penetration Temperature
MS	Mass Spectrometry
NEDC	New European Driving Cycle
NOx	Nitrogen Oxides
NTA	Nanoparticle tracking analysis
O	Octanol
NTC	Negative Temperature Coefficient
PAHs	Polycyclic Aromatic Hydrocarbons
PCCI	Premixed Charge Compression Ignition
PI	Pilot Injection
PM	Particulate Matter
Pt	Platinum
RMS	Root Mean Square
RON	Research Octane Number
SCR	Selective Catalytic Reduction
SMD	Sauter Mean Diameter
STP	Standard Temperature and Pressure
THC	Total Unburned hydrocarbons
U	UREA
UHC	Unburned Hydrocarbons
ULSD	Ultra Low Sulphur Diesel
VDV	Vibration Dose Value
VIT	Variable Injection Timing
W	Water
WDP	Water Dipole Power

List of Tables

Table 2-1 Comparison of advantages and disadvantages of various fuel types.....	- 29 -
Table 2-2 Breakup modes and breakup times of droplets with different Weber number [147]	- 43 -
Table 2-3 The factors of droplet puffing and micro-explosion for different liquids	- 47 -
Table 3-1 Experiment setup specifications and operational condition.....	- 57 -
Table 3-2 Experiment fuel properties and characteristics.....	- 61 -
Table 3-3 Relative decrease of different volumes droplets after entering the chamber ..	- 72 -
Table 3-4 Phenomenon of stopping state at different accelerations of droplets	- 74 -
Table 3-5 Droplet travel time.....	- 74 -

List of Figures

Figure 2.1 Health issue causing by diesel and petrol emissions [80]	- 6 -
Figure 2.2 Heavy duty diesel vehicles emissions and Euro VI emissions standard [81]	- 6 -
Figure 2.3 Comparison of biofuel production, GHG emissions and energy supply sources [85][86].....	- 8 -
Figure 2.4 Biodiesel feedstocks from vegetable oils, animal fats and reclaimed cooking oil [87]	- 9 -
Figure 2.5 Process flow schematic for biodiesel production [88]	- 9 -
Figure 2.6 Density and kinematic viscosity of biodiesel at various fuel temperature [90] -	10 -
Figure 2.7 Fuel temperature effect on spray tip penetration of biodiesel [90]	- 10 -
Figure 2.8 Spray tip penetration of BD, WDP25, IPA25 and diesel at 30MPa, 40MPa, 60MPa [91]	- 11 -
Figure 2.9 RMS, VDV and power curves for diesel and biodiesel fuel blends at speed of 1800 rpm and full-load engine [94]	- 12 -
Figure 2.10 Process schematic for HVO production [97].....	- 14 -
Figure 2.11 HVO and diesel spray tip penetration and angle, at 60MPa,120MPa and 180MPa [105]	- 16 -
Figure 2.12 Process flow schematic for bio methanol production [106]	- 16 -
Figure 2.13 Effect of isomerization on RON of various families of chemicals [111]	- 17 -

Figure 2.14 Concentration of hydrogen in various liquid state fuel compounds in terms of kg·m ³ relative to LH ₂ [111]	- 18 -
Figure 2.15 Energy storage capacity of various fuels in terms of energy stored per unit mass or volume [111].....	- 19 -
Figure 2.16 Process flow schematic for bioethanol production [114]	- 20 -
Figure 2.17 Emitted NO _x , CO and HC at 1.4 bar, 2.57 bar and 5.37 bar for neat diesel fuel and 5%, 10% and 15% ethanol blends [117]	- 21 -
Figure 2.18 Change in the miscibility of M100 and M10-diesel manipulating n-octanol as cosolvent at 10°C, 20°C, and 30°C [121]	- 23 -
Figure 2.19 BSFC comparison of diesel and D-BD-E at 1200 and 1600rpm [123].....	- 25 -
Figure 2.20 BD-E blend cloud point, density and dynamic viscosity at different blending ratio [127]	- 27 -
Figure 2.21 Temporal evolution of total soot mass and corresponding cross-sectional averaged equivalence ratio at LOL, 800K [130]	- 29 -
Figure 2.22 Diesel spray burning process in combustor [131]	- 33 -
Figure 2.23 Schematic of fuel spray droplet evaporation process in combustor [132]	- 34 -
Figure 2.24 Rapeseed oil-water emulsion droplet puffing at 1120K [135]	- 38 -
Figure 2.25 Rapeseed oil-water emulsion droplet micro-explosion at 1120K [135].....	- 40 -
Figure 2.26 Droplet breakup regimes with corresponding Weber numbers [146].....	- 43 -

Figure 2.27 Schemes of droplet evaporation, puffing and micro-explosion regimes: (a)evaporation ($T_a = 473 \pm 5$ K), (b)puffing ($T_a = 573 \pm 5$ K), (c)micro-explosion ($T_a = 673 \pm 5$ K) [148]	- 46 -
Figure 2.28 Temperature ranges of droplet behaviour regimes of kerosene- distilled water emulsion , $V_d = 15 \pm 1$ μ L, $U_a = 2 \pm 0.1$ m/s) [162]	- 50 -
Figure 2.29 Micro-explosion mechanism of water emulsified diesel droplet [163]	- 51 -
Figure 2.30 (a) Image of HNBS in gasoline. (b) Size distribution of HNBS just after nanobubble fabrication [167]	- 53 -
Figure 3.1 Multi-fuel blends microdroplet transient behaviours test setup LDBOS	- 56 -
Figure 3.2 Schematic diagram of the LDBOS	- 56 -
Figure 3.3 Schematic of fuel droplet temperature corresponding to the fuel spray liquid phase penetration length [67]	- 66 -
Figure 3.4 Schematic of fuel droplet transportation process.....	- 70 -
Figure 3.5 Sketch of mathematical model on parametric study of delivery	- 71 -
Figure 3.6 Relative decrease of different volumes droplets after entering the chamber at different initial velocities	- 72 -
Figure 3.7 Droplet travel time at different acceleration	- 75 -
Figure 4.1 1.5 μ L single diesel microdroplet evaporation at LLPT, atm	- 78 -
Figure 4.2 1.5 μ L single D-W microdroplet evaporation at LLPT, atm.....	- 81 -

Figure 4.3 1.5 μ L single D-BD microdroplet evaporation at LLPT, atm.....	- 82 -
Figure 4.4 1.5 μ L single D-HVO microdroplet evaporation at LLPT, atm.....	- 83 -
Figure 4.5 1.5 μ L single diesel microdroplet evaporation at MLPT, atm.....	- 83 -
Figure 4.6 1.5 μ L single diesel microdroplet nucleation at MLPT, atm	- 84 -
Figure 4.7 1.5 μ L single D-W microdroplet evaporation at MLPT, atm	- 85 -
Figure 4.8 1.5 μ L single D-BD microdroplet evaporation at MLPT, atm	- 85 -
Figure 4.9 1.5 μ L single D-HVO microdroplet evaporation at MLPT, atm	- 86 -
Figure 4.10 1.5 μ L single D-HVO microdroplet soot residue increasing, (a)D60HVO40, (b)D70HVO30, (c)D80HVO20 at MLPT, atm	- 86 -
Figure 4.11 1.5 μ L single diesel microdroplet micro-explosion at HLPT, atm	- 88 -
Figure 4.12 1.5 μ L single diesel microdroplet combustion at HLPT, atm	- 88 -
Figure 4.13 1.5 μ L single D-W microdroplet expansion at HLPT, atm.....	- 89 -
Figure 4.14 1.5 μ L single D-BD microdroplet evaporation at HLPT, atm.....	- 90 -
Figure 4.15 1.5 μ L single D-BD microdroplet combustion at HLPT, atm.....	- 90 -
Figure 4.16 1.5 μ L single D-HVO microdroplet combustion at HLPT, atm	- 91 -
Figure 4.17 1.5 μ L single diesel microdroplet normalized squared diameter at LLPT, MLPT, HLPT, atm.....	- 92 -

Figure 4.18 1.5 μ L single D-BD and D-HVO microdroplet evaporation rate at LLPT, MLPT, HLPT, atm	- 92 -
Figure 4.19 1.5 μ L single diesel, D-W, biodiesel and HVO microdroplet evaporation rate at LLPT, MLPT HLPT, atm.....	- 93 -
Figure 4.20 1.5 μ L single diesel microdroplet evaporation rate at of 1h,3h, 5h gas injectionat MLPT, atm	- 94 -
Figure 5.1 1.5 μ L single D-M-O microdroplet behaviour, (a)evaporation, (b)bursting, (c)nucleation, (d)puffing at LLPT, atm	- 99 -
Figure 5.2 1.5 μ L single D-M-O microdroplet behaviours at LLPT, atm.....	- 100 -
Figure 5.3 1.5 μ L single D-BD-E microdroplet nucleation at LLPT, atm.....	- 101 -
Figure 5.4 1.5 μ L single D-BD-E microdroplet behaviours at LLPT, atm	- 103 -
Figure 5.5 1.5 μ L single D-M-U microdroplet behaviour at LLPT, atm	- 104 -
Figure 5.6 1.5 μ L single D-M-O microdroplet behaviour, (a)nucleation, (b)puffing, (c)micro-explosion at MLPT, atm	- 104 -
Figure 5.7 1.5 μ L single D-M-O microdroplet behaviours at MLPT, atm.....	- 106 -
Figure 5.8 1.5 μ L single D-BD-E microdroplet puffing at MLPT, atm.....	- 107 -
Figure 5.9 1.5 μ L single D-BD-E microdroplet behaviours at MLPT, atm	- 108 -
Figure 5.10 1.5 μ L single D-M-U microdroplet behaviour at MLPT, atm	- 109 -

Figure 5.11 1.5 μL single D-M-O microdroplet behaviour, (a) nucleation, (b) burning, (c) boiling, (d)sooting at HLPT, atm	- 110 -
Figure 5.12 1.5 μL single D-M-O microdroplet behaviours at HLPT, atm.....	- 111 -
Figure 5.13 1.5 μL single D-BD-E microdroplet micro-explosion at HLPT, atm	- 113 -
Figure 5.14 1.5 μL single D-BD-E microdroplet behaviours at HLPT, atm	- 114 -
Figure 5.15 1.5 μL single D-M-U- microdroplet behaviour at HLPT, atm	- 115 -
Figure 5.16 Probability heatmap of nucleation, puffing and micro-explosion under varying temperature and D-M-O ratio	- 117 -
Figure 5.17 Probability of puffing and micro-explosion under varying temperature and D-M-O ratio	- 119 -
Figure 5.18 Puffing change rate under varying temperature and D-M-O ratio	- 120 -
Figure 5.19 Probability heatmap of nucleation, puffing and micro-explosion under varying temperature and D-BD-E ratio.....	- 122 -
Figure 5.20 Probability of puffing and micro-explosion under varying temperature and D-BD-E ratio	- 124 -
Figure 5.21 Puffing change rate under varying temperature and D-BD-E ratio.....	- 125 -
Figure 5.22 D70M15O15 with 10%, 20%, 50% water sub-droplet size distribution at TLPT, atm	- 127 -
Figure 5.23 D50M25O25 with 10%, 20%, 50% water sub-droplet size distribution at TLPT, atm	- 131 -

Figure 5.24 D20M40O40 with 10%, 20%, 50% water sub-droplet size distribution at TLPT, atm - 134 -

Figure 6.1 1.5 μ L single BD-E microdroplet nucleation at LLPT, atm..... - 139 -

Figure 6.2 1.5 μ L single BD-E microdroplet behaviours at LLPT, atm..... - 140 -

Figure 6.3 1.5 μ L single HVO-M-O microdroplet evaporation at LLPT, atm - 141 -

Figure 6.4 1.5 μ L single HVO-M-O microdroplet behaviour at LLPT, atm - 142 -

Figure 6.5 1.5 μ L single BD-E microdroplet behaviour at MLPT, atm..... - 144 -

Figure 6.6 1.5 μ L single BD-E microdroplet behaviours at MLPT, atm - 144 -

Figure 6.7 1.5 μ L single HVO-M-O microdroplet evaporation at MLPT, atm - 145 -

Figure 6.8 1.5 μ L single HVO-M-O microdroplet behaviour at MLPT, atm..... - 147 -

Figure 6.9 1.5 μ L single BD-E microdroplet behaviour (a)puffing, (b)weak micro-explosion, (c)strong micro-explosion at HLPT, atm - 148 -

Figure 6.10 1.5 μ L single BD-E microdroplet behaviours at HLPT, atm - 149 -

Figure 6.11 1.5 μ L single HVO-M-O microdroplet micro-explosion at HLPT, atm..... - 150 -

Figure 6.12 1.5 μ L single HVO-M-O microdroplet behaviour at HLPT, atm - 151 -

Figure 6.13 Probability heatmap of puffing and micro-explosion under varying temperature and BD-E ratio - 152 -

Figure 6.14 Probability of puffing and micro-explosion under varying temperature and BD-E ratio..... - 154 -

Figure 6.15 Puffing change rate under varying temperature and BD-E ratio..... - 156 -

Figure 6.16 Probability heatmap of puffing and micro-explosion under varying temperature and HVO-M-O ratio - 160 -

Figure 6.17 Probability of puffing and micro-explosion under varying temperature and HVO-M-O ratio..... - 162 -

Figure 6.18 Puffing change rate under varying temperature and HVO-M-O ratio - 163 -

Figure 8.1 Fuel and multi-fuel blend droplet behaviours at LLPT, MLPT and HLPT, atm . - 178 -

Chapter 1 Introduction

1.1 Background

Energy and environmental concerns have garnered widespread attention [1], leading to a growing focus on reducing energy consumption [2] and mitigating environmental impacts [3]. This focus has driven significant investments in upgrading existing powertrain systems [4] and exploring innovative strategies to enhance fuel efficiency [5] and comply with emissions regulations [6]. Conventional petroleum-based fuels face challenges such as incomplete atomization [7][8], group adhesion [9], and corrosion [10] due to their inherent physical characteristics [11]. These challenges contribute to incomplete combustion [12], the emission of unburned hydrocarbons (UHC) [13], greenhouse gases (GHG) [14], and toxic substances in exhaust gases [15].

In response to stringent policies [16] and regulations [17] targeting toxic emissions [18] from diesel-powered vehicles [19] and heavy-duty lorries [20], extensive research in recent decades has explored alternative fuels [21][22][23][24][25][26][27] as potential replacements for conventional petroleum-based fuels in internal combustion engines (ICEs). Among these research efforts, the study of alternative liquid fuel atomization [28][29][30] has emerged as a critical area, given its importance in optimizing ICEs efficiency [31][32][33][34] and performance [35][36][37][38]. This line of inquiry focuses on understanding the properties [39][40] and behaviour [41][42] of alternative fuels within the engine [43][44][45].

Liquid fuel atomization is fundamental to the efficient functioning of ICEs. [46][47][48][49] By breaking liquid fuel into fine droplets [50], atomization maximizes the fuel's surface area [51], promoting enhanced fuel-air mixing [52]. This process accelerates vaporization [53], ensuring a more homogeneous mixture [54] in the combustion chamber. An optimally mixed fuel-air combination leads to more complete combustion [55], maximizing energy release [56] and power output [57]. Improved combustion also reduces pollutants such as

UHC [58], carbon monoxide (CO) [59][60], carbon dioxide (CO₂) [61][62], nitrogen oxides (NO_x) [63][64] and particulate matter (PM) [65][66]. The finely atomized droplets [67], with a higher surface-to-volume ratio [68], accelerate evaporation [69] and combustion [70]. They ignite more swiftly [71], ensuring a rapid and controlled spread of flame within the combustion chamber [72], fostering stable and efficient combustion [73][74]. This process not only reduces backfire risks but also curtails instances of incomplete combustion. [75]

In summary, liquid fuel atomization is crucial for optimizing fuel-air mixing, promoting complete combustion, reducing emissions, and enhancing overall engine performance and efficiency. [76][77] This study focuses on investigating liquid fuel atomization, particularly the behaviour of droplets in multi-fuel blends, including phenomena such as evaporation, puffing, micro-explosion, secondary breakup, burning, and soot formation. These behaviours are studied in an environment that simulates the high-temperature air conditions of an engine chamber. Using the diffused back-illumination macro photography (DBIMP) technique to observe single fuel, binary, and ternary fuel blend droplets introduced into a high-temperature furnace, the transient behaviours of atomization can be analysed in detail. The single fuel and multi-fuel blends investigated in this study include diesel, two generations of biodiesel—biodiesel and hydrotreated vegetable oil (HVO) and bio-alcohols, such as bio-methanol and bioethanol. These fuels are considered environmentally friendly alternatives for use in current ICEs due to their favourable chemical and physical properties. Biodiesel (C₁₂-C₂₄) and HVO (C₁₅-C₁₈), with carbon numbers, cetane numbers, and densities similar to those of diesel (C₁₂-C₂₅), are widely applied in ICEs. Likewise, bio methanol (CH₃OH) and bioethanol (C₂H₅OH), which have lower boiling points and higher oxygen content, are also promising alternatives due to their ability to improve combustion and reduce emissions.

1.2 Project Aim and Objectives

The overarching goals of this study can be summarized as follows:

1. Explore the limitations of alternative fuel and multi-fuel atomization in ICEs and identify strategies to enhance their application potential. The aim focuses on contributing to the development of more sustainable and environmentally friendly engine technologies.
2. Develop a comprehensive understanding of multi-fuel blend atomization characteristics by investigating the transient behaviour of droplets with various compositions and proportions. This includes identifying conditions that promote effective atomization, which is crucial for enhancing the overall atomization process and improving performance of alternative fuels in ICEs.

The study is driven by the following core objectives:

1. Exploration of the properties and attributes of diesel, biodiesel, HVO and short carbon chain bio-alcohols (bio-methanol, bioethanol). This includes analysing the mixing processes of these fuels and the resultant properties of their mixtures.
2. Analysis of the effect of temperature gradients on droplet behaviour. This objective aims to understand how varying temperatures impact droplet evaporation, puffing, and other transient phenomena.
3. Analysis of the effect of fuel composition on droplet behaviour. This explores how different fuel components contribute to phenomena such as evaporation, puffing, micro-explosion, and secondary breakup.
4. Analysis of the effect of fuel blending ratios on droplet behaviour. This objective focuses on examining how various blending ratios of multi-fuel components influence atomization characteristics.
5. Analysis of the effect of water and gas additives on droplet behaviour. This investigates how the inclusion of water and gas impacts fuel droplet atomization and combustion.
6. Identification of threshold conditions for droplet behaviour. The goal is to determine the conditions under which droplets experience evaporation, puffing, secondary breakup, and combustion—critical factors for optimizing fuel combustion in ICEs.

These objectives aim to provide a clearer understanding of how multi-fuel blends behave in high-temperature environments, thereby contributing to advancements in fuel atomization and combustion processes for ICEs technologies.

1.3 Thesis Structure

The work presented in this study is detailed across the following chapters:

Chapter 1 outlines the study background, emphasizing current policies and regulations related to ICEs energy consumption and emissions. It illustrates the significance of liquid fuel atomization in influencing engine combustion efficiency, energy consumption and pollutant emissions. This chapter also delineates the research objectives and offers an overview of the thesis structure.

Chapter 2 reviews prior research related to the physical and chemical characteristics of fuels used in ICEs, with an emphasis on alternative fuels such as biodiesel and bio-alcohols, as well as multi-fuel blends. This chapter also explores the mechanisms of liquid fuel atomization and examines the factors influencing atomization, including droplet behaviours such as evaporation, puffing, micro-explosion, secondary breakup, and auto-ignition.

Chapter 3 details the experimental setup, subjects, methods, conditions, and procedures employed to investigate the behaviour of single fuel and multi-fuel blend droplets at high-temperature environments.

Chapter 4 focuses on the behaviours of single microdroplet of pure diesel and its blends with water and biodiesel (both first- and second-generation) at high temperatures. This chapter discusses the observed droplet behaviours, explores their underlying causes, and provides comparisons between them.

Chapter 5 examines the behaviours of single microdroplets of pure diesel and its blends with short carbon chain bio-alcohols (bio-methanol and bioethanol) at high temperatures.

This chapter discusses and compares the observed droplet behaviours, providing insights into their underlying causes.

Chapter 6 investigates the behaviours of single microdroplet of biodiesel (first- and second-generation) and short carbon chain bio-alcohols (bio-methanol and bioethanol) blends at high temperatures. This chapter explores the various droplet behaviours, their causes, and providing comparisons among the different fuel blends.

Chapter 7 establishes a numerical model to elucidate the relationship between the thermodynamic system and microdroplet behaviours, including evaporation, break up and combustion. The model examines how high environmental temperatures, fuel composition, and multi-fuel blending ratios influence microdroplet dynamics, with the aim of enhancing fuel efficiency and reducing emissions by precisely controlling microdroplet and nanoscale droplet.

Chapter 8 summarizes the behaviours of pure diesel, its blends with water and two generation of biodiesel, as well as short carbon chain bio-alcohols at high temperatures. It also discusses the behaviours of biodiesel and bio-alcohol blends, reflecting on how these fuel compositions and their mixing properties enhance liquid fuel atomization. Furthermore, the chapter provides suggestions for future work, including potential improvements in experimental test conditions and recommendations for conducting experimental and numerical engine performance tests.

Chapter 2 Fuel and Fuel Atomization

2.1 Fuels and Multi-Fuel Blends

2.1.1 Diesel

Diesel (D) is well known for its excellent compression ignition characteristics, which allow it to ignite without a spark by compressing the inlet air and then injecting the fuel. The auto-ignition temperature of diesel ranges from approximately 483K to 583K, depending on its composition and quality. [78] As a fuel for ICEs, diesel offers several advantages, including high energy density, thermal efficiency, cost-effectiveness, durability, and reliability. [78] [79] However, diesel combustion also produces exhaust emissions such as CO, CO₂, NO_x and PM, and contributes to noise, vibration, and various environmental and health concerns, as illustrated in Figure 2.1 and Figure 2.2. [80][81]

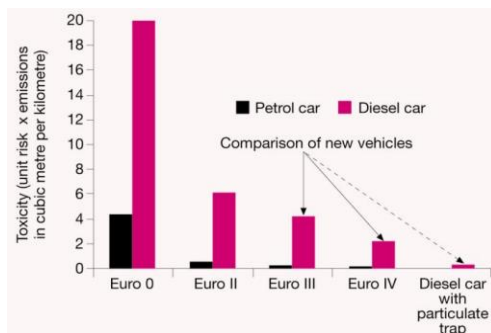


Figure 2.1 Health issue causing by diesel and petrol emissions [80]

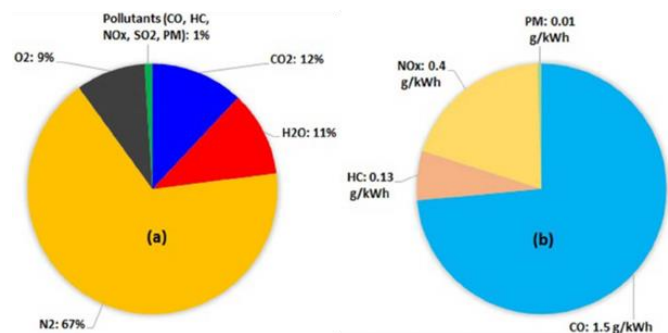


Figure 2.2 Heavy duty diesel vehicles emissions and Euro VI emissions standard [81]

The evaporation and combustion characteristics of diesel have been extensively studied, focusing on diesel composition and fuel injection strategies to optimize fuel efficiency and reduce emissions. Sulphur content in diesel fuel is crucial factor influencing both the composition and emission factors of various elements in exhaust gases. Research has shown

that emission factors for several elements are higher when using low sulphur diesel (LSD) compared to ultra-low sulphur diesel (ULSD). Reducing the sulphur content in diesel has been observed to not only lower PM emissions but also affect the emissions of other pollutants, including CO₂, NO_x and polycyclic aromatic hydrocarbons (PAHs). These findings illustrate the broader environmental implications of diesel fuel sulphur content on exhaust emissions, necessitating further investigation into the comprehensive effect of diesel' other constituents across pollutant categories. [82] When oxygen is the sole oxidant, the soot oxidation temperature is highly dependent on the type of diesel used. However, the presence of NO_x and an upstream platinum (*Pt*) catalyst significantly lowers the soot oxidation temperature, leading to reduced variability between different soot samples compared to conditions with pure oxygen. When the sulphur content of the fuel has a minimal impact on soot oxidation temperature, the aromatic content is a key determinant. Fuels with low aromatic content result in significantly higher soot oxidation temperatures, whereas fuels with a high concentration of aromatics, particularly diaromatics, lead to lower oxidation temperatures. This indicates that the aromatic composition of diesel fuel plays a crucial role in influencing the efficiency of soot oxidation. [83] By reducing the diameter of the exhaust valve volume and the high-pressure oil pipe, the injection quantity increases, accelerating the jet rate and boosting the injection pressure. This results in a reduction in the Sauter Mean Diameter (SMD), an increase in the spray angle by 5°, while NO_x emissions remain unaffected. Carbon smoke emissions are reduced by 65.4%, fuel consumption decreases by 2.18%, and indicator power improves 2.21%. This optimization leads to more efficient combustion and lower pollutant emissions. [84]

Due to the non-renewable nature of diesel and the growing environmental awareness, coupled with advancements in technology, diesel is increasingly being supplanted by greener, renewable fuels such as biodiesel, HVO, bio-alcohols, and synthetic fuels, as illustrated in Figure 2.3. These alternatives provide more sustainable solutions for reducing emissions and mitigating the environmental impact associated with conventional diesel fuels. [85][86]

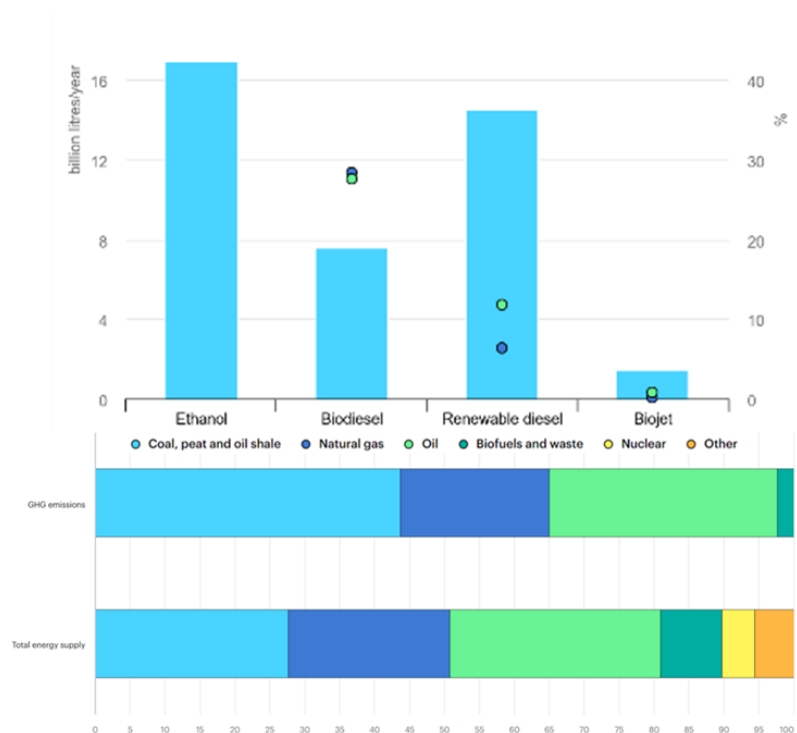


Figure 2.3 Comparison of biofuel production, GHG emissions and energy supply sources [85][86]

2.1.2 Biodiesel

Biodiesel (BD) is an alternative fuel derived from sustainable feedstocks, such as vegetable oils, animal fats, and reclaimed cooking oil, as shown in Figure 2.4. [87] The process flow schematic for biodiesel production is illustrated in Figure 2.5. [88] One of the primary advantages of biodiesel is its compatibility with existing engine designs, requiring no modifications. Although biodiesel closely mirrors the physicochemical properties of conventional diesel, it offers several significant environmental benefits, positioning it as a more sustainable alternative. [89]

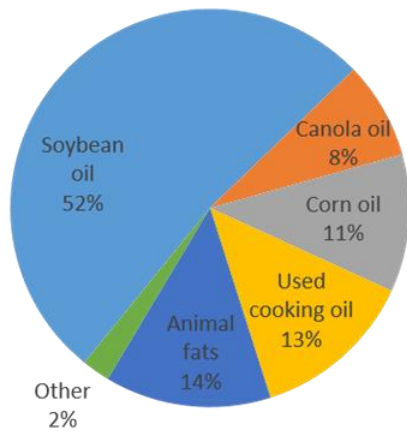


Figure 2.4 Biodiesel feedstocks from vegetable oils, animal fats and reclaimed cooking oil [87]

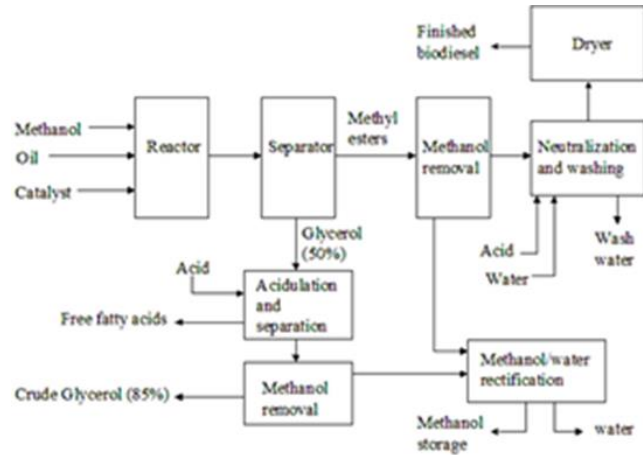


Figure 2.5 Process flow schematic for biodiesel production [88]

Experimental studies have investigated the effects of various factors, such as biodiesel feedstocks variations, fuel temperature, ambient environment temperature, and the blending ratio of biodiesel and diesel, on evaporation and spray characteristics, as well as on combustion and emissions. Increasing the fuel temperature from 300 K to 360 K had minimal impact on the spray liquid tip penetration, as shown in Figure 2.6 and Figure 2.7. However, the rise in fuel temperature significantly enhanced the evaporation of fuel droplets, particularly in the central region of the spray axis, where the highest concentration of vaporized fuel was observed. An increase in ambient gas temperature from 300 K to 450 K resulted in greater spray liquid tip penetration, indicating that the spray could extend further in higher ambient temperatures. Additionally, higher ambient temperatures accelerated fuel evaporation, contributing to more efficient combustion. [90]

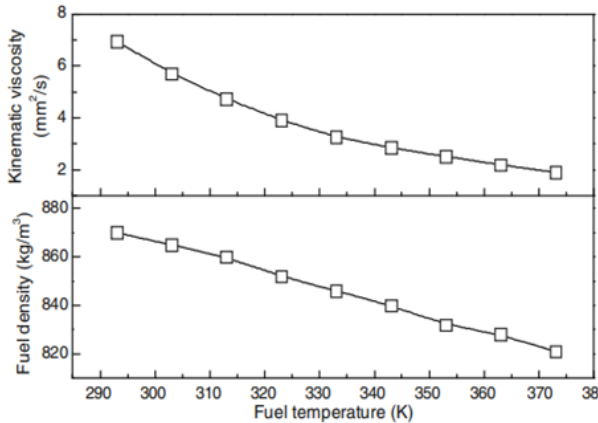


Figure 2.6 Density and kinematic viscosity of biodiesel at various fuel temperature [90]

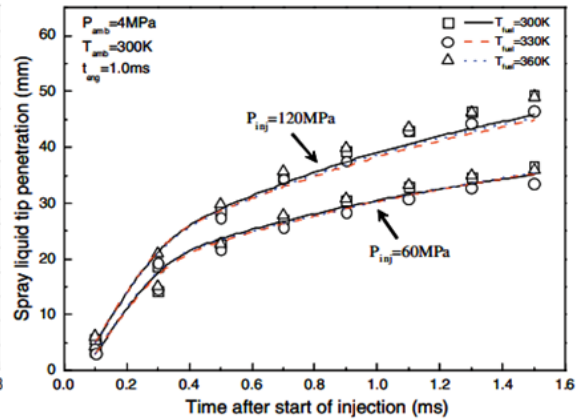


Figure 2.7 Fuel temperature effect on spray tip penetration of biodiesel [90]

Biodiesel contains a significant amount of oxygen, which effectively reduces exhaust emissions by enhancing internal combustion within the engine. However, its high viscosity poses challenges for low-temperature flow. In a study examining spray behaviour and atomization characteristics, non-esterified biodiesel was combined with fuel additives, water dipole power (WDP) and isopropyl alcohol (IPA), to assess their effects. A visualization system consisting of a halogen lamp and a high-speed camera was utilized to capture the spray process, while atomization characteristics were analysed using a Laser Diffraction Particle Size Analyzer (LDPA). When WDP and IPA were mixed with biodiesel, improvements in atomization and spray characteristics were observed, as shown in Figure 2.8. At an injection pressure of 30 MPa, the SMD of the mixed fuel WDP25 at a distance of 6 cm from the nozzle tip was reduced by 33.9%. Additionally, the time required for each fuel spray to develop decreased as injection pressure increased, with the spray initiation and development of WDP25 occurring faster than BD100. The span factor of WDP25 was also lower than that of BD100, indicating a narrower droplet size distribution due to viscosity reduction. As the injection pressure increased, the SMD of WDP25 continued to decrease, consistently remaining smaller than that of BD100. This study demonstrated that biodiesel, when mixed with WDP, can be effectively applied in high-pressure injection engines. [91]

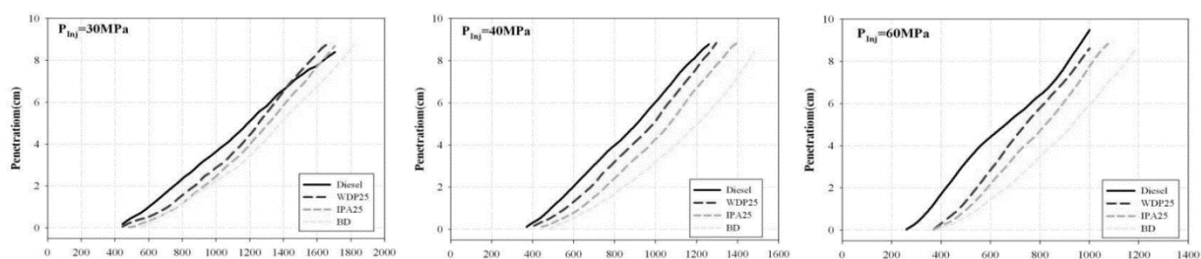


Figure 2.8 Spray tip penetration of BD, WDP25, IPA25 and diesel at 30MPa, 40MPa, 60MPa [91]

Another study demonstrated that when the fuel temperature was maintained at 333 K, there was little difference in injection amount and penetration length between diesel-biodiesel blends and pure diesel. This suggests that, with proper regulation fuel temperature, adjustments to injection duration or pressure may not be necessary during engine tests. However, the study found that the spray distribution of diesel-biodiesel blends, those made from canola and soybean oils, were more uniform compared to pure diesel, which suggest poorer evaporation characteristics. This suboptimal atomization can directly impact the fuel evaporation process, potentially reducing combustion efficiency. In visualization experiments of the combustion flame, the flame characteristics of diesel-biodiesel blends and pure diesel were generally similar. However, white smoke was observed during the initial ignition stage of the diesel-biodiesel blends, likely due to their inferior atomization characteristics. Emission tests revealed that NO_x emissions from diesel-biodiesel blends were higher than those from pure diesel, likely due to the higher oxygen content in biodiesel and its more rapid combustion, which accelerates NO_x formation. Conversely, PM emissions from diesel-biodiesel blends were significantly lower than those from pure diesel, indicating a reduction in PM emissions when using diesel-biodiesel blends. [92]

At low temperatures of 268 K and 265 K, experimental results showed that the injection delay remained unaffected for BD20, BD50, and pure biodiesel (BD100). However, the injection closing delay increased with higher biodiesel content, with BD100 exhibiting the most pronounced delay. The emission coefficients of all fuels were lower at low

temperatures compared to room temperature, and they did not vary significantly with increasing biodiesel content in the mixture. While fuel viscosity appears to influence both the closing delay and emission coefficients, it is not the sole factor affecting injector performance at sub-zero temperatures. Notably, BD100 exhibited a much lower emission coefficient compared to diesel and biodiesel blends. As fuel temperature decreases, the emission coefficients of diesel and biodiesel blends tend to converge. The spray behaviour results indicate that spray penetration increases, while the spray angle decreases significantly, particularly for BD100. These effects become more pronounced as the fuel temperature approaches the cloud point, leading to a deterioration in flow properties and spray characteristics for BD100 at low temperatures. [93]

A study found that the fuel mixture significantly impacted injector spray, subsequently influencing combustion, vibration, and power variations. Under full-load engine conditions, the highest and lowest vibrations were observed for B40 and B20, D100 and B80, respectively. The most severe vibration shocks occurred with B40 and B20, while D100 and B80 exhibited the least. Specifically, B40 experienced significant combustion energy loss due to uncontrolled vibrations, as shown in Figure 2.9. However, engine performance was smoothest for B40. [94] In practical ICEs, biodiesel content is generally kept under 20%. Standard retail diesel, known as B7, contains up to 7% biodiesel, with the remainder being fossil fuel diesel. Blends containing more than 10% biodiesel are classified as high-blend biodiesel. [95]

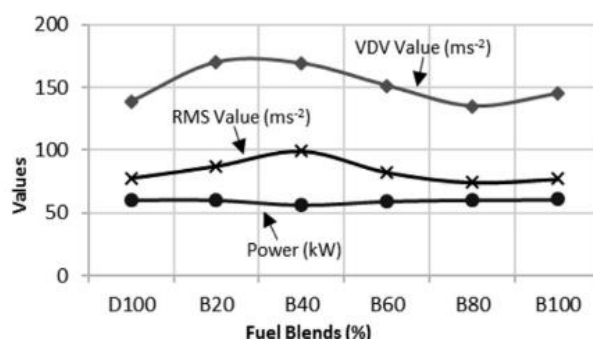


Figure 2.9 RMS, VDV and power curves for diesel and biodiesel fuel blends at speed of 1800 rpm and full-load engine [94]

As a first-generation biofuel, biodiesel is often compared with HVO, a second-generation biodiesel, in terms of fuel efficiency and emissions control. Both alternative fuels are gaining prominence in the automotive supply chain, yet they differ significantly in their physical properties and autoignition characteristics. HVO has a lower viscosity and a higher cetane number, whereas biodiesel exhibits higher viscosity and a lower cetane number. These differences significantly impact mixture formation and the subsequent combustion process, which can lead to suboptimal performance and increased emissions if an engine optimized for one fuel is used with the other. [96]

To assess the extent of this issue, an injection pressure sweep was conducted around a stock engine calibration designed for low NO_x and low PM emissions, utilizing split fuel injection. The results indicated that both biodiesel and HVO performed better at lower injection pressures compared to conventional diesel, with the added benefit of simultaneously reducing all emission indicators. Additionally, lowering the injection pressure for biodiesel from 80 MPa to 60 MPa at low engine loads improved brake thermal efficiency (BTE) by 1 percentage point, primarily due to reduced parasitic losses in the common rail system. These findings illustrate the potential for optimizing injection parameters to enhance the performance of alternative, such as fuels biodiesel and HVO. [96]

2.1.3 HVO

HVO is a paraffin-based fuel derived from renewable sources, such as vegetable oils, and is free from FAME, sulphur and fossil ingredients. Unlike conventional biodiesel production, which utilizes methanol as a catalyst, HVO is produced through hydrogenation, as shown in Figure 2.10. [97] This process results in cleaner combustion, leading to reduced PM, NO_x and other harmful emissions compared to conventional diesel. [98][99] Additionally, by utilizing waste materials as feedstock, HVO supports a circular economy by recycling resources that would otherwise be destined for landfills or incinerated. This sustainable approach not only lower GHG emissions but also reduces the carbon footprint of commercial fleets. [100]

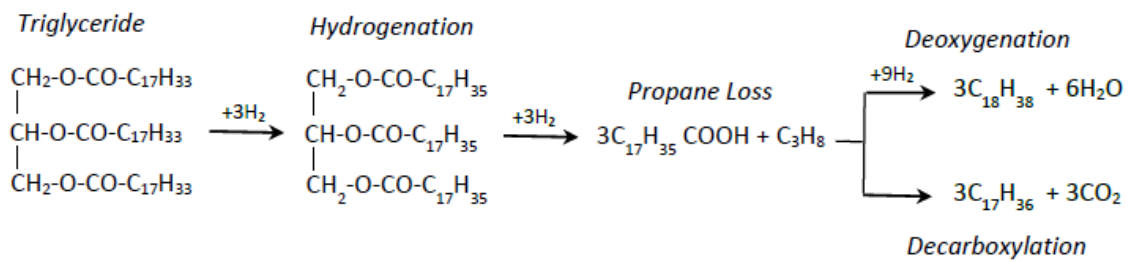


Figure 2.10 Process schematic for HVO production [97]

The inherent versatility of HVO allows for seamless integration with existing diesel infrastructure, making it an attractive option for a wide range of commercial applications. In tests conducted on two heavy-duty engines and two city buses powered by HVO and sulphur-free EN 590 diesel, significant emission reductions were observed with HVO compared to EN 590 fuel. Specifically, NO_x emissions decreased by 7% to 14%, PM by 28% to 46%, CO by 5% to 28%, and hydrocarbons (HC) by 15% to 48%. [101] Regarding engine performance, iso-HVO outperformed BD, slightly exceeded HVO, but fell below diesel. Emissions-wise, both iso-HVO and HVO diesel blends produced lower total unburned hydrocarbons (THC) and CO than biodiesel, although the NO_x and PM emissions of iso-HVO were similar to those of BD. All three 50% biofuel blends showed lower particle concentrations across all size ranges compared to diesel. [102] In another experiment examining the emissions characteristics of HVO in a light-duty Euro 5 diesel engine during steady-state operation and the New European Driving Cycle (NEDC), HVO significantly reduced all regulated emissions, including NO_x, smoke, CO, CO₂, and HC, when compared to conventional diesel. The study also found that adjustments to Main Injection Timing (MIT) and Exhaust Gas Recirculation (EGR) further optimized HVO's emission reduction potential, enhancing its advantage over conventional diesel. [103]

Furthermore, a study on the ignition probability of HVO revealed that as the HVO percentage in the blend increased, the ignition probability also increased. Although the SMD of HVO was greater than that of diesel but lower than biodiesel, blends with up to 30% HVO were found to be feasible for use in current diesel engines due to their similar viscosity

(2.54, 2.59 and 2.62 cSt) and heating values (42.41, 42.29 and 42.08 MJ/kg) to diesel (2.51 cSt and 42.58 MJ/kg). However, pure HVO or blends with HVO content exceeding 30% are not suitable for existing engines due to their high cetane index, which could negatively impact engine power output. Consequently, using higher HVO blends would necessitate engine modifications, which is impractical for current diesel engines. [104]

A recent study utilizing the DBI technique analysed the spray characteristics of HVO fuel at three different injection pressures, comparing them to those of conventional diesel fuel. The findings indicated that as injection pressure increased, the peak injection rates for both HVO and diesel similarly increased. At injection pressures exceeding 120 MPa, the injection rates for the two fuels were nearly identical, although differences were observed at lower pressures. Additionally, increasing the injection pressure reduced the injection delay. HVO fuel exhibited distinctive spray characteristics compared to diesel, including shorter spray tip penetration, a lower equivalence ratio, a larger spray angle, and greater spray volume, as shown as Figure 2.11. However, the stability of the spray angle in HVO was lower than that observed for diesel. The ambient gas entrainment rate was observed to occur in two primary stages, which were significantly influenced by the spray breakup development phase. In the case of diesel fuel, the injection pressure predominantly affected the equivalence ratio near the nozzle, with minimal impact on the downstream region of the spray. [105]

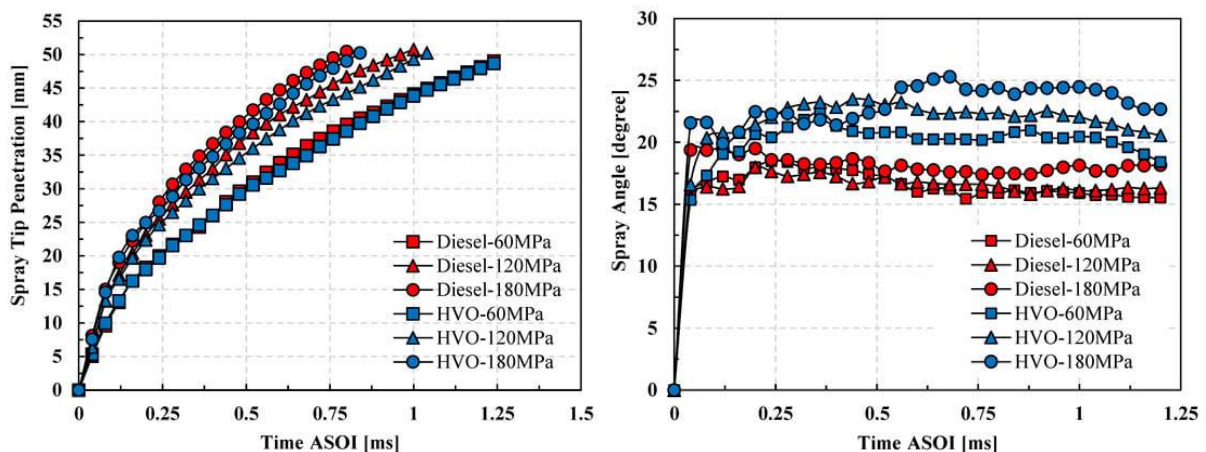


Figure 2.11 HVO and diesel spray tip penetration and angle, at 60MPa,120MPa and 180MPa [105]

2.1.4 Methanol

Bio-methanol (M) is a type of methanol produced from renewable energy sources such as biomass or biogas, in contrast to conventional methanol, which is primarily derived from natural gas or coal. The production process for bio-methanol is illustrated in Figure 2.12. [106] This renewable production pathway offers a more sustainable alternative by reducing reliance on fossil fuels and contributing to lower GHG emissions. [107]

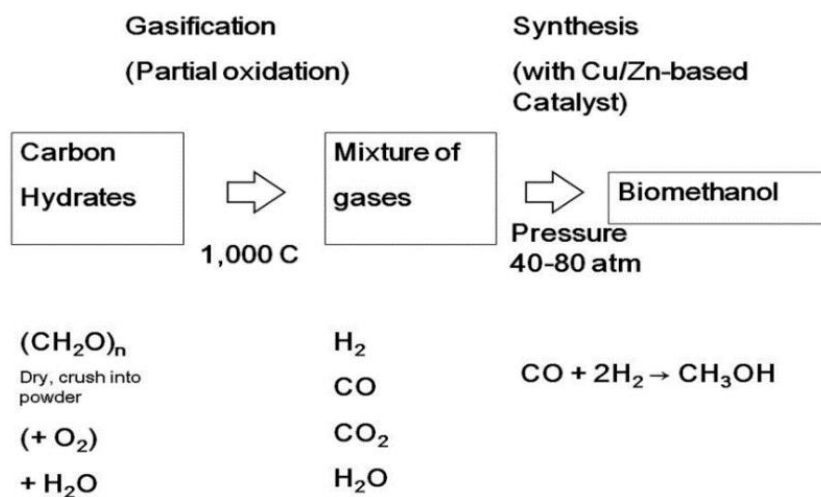


Figure 2.12 Process flow schematic for bio-methanol production [106]

Bio-methanol can be used either as a direct fuel or blended with diesel to reduce emissions, offering lower tailpipe emissions when incorporated into diesel engine combustion. It is also associated with reduced GHG emissions. In a study examining the performance and emissions characteristics of a direct injection diesel engine using methanol-diesel blends (5%, 10%, and 15% methanol), results indicated that brake specific fuel consumption (BSFC), brake specific energy consumption (BSEC), and NOx emissions increased with higher methanol content in the blend. Conversely, BTE, smoke opacity, CO, and THC levels decreased as methanol content increased. For all fuel blends tested, increasing injection

pressure and advancing injection timing led to reductions in smoke opacity, CO, and THC emissions, but also resulted in higher NO_x emissions. [108] In a test involving a four-cylinder direct injection diesel-methanol compound combustion system (DMCC), the DMCC configuration reduced both smoke and NO_x emissions compared to the original engine under idle and five engine load conditions. However, the DMCC system led to increased HC and CO emissions. The use of an oxidation catalyst in conjunction with the DMCC system further reduced CO, HC, NO_x, and smoke emissions, underscoring its effectiveness in mitigating emissions. [109]

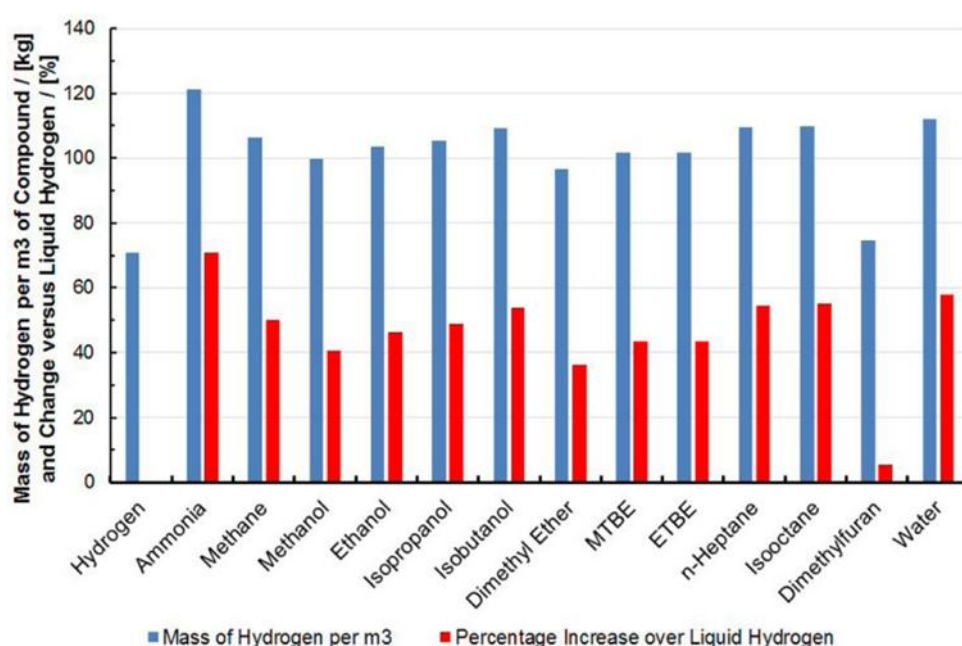


Figure 2.13 Effect of isomerization on RON of various families of chemicals [111]

Figure 2.13 illustrates the research octane number (RON) of saturated molecules plotted against the number of carbon atoms in each molecule. The figure clearly demonstrates that for normal alkane molecules, knock resistance significantly decreases as the carbon chain length increases. In contrast, molecules with a high degree of isomerization maintain a consistently high RON, typically around 100. Methanol and ethanol exhibit inherently high knock resistance, primarily due to the absence of negative temperature coefficient (NTC) behaviour. As the carbon chain lengthens in alcohols, their knock resistance decreases;

however, this decline can be mitigated through isomerization, mirroring patterns observed in other molecular families. The high-octane number of alcohols is particularly noteworthy, since alcohols are the only molecular family with fewer than four carbon atoms that remain in liquid form at standard temperature and pressure (STP). This characteristic makes them particularly suitable as fuel options, as their physical state and high knock resistance enhance their effectiveness in ICEs. [110][111]

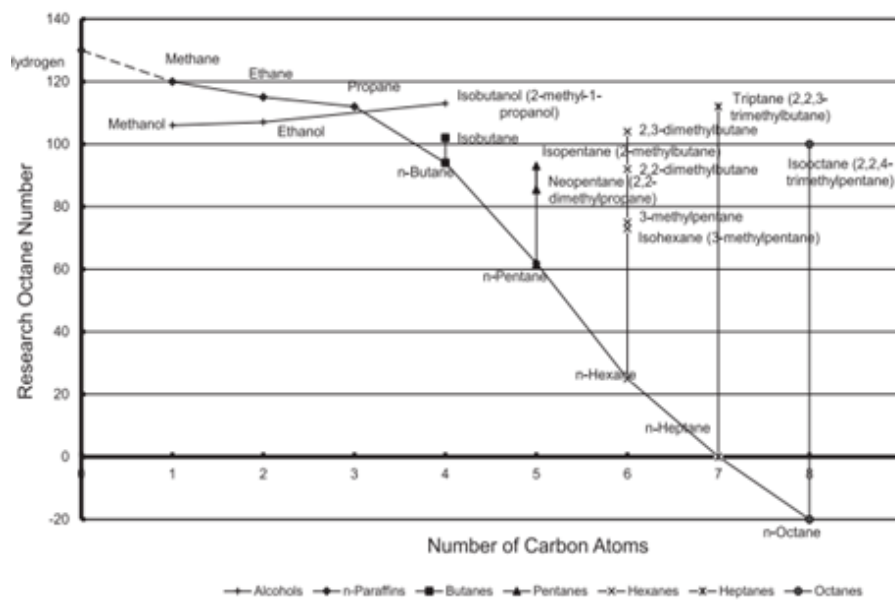


Figure 2.14 Concentration of hydrogen in various liquid state fuel compounds in terms of kg·m³ relative to LH₂ [111]

Figure 2.14 illustrates that, per unit volume, methanol contains 40% more hydrogen than liquid hydrogen (LH₂), without the significant energy demands associated with the storage of molecular hydrogen. These challenges, particularly for liquid hydrogen, are emphasized by the US Department of Energy (DoE), which illustrates the substantial energy required to maintain hydrogen at cryogenic temperatures. Methanol presents a more practical solution for hydrogen storage due to its liquid state under ambient conditions, making it a more efficient and accessible hydrogen carrier. [112]

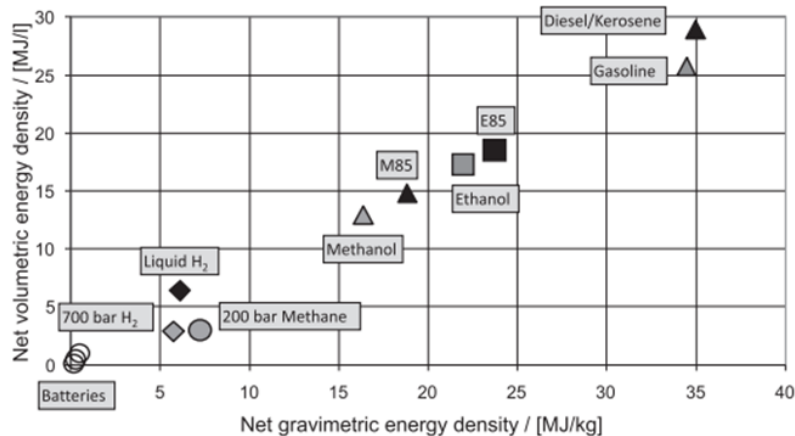


Figure 2.15 Energy storage capacity of various fuels in terms of energy stored per unit mass or volume [111]

However, methanol has a lower energy density compared to gasoline and diesel, as illustrated in Figure 2.15. This reduced energy density necessitates a larger volume of methanol to cover the same distance as gasoline or diesel, leading to higher fuel consumption for equivalent driving ranges. While methanol offers advantages such as cleaner combustion and higher knock resistance, its lower energy content per unit volume poses a challenge to fuel efficiency in vehicles. [111]

2.1.5 Ethanol

Bioethanol (E), produced from organic biomass and biodegradable feedstocks, is increasingly regarded as a potential alternative or additive to diesel fuel in ICEs. One of the primary advantages of bioethanol is its renewable nature. [113] Unlike conventional diesel, which is finite and derived from fossil reserves, bioethanol is produced from renewable agricultural sources, such as corn, sugarcane, and various other crops. The production process of bioethanol, shown in Figure 2.16, illustrates its role as a sustainable energy source that can help reduce reliance on non-renewable fossil fuels. [114]

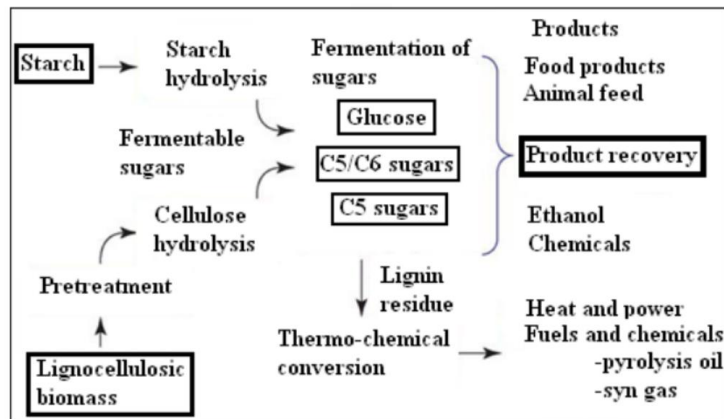


Figure 2.16 Process flow schematic for bioethanol production [114]

Another notable advantage of bioethanol is its environmental benefits. The combustion of bioethanol results in lower GHG emissions compared to conventional diesel, thereby reducing the carbon footprint of vehicles. This reduction in emissions is significant in addressing global climate change and improving air quality. In performance tests using a variable compression ratio compression ignition engine with an ethanol-diesel blend, the addition of 4% ethanol to diesel increased engine power output and efficiency while reducing BSFC at various compression ratios. The highest efficiency was observed at a compression ratio of 21, where engine efficiency increased by more than 3.5%. This illustrates bioethanol's potential to enhance both environmental performance and engine efficiency when blended with diesel. [115] The addition of ethanol to diesel can reduce the cetane number, high calorific value, aromatic content, and kinematic viscosity of the ethanol-diesel blend, while also altering the distillation temperature. To maintain the homogeneity and stability of the blend, additives are often used, alongside ignition improvers to increase the cetane number. These additives positively influence the ignition and combustion-related physical and chemical properties of ethanol-diesel blends containing 10% and 30% ethanol by volume. At high engine loads, the blended fuel significantly reduced smoke emissions compared to conventional diesel, while emissions of CO, acetaldehyde, and unburned ethanol remain relatively low. Additionally, NO_x and CO₂ emissions from the blended fuel are slightly reduced. However, at low engine loads, the smoke reduction effect is less pronounced due to the overall leanness of the mixture. The

use of additives and ignition improvers can slightly reduce the emissions of CO, unburned ethanol, and acetaldehyde from the blended fuel, with THC emissions even lower than those of diesel. This demonstrates that ethanol-diesel blends, when properly optimized with additives, offer cleaner combustion, particularly at higher loads. [116] When using ethanol-diesel blends, the ignition delay is extended, while the maximum cylinder pressure remains unaffected and the cylinder temperature decreases slightly. Compared to pure diesel, ethanol-diesel blends lead to a significant reduction in smoke density, NO_x emissions, and CO emissions. Moreover, the higher the ethanol percentage in the blend, the more pronounced the reduction, as illustrated in Figure 2.17. However, the use of ethanol-diesel blends results in an increase in THC emissions compared to pure diesel, with higher ethanol content in the blend causing a greater rise in THC emissions. [117]

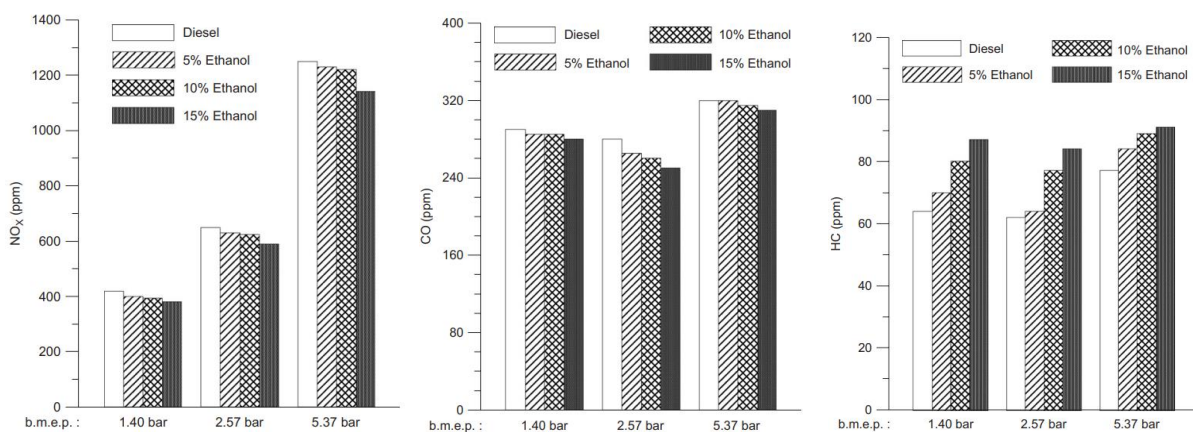


Figure 2.17 Emitted NO_x, CO and HC at 1.4 bar, 2.57 bar and 5.37 bar for neat diesel fuel and 5%, 10% and 15% ethanol blends [117]

Using bioethanol in diesel engines also presents several challenges. Firstly, bioethanol has a lower energy density compared to diesel, meaning it contains less energy per unit volume, which can potentially reduce engine performance and fuel economy. [111] Additionally, engines often require modifications to be optimized for bioethanol usage, leading to increased costs. [118][119] Another significant challenge is the competition between food and fuel. Since bioethanol production relies heavily on crops that are also used for food,

there is a risk of escalating food prices and exacerbating food scarcity in certain regions. This raises ethical concerns about diverting agricultural resources for fuel production.

Furthermore, while bioethanol combustion generates fewer GHG, the overall lifecycle emissions, considering agricultural practices and the processing of crops into ethanol, may diminish some of these environmental benefits. [113]

2.1.6 Diesel-methanol-octanol blend

Methanol and diesel are almost immiscible, which significantly limits further research and the broader adoption of methanol-diesel blends. To address this challenge, octanol has been introduced as a co-solvent to form diesel-methanol-octanol blends, which have been investigated as potential alternatives for ICEs in several studies, focusing on their combustion efficiency and emissions.

In an experimental study using a diesel and M10 fuel blend (10% methanol) supplemented with iso-octyl alcohol and iso-octyl nitrate, tested on a 4100 turbocharged intercooled diesel engine, the results indicated that the maximum cylinder pressure and peak heat release rate (HRR) of the M10 fuel were higher than those of diesel during the initial stage of combustion. Additionally, carbon smoke emissions were lower, although NO_x emissions were slightly higher compared to diesel. Conversely, when dimethyl ether was added to the M10 fuel, the maximum cylinder pressure and peak HRR were lower than those of diesel in the early combustion phase. Both NO_x and carbon smoke emissions were significantly reduced with this fuel blend. The power performance of both mixed fuels (iso-octyl alcohol/nitrate and dimethyl ether) was slightly lower than that of diesel, though the difference was minimal. HC emissions showed a slight increase, while CO emissions decreased slightly. This suggests that adding iso-octyl alcohol/nitrate and dimethyl ether to M10 fuel influences combustion characteristics and emissions in different ways, achieving a balance between NO_x and particulate emissions. [120]

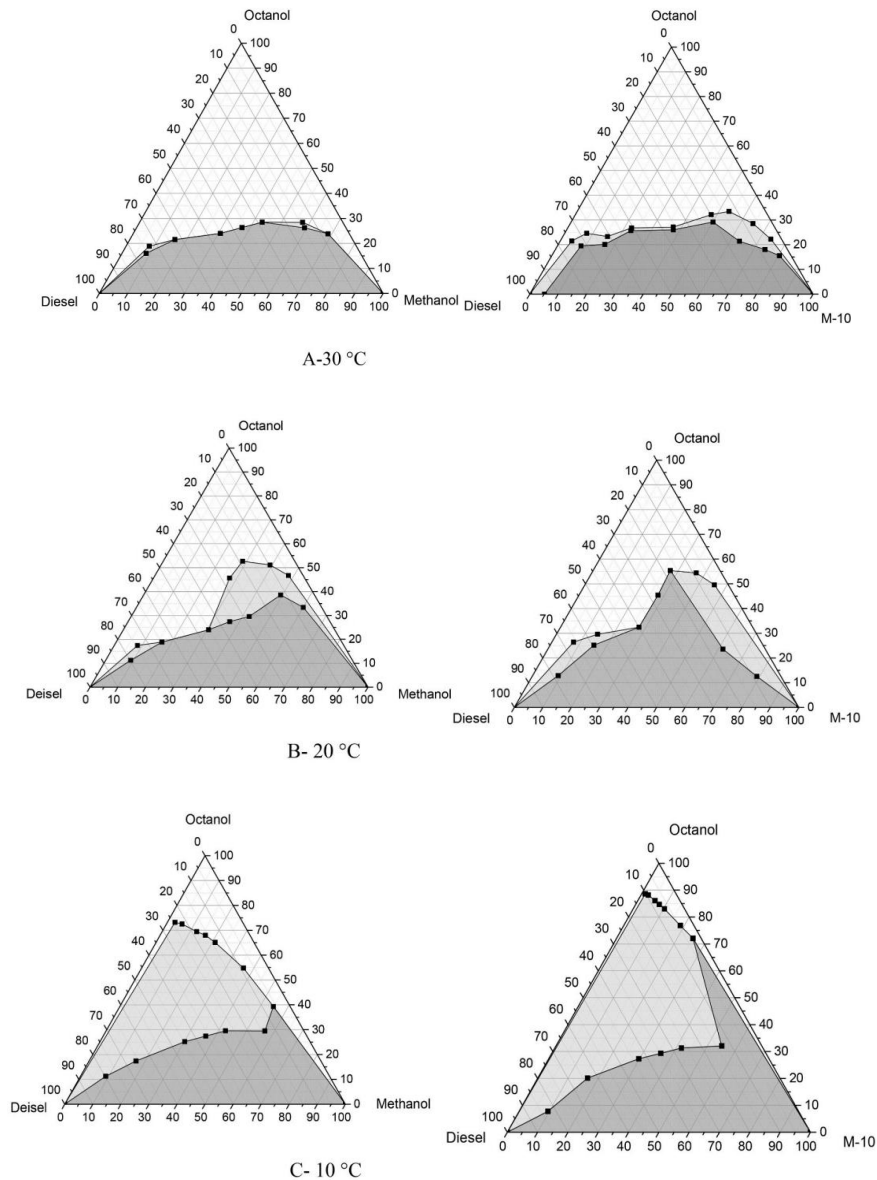


Figure 2.18 Change in the miscibility of M100 and M10-diesel manipulating n-octanol as cosolvent at 10°C, 20°C, and 30°C [121]

Another study highlighted that pure methanol (M100-diesel) and hydrated methanol (MH10-diesel) blends were unstable at temperatures of 10°C, 20°C, and 30°C, even when n-octanol was used as a co-solvent, as illustrated in Figure 2.18. In tests assessing the combustion and emission characteristics of three different M100-diesel blends DM5, DM10 and DM15—containing 5%, 10%, and 15%, M100-diesel with 25% n-octanol and 5% diethyl ether (DEE), the BTE of the blends decreased, while BSFC increased compared to pure

diesel. Additionally, the blends exhibited reductions in NO_x emissions and smoke opacity but increases in CO and UHC. When nanoparticles were added to the DM5 and DM10 blends, the results showed further reductions in NO_x, CO, UHC, and smoke opacity by up to 35%, compared to the non-nanoparticle DM5 and DM10 blends. This suggests that the inclusion of nanoparticles can improve the emissions profile of methanol-diesel blends, enhancing their potential as cleaner fuel alternatives. [121]

2.1.7 Diesel-biodiesel-ethanol blend

Biodiesel can function as an effective amphiphile in ethanol-diesel blends, making these blends a viable alternative fuel for ICEs. Studies investigating the phase behaviour of the diesel-biodiesel-ethanol (D-BD-E) ternary blend have shown that stable microemulsions can form across a wide range of the phase triangle, contingent on the concentrations of the components. The single-phase region of the D-BD-E blend is most extensive when biodiesel concentrations are higher. As diesel concentrations increase, the biodiesel-to-ethanol ratio must exceed 1:1 to maintain a stable microemulsion. This finding illustrates the critical role of biodiesel in stabilizing ethanol-diesel blends, thereby enhancing the potential for increased ethanol content and fuel blend stability. [122]

The feasibility of using biodiesel as a co-solvent and performance enhancer in diesel-ethanol blends with high ethanol content was investigated. Experiments were performed on a multi-cylinder DI diesel engine with an original injection timing of 13° crank angle (CA) before top dead centre (BTDC). At this timing, the engine unable to operate with the D50E30B20 (50% diesel, 20% biodiesel, and 30% ethanol) and D50E40B10 (50% diesel, 10% biodiesel, and 40% ethanol) blends, necessitating an advancement of the injection timing to 18° and 21° CA BTDC, respectively. Advancing the timing nearly doubled NO_x emissions and increased peak combustion pressure. The results indicated that the combustion process for these blends was delayed at low loads but closely mirrored diesel combustion at high loads. Compared to baseline diesel, the blends exhibited a significant increase in BSFC, as shown in Figure 2.19, along with a slight improvement in thermal efficiency and a substantial

reduction in smoke opacity at high loads. NO_x emissions varied depending on operating conditions, while CO emissions increased sharply at low loads. The D50E30B20 blend, which replaced 50% of diesel fuel with a blend containing 12.21% oxygen by weight, exhibited satisfactory performance during steady-state operation at speeds up to 1600 rpm. However, it did not show any advantage in reducing peak smoke emissions during free acceleration tests, underscoring some limitations in its performance under dynamic conditions. [123]

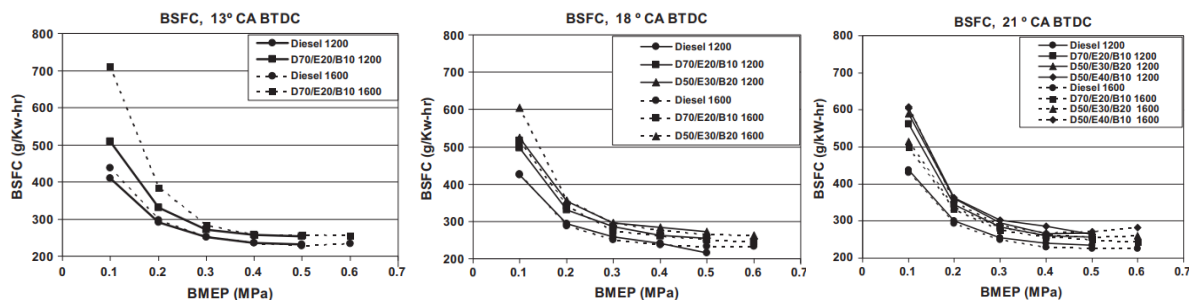


Figure 2.19 BSFC comparison of diesel and D-BD-E at 1200 and 1600rpm [123]

In another study conducted under steady-state conditions at a constant speed of 2000 rpm and three different engine loads (0.17 MPa, 0.69 MPa and 1.20 MPa), the effects of bioethanol as an additive in diesel-biodiesel blends were examined for performance, emissions, and combustion characteristics in a four-cylinder high-pressure common rail DI diesel engine. The results indicated that BTE and BSFC were higher when using diesel-biodiesel-ethanol blends compared to diesel alone. In terms of emissions, the diesel-biodiesel-ethanol blends demonstrated lower CO, NO_x, and smoke emissions than diesel. Regarding combustion characteristics, the peak pressure and peak HRR of the D75B20E5 blend (75% diesel, 20% coconut biodiesel, and 5% ethanol) were slightly lower at an operating load of 0.17 MPa. This suggests that while diesel-biodiesel-ethanol blends can improve emissions performance and fuel efficiency, their combustion characteristics may be slightly altered, particularly at lower loads. [124]

Numerical studies have been conducted to investigate the combustion performance of diesel-biodiesel-ethanol/methanol blends. When compared to pure diesel, the use of JB20

(20% jatropha biodiesel and 80% diesel) led to a reduction in thermal efficiency, whereas ethanol blends slightly improved engine thermal efficiency, with E20 (20% ethanol and 80% diesel) showing a greater improvement than JBE20 (20% jatropha biodiesel, 20% ethanol and 60% diesel). Diesel exhibited the lowest BSFC, while JBE20 had the highest BSFC due to the distinct combustion characteristics of jatropha oil and ethanol blends. In terms of emissions, JB20 increased NO_x emissions, whereas E20 and JBE20 reduced NO_x emissions, with E20 showing the largest reduction. The trend for CO₂ emissions mirrored that of NO_x, with JB20 increasing CO₂ emissions and E20 and JBE20 reducing them. Under full load conditions, diesel produced the highest PM and smoke emissions, followed by E20, while JB20 resulted in the lowest emissions. E20 also had the highest exhaust temperature, followed by JB20, with pure diesel having the lowest. The higher exhaust temperature observed in ethanol blends are due to their faster combustion rates, which alter the combustion dynamics. [125] Experimental results using Diesel-RK simulations on a single-cylinder naturally aspirated DI four-stroke diesel engine showed that, aside from a slight increase in BSFC, the emission characteristics of diesel-biodiesel-ethanol blends were better than those of diesel, with the exception of NO_x emissions, which remained higher in the blends. This suggests that diesel-biodiesel-ethanol blends offer potential benefits in terms of emissions control, though NO_x emissions may still require attention. [126]

2.1.8 Biodiesel-ethanol blend

In the study of biodiesel-ethanol blends, it was observed that the cloud point of the blended fuel decreases as the ethanol content increases, as illustrated in Figure 2.20. This suggests that the cold flow properties of biodiesel are improved with higher ethanol blending ratios. Additionally, the specific gravity of the fuel decreases linearly with increasing temperature. For instance, when 20% ethanol by volume is added to biodiesel, the specific gravity decreases by about 1.6% compared to pure biodiesel. The dynamic viscosity of the blend follows an inverse exponential relationship with temperature, meaning that viscosity decreases as temperature rises. Furthermore, as the ethanol content in the blend increases, the dynamic viscosity decreases due to the greater proportion of ethanol, which is less

viscous than biodiesel, as illustrated in Figure 2.20. This finding illustrates how ethanol enhances the fluidity and cold flow characteristics of biodiesel, making it a more viable alternative in colder conditions. [127]

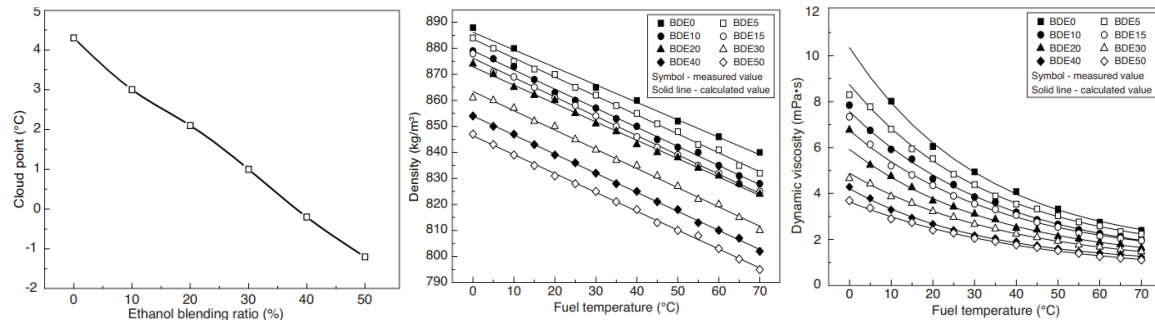


Figure 2.20 BD-E blend cloud point, density and dynamic viscosity at different blending ratio [127]

An experimental study conducted on a two-cylinder four-stroke direct injection water-cooled diesel engine, tested at five load ranging from no load to full load (3000 rpm), evaluated the performance of standard diesel, pure biodiesel, biodiesel-methanol (B85M15), and biodiesel-ethanol (B85E15) blends. The results indicated that biodiesel-alcohol blends (both B85M15 and B85E15) reduced NO_x emissions at engine loads below 70%, but they also led to increased CO and HC emissions compared to standard diesel. Among the blends, biodiesel-ethanol (B85E15) was more effective than biodiesel-methanol (B85M15) in reducing emissions and improving overall engine performance. This suggests that ethanol may be a more suitable alcohol additive than methanol for biodiesel blends, offering better emissions control and improved engine efficiency. [128]

2.1.9 Biodiesel-methanol-octanol blend

Methanol is considered a promising renewable fuel for diesel engines due to its sustainability, availability, and reasonable cost. [107] However, challenges such as phase separation, low cetane number and high latent heat of vaporization limit its use in diesel engines. To address these issues, efforts have been made to enhance the usability of

methanol by incorporating n-octanol and ethyl ether as co-solvents and ignition improvers. Experimental studies found that pure methanol and waste cooking oil biodiesel mixtures were stable at temperatures of 10°C, 20°C, and 30°C. To further improve the solubility of aqueous methanol and waste cooking oil biodiesel mixtures, n-octanol was used as a co-solvent. The engine combustion and emission characteristics were evaluated using three different ratios of methanol (15%, 25%, and 35%) with 10% n-octanol and 2.5% ethyl ether added to the waste cooking oil biodiesel. The results indicated that the maximum cylinder pressure, HRR, and pressure rise rate for the methanol and waste cooking oil biodiesel-n-octanol/ethyl ether mixtures were lower compared to pure waste cooking oil biodiesel. Additionally, the thermal efficiency of the blends decreased, while BSFC increased relative to waste cooking oil biodiesel. In terms of emissions, NO_x levels decreased with the methanol blends, but CO and smoke opacity increased compared to waste cooking oil biodiesel. These findings suggest that while methanol blends with n-octanol and ethyl ether can enhance certain aspects of engine performance, they also lead to drawbacks in fuel efficiency and emissions control. [129]

Methanol is considered a promising alternative fuel for in ICEs, but its direct use in ICEs poses significant challenges, particularly due to ignition difficulties under low-load conditions. To mitigate these issues, methanol was mixed with hydro catalytic biodiesel (HCB) using n-octanol as a co-solvent. The spray and combustion characteristics of two ternary mixtures were studied in a constant volume combustor (CVC) with a single-hole injector. The experimental results revealed an overlap between the liquid phase of the fuel and the flame for all three fuel combinations: HCB-octanol-methanol (68%HCB, 25% methanol and 17% octanol), HCB-octanol-methanol (58%HCB, 25% methanol and 17% octanol) and pure HCB. This overlap was observed across all operating points. The reduction in liquid length (LL) after ignition was more pronounced for pure HCB, attributed to its shorter lift-off length (LOL). As the methanol proportion in the blend increased, the LL also extended, mainly due to methanol's high latent heat of vaporization. Additionally, higher methanol content led to a significant reduction in soot generation within the flame. This was attributed to leaner combustion, a longer flame LOL and a higher oxygen content in the fuel

mixture, as illustrated in Figure 2.21. These findings indicate that increasing methanol content in HCB blends can help reduce soot emissions and promote cleaner combustion, although the increased LL may impact the overall combustion efficiency. [130]

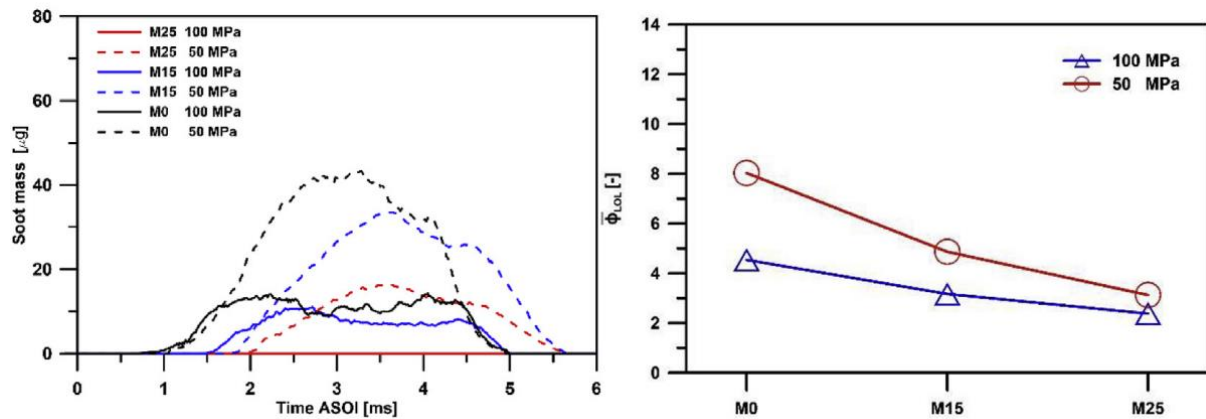


Figure 2.21 Temporal evolution of total soot mass and corresponding cross-sectional averaged equivalence ratio at LOL, 800K [130]

2.1.10 Summary

This section review explores alternative fuels for in ICEs, including diesel, two generations of biodiesel, diesel-biodiesel/HVO blends, diesel-alcohol blends, and biodiesel/HVO-alcohol blends. A comparative summary of the key findings is provided in Table 2-1.

Table 2-1 Comparison of advantages and disadvantages of various fuel types

Fuel Type	Advantage	Disadvantage
Diesel	<ul style="list-style-type: none"> High energy density [78][79] High thermal efficiency [78][79] 	<ul style="list-style-type: none"> Non-renewable [78][79] High emissions (CO, CO₂, NO_x, PM, soot) [80] High vibration levels [80]
Biodiesel	<ul style="list-style-type: none"> Renewable [89] Lower emissions (CO, CO₂, PM, soot) [92] Lower vibration [94] 	<ul style="list-style-type: none"> Poor atomization [92] Lower energy density and thermal efficiency compared to diesel [92] Higher NO_x emissions [92]
HVO	<ul style="list-style-type: none"> Renewable [97][98] 	<ul style="list-style-type: none"> Better atomization than biodiesel but inferior to diesel [104] lower content usage (<30%) [104]

	<ul style="list-style-type: none"> Lower emissions compared to biodiesel (CO, CO₂, and PM, soot) [101][102][103] 	
Methanol	<ul style="list-style-type: none"> Renewable [106] Lower emissions (HC, CO, CO₂, NO_x, PM, soot) with oxidation catalyst [108][109] 	<ul style="list-style-type: none"> Lower cetane number [110][111] Lower energy density and thermal efficiency [110][111]
Ethanol	<ul style="list-style-type: none"> Renewable [112] Lower emissions (CO, CO₂, NO_x, PM, soot) [115][116] 	<ul style="list-style-type: none"> Lower cetane number [111] Lower energy density and thermal efficiency [111] Higher THC emissions with increased ethanol content [116]
Diesel-methanol-octanol blend	<ul style="list-style-type: none"> Lower emissions (NO_x, CO, PM, soot) [120] 	<ul style="list-style-type: none"> Lower thermal efficiency [120]
Diesel-biodiesel-ethanol blend	<ul style="list-style-type: none"> Lower emissions (NO_x, CO, soot) [122] 	<ul style="list-style-type: none"> Lower engine load [122] Higher ethanol content requires advancing injection timing [122] Increases NO_x, CO, and soot [122]
Biodiesel-ethanol blend	<ul style="list-style-type: none"> Lower emissions (NO_x) compared to BD-M [127] 	<ul style="list-style-type: none"> Higher emissions (CO, HC) [127]
Biodiesel-methanol-octanol blend	<ul style="list-style-type: none"> Better atomization and lower soot compared to BD [129] 	<ul style="list-style-type: none"> Lower thermal efficiency [129] Higher emissions (NO_x, CO) compared to BD [129]

The transition to greener, more sustainable fuels is driven by the need to reduce GHG emissions, improve air quality and decrease dependence on non-renewable fossil fuels. Although diesel remains a reliable fuel source due to its high energy density, efficiency, and engine durability, it presents significant environmental challenges, particularly in terms of PM, NO_x and other pollutant emissions.

Diesel-biodiesel/HVO blends

Biodiesel, derived from renewable sources such as vegetable oils and animal fats, has been widely considered an alternative to diesel. First-generation biodiesel contains oxygen, leading to cleaner combustion and reduced PM emissions compared to pure diesel. However, biodiesel has higher viscosity and lower cold flow properties, posing challenges in

cold environments. Second-generation biodiesel, such as HVO, offers improved physical properties, including a higher cetane number and better flow properties at lower temperatures. Studies have shown that blends of diesel and HVO can effectively reduce emissions while maintaining engine performance.

Despite these advantages, the fuel atomization and combustion characteristics of diesel-biodiesel/HVO blends can be inconsistent at high biodiesel content. The addition of biodiesel/HVO alters the combustion process and may lead to increased fuel consumption and changes in the spray pattern and ignition delay. These factors affect overall engine efficiency and emissions which have yet to be fully optimized for all operating conditions.

Diesel-alcohol blends

The use of alcohols such as methanol and ethanol as additives in diesel fuels is another alternative under investigation. Alcohols improve cold flow properties and reduce NO_x and PM emissions due to their cleaner combustion and oxygen content. For instance, diesel-biodiesel-ethanol blends have been shown to decrease smoke opacity and CO emissions. However, these blends often lead to higher THC and NO_x emissions at low engine loads and require adjustments in injection timing and pressure for optimal performance.

Methanol is appealing due to its sustainability and cost-effectiveness, but its low cetane number and high latent heat of vaporization pose challenges in ICEs. The phase separation issues in diesel-methanol blends at lower temperatures, as well as the increased fuel consumption due to methanol's lower energy density, require the use of co-solvents and ignition improvers. Experimental studies using n-octanol and ethyl ether as co-solvents have shown promise, stabilizing diesel-methanol blends and improving ignition and combustion characteristics.

Biodiesel/HVO-alcohol blends

Combining biodiesel or HVO with alcohols in various ratios has been explored to harness the advantages of both fuels. For example, biodiesel-ethanol blends improve cold flow properties and reduce NO_x and PM emissions compared to diesel but may lead to increases in CO and THC emissions. Similarly, HVO-ethanol blends have shown improvements in combustion efficiency, but detailed investigations on atomization, fuel temperature and engine performance are needed, especially at high alcohol content. The high latent heat of vaporization in alcohols can influence spray and combustion dynamics leading to longer ignition delays and potential performance issues under specific conditions.

Summary of challenges

While diesel-biodiesel/HVO, diesel-alcohol, and biodiesel/HVO-alcohol blends offer promising alternatives for cleaner combustion and emissions reduction, several challenges remain. The fuel applicability, particularly in terms of atomization and combustion characteristics, is not yet fully understood under certain operating conditions, such as variations in fuel temperature, ambient temperature, and different blending ratios. Therefore, this study aims to explore the limitations of alternative fuel and multi-fuel atomization in ICEs and identify strategies to enhance their potential application, thereby contributing to the development of more sustainable and environmentally friendly engine technologies. Additionally, the study seeks to develop a comprehensive understanding of multi-fuel blend atomization characteristics by investigating the transient behaviour of droplets with various compositions and proportions, identifying conditions that promote effective atomization and improving the performance of alternative fuels in ICEs.

2.2 Fuel Atomization

2.2.1 Evaporation

In ICEs, fuel droplet evaporation begins as the liquid fuel spray is injected into the combustion chamber through a nozzle. [46] The heat energy from the surrounding

entrained gas heats the liquid fuel, causing it to evaporate. Once the fuel has travelled a certain distance (LL) from the nozzle, all the liquid fuel transitions to the gas phase. [50] The gas-phase fuel-air mixture then continues to penetrate downstream, further entraining high-temperature gas from the surrounding environment, which initiates a series of chemical reactions associated with low-temperature ignition. Following the low-temperature ignition phase, a high-temperature combustion stage occurs, during which final combustion products like CO₂ and water are formed. Concurrently, in regions where the fuel is rich and oxygen is scarce, high-temperature combustion leads to the rapid formation of soot precursors such as polycyclic PAHs. These soot precursors then generate soot particles downstream of the spray, as illustrated in Figure 2.22. [131]

The primary atomization, which is mainly based on the evaporation of droplets, directly affects the mixing efficiency and combustion speed of the fuel, also has an important impact on the generation and emission of pollutants. The evaporation formation of fuel vapor is a prerequisite for subsequent chemical reactions. The evaporation process determines the spatial distribution of the equivalence ratio and thus strongly influences the time and location of ignition. Understanding the dynamics of fuel droplet evaporation and the chemical changes that follow is crucial for optimizing combustion and reducing emissions in modern engines. [132]

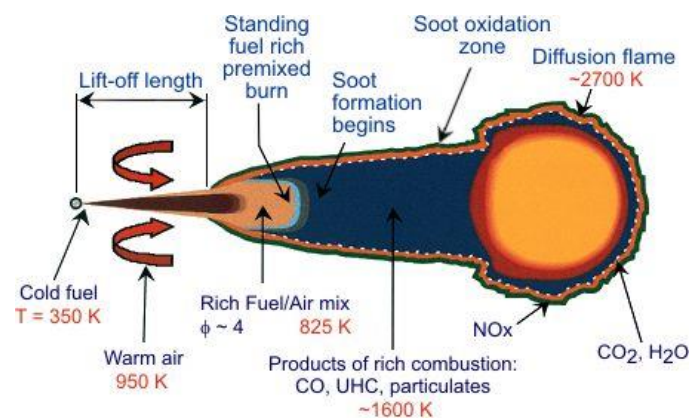


Figure 2.22 Diesel spray burning process in combustor [131]

Heat transfer mechanisms conductive, convective, and radiative facilitate the energy transfer from the high-temperature gas within the combustion chamber to the cooler fuel droplets. [46] This energy drives the evaporation process, resulting in the diffusion and convective mass transfer of fuel vapor from the droplet surface's boundary layer into the surrounding gas, as illustrated in Figure 2.23. This fuel vapor then influences the temperature, velocity, and vapor concentration in the gas phase, which are essential parameters for combustion. The close interdependence between the evaporation rate and the surrounding gas conditions means that heat and mass transfer processes are closely linked. Therefore, these processes must always be calculated together to accurately model the evaporation dynamics and their effect on combustion. This interconnectedness between evaporation and combustion has far-reaching implications for engine performance, pollutant formation, and overall fuel efficiency. [132]

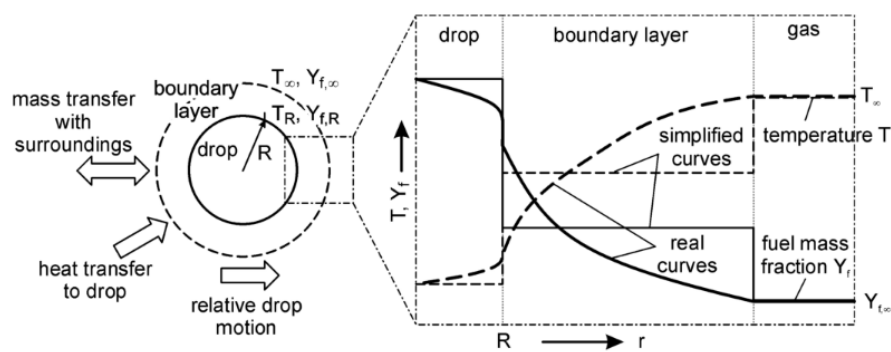


Figure 2.23 Schematic of fuel spray droplet evaporation process in combustor [132]

To mathematically describe the evaporation process of fuel droplets, several simplifying assumptions are typically made [132]:

- Radiation heat transfer. Radiation is neglected as its contribution to heat transfer is minimal compared to convective heat transfer.
- Flow field resolution. Since resolving the flow field around each droplet in a spray is impractical, evaporation models are based on average flow conditions around droplets, utilizing average transfer coefficients.

- Droplet shape. Droplets are usually assumed to be spherical, simplifying calculations of their behaviour.
- Neglecting droplet interactions. Deformation, breakup, collision and other interactions between droplets are ignored in evaporation modelling.
- Well-mixed droplet assumption. It is assumed that droplets are well mixed internally, meaning that quantities such as liquid temperature, fuel component concentration, boiling and critical temperatures, and heat of evaporation have no spatial gradients within the droplet and are only time dependent.
- Ignoring solubility and surface tension effects. The solubility of the surrounding gas in the liquid and the effect of surface tension on vapor pressure are also neglected.
- Phase equilibrium. The phase change (from liquid to vapor) is assumed to occur much faster than the transport of vapor from the surface to the surrounding gas, meaning that phase equilibrium is always reached immediately, regardless of changing conditions in the gas phase or within the droplet.

The concentration of fuel vapor and the properties of the mixed gas in the boundary layer around the droplet depend strongly on the droplet radius, as shown in Figure 2.23.

Simplified vapor concentration curves are typically used to obtain representative values for calculating diffusive mass transport in the evaporation process. [132]

Among the various theories and models describing droplet evaporation, the D^2 -law is widely used. The D^2 -law states that the square of the droplet diameter decreases linearly with time as the droplet evaporates, making it a fundamental tool in predicting the evaporation rate and lifespan of droplets in fuel sprays. This model serves as an effective representation of the complex heat and mass transfer processes that occur during droplet evaporation in ICES. [133][134]

The formula D^2 for diesel droplet evaporation in air typically describes the process by which a droplet evaporates when exposed to elevated temperatures. The derivation of this formula involves considering the effects of surface evaporation, heat and mass transfer

processes, and the relationship between the droplet surface temperature and the ambient temperature. [132] The formula D^2 can be derived as follows

1.The assumptions are typically made

- The droplet is spherical and maintains its shape during evaporation.
- The evaporation process is quasi-steady, meaning the surface temperature of the droplet changes slowly and can be approximated as constant.
- The ambient temperature is uniform, and the thermal conductivity and convection in the air do not significantly affect the temperature distribution of the droplet.

2.Mass conservation

$$\frac{dm}{dt} = -\dot{m}_e = -\rho_l \cdot A \cdot v_e \quad (2.1)$$

where, m is the droplet mass, t is time, ρ_l is the density of liquid fuel, A is the surface area of Heat conservation equation

3.Considering the heat absorbed by the droplet during evaporation

$$\frac{dQ}{dt} = h \cdot A \cdot (T_\infty - T_s) = \lambda \cdot \frac{dm}{dt} \quad (2.2)$$

where Q is the heat energy, h is the convective heat transfer coefficient, T is the ambient air temperature, T_s is the droplet surface temperature, λ is the latent heat of vaporization for liquid fuel.

4.Combining mass and heat conservation

By combining the mass conservation equation with the heat conservation equation, the evaporation rate of the droplet is

$$\dot{m}_e = \frac{h \cdot A \cdot (T_\infty - T_s)}{\lambda} \quad (2.3)$$

For a spherical droplet, the surface area A is related to the radius R by

$$A = 4\pi R^2 \quad (2.4)$$

5. Rate of change of droplet radius

The rate of change of the droplet radius over time can be expressed as

$$\frac{dR}{dt} = -\frac{\dot{m}}{\rho_l \cdot 4\pi R^2} \quad (2.5)$$

Substituting the evaporation rate into this equation gives the expression for the change in droplet radius

$$\frac{dR}{dt} = -\frac{h \cdot (T_\infty - T_s)}{\lambda \cdot \rho_l} \quad (2.6)$$

6. Derivation of formula D^2

By combining and rearranging the above equations, we arrive at the final formula D^2 , which describes the change in the droplet radius over time during evaporation

$$R(t) = \sqrt{R_0^2 - \frac{2h(T_\infty - T_s)}{\lambda \cdot \rho_l} \cdot t} \quad (2.7)$$

where, R_0 is the initial droplet radius, t is time.

Although the D^2 -law can effectively predict the evaporation rate of droplets in many cases, the evaporation process of droplets is more complex in practical applications. Several

factors contribute to evaporation in fuel droplets, such as ambient temperature, pressure, humidity and fuel components.

2.2.2 Puffing

Puffing is a phenomenon in which fuel droplets experience rapid expansion and disintegration, primarily caused by the formation of vapor bubbles inside the droplet, leading to increased internal pressure. As fuel droplets heat up while traveling through the combustion chamber of ICEs, they begin to evaporate. This evaporation occurs unevenly, especially in larger droplets. The outer layers of the droplet evaporate first, while the core retains a significant amount of liquid. Under specific temperature and pressure conditions, vapor bubbles form within the droplet's interior rather than on its surface. These bubbles are a result of localized boiling or conditions that prevent vapor from escaping, trapping it inside the droplet. As the bubbles grow, internal pressure increases. When this pressure exceeds the surface tension of the liquid shell, the droplet undergoes an explosive breakup, fragmenting into smaller secondary sub-droplets. This disintegration process is known as puffing due to the puffy, explosive appearance of the droplets during their breakup, as illustrated in Figure 2.24. [135]

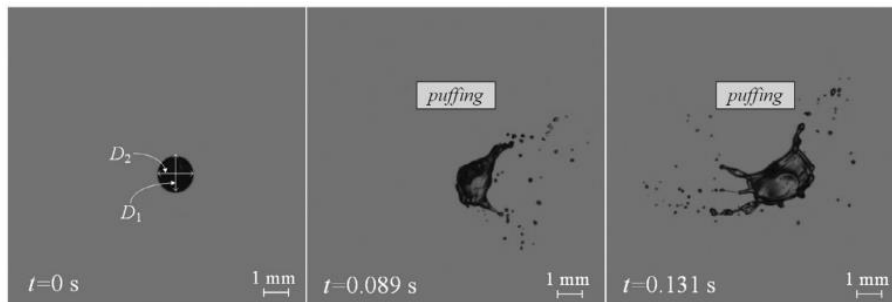


Figure 2.24 Rapeseed oil-water emulsion droplet puffing at 1120K [135]

The explosive breakup of fuel droplets significantly increases the surface area available for combustion, enhancing the combustion rate and influencing flame stability and structure. Understanding puffing is essential for optimizing fuel atomization strategies and improving

fuel combustion performance in ICEs. Several key factors contribute to the occurrence and frequency of puffing in fuel droplets as follows

- Droplet size: Larger droplets are more prone to puffing because their higher volume-to-surface-area ratio allows them to capture more heat and vapor internally before the surface layer fully evaporates. This creates favourable conditions for vapor bubbles to form within the droplet. [136]
- Temperature gradients: When there is a significant temperature gradient between the droplet's interior and its surroundings, rapid vaporization occurs at the droplet's boundaries. The surface of the droplet evaporates faster than the heat can penetrate the interior, trapping liquid and vapor inside, which leads to the formation and expansion of internal vapor bubbles, resulting in puffing. [137]
- Volatility of fuel: More volatile fuels with lower boiling points vaporize quickly and are more susceptible to puffing. Faster vaporization increases the probability of vapor bubble formation within the droplet, promoting explosive breakup. [138]
- Viscosity: Fuels with higher viscosity hinder the release of vapor from the droplets, causing vapor to accumulate internally, which facilitates puffing. [139]
- Ambient pressure: Lower ambient pressure favours vapor bubble formation within the droplet. Reduced pressure lowers the boiling point of the fuel, making it easier for vapor to form and expand inside the droplet. [140]
- Impurities and additives: The presence of additives or impurities in the fuel can affect its vaporization characteristics. These substances may act as nucleation sites for vapor bubble formation within the droplet, further promoting puffing. [141]
- Environmental conditions: If the surrounding air is saturated with fuel vapor, it reduces the rate of vapor escape from the droplet, leading to internal vapor accumulation. Additionally, droplets that are at a higher temperature before entering the combustion environment are more likely to undergo internal vaporization, increasing the chances of puffing. [142]
- Droplet interactions: In dense sprays, droplets may collide or merge, forming larger transient droplets that swell due to the heat they have accumulated. This can

increase the probability of puffing as the larger droplets trap more vapor internally. [143]

2.2.3 Micro-explosion

Micro-explosion refers to the sudden and violent fragmentation of fuel droplets into smaller sub-droplets or fragments, a phenomenon more intense than puffing, as shown in Figure 2.25. This effect is pronounced in droplets containing multiple components or phases, such as multi-fuel blends or emulsified fuels. [135]

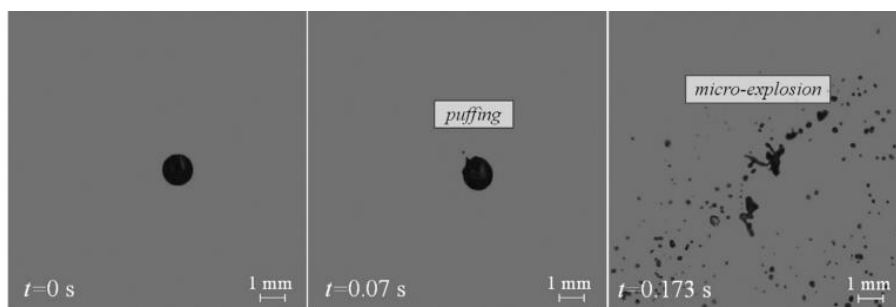


Figure 2.25 Rapeseed oil-water emulsion droplet micro-explosion at 1120K [135]

Several key factors contribute to the occurrence and frequency of micro-explosions in fuel droplets as follows

- Superheat limit: The superheat limit, or the extent to which a fuel can be heated beyond its boiling point without evaporating, impacts the intensity of micro-explosions. Fuels or mixtures with higher superheat limits can store more energy before vaporization, leading to more intense explosions when they occur. [137]
- Volatility of fuel components: In multi-fuel mixtures, components with lower boiling points tend to evaporate first, creating internal vapor pockets that increase the probability of micro-explosions. [138]
- Viscosity and surface tension: The viscosity and surface tension of the mixture also influence the intensity of micro-explosions. Higher viscosity reduces the probability

of violent explosions, while lower surface tension makes the droplets more susceptible to disintegration. [139]

- Water content in emulsified fuels: In mixtures containing emulsified water, such as biofuels or specialty emulsions, water evaporates at specific temperature thresholds. This rapid vaporization can lead to a sharp increase in internal pressure, increasing the frequency of micro-explosions. [140]
- Inhomogeneity in droplet composition: Some multi-fuel mixtures are not evenly mixed at the molecular level, leading to compositional differences within the droplet. These inhomogeneities foster conditions favourable for micro-explosions. [144]
- Energy density of fuels: The energy content of the fuels within the mixture affects the intensity of micro-explosions. Fuels with higher energy density or those that vaporize quickly can result in more violent micro-explosions. [145]

2.2.4 Secondary breakup

The breakup of fuel droplets during combustion can be categorized into two stages, primary breakup and secondary breakup.

- Primary breakup refers to the initial disintegration of a liquid fuel jet or sheet into relatively larger ligaments or droplets.
- Secondary breakup occurs when these larger droplets are further fragmented into smaller sub-droplets due to aerodynamic and internal forces.

Effective secondary breakup is crucial for creating finer sub-droplet size distributions, which leads to better atomization. Improved atomization enhances fuel-air mixing and promotes more efficient combustion. Smaller droplets vaporize more quickly and burn more completely, reducing emissions of UHC and PM. [132]

The mechanism driving secondary breakup is complex and influenced by several factors. The breakup of droplets is primarily caused by aerodynamic forces, such as friction and pressure, which arise due to the relative velocity between the droplet and the surrounding gas. These aerodynamic forces induce instabilities at the gas-liquid interface or within the droplet itself, leading to the formation of smaller sub-droplets. As aerodynamic forces act on the droplet, surface tension tries to counteract these deformations by maintaining the spherical shape of the droplet. The surface tension's strength depends on the droplet's size and curvature: smaller droplets exhibit greater surface tension, requiring higher critical relative velocities for instability and breakup to occur. The interaction between aerodynamic forces and surface tension can be described using the Weber number. The Weber number (We) is a dimensionless parameter that expresses the ratio of the aerodynamic forces acting on the droplet to the surface tension forces. This behaviour is expressed in terms of the gas phase Weber number

$$We_g = \frac{(\rho_g \cdot u_{rel}^2 \cdot d)}{\sigma} \quad (2.8)$$

where d is the droplet diameter before break-up, σ is the surface tension between liquid and gas, u_{rel} is the relative velocity between droplet and gas, and ρ_g is the gas density. The Weber number represents the ratio of aerodynamic (dynamic pressure) and surface tension forces. [132] A higher Weber number indicates stronger aerodynamic forces relative to surface tension, leading to greater deformation and more intense secondary breakup. As the droplet size decreases and surface tension increases, the Weber number must reach a critical value for the droplet to break up, as shown in Figure 2.26. [146]




















Category					Weber Number
Vibrational breakup					~ 12
Bag breakup					< 20
Bag/ streamer breakup					< 50
Stripping breakup					< 100
Catastrophic breakup					> 100

Figure 2.26 Droplet breakup regimes with corresponding Weber numbers [146]

Study distinguishes between seven different droplet breakup modes [147], which are all described using semi-empirical relationships for the resulting droplet sizes and breakup times,

$$t_{bu} = \tau_{break} \frac{d}{u_{rel}} \cdot \sqrt{\frac{\rho_l}{\rho_g}} \quad (2.9)$$

where τ_{break} is given in Table 2-2. Some of them appear within the same range of the Weber number.

Table 2-2 Breakup modes and breakup times of droplets with different Weber number [147]

Break-up mode	Break-up time τ_{break}	Weber number
Vibrational	$\frac{\pi}{4} \left[\frac{\sigma}{\rho d^3} - 6.25 \frac{\mu_l}{\rho_l d^2} \right]^{-0.5}$	$W_{eg} \approx 12$
Bag	$6(W_{eg} - 12)^{0.25}$	$12 \leq W_{eg} \leq 18$
Bag and streamer	$2.45(W_{eg} - 12)^{-0.25}$	$18 \leq W_{eg} \leq 45$
Chaotic	$14.1(W_{eg} - 12)^{-0.25}$	$45 \leq W_{eg} \leq 100$
Sheet stripping	$14.1(W_{eg} - 12)^{-0.25}$	$100 \leq W_{eg} \leq 350$
Wave crest stripping	$0.766(W_{eg} - 12)^{0.25}$	$350 \leq W_{eg} \leq 1000$
Catastrophic	$0.766(W_{eg} - 12)^{0.25}$	$1000 \leq W_{eg} \leq 2760$

2.2.5 Auto-ignition

The auto-ignition of hydrocarbons in diesel engines involves a chain-branching process, which includes four key reaction stages: chain initiation, propagation, branching and termination. Ignition occurs following a specific induction period known as the ignition delay. During this delay, the fuel vaporizes, forming an ignitable mixture with an air-fuel ratio between 0.5 and 0.7. For combustion to begin, sufficient fuel radicals must be produced through chemical reactions. Initially, chain initiation generates radicals from stable fuel molecules, but this process is slow. Once a critical concentration of radicals is reached, chain propagation and branching reactions accelerate the production of additional radicals. While chain propagation alters the nature of the radicals, chain branching significantly increases their number, speeding up the reactions and ultimately leading to ignition. The ignition delay is highly temperature-sensitive, with shorter delays at higher temperatures. [132]

The multi-stage ignition process can be classified into three temperature regimes: low-temperature (cool flame regime), intermediate-temperature and high-temperature oxidation. The cool flame regime occurs at temperatures between 600 and 800 K, with slow reactions and minimal temperature increase. As the temperature rises, radical production decreases due to faster reverse reactions, known as degenerate chain branching. This intermediate regime is marked by the negative temperature coefficient (NTC) effect, which lengthens the ignition delay at higher temperatures. Once the cylinder charge reaches a critical temperature, the heat from the cool flame reactions triggers high-temperature chain branching reactions ($T > 1000\text{K}$), culminating in combustion. [132]

2.2.6 Summary

After reviewing the literature on multi-fuel blends, extensive studies on the atomization characteristics of these blends were explored. Fundamental concepts such as evaporation, puffing, micro-explosion, secondary breakup and auto-ignition were detailed with particular

emphasis placed on puffing, micro-explosion and secondary breakup due to their significant impact on fuel efficiency. Figure 2.27 illustrates the known regimes of fuel emulsion droplet behaviour during heating, thermal expansion, evaporation, puffing and micro-explosion. Each regime is influenced by factors such as droplet composition, temperature and surrounding conditions.

Monotonous evaporation regime: In this regime, the fuel droplet undergoes rapid heating and evaporation without breaking into secondary fragments, as shown in Figure 2.27 (a).

Puffing regime: Puffing occurs when bubble nucleation takes place locally within the droplet rather than throughout the entire volume. In this case, the bubble's implosion leads to small droplet fragments breaking off, as shown in Figure 2.27 (b). This regime is characterized by minor disruptions to the droplet, but enough to enhance evaporation rates and atomization.

Micro-explosion regime: This regime is characterized by intense bubble nucleation throughout the entire volume of the droplet, typically occurring at higher gas temperatures or with higher concentrations of volatile components in the liquid. As shown in Figure 2.27 (c), the droplet initially remains intact during heating, suddenly loud popping sound signals the instant fragmentation of the droplet into an aerosol. The micro-explosion significantly accelerates the evaporation process, producing a fine mist of fuel vapor and enhancing combustion efficiency. [149]

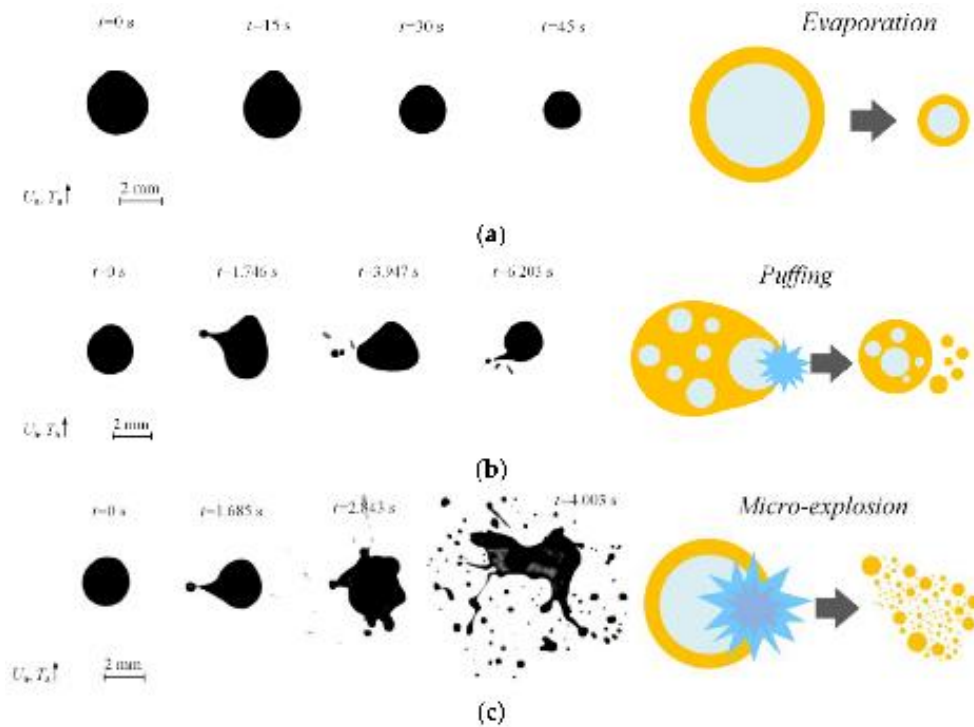


Figure 2.27 Schemes of droplet evaporation, puffing and micro-explosion regimes: (a) evaporation ($T_a = 473 \pm 5$ K), (b) puffing ($T_a = 573 \pm 5$ K), (c) micro-explosion ($T_a = 673 \pm 5$ K) [148]

Recent research has highlighted the significance of these phenomena in enhancing fuel atomization, facilitating better fuel-air mixing and optimizing the overall combustion process. Understanding these mechanisms has become central to optimize multi-fuel blends for ICEs. The behaviour of fuel droplets under varying conditions, particularly during puffing and micro-explosion, is crucial for determining how different liquids perform in combustion. These phenomena involve the rapid expansion and breakup of fuel droplets, which leads to finer droplet sizes and increases the surface area for combustion, ultimately improving fuel efficiency and reducing emissions. The specific factors of puffing and micro-explosion for different liquids have been summarized in Table 2-3. The key factors influencing the occurrence and frequency of puffing, micro-explosions, and secondary breakup include temperature gradients between the droplet and its surrounding environment, as well as fuel composition, such as blending ratios and the presence of water or gas additives, which require further investigation.

Table 2-3 The factors of droplet puffing and micro-explosion for different liquids

Composition	Factors Covered
Water-in-diesel emulsion [136]	- Parent droplet size - Viscosity, interfacial, and surface tension
Biodiesel-acetone-butanol-ethanol (ABE) blends [137]	- Component concentrations
Diesel-biodiesel-ethanol blends [138]	- Component concentrations
Rapeseed oil-water-coal-microparticles) [139]	- Concentration, size and type of solid coal particles
Diesel-biodiesel-ethanol emulsion [150]	- Fragmentation regimes
Biodiesel-ethanol blends [151]	- Ethanol content - Heating temperature - Gas flow
GTL-diesel blends [152]	- Component concentrations - Fragmentation regimes
Water-in-sunflower oil emulsion [153]	- Diameter of the dispersed water - Surface and kinetic energies
Diesel-rapeseed oil-water [154]	- Energy supply scheme - Holder material - Component concentration - Parent droplet size - Parent droplet type
Rapeseed oil-water droplets [155]	- Initial water temperature
Rapeseed oil-water droplets [156]	- Ambient gas temperature
Diesel-rapeseed oil-water droplet [157]	- Joint effects during micro-explosion

2.3 Evaporation, Puffing, Micro-explosion and Secondary Breakup Impact Factors

2.3.1 Temperature gradient impact

Temperature is a critical factor in determining puffing and micro-explosion behaviour. Puffing typically occurs at 400-600K while micro-explosion happens at 600-1500K. Higher temperatures result in more intense micro-explosions and producing more sub-droplets with smaller sizes. Increased temperature also leads to a larger surface area for evaporation thereby enhancing evaporation efficiency. [149]

The ambient gas temperature affects both the breakup regime and the size of the resulting sub-droplets. References indicate that as the temperature rises, the average size of the sub-droplets decreases which significantly increases the free surface area of fuel and air after breakup. As the temperature of the gas medium increases, the total breakup time of droplets decreases nonlinearly. They also found that in the temperature range of 523–623K, the differences in breakup times for multicomponent droplets are the largest, reaching up to 50-60%. Above 673K, the heating and breakup times of the droplets tend to stabilize. For two-component droplets (water and oil), explosive breakup becomes more prominent as the temperature rises to 773K, especially when the water fraction is low (3%), significantly shortening the breakup time. [156][158] Additionally, in higher temperature ranges (673–823K), the heating of all droplet layers becomes significant due to thermal conduction and convection, leading to increased bubble growth and number near the interfaces, which accelerates the droplet breakup and produces a large number of fine child droplets. At a high gas flow temperature of 623K, droplets containing four components (water, oil, kerosene, and petroleum) showed a more than 30-fold increase in evaporation surface area after breakup. This phenomenon is linked to the increased number of interfaces between components with different thermophysical, rheological, and thermodynamic properties.[156]

2.3.2 Fuel composition impact

Puffing and micro-explosion phenomena in fuel droplets are greatly influenced by the composition of the fuel, particularly in emulsified mixtures of hydrocarbons with water. [135]

Various studies have investigated how the inclusion of different fuel components, such as water, alcohols and biofuels, affects the droplet dynamics, particularly under high-temperature conditions. [149][150][151] The type of hydrocarbon used in the emulsion influences the puffing and micro-explosion phenomena. For instance, adding flammable liquids like petroleum or kerosene can shorten the heating time, promote bubble

nucleation, and accelerate the explosive breakup of the droplets. The thermal and physical properties of the components in the droplets also determine the breakup mechanisms under different conditions, such as puffing and micro-explosion. Adding a small amount of petroleum can significantly increase the number of sub-droplets formed after breakup, while adding a third component, such as kerosene, can reduce the breakup time and greatly increase the evaporation surface area. [156] Biodiesel which has a higher boiling point than water remains stable at lower temperatures but starts contributing to micro-explosion as temperatures approach its boiling point. [159]

Lighter hydrocarbons such as alcohols have lower boiling points and can induce puffing at lower temperatures, similar to water. The characteristics of the sub-droplets are also influenced by the composition of the initial droplet. [160] Research has shown that the number, size and velocity of sub-droplets are strongly affected by the surface tension and viscosity of the multi-component liquid. Adjusting these liquid properties can enhance the efficiency of the micro-explosion process by 6 to 7 times. [161]

2.3.3 Water and gas additives impact

2.3.3.1 Water in fuel

Figure 2.28 illustrates the different temperature regimes where evaporation, boiling, puffing and micro-explosion occur for two-liquid droplets containing 95% distilled water and 5% kerosene. The behaviour of the blend is predominantly influenced by the lower boiling point of water, leading to increased droplet activity at lower temperatures compared to pure kerosene. The addition of water to the fuel blend significantly enhances the droplet's activity at lower temperatures. Water evaporates and boils much earlier than kerosene (starting at 373 K), leading to an early onset of puffing and micro-explosion phenomena. This increased internal pressure, driven by water vapor, leads to puffing at around 523 K and micro-explosion at around 623 K. In contrast, pure kerosene droplets remain relatively stable at these lower temperatures due to the higher boiling point of kerosene. Puffing

caused by the localized boiling of water inside the droplet, creates intermittent vapor bursts that increase droplet activity at relatively low temperatures. As temperature increases above 573 K, puffing becomes more intense and the droplet transitions into the micro-explosion regime. The micro-explosion occurs when vapor bubbles from both water and kerosene rapidly expand, causing the droplet to rupture violently into smaller fragments. This rapid fragmentation increases the evaporation surface area, promoting efficient fuel atomization. Water addition to the fuel blend facilitates early evaporation and puffing, increasing internal pressure at lower temperatures, which leads to micro-explosion at around 623 K. This phenomenon significantly enhances fuel atomization, improves combustion efficiency and potentially reduces emissions by creating a homogeneous fuel vapor-air mixture. The presence of water accelerates the droplet's response to heat, resulting in more intense activity at lower temperatures. [162]

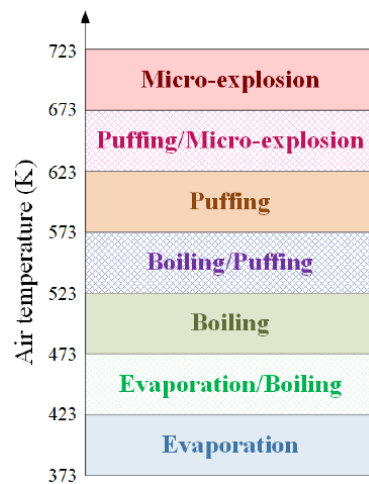


Figure 2.28 Temperature ranges of droplet behaviour regimes of kerosene- distilled water emulsion , $V_d = 15 \pm 1 \mu\text{L}$, $U_a = 2 \pm 0.1 \text{ m/s}$ [162]

Figure 2.29 reveals micro-explosion mechanism of water emulsified diesel droplet. Micro-explosion is typically caused by superheating at the water-fuel interface. The rapid expansion of water droplets in the fuel leads to explosive fragmentation, producing multiple smaller sub-droplets and significantly increasing the evaporation surface area. [163] Water-in-fuel emulsions promote micro-explosion, which enhances combustion efficiency. As

water droplets in the emulsion evaporate during heating, they cause rapid fragmentation and secondary atomization of the fuel. The size and concentration of water droplets in the emulsion have a significant impact on the intensity of micro-explosion. Smaller water droplets tend to induce more intense micro-explosion events. Thus, the presence of water facilitates early vaporization and increases the droplet's internal pressure, which enhances the probability of puffing and micro-explosion at lower temperatures. This results in more efficient fuel atomization, potentially improving combustion performance by creating smaller droplets through micro-explosions. In summary, water addition accelerates the droplet's response to heat, leading to more intense droplet activity at lower temperatures.

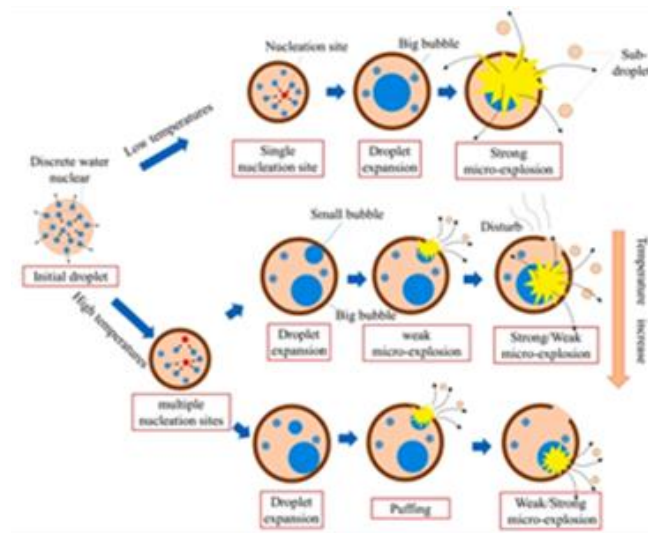


Figure 2.29 Micro-explosion mechanism of water emulsified diesel droplet [163]

Another study also emphasizes the importance of the puffing and micro-explosion phenomena, where the rapid vaporization of water within the emulsion causes the fuel droplet to explode, leading to secondary atomization. This process significantly improves air-fuel mixing, leading to more efficient combustion. The water vaporization process cools the combustion temperature, leading to lower NOx emissions, while the presence of water reduces soot formation and enhances the burnout of soot particle. Different water content levels in the emulsion can have varying effects on engine performance. Research suggests

that water-in-diesel emulsions can improve BTE and reduce fuel consumption due to the improved atomization caused by micro-explosion. [164]

A study examines the microstructure of emulsions using optical microscopy and dynamic light scattering techniques, revealing that adjusting the Span80 to Tween80 ratio allows optimization of the Hydrophile-Lipophile Balance (HLB) to produce smaller droplet sizes. Optimal performance occurs at an intermediate HLB (9.7). Higher surfactant concentrations (10%) lead to smaller droplets and greater stability, forming nano emulsions with droplet sizes as small as 159 nm. Emulsions with 10% surfactant concentration remained stable for up to 50 days at 298 K, exhibiting no macroscopic phase separation and only a slight increase in droplet size from 159 nm to 330 nm. [165]

2.3.3.2 Gas in fuel

The introduction of microbubbles into liquid fuels has been shown to enhance atomization, leading to smaller droplet sizes during fuel injection. This occurs because the presence of gas bubbles within the fuel reduces surface tension and increases turbulence, improving fuel-air mixing in the combustion chamber. Improved atomization results in more uniform combustion, as smaller fuel droplets provide a larger surface area for vaporization and mixing with air, contributing to more complete combustion.

A study investigated the effects of microbubble (MB)-mixed fuels on performance and emissions in a single-cylinder four-stroke diesel engine under varying engine speeds. The MBs were generated via the hydraulic cavitation method using a Venturi nozzle in diesel fuel (D100) and a diesel-biodiesel blend (BD10). The results indicated that the presence of MBs led to a slight decrease in both the density (up to 0.013%) and calorific value (up to 0.123%), while viscosity increased by up to 0.025% for both fuel types. Regarding performance, the MB-mixed B10 fuel showed an average improvement of 1.5% in brake thermal efficiency (BTE) and a reduction of 1.4% in brake specific energy consumption (BSEC). However, in terms of emissions, an increase in CO₂ and NO_x emissions was observed when MBs were

incorporated into both fuel types. In conclusion, the study found that an engine fuelled with MB-mixed B10 demonstrated better efficiency in performance and emissions compared to MB-mixed D100. Given their ease of production and low cost, MBs hold significant potential as a fuel additive. [166] Another study investigated the presence and long-term stability of hydrogen nanobubbles (HNBs) in gasoline fuel, as shown in Figure 2.30. A HNB–gasoline blend was fabricated using a nanobubble generator, which consists of a gas–liquid dispersion system. After generating HNBs in gasoline, the presence and stability of HNBs in the blend were experimentally examined over a period of 121 days at a constant temperature of 298.15 K using nanoparticle tracking analysis (NTA). The results indicated that the mean diameter and concentration of HNBs were 159.00 ± 31.91 nm and $11.25 \pm 2.77 \times 10^8$ particles/ml, respectively, immediately after generation. After 121 days, no significant changes were observed in the mean diameter or concentration of the HNBs. Gas chromatography/mass spectrometry (GC/MS) analysis suggested that certain compounds in the HNB–gasoline blend might acquire functional groups through replacement reactions, leading to a decrease in non-main components. Additionally, the zeta potential (ζ -potential) of the HNB–gasoline blend was approximately -30 mV after 121 days, confirming the existence and stability of HNBs in gasoline fuel over an extended period. [167]

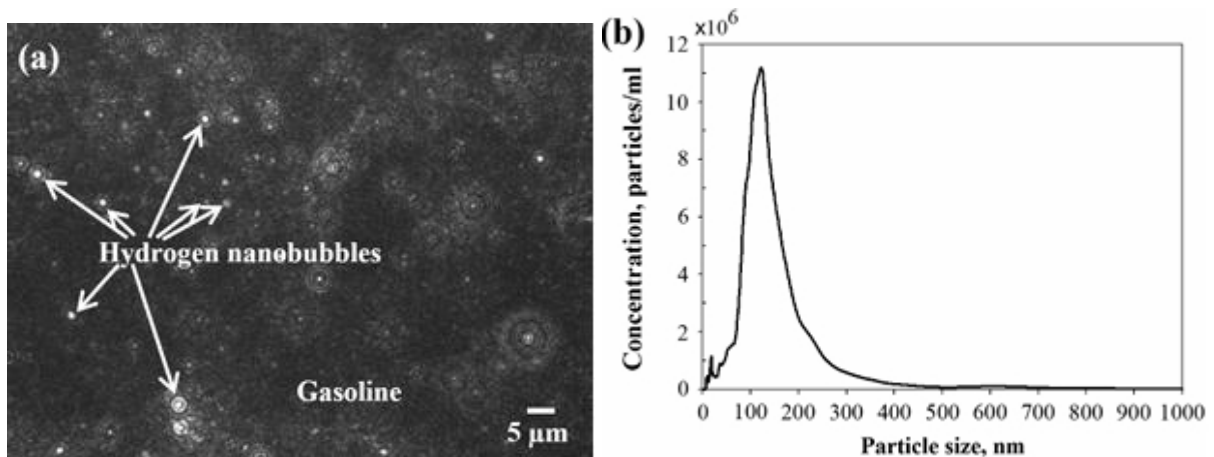


Figure 2.30 (a) Image of HNBs in gasoline. (b) Size distribution of HNBs just after nanobubble fabrication [167]

Gas bubbles particularly when oxygenated can enhance the oxygen content of the fuel. These bubbles dissolve within the fuel which can supply additional oxygen during combustion. This results in improved combustion efficiency as oxygen-rich fuels burn more completely. Studies have shown that oxygen-enriched fuels decrease the formation of CO and UHC due to more complete oxidation of the fuel components. The study observed that the dissolved oxygen from bubbles in fuel improved combustion characteristics, resulting in a reduction in specific fuel consumption and an increase in BTE. The research on gas bubble injection particularly micro and nano-sized bubbles into liquid fuels has demonstrated significant impacts on combustion efficiency and emission characteristics. [168][169]

Improved combustion has been shown to reduce PM and UHC, as demonstrated in several studies. However, the increase in combustion temperature resulting from enhanced fuel oxidation can also lead to higher NO_x emissions. This is because NO_x formation is strongly linked to combustion temperature and the availability of oxygen, both of which are affected by the presence of oxygenated bubbles in the fuel. [170]

2.4 Summary

This chapter has highlighted the ongoing need to improve ICEs for health, environmental, efficiency and legislative motives. From the strategies discussed, two were selected as key focal points for this thesis, utilizing multi-fuel blends including diesel, biodiesel, and bio-alcohol as alternative fuels, and enhancing their atomization efficiency at high temperatures. The chapter began with a review of diesel, biodiesel, HVO and their blends using in current ICEs, making the case for the continued necessity of ICEs despite the push for hybrid and EVs.

The next section explored fundamental concepts related to multi-fuel blends, such as diesel-alcohol and biodiesel/HVO-alcohol blends. It was argued that the applicability of these blends under certain conditions remains unclear, particularly regarding factors like temperature and blending ratios. This gap was identified as the first aim of this thesis.

Following the literature review, studies on the atomization characteristics of multi-fuel blends were examined. Key concepts such as evaporation, puffing, micro-explosion, secondary breakup and auto-ignition were discussed, with particular emphasis on puffing, micro-explosion and secondary breakup due to their crucial role in improving combustion efficiency. A dedicated section reviewed the factors influencing the occurrence and frequency of these phenomena, focusing on the evolution of temperature gradients and the impact of fuel composition—both of which are core concerns of this study.

A gap was identified in the literature regarding the physical and chemical characteristics of multi-fuel blends, particularly in terms of factors influencing the intensity of puffing, micro-explosion and secondary breakup. These phenomena are vital for optimizing combustion processes and addressing this gap was established as the second aim of this thesis.

The final part of the chapter addressed the use of water and gas additives in multi-fuel blends, reviewing the current understanding of their effects on fuel atomization. Conflicting results from various studies were evaluated, revealing that while water and gas additives can significantly affect atomization, the extent and nature of their impact remain uncertain. These inconsistencies illustrate the need for further investigation to clarify their role in enhancing or fuel atomization efficiency.

In summary, while substantial progress has been made in identifying alternatives to conventional diesel for ICEs, challenges remain in optimizing blends of biodiesel, HVO and alcohols. Further research is crucial to better understand fuel stability, atomization, combustion characteristics and emissions under different conditions. A deeper understanding of these parameters is key to unlocking the full potential of these blends for reducing environmental impact while maintaining engine performance and efficiency. This study seeks to shortlist potential fuel blends suitable for current ICEs and evaluate their atomization characteristics under controlled ambient conditions.

Chapter 3 Experimental Techniques and Methodologies

3.1 Experiment Equipment

In this study, physical experiment was conducted using the Liquid Droplet Behaviour Observation System (LDBOS) at the Centre for Advanced Powertrain and Fuels (CAPF), Brunel University London, UK. The LDBOS is designed to analyse the transient behaviours of fuel droplets in high-temperature gaseous environments simulating the conditions in ICEs, as illustrated in Figure 3.1 and Figure 3.2. This system enables detailed observation of droplet behaviours such as evaporation, puffing, micro-explosion and secondary breakup, providing critical insights into the atomization characteristics of multi-fuel blends under engine-relevant conditions.



Figure 3.1 Multi-fuel blends microdroplet transient behaviours test setup LDBOS

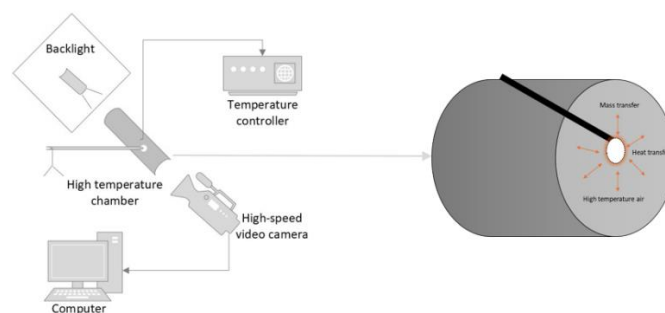


Figure 3.2 Schematic diagram of the LDBOS

As discussed in Chapter 2, replicating the operating conditions of a diesel engine combustion chamber particularly within the temperature range of 573K to 773K requires the integration of several specialized systems. The LDBOS used in this study is composed of four major modules.

- Fuel droplet heating module: This module is designed to simulate the high-temperature environment that fuel droplets experience in a combustion chamber. It ensures that the droplets are exposed to controlled engine-relevant temperatures ranging from LLPT to HLPT.
- Fuel droplet observation module: This module captures high-speed, real-time imagery of the droplet behaviours. It allows for detailed observation of phenomena such as evaporation, puffing, micro-explosion and secondary breakup.
- Fuel droplet generation module: This module is responsible for producing uniform droplets of the fuel and fuel blend under investigation, ensuring consistent size and volume for accurate comparison and analysis.
- Fuel droplet transportation module: This module ensures the controlled delivery of droplets to the observation chamber, maintaining stability during the experiment to precisely monitor the transient behaviours of the droplets.

The detailed specifications for experiment setup are provided in Table 3-1, illustrating the capabilities and parameters of each module used to replicate combustion chamber conditions and observe fuel droplet behaviours effectively.

Table 3-1 Experiment setup specifications and operational condition

Experiment setup	Specifications
Light source	Single LED bulb, 10W/220V
White shadow board	L250mmxH250mmxt10mm
Insulation quartz glass	Ø100mmxt30mm
Heat element	Watlow ST. LOUIS, 1200W 1518 MB2A2AN2Metal, Stainless Steel Nozzle Heater Maximum Operating Temperature 1033K

Heat controller	Watlow ST. LOUIS, EZ-Zone PM Controller 4= 1/4 DIN Panel Cut-out 92 mm X 92 mm
High-speed camera	Phantom Miro 4 (maxi FPS 35,000) Lens: Tokina atx-I Macro-lens
Stirrer	Magnetic stirrer with heating, RET basic, Temperature (0~613K), Speed (0~1700rpm)
Micro pipettor	SP002.5-AUTO SciPette Autoclavable Variable Pipettor 0.1 - 2.5µl Volume,
Thermocouple	K type, temperature: 0~900°C, diameter: 75 µm, heat conductivity: 80 W/m·K
Thermometer	RS 206-3722

3.1.1 Fuel droplet heating module

The fuel droplet heating module comprises several key components, a nozzle heater, digital temperature controller, metal furnace, thermocouple, thermometer and two insulation glasses.

The nozzle heater used in this study is a high-performance MI (mineral insulation) nozzle heater sourced from Watlow ST. LOUIS in the United States. This heater stands out for its superior thermal conductivity, utilizing a thin layer of MI material to insulate the element wire from the heater sheath. Additionally, a thicker layer with lower thermal conductivity supports the element wire, directing heat inward towards the heated part, optimizing heat transfer efficiency. This results in lower wire temperatures and longer heater lifespan, making it suitable for raising the experimental environment temperature. The Watlow ST. LOUIS nozzle heater is mounted on a metal tube to heat the internal air during testing.

The temperature controller used is the EZ-Zone PM Controller, also from Watlow ST. LOUIS. This controller is based on a PID algorithm that works in tandem with the nozzle heater, K-type thermocouple and thermometer to regulate the internal air temperature within the furnace during the experiments.

The metal furnace used in this study is a $\varnothing 50 \times L 70$ mm 316L stainless steel tube, capable of operating at temperatures up to 973K. It creates a high-temperature gas environment for the test fuel droplet. Insulation glasses are mounted on both ends of the tube to maintain consistent internal temperatures.

3.1.2 Fuel droplet observation module

The fuel droplet observation module includes a high-speed camera, sunshade and light source.

The Phantom Miro 4 high-speed camera is used for capturing fuel droplet behaviours, chosen for its exceptional imaging capabilities and ability to capture fast-moving phenomena. With a maximum frame rate of 1,500 frames per second (FPS) at full resolution, this camera is utilized for studying the rapid and complex motions of fuel droplets, such as their evaporation, dispersion and combustion characteristics.

A sunshade is used in conjunction with the camera. The sunshade allows light to pass through the fuel droplet forming a shadow for the camera to capture while also reducing the intensity of the light beam to protect the camera from damage.

The light source is a 10W/220V LED bulb, providing strong white light that passes through the sunshade and illuminates the fuel droplet. This setup helps to cast a clear droplet shadow, allowing the high-speed camera to capture detailed images of the droplet's behaviours.

3.1.3 Fuel droplet generation module

The fuel droplet generation module consists of a pipettor with micro pipette filter and a thermocouple.

The pipettor used in this study is sourced from SciQuip and has a volume range of 0.1 to 2.5 μL . The fuel droplet is generated by adjusting the volume scale on the pipettor and injecting the desired amount of fuel through the micro filter at the front of the thermocouple. The resulting fuel droplet is typically spherical or near spherical in shape, ensuring consistent and controlled testing conditions.

3.1.4 Fuel droplet transportation module

The fuel droplet transportation module includes a slide rail and a slider.

The slider consists of a slide block and a cylinder stand, which forms an integrated movable carrier for the fuel droplet. This system allows precise transport of the fuel droplet into and out of the high-temperature experimental environment.

The slide rail made of stainless steel is mounted on the experiment table. It facilitates smooth and accurate movement of the slider, ensuring that the fuel droplet is correctly positioned inside the high-temperature testing area. The material ensures the rail can operate effectively in high-temperature environments.

3.2 Experiment Subjects and Materials

3.2.1 Experiment test fuel and properties

In this study, fuels were utilized for testing including diesel, biodiesel, HVO and bio-alcohols methanol, ethanol and octanol. The properties of these fuels are presented in Table 3-2. The specific sources of these fuels are as follows

- Diesel was sourced from Shell UK, marketed as their Regular Diesel variant.
- Biodiesel was procured from ZhongKai, China, with the product code ZK-1082.
- HVO was obtained from New Era, UK, under the product name GreenD + HVO.
- Alcohols (methanol, ethanol, octanol) and UREA were sourced from Merck, UK.

The tested fuels were categorized into three groups based on their composition as follows

1) Single fuels

- Diesel (D100)
- Biodiesel (BD100)
- HVO (HVO100)

2) Binary fuel blends (by volume percentage)

- Diesel-Water Emulsion: D65W35
- Diesel-Biodiesel Blends: D90BD10, D80BD20, D70BD30, D60BD40, D50BD50, D40BD60, D30BD70, D20BD80, D10BD90
- Diesel-HVO Blends: D90HVO10, D80HVO20, D70HVO30, D60HVO40, D50HVO50, D40HVO60, D30HVO70, D20HVO80, D10HVO90
- Biodiesel-Ethanol Blends: BD90E10, BD80E20, BD70E30, BD60E40, BD50E50, BD40E60, BD30E70, BD20E80, BD10E90

3) Ternary fuel blends (by volume percentage)

- Diesel-Methanol-Octanol Blends: D90M5O5, D80M10O10, D70M15O15, D60M20O20, D50M25O25, D40M30O30, D30M35O35, D20M40O40
- Diesel-Biodiesel-Ethanol Blends: D90BD5E5, D80BD10E10, D70BD15E15, D60BD20E20, D50BD25E25, D40BD30E30, D30BD35E35, D20BD40E40
- HVO-Methanol-Octanol Blends: HVO90M5O5, HVO80M10O10, HVO70M15O15, HVO60M20O20, HVO50M25O25, HVO40M30O30, HVO30M35O35, HVO20M40O40
- Diesel-Methanol-UREA Blend: D60M30U10

Table 3-2 Experiment fuel properties and characteristics

Properties	Diesel	Biodiesel	HVO	Methanol	Ethanol	Octanal
Molecular formula	C ₁₂ -C ₂₅	C ₁₂ -C ₂₄	C ₁₅ -C ₁₈	CH ₃ OH	C ₂ H ₅ OH	C ₈ H ₁₆ O
Cetane number	40-55	50-65	70-90	3-5	8	30

Density at 288K (g/cm ³)	0.82-0.85	0.88-0.90	0.78-0.82	0.791	0.789	0.83
Oxygen content (%)	0	10-12	0	50	34.7	11
Kinematic viscosity at 313 K (mm ² /s)	2.0-4.5	4.0-5.0	2.8-4.1	0.59	1.2	1.5
Low heat value (MJ/kg)	42.5	37.8-40	44	19.9	26.8	30
Flash point (K)	326-361	423-453	311-343	285	286	313
Boiling point (K)	453-633	553-593	483-573	337	351	470
Critical temperature (K)	720	900	820	512	514	680

3.2.2 Experiment test fuel mixing process

1) Single fuel

In this study, the single fuels used for testing include diesel (D100), biodiesel (BD100), and HVO (HVO100). These fuels are securely stored in a yellow chemical cabinet within the laboratory before testing. They are utilized directly without blending and serve as the basis for observing fuel droplet transient behaviours in high-temperature air environments.

2) Diesel and water emulsion

Since diesel and water are immiscible, an emulsifying agent, Span80, is introduced during the blending process. A mixture of 65% diesel and 35% water, denoted as D65W35, is prepared using Span80. Water is incrementally added to diesel while stirring at 500 rpm with a magnetic stirrer. Subsequently, Span80 is injected into the mixture, and stirring continues for an additional hour. [163]

3) Diesel and biodiesel blend

Diesel and biodiesel are fully miscible and do not require surfactants for blending. [90] Various diesel-biodiesel (D-BD) blends are formulated in different ratios described in § 3.2.1-2. Each new batch of D-BD blend is securely stored in a centrifugal tube, clearly labelled with its mixing ratio and production date.

4) Diesel and HVO blend

Diesel and HVO are also miscible without the need for surfactants. [96] Various diesel-HVO (D-HVO) blends are prepared in the ratios outlined in § 3.2.1-2. Each new batch is stored in a centrifugal tube, labelled with the corresponding mixing ratio and production date.

5) Diesel, methanol, and octanol blend

Diesel and methanol are immiscible, requiring octanol as a co-solvent. The blending process involves first adding methanol to octanol, followed by the introduction of diesel. [120] Various diesel-methanol-octanol (D-M-O) blends are prepared in different ratios detailed in § 3.2.1-3. The prepared D-M-O blends are stored in centrifugal tubes, labelled with the mixing ratio and production date.

6) Diesel, biodiesel, and ethanol blend

While diesel and biodiesel mix naturally, diesel and ethanol do not. In this case, biodiesel is used as a co-solvent to facilitate the blending of diesel and ethanol. [122] The diesel-biodiesel-ethanol (D-BD-E) blends are prepared in various proportions described in § 3.2.1-3. The resulting blends are stored in centrifugal tubes, clearly marked with the blending ratio and the date of production.

7) Diesel, methanol, and UREA blend

Diesel, methanol, and UREA do not mix naturally, so an emulsifying agent, Span80, is introduced during the blending process. A blend of 60% diesel, 30% methanol, and 10% UREA (D60M30U10) is prepared. Methanol is gradually added to diesel under stirring at 500 rpm, followed by the sequential addition of Span80 and UREA, with continuous stirring for an additional hour.

8) Biodiesel and ethanol blend

Various biodiesel-ethanol (BD-E) blends are prepared in different ratios referred to in § 3.2.1-2. [127] After production, the BD-E fuel blends are stored in a centrifugal tube, labelled with the blending ratio and production date.

9) HVO, methanol, and octanol blend

HVO and methanol do not mix naturally, so octanol is used as a co-solvent during the blending process. The blending involves adding methanol to octanol before incorporating HVO. Various HVO-methanol-octanol (HVO-M-O) blends are prepared in the proportions specified in § 3.2.1-3. [139] The resulting HVO-M-O blends are stored in centrifugal tubes, clearly marked with the mix ratio and production date.

10) Diesel with gas bubble injection

For this test, pure diesel is used as the base fuel. Diesel is injected with gas bubbles using a FEDOUR Aquarium air pump equipped with 3 Air Stones. The pump, operating at a maximum airflow rate of 4L /min (240L /H) and air pressure of 16 Kpa, is used to inject gas bubbles into the diesel. The gas injection durations are set at 1 hour, 3 hours, and 5 hours. After injection, the diesel batches are stored in centrifugal tubes and labelled with the production date.

3.3 Experiment Methodology

The experiment image data collection method used in this study is the diffused back-illumination macro photography (DBIMP) technique [171]. To observe and capture the instantaneous behaviours of a transparent microliter fuel droplet in high-temperate air environment, this method combines a high-speed camera and shadow photography using a background light source.

The process works by placing a single light source on one side of the heat element, directing the light through the element. On the opposite side, the high-speed camera captures the

shadow of the droplet as it interacts with the heated environment. This setup allows for the clear visualization of the fuel droplet's transient behaviours such as evaporation, puffing, and micro-explosion.

The experiment image data is collected and analysed using PCC 3.7 software and MATLAB image processing. The image processing code and partial images are presented in Appendix A and B. These tools enable precise analysis of droplet behaviours, including measurements of size, shape, and movement, providing insights into the atomization and combustion characteristics of the fuel blends.

3.4 Experiment Condition

3.4.1 Experiment test temperature setting

In this study, the experimental test temperatures are set at three ambient levels, low liquid penetration temperature (LLPT), medium liquid penetration temperature (MLPT) and high liquid penetration temperature (HLPT) to simulate conditions in a diesel-like chamber, as illustrated in Figure 3.3. Before entering the furnace, the fuel microdroplet is at room temperature, approximately $293 \pm 5\text{K}$. The three specific temperature settings for the furnace are, LLPT— $573 \pm 5\text{K}$, MLPT— $673 \pm 5\text{K}$, and HLPT— $773 \pm 5\text{K}$. These temperature levels are chosen to replicate the thermal conditions experienced by fuel droplets inside a combustion chamber, allowing for a detailed study of their behaviours, such as evaporation, puffing, micro-explosion, and secondary breakup, under varying heat intensities.

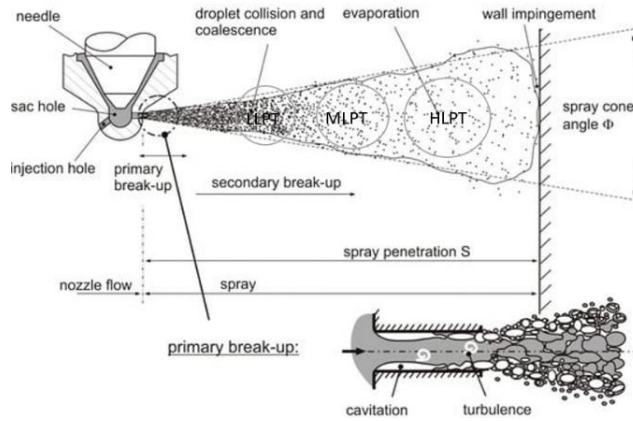


Figure 3.3 Schematic of fuel droplet temperature corresponding to the fuel spray liquid phase penetration length [67]

3.4.2 Fuel droplet size setting

The microdroplet volume is maintained at a constant value of 1.5 μL for each test. The selection of this droplet volume along with the transportation speed is discussed in § 3.6. Given the varying surface tensions of the multi-fuel blends, each single microdroplet is assumed to have a spherical shape. To facilitate consistent analysis across different fuel types, the droplet size is normalized when analysing its transient behaviours, ensuring comparability between the fuels despite differences in physical properties.

3.4.3 Limitations of experiment condition

In this study, a high-speed camera with a macro lens is used to capture the transient behaviours of fuel droplets, which occurs over the span of several seconds. However, the camera's observation area is quite limited during the tests. When the fuel droplet undergoes a strong micro-explosion, some of the smaller sub-droplets may leap out of the recording area, preventing the tracking of part of their behaviours.

In macro photography, depth of field is shallow, meaning only a small region of the image remains in sharp focus. Increasing the depth of field can be achieved by decreasing the lens aperture (increasing the f-number), but this reduces the amount of light entering the

camera. To compensate, either a longer exposure time or a brighter light source is required. However, both options present challenges, a longer exposure time can cause motion blur, when capturing fast-moving sub-droplets, resulting in unclear or fuzzy images. A brighter light source may over-illuminate the droplets, making them invisible, as transparent droplets may not reflect enough light to create a discernible image. Thus, the quality of the recorded images of transient droplet behaviours is governed by the careful balance between camera exposure time, lens aperture, and the light source.

Additionally, there is an inverse relationship between FPS and resolution in high-speed cameras. This limitation arises from the camera's data processing capacity and transmission bandwidth. Higher resolution increases the number of pixels per frame, resulting in more data to be processed and stored in a very short time. As resolution increases, the time needed to process each frame also increases, which consequently lowers the maximum achievable frame rate. Thus, a balance must be struck between resolution and frame rate. A higher resolution provides more detailed images of the sub-droplets but requires sacrificing FPS, reducing the ability to capture the fast dynamics of transient behaviours. Conversely, increasing the FPS reduces resolution but allows for more detailed tracking of fast-moving phenomena. This balance is essential for influencing the quality of the recorded droplet and sub-droplet transient behaviours during testing.

3.5 Experiment Procedure

1. Test temperature setting

The first step of the experiment is to raise the air temperature inside the furnace to the desired operating temperature. The Watlow ST. LOUIS nozzle heater is mounted on a $\varnothing 50 \times L70$ mm stainless-steel furnace to elevate the internal gas temperature. The heater is connected to a digital temperature controller, allowing the configuration of the experimental operating temperature for each test. Due to the high thermal conductivity and efficient heat output of the heater, it takes approximately 40 minutes to reach the minimum

experimental temperature. An additional 10 minutes is needed to stabilize the hot air temperature, which is monitored by two K-type thermocouples and thermometers. One thermocouple is placed horizontally, while the other is placed vertically at the test position.

- The horizontal thermocouple is connected to an RS thermometer to provide live air temperature monitoring at the test point.
- The vertical thermocouple is connected to the Watlow ST. LOUIS EZ-Zone PM controller, adjusting the live air temperature inside the furnace to maintain the desired test conditions.

2. Test record setting

The next step is configuring the Phantom Miro 4 high-speed camera with a Tokina atx-I Macro-lens to capture the droplet transient behaviours. The camera settings are adjusted to record the entire evaporation or combustion process.

- The pixel resolution is set to 256 x 256 to ensure that the entire microdroplet evaporation or combustion event is captured within the frame.
- The frame rate is set to 8,100 FPS, which is the maximum frame speed for the Phantom Miro 4 at this resolution, allowing for detailed observation of rapid droplet behaviours.

3. Test droplet generation

In the third step, a constant-volume single microdroplet is generated for the test. The droplet volume is maintained at 1.5 μL . The droplet is produced using a SciQuip micro pipettor, forming a spherical or near-spherical shape. It is then suspended on the free end of a K-type thermocouple. The initial temperature of the droplet is room temperature, approximately $293 \pm 5 \text{ K}$.

4. Test droplet transportation

The final step involves transporting the suspended micro droplet into the heating furnace along a slide track at a controlled velocity. Once inside the furnace, the evaporation or combustion of the droplet is recorded using PCC 3.7 software, enabling detailed observation and analysis of its behaviours.

This sequence of steps is repeatable throughout the study to ensure consistent experimental conditions and reliable data collection.

3.6 Experimental and Parametric Study of Droplet Delivery Variable

3.6.1 Overview

The fuel droplet transportation process as shown in Figure 3.4, the mathematic model can be expressed as:

$$S = ut + \frac{1}{2}at^2 \quad (3.1)$$

where s represents the fuel droplet moving distance moved, u represents the fuel droplet initial velocity, a represents acceleration, and t represents time, under the assumption of constant acceleration. In practical experiment conditions, maintaining constant acceleration can be challenging. Therefore, the equation in its integral can be expressed as:

$$S(t) = S_0 + \int_{t_0}^t V(t)dt, V(t) = V_0 + \int_{t_0}^t a(t)dt \quad (3.2)$$

$$S = S_0 + \int_T^{T+\Delta T} \left(\int_T^{T+\Delta T} a(t) dt \right) dt \quad (3.3)$$

where S_0 represents the initial moment, V_0 represents the initial velocity, and T_0 represents the initial time, $a(t)$ represents the acceleration at that moment. It can be seen from the above equation that when the fuel droplet moving distance S distance is determined, the experiment can be designed as a function of time.

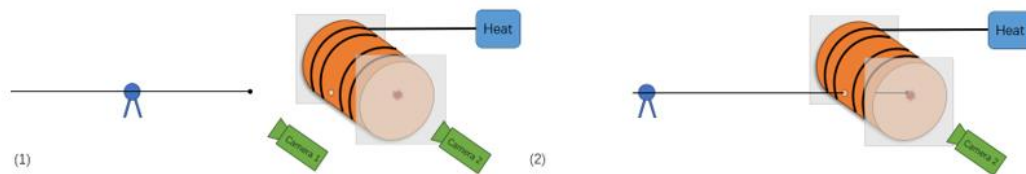


Figure 3.4 Schematic of fuel droplet transportation process

3.6.2 Design and process of experiment

Under practical experimental conditions, the equation becomes more complex due to the need to account for the initial velocity of the fuel droplet and high temperature environment. Once introduced into the furnace, the fuel droplet is exposed to an immediate thermal environment change, initiating the heating process instantly. The timing of the droplet's entry into the furnace is crucial. When the delivery time is too long, the droplet fully vaporize before the LDBOS system begins recording. On the other hand, when the delivery time is too short, the rapid thermal transition can destabilize the droplet, causing it to descend and potentially splash.

Considering these complex dynamics, a supplementary experiment focusing on parametric comparisons has been proposed. This approach utilizes photographic analysis to visually compare the liquid volume before and after its introduction into the chamber. The objective is to evaluate the impact of delivery speed and duration on the effectiveness of the LDBOS system.

§ 3.6.3 explores in greater detail the relationship between the initial velocity of the fuel droplet and its behaviour within the furnace. A slower entry can increase the droplet's dwell time, whereas an overly high speed may compromise its suspension within the furnace environment.

3.6.3 Result and discussion

3.6.3.1 Mathematical model and its research based on initial velocity

To investigate the effect of fuel droplet initial velocity u on the outcome, the assumption of constant acceleration is initially made. Additionally, with the chamber tube wall thickness considered negligible as shown in Figure 3.5, the mathematic model can be expressed as

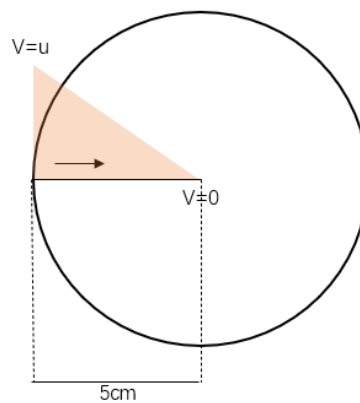


Figure 3.5 Sketch of mathematical model on parametric study of delivery

$$V^2 = u^2 + 2as \quad (3.4)$$

where V represents the final velocity, u represents the initial velocity, a represents constant acceleration, and s represents the stroke.

Three different initial volumes of diesel droplets were selected at nine distinct delivery speeds, each tested in a high-temperature environment of 573K, as shown in Table 3-3. The volume changes between two photographs taken of droplet before and after entering

chamber were compared, and the process was repeated for 10 groups to calculate the average. The results are presented in Figure 3.6.

Table 3-3 Relative decrease of different volumes droplets after entering the chamber

Initial velocity(cm/s)	1 μ L	1.5 μ L	2 μ L	a(cm/s ²)	T _{tra} (s)
40	100.00%	100.00%	100.00%	-160	0.25
30	10.90%	100.00%	100.00%	-90	0.333333
25	9.90%	9.00%	100.00%	-62.5	0.4
20	7.90%	8.10%	8.20%	-40	0.5
15	6.00%	6.10%	6.90%	-22.5	0.666667
10	8.40%	8.30%	9.70%	-10	1
5	16.10%	18.60%	20.90%	-2.5	2
2.5	31.50%	35.80%	39.40%	-0.625	4
1	89.10%	95.50%	96.00%	-0.1	10

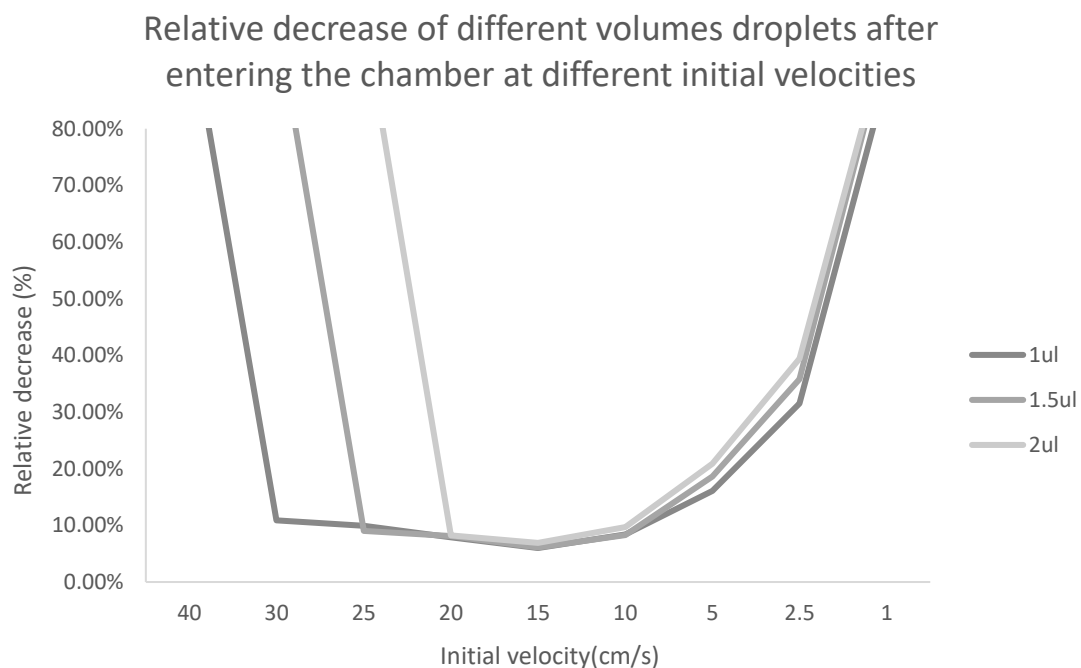


Figure 3.6 Relative decrease of different volumes droplets after entering the chamber at different initial velocities

Based on the data and visualizations in Table 3-3 and Figure 3.6, several key observations emerge regarding the behaviour of liquid droplets of varying volumes. Notably, larger

volume liquids appear more prone to splashing or falling. For droplets with a volume of 1 μL , there exists an optimal range of initial velocities to best observe the micro-explosion phenomenon. Under the assumption of constant acceleration, these droplets achieve the best results with an initial velocity ranging between 30cm/s and 10cm/s. Beyond this range, particularly at elevated velocities, droplets risk deviating from their path due to splashing. On the other hand, velocities below this range may cause the droplets to experience significant evaporation during transit, thus altering their inherent properties.

The criteria become even stricter for 2 μL droplets. Their ideal velocity narrows to a range between 20cm/s and 10cm/s, highlighting the heightened sensitivity of larger droplets to their surrounding conditions.

As detailed in the Table 3-3, droplets propelled at speeds from 30cm/s to 10cm/s remain within the chamber for durations spanning 0.4s to 1s. Though brief, this timeframe is crucial. It's clear that acceleration is essential in determining whether a droplet maintains its trajectory, ensuring its successful delivery to the capture system. Factors such as the droplet's stability, motion, and final resting position are profoundly influenced by its acceleration.

3.6.3.2 Acceleration-based studies and their fitting curves

To further investigate the effect of acceleration on droplet behaviours, a specialized experiment was conducted. In this experiment, 1.5 μL droplets were selected as the test subjects. The droplets were subjected to varying levels of acceleration to study how their paths and final positions were influenced at the capture point. The experiment focused on documenting observations through high-speed photography, capturing images of the droplets upon arrival at the target point. The analysis included measuring the degree of oscillation experienced by the droplets due to acceleration, which provided valuable insights into the dynamic effects on their stability, shape deformation, and behaviours during

transport. This information is critical for understanding how acceleration impacts fuel atomization processes in combustion environments.

Table 3-4 Phenomenon of stopping state at different accelerations of droplets

a(cm/s²)	-35	-30	-25	-20	-15	-10
Phenomenon	Fall	Fall	Shaking	Shaking	Steady	Steady

Based on the data described in the Table 3-4, acceleration is crucial in determining whether droplets can remain stably suspended. whether droplets can remain stably suspended. When the acceleration exceeds 30 cm/s², there is a high probability of splashing during an emergency stop. In scenarios where the acceleration is between 20 and 25 cm/s², splashing is less; however, jittering or shaking occurs during the sudden stop. This jittering is problematic as it accelerates droplet evaporation by constantly altering the surface area, which is an undesirable effect in the LDBOS. Therefore, the principle of reasonable acceleration involves avoiding droplet detachment or splashing while ensuring that the final acceleration does not induce shaking. The goal is to achieve stable droplet transport with the quickest possible arrival time without compromising the droplet's integrity.

Table 3-5 Droplet travel time

t	0.25	0.5	0.75	1
a(cm/s ²)	-30	-20	-15	-10

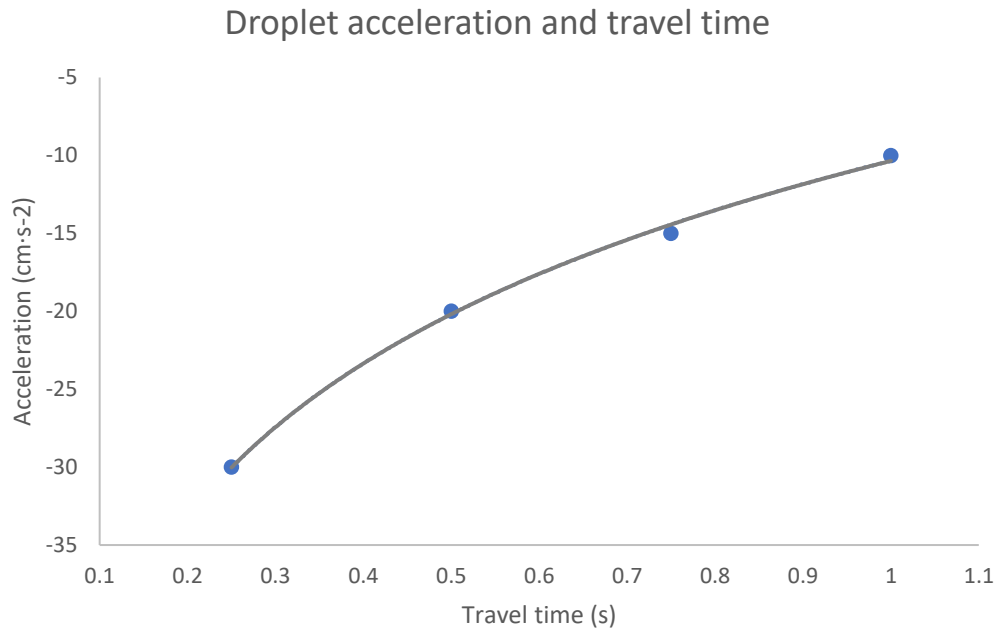


Figure 3.7 Droplet travel time at different acceleration

According to the Table 3-5 sample points respectively, the maximum acceleration of the four sampling points does not exceed 30 cm/s² and is not less than 10 cm/s², and the overall travel time is 1 second. Using the acceleration of diesel microdroplet with travel time, a fitting curve was generated to characterize the relationship as shown in Figure 3.7. This can be mathematically expressed as

$$a = 14.198 \ln(t) - 10.353 \quad (3.5)$$

Among the results, the coefficient of determination R² is 0.9978. Through integration, the initial velocity u can be determined to satisfy the following equation:

$$u = \int_0^1 (14.198 \ln(t) - 10.353) dt \quad (3.6)$$

After calculation, u is equal to -27.49cm/s. According to Table 3-3, for 1.5 μL, there is a possibility of splashing at the initial speed, so the results need to be adjusted.

$$u = \int_{0.2}^1 (14.198 \ln(t) - 10.353) dt \quad (3.7)$$

When the acceleration time is from 1s to 0.8 seconds, the initial result before deceleration is $u=-12.11\text{cm/s}$, which is compounded by the requirements mentioned above.

3.6.3.3 Conclusion

In summarizing these findings, it's evident that the initial conditions, particularly the entry speed and acceleration, significantly influence droplets behaviour during their transit through a given chamber. The data highlights the importance of an initial velocity of 12.11 cm/s for achieving desired outcomes.

Furthermore, the acceleration pattern is paramount. The optimal model observed adheres to the formula $a=14.198 \ln(t)-10.353$. This acceleration is not a static value but varies logarithmically with time, suggesting intricate interactions of forces or conditions as the particle advances.

Additionally, the duration of the deceleration process, clocked at 0.8 s in studies, is crucial for a seamless transition to the intended LDBOS capture point. Ensuring a smooth approach to the capture point, particularly at higher velocities, is essential for optimizing the overall efficiency of the system's transportation process.

Chapter 4 Diesel and Biodiesel Blends Droplet Behaviour at Ambient Temperatures

4.1 Introduction

This chapter explores the behaviour of single microdroplets of diesel, D-W emulsion, D-BD blends, and D-HVO blends under various high-temperature conditions at LLPT, MLPT, and HLPT environments. During the experiments, several fuel atomization phenomena were observed, including bubble formation, secondary breakup, and spontaneous ignition accompanied by soot formation.

A key focus of this chapter is to analyse and compare the evaporation rates of different multi-fuel blends. This involves a thorough comparison of the behaviour of these blends against pure diesel under the same temperature conditions. By examining these interactions, the chapter aims to identify optimal blending ratios that could enhance performance in ICEs.

Additionally, the chapter provides insights into how the composition of various fuel blends influences their evaporation and combustion characteristics. This includes a detailed investigation into how different blending ratios affect fuel atomization and combustion characteristics. The findings contribute to a better understanding of how multi-fuel blends can be optimized to improve engine performance and reduce environmental impact.

4.2 Diesel, D-W Emulsion, D-BD and D-HVO Droplet Behaviour at LLPT

Under the LLPT test condition, various physical and chemical processes occur within the single diesel microdroplet. These include the evaporation [172] and diffusion of diesel molecules [173], the development of a non-uniform temperature distribution inside the

droplet [174], and gas-phase reactions [175] such as the oxidation of diesel molecules [176].

As the single diesel microdroplet is exposed to the LLPT air environment, it begins to warm up. During the heating process, evaporation of the microdroplet commences, leading to a gradual decrease in its surface tension. [177] The droplet size decreases over time, while the temperature within the droplet continues to rise [178], as shown in Figure 4.1. The evaporation of the single diesel microdroplet follows the D^2 -law [179], as illustrated in Figure 4.17.

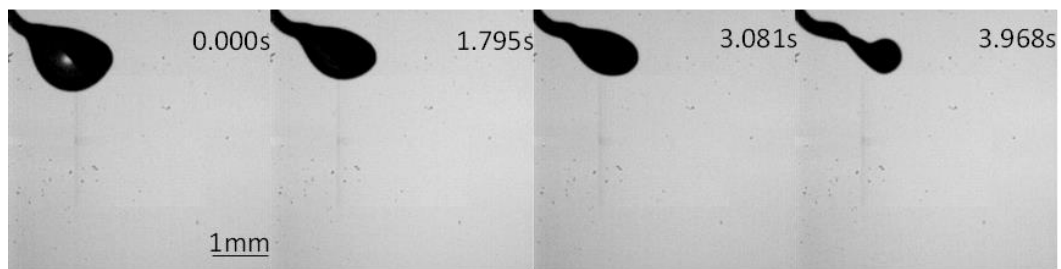


Figure 4.1 1.5 μ L single diesel microdroplet evaporation at LLPT, atm

Evaporation is the process by which diesel molecules at the surface of the single diesel microdroplet gain enough kinetic energy to escape into the surrounding air as vapor [180]. This process occurs because the surrounding air is at a much higher temperature 573K than the diesel microdroplet itself, leading to heat transfer from the air to the microdroplet. [181] As a result, the diesel molecules gain energy and transition from the liquid phase to the gas phase. [182]

Diffusion is the movement of diesel molecules within the single diesel microdroplet, driven by concentration gradients. [183] As diesel molecules evaporate from the droplet's surface, a lower concentration region is created near the surface, while the interior retains a higher concentration. [184] This concentration gradient drives the movement of diesel molecules from the interior to the surface, thereby facilitating the ongoing evaporation process. [185]

At this temperature, lighter hydrocarbons [186] and low-boiling hydrocarbons (C_{10} - C_{14}) [187] in the single diesel microdroplet, including decane [188], undecane [189], dodecane [190], tridecane [191], tetradecane [192], and aromatic hydrocarbons [193], begin to pyrolyze [194]. This pyrolysis results in the breakdown of these hydrocarbons [195], producing intermediates [196], free radicals [197], and smaller molecules [198]. Free radicals are the initial products of pyrolysis reactions and further react with other molecules or free radicals to form new compounds or additional free radicals. [199] These free radicals include hydrogen radicals ($H\bullet$) [200], methyl radicals ($CH_3\bullet$) [201], ethyl radicals ($C_2H_5\bullet$) [202], and other longer-chain alkyl radicals [203].

Inside the single diesel microdroplet, the temperature distribution is non-uniform. [204] This non-uniformity arises due to several factors in this test, including the temperature gradient between the microdroplet's surface and its core [205], as well as the variations in heating and heat transfer within the microdroplet. [206] The surface of the microdroplet exposed to the LLPT air is significantly hotter than its core. This temperature gradient leads to variations in physical and chemical processes within the microdroplet which affect the rate of evaporation [207] and influencing the possibility of combustion reactions occurring inside the microdroplet [208].

At a high temperature in the LLPT test, where there is sufficient oxygen supply, a reaction zone or flame [209] can potentially form within the diesel droplet. This occurs when the diesel molecules in the gas phase around the droplet's surface ignite [210] and sustain a combustion reaction [210]. The heat generated by the combustion further raises the temperature inside the diesel droplet, promoting more vigorous evaporation and combustion. [211] The presence of a flame within the diesel droplet could significantly alter its behaviour, leading to more rapid vaporization and combustion. [212] However, no combustion reaction with a flame was observed during the LLPT test. This could be due to several factors in this test, including the low pressure of the air [213] inside the heating furnace, insufficient activation energy [214], slow pyrolysis [215] or oxidation reaction rates [216] and the stability of heavy hydrocarbons [217], long-chain alkanes (C_{19} - C_{25}) and PAHs

which are not easily decomposed or oxidized at this temperature, are still relatively stable at this temperature and are not easy to decompose or react with oxygen. [218] Additionally, the improper diesel-to-air molecular ratio could contribute to the lack of combustion. [219] Although the autoignition temperature of diesel is generally between 483 K and 523K [79], the required temperature for autoignition is higher under low-pressure conditions. [172] Diesel pyrolysis and oxidation reactions demand high activation energy [214], and while the LLPT environment is relatively high in temperature, it is still insufficient to provide the necessary activation energy for the full decomposition or oxidation of diesel. At LLPT, the rate of pyrolysis or oxidation reaction of diesel is not sufficient to cause immediate spontaneous combustion. [215] Consequently, at LLPT, the pyrolysis or oxidation rates of diesel are not sufficient to cause spontaneous combustion. [216] Although some light hydrocarbons begin to decompose at LLPT, most components remain relatively stable. [172] At LLPT, the diesel droplet evaporates rapidly but does not enter an active boiling stage. These vapours mix with the surrounding air and dilute to a safer concentration range, thereby preventing spontaneous combustion. [219]

Upon exposure to the LLPT air, the single D-W microdroplet begins to warm up. The water content in the emulsion evaporates earlier than the lighter hydrocarbons and low-boiling hydrocarbons (C_{10} - C_{14}) in diesel, as the ambient temperature is significantly higher than water's boiling point of 373K at atmospheric pressure. [142] As the more volatile water molecules evaporate, the differential surface tension induced by the Marangoni Effect causes internal flow within the D-W microdroplet, leading to its expansion and eventual swelling and bursting. [220] Tiny liquid sub-droplets continually burst from the surface of the suspended D-W microdroplet and are ejected into the surrounding air. Some of these sub-droplets undergo secondary breakup due to their high motion at 1.830s, as shown in Figure 4.2, which enhances the mixing of fuel with air when the fuel is injected and mixed with high-temperature and high-pressure air inside the engine chamber. [141] However, some smaller bumps lack the kinetic energy needed to break the surface tension and thus return to the droplet's surface. [153] The rapid evaporation of water also creates a cooling effect on the surrounding diesel, slowing down its vaporization and contributing to this

occurrence. [220] The escaped sub-droplets and returning bumps induce internal oscillations within the droplet, accelerating its transformation from liquid to gas and improving fuel-air mixing. [163] Following this unsteady evaporation phase, the D-W microdroplet undergoes faster evaporation and disappears more quickly compared to a pure diesel microdroplet, the evaporation rate comparison as presented in Figure 4.19. The overall evaporation time of the D-W microdroplet is shorter than that of the pure diesel microdroplet at this temperature. The average evaporation rate of the D-W microdroplet increases by 7.4% compared to that of the pure diesel microdroplet.

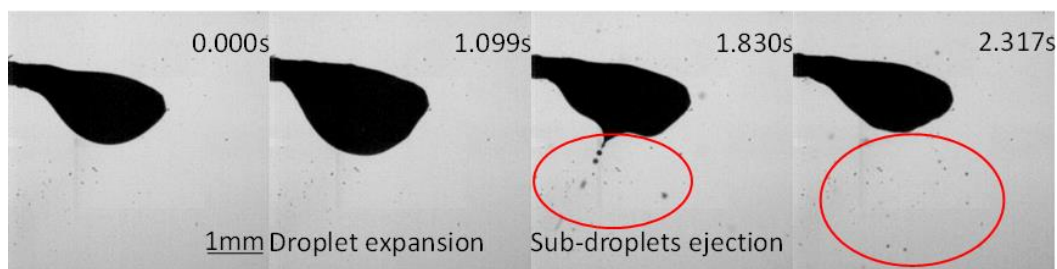


Figure 4.2 1.5 μ L single D-W microdroplet evaporation at LLPT, atm

Various mixing ratios of D-BD single microdroplets exhibit different behaviours in the LLPT air environment. As shown in Figure 4.3, all tested D-BD droplets undergo steady evaporation and diffusion processes at this temperature, [151] consistent with the behaviour of the single diesel microdroplet. The evaporation rates of D-BD droplets with different mixing ratios are presented in Figure 4.18.

The lifetime of the D-BD droplet increases with higher biodiesel content, indicating that a higher percentage of diesel in the D-BD blend increases fuel volatility. Consequently, an increase in vaporization content leads to a reduction in the overall vaporization time of the fuel, which is reflected in a shorter droplet lifetime. In this scenario, Marangoni convection has two components: solutal and thermal. [222] The solutal component arises from changes in surface tension due to variations in diesel and biodiesel composition, while the thermal component is driven by surface tension changes caused by the temperature gradient. [221]

No puffing, micro-explosion, boiling, or combustible reactions between the droplet and hot air were observed during the heating of the D-BD microdroplet in the LLPT air environment. The D-BD microdroplet smoothly decreases in volume until it completely disappears.

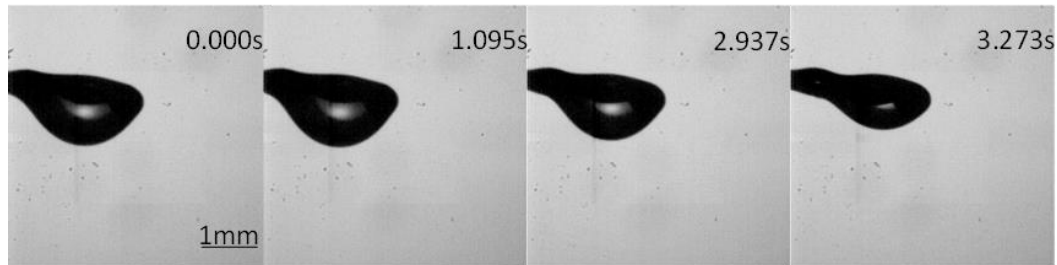


Figure 4.3 1.5 µL single D-BD microdroplet evaporation at LLPT, atm

When the single D-HVO microdroplet enters the LLPT air environment, it begins to warm up. During the heating process, the surface tension of the droplet gradually decreases. [223] The commencement of the evaporation process for the D-HVO microdroplet is shown in Figure 4.4. The evaporation behaviours of the D-HVO microdroplet is consistent with that of D-BD and pure diesel droplets. The overall evaporation time for the D-HVO microdroplet is slightly shorter than that of D-BD at the same mixing ratio, due to the lower viscosity of HVO, [223] as presented in Figure 4.18. Similarly, the lifetime of the D-HVO droplet increases with higher HVO content, indicating that a greater percentage of HVO in the blend decreases the volatility of the fuel. [99] During heating, the D-HVO microdroplet undergoes volumetric expansion and steady evaporation. [138] No puffing, micro-explosion, boiling, or combustible reactions were observed between the droplet and the hot air during the LLPT test. The D-HVO microdroplet smoothly decreases in volume until it completely disappears.

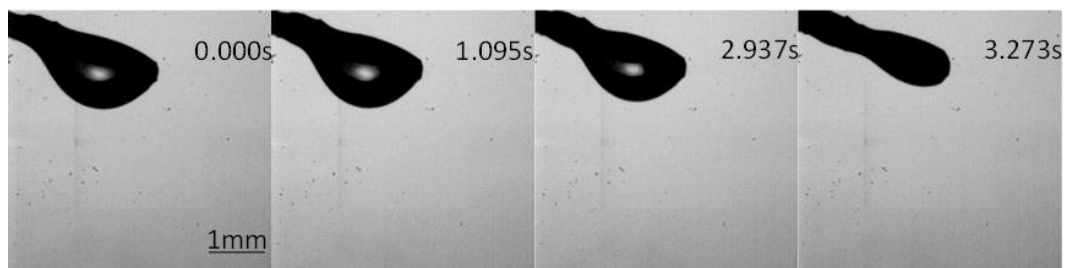


Figure 4.4 1.5 μL single D-HVO microdroplet evaporation at LLPT, atm

4.3 Diesel, D-W Emulsion, D-BD and D-HVO Droplet Behaviour at MLPT

At the elevated temperatures of the MLPT air environment, the single diesel microdroplet exhibits significantly faster evaporation compared to the LLPT test conditions, as shown in Figure 4.5. This accelerated evaporation is accompanied by a more rapid reduction in the droplet's size, as shown in Figure 4.17. During the evaporation process, diesel vapor is released and disperses into the surrounding air. [79] Mild ebullition and vapor bubble formation are observed at the centre of the diesel microdroplet, as shown in Figure 4.6. These phenomena suggest that the diesel microdroplet becomes more active and unstable when exposed to the MLPT air environment than when heated at LLPT. The overall evaporation and diffusion processes are notably accelerated under MLPT conditions, leading to a higher rate of diesel molecules transitioning from the liquid phase to the gas phase. [138] Additionally, smaller sub diesel microdroplets escape from the suspended droplet and disperse into the air due to rapid pyrolysis reactions. However, no visible diesel vapor cloud forms around the droplet and no combustion reaction with a flame is observed during the MLPT test. The average evaporation rate of the single diesel microdroplet increases by 27.2% compared to that in the LLPT environment, as illustrated in Figure 4.19. Despite these changes, the evaporation of the microdroplet still adheres to the D^2 -law.

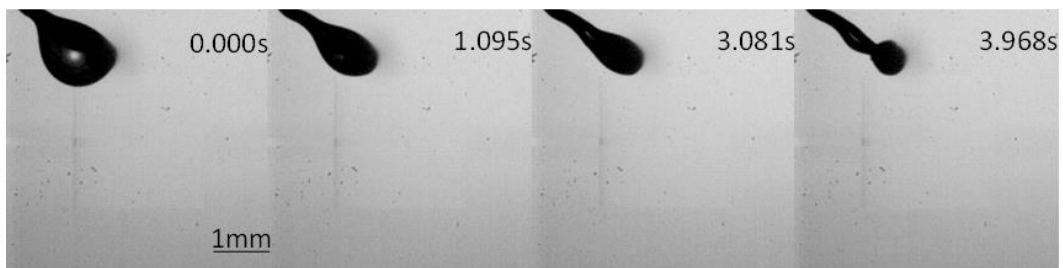


Figure 4.5 1.5 μL single diesel microdroplet evaporation at MLPT, atm

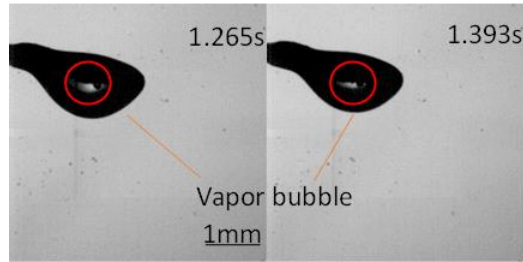


Figure 4.6 1.5 μL single diesel microdroplet nucleation at MLPT, atm

When the single D-W microdroplet is exposed to MLPT air environment, both the diesel and water components within the droplet begin to heat up. The droplet undergoes a similar evaporation and diffusion process as observed under LLPT condition but with increased activity. Compared to heating at LLPT, the D-W microdroplet in MLPT exhibits more pronounced surface dynamics with a greater number of small bumps forming on its surface. The droplet expands to a twice larger size and the centre of the droplet thins into a film nearly breaking into two fragments, as shown in Figure 4.7. However, the droplet does not fully divide due to several factors: the insufficient heating temperature and the non-uniform distribution of water content within the emulsion. [145] A significant number of vapor bubbles were observed inside the droplet which attributed to the evaporation of the water content at this temperature. These vapor bubbles continuously absorb heat from the surrounding high-temperature air, attempting to escape from the droplet. As the droplet expands further and the vapor bubbles gain sufficient kinetic energy, the droplet may disintegrate into two or multiple pieces instantaneously, then undergo micro-explosion. Compared to the single diesel microdroplet, the average evaporation rate of the D-W microdroplet increases by 11.8%, as illustrated in Figure 4.19.

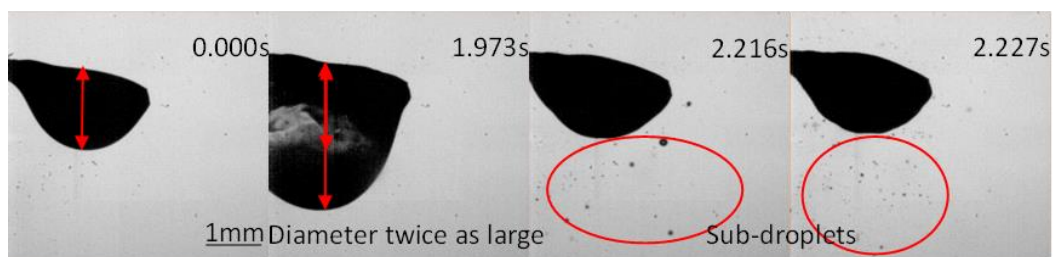


Figure 4.7 1.5 μL single D-W microdroplet evaporation at MLPT, atm

As the air temperature increases to MLPT level, the D-BD droplet undergoes faster evaporation and diffusion due to the elevated temperature, as illustrated in Figure 4.8. The high temperature reduces the D-BD blend's surface tension to evaporation, allowing the molecules within the droplet to absorb more heat, which accelerates the evaporation. [153] The temperature gradient between the droplet and the hot air is a key factor in determining the evaporation rate. [142] A larger temperature gradient results in a higher rate of heat transfer, further accelerating the evaporation process, as shown in Figure 4.18. [156] The overall evaporation time decreases as the biodiesel percentage decreases at the same temperature. Notably, no vapor bubbles, puffing, micro-explosions, boiling, or combustion reactions were observed during this heating test.

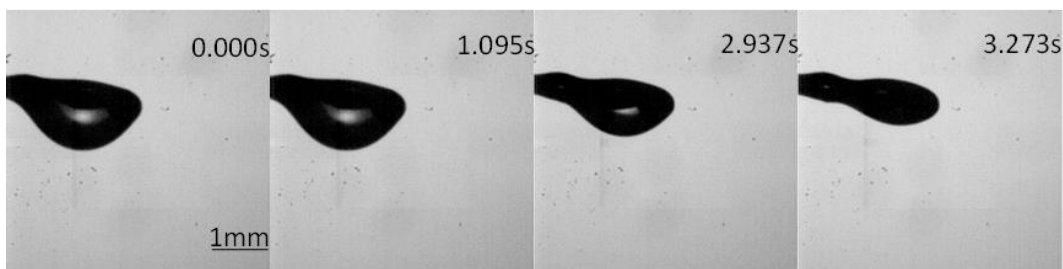


Figure 4.8 1.5 μL single D-BD microdroplet evaporation at MLPT, atm

When the single D-HVO microdroplet is exposed to the MLPT air environment, it undergoes faster evaporation and diffusion compared to the conditions observed in LLPT, as shown in Figure 4.9. The droplet lifetime increases with the rising HVO content, consistent with the results from the LLPT tests. At the end of the evaporation process, soot formation is observed on the free end of the thermocouple when the HVO content in the D-HVO blend is below 50%, as shown in Figure 4.10. The probability of soot formation increases with higher diesel content in the D-HVO blend. This is because HVO is primarily composed of saturated and unsaturated alkanes (hydrocarbons), and lacks impurities such as sulphur, aromatic hydrocarbons, and PAHs, which are more prevalent in diesel and contribute to soot production. [104] Throughout the MLPT test, no vapor bubbles, puffing, micro-explosions,

or combustion with flame were observed. The overall evaporation time of the D-HVO droplet is slightly shorter than that of a D-BD droplet at the same mixing ratio, as shown in Figure 4.18, indicating that the evaporation rate of D-HVO is slightly higher than that of D-BD. When compared to a pure diesel microdroplet, the evaporation rates follow the order: diesel > D-HVO \approx D-BD under the same temperature and mixing ratio conditions.

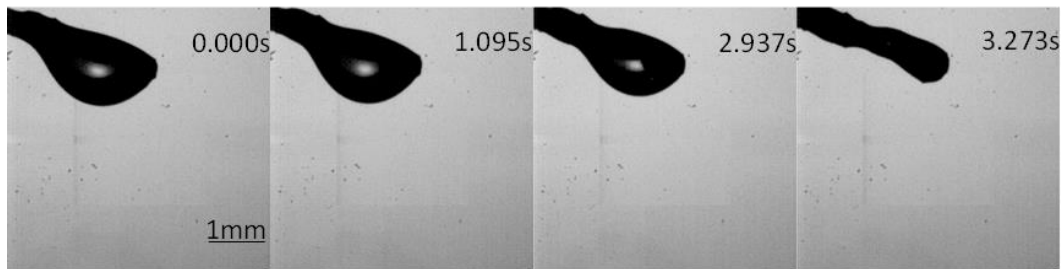


Figure 4.9 1.5 μ L single D-HVO microdroplet evaporation at MLPT, atm

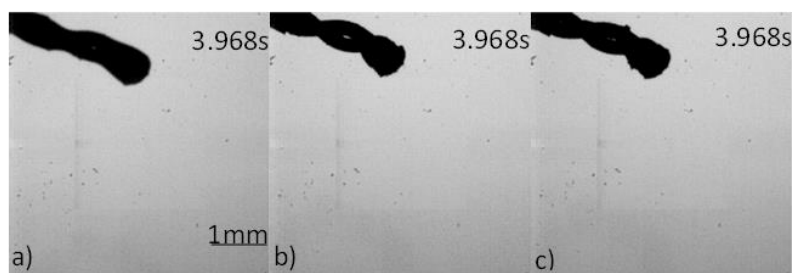


Figure 4.10 1.5 μ L single D-HVO microdroplet soot residue increasing, (a)D60HVO40, (b)D70HVO30, (c)D80HVO20 at MLPT, atm

4.4 Diesel, D-W Emulsion, D-BD and D-HVO Droplet Behaviour at HLPT

When the diesel fuel droplet enters the high-temperature air of the HLPT environment, it initially undergoes a rapid evaporation process. Volatile components in the diesel such as light hydrocarbons quickly transition into the gas phase at HLPT, leading to a rapid reduction in the droplet's volume. [79] As vapor bubbles form at its centre, migrate to the edge and burst into the surrounding gas, creating sub-droplets and causing the droplet to expand to

nearly twice its original size. As the droplet heats up, the internal pressure rapidly increases, eventually exceeding the surface tension that holds the droplet together. [153] This pressure buildup leads to an explosive breakup of the droplet into hundreds of sub-droplets, as shown in Figure 4.11. [162]

During evaporation, diesel molecules are released into the surrounding air as vapor, which quickly diffuses and fills in the surrounding air. The rapid evaporation of the diesel droplet also affects the ambient air temperature because evaporation requires the absorption of heat, the surrounding air temperature slightly decreases, particularly when the evaporation rate is high. [156] As diesel molecules evaporate from the droplet's surface into the air, they participate in gas-phase reactions. With sufficient oxygen, the oxidation of diesel molecules occurs, leading to more rapid vaporization and visible combustion with flames. The single diesel microdroplet reacts with the surrounding high-temperature air, resulting in a significant reduction in its volume. [157] The droplet enters an oscillatory state due to the heat released by the combustion reaction, causing it to swing violently.

Additionally, the temperature gradient between the droplet's surface and its core leads to irregular expansion and further destabilization. [142] This instability enhances the evaporation rate, causing more diesel vapor to mix with the high-temperature air, which in turn accelerates the combustion reaction. [142] A bright flame is visible surrounding the diesel droplet accompanied by the formation of a soot cloud that floats in the air, as shown in Figure 4.12. The remaining small volume of the diesel droplet, which is not completely combusted, continues to evaporate rapidly due to the heat released by the ongoing combustion. [157] The experimental results indicate that diesel vapor exhibits combustible properties at such high temperatures. The evaporation phase of the single microdroplet still follows the D^2 -law, as shown in Figure 4.17. [156] Compared to the MLPT test conditions, the average evaporation rate of the single diesel microdroplet increases by 57.2%, as illustrated in Figure 4.19.

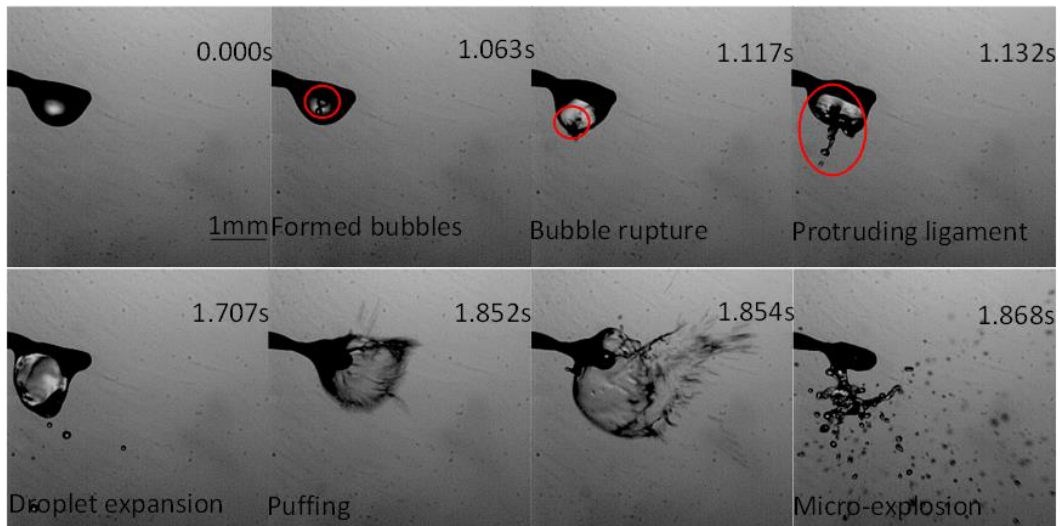


Figure 4.11 1.5 μL single diesel microdroplet micro-explosion at HLPT, atm

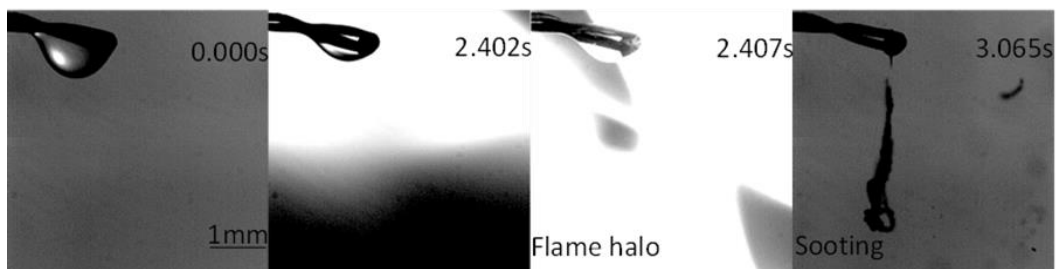


Figure 4.12 1.5 μL single diesel microdroplet combustion at HLPT, atm

When exposed to the high-temperature air of the HLPT environment, the single D-W microdroplet undergoes rapid heating, leading to a faster evaporation and diffusion process compared to previous tests. [138] The droplet experiences violent expansion and deformation, as captured by high-speed camera footage. Large vapor bubbles form and boil inside the droplet, leading to the ejection of numerous smaller sub-droplets into the surrounding air, which enhances the mixing of fuel and air, as shown in Figure 4.13. During the puffing phase, a relatively large sub-droplet is observed breaking down from the suspended D-W microdroplet, however, no secondary breakup occurs during its lifetime. In contrast, secondary breakup is observed in the smaller sub-droplets. This difference could be attributed to several factors: the smaller sub-droplets have higher kinetic energy [153],

making them more active and unstable, and thus more intend to disintegrate when exposed to high-temperature air. Due to their small volume, the water content in the sub-droplets rapidly transitions from the liquid phase to the gas phase, with the resulting water vapor contributing to the secondary breakup of these droplets. [145]

After undergoing evaporation, oscillation, deformation, and disintegration, the volume of the single D-W microdroplet gradually decreases until it completely vaporizes. Compared to the single diesel microdroplet, the average evaporation rate of the single D-W microdroplet increases by 46.1%, as illustrated in Figure 4.19.

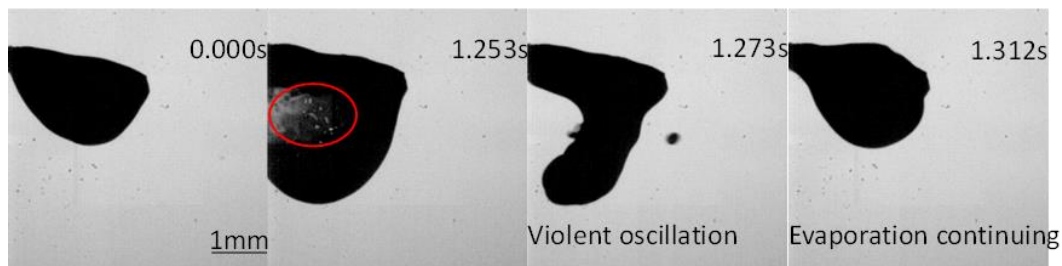


Figure 4.13 1.5 µL single D-W microdroplet expansion at HLPT, atm

In the high-temperature air environment of TLPT, the D-BD microdroplet undergoes rapid evaporation compared to previous test temperatures, as shown in Figure 4.14. Shortly after the droplet begins to warm up, bubbles start forming inside the droplet, as shown in Figure 4.15. These bubbles grow and move within the droplet, causing it to vibrate violently. [143] The movement of the bubbles generates waves across the droplet's surface, leading to its expansion and irregular shape. [153] As the droplet continues to transform from the liquid phase to the gas phase, it mixes with the surrounding high-temperature air, and its volume decreases rapidly. When the droplet's diameter reduces to half of its initial size, a flame ignites at the centre of the droplet and gradually spreads across the entire droplet, indicating an ongoing combustion reaction, as shown in Figure 4.15. The remaining small volume of the droplet that continues to evaporate and burn rapidly, driven by the heat released from the combustion reaction, while still suspended on the thermocouple. [157]

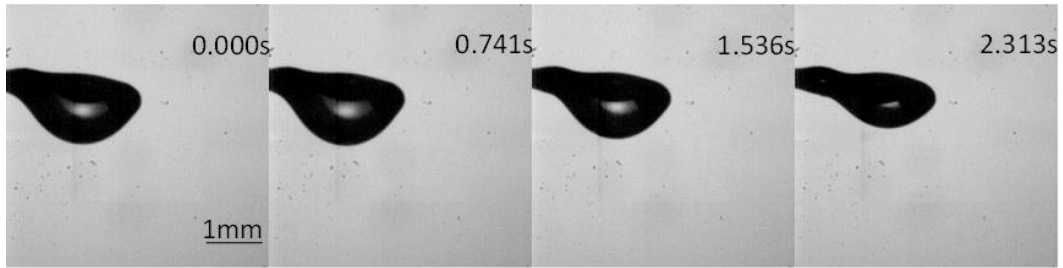


Figure 4.14 1.5 µL single D-BD microdroplet evaporation at HLPT, atm

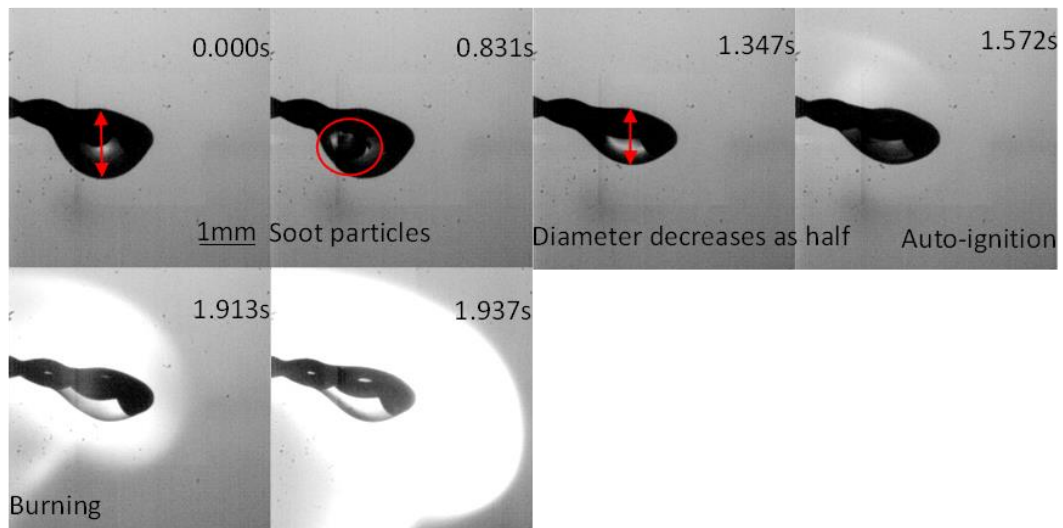


Figure 4.15 1.5µl single D-BD microdroplet combustion at HLPT, atm

When the single D-HVO microdroplet is heated in the HLPT air environment, it undergoes more rapid evaporation than in MLPT and LLPT conditions. A combustion reaction with visible flames and soot formation occurs, as shown in Figure 4.16. As the HVO content in the D-HVO blend decreases, the concentration of forming soot increases. [91] The inclusion of HVO in the blend can reduce soot formation compared to pure diesel during combustion. [93] Compared to the single D-BD microdroplet with the same mixing ratio, the D-HVO droplet has a shorter heating time to reach auto-ignition. No puffing or micro-explosion were observed during the tests due to the similar boiling points of diesel and HVO.

At HLPT, the evaporation rate of the D-HVO droplet remains higher than that of the D-BD droplet, as shown in Figure 4.18. This difference can be attributed to the composition of

biodiesel which contains a significant amount of fatty acid methyl esters (FAME). [88] The molecular weight and boiling point of FAME molecules are relatively high, resulting in a lower evaporation rate at room temperature. Additionally, the polar ester groups in FAME molecules create stronger intermolecular forces, increasing the energy required for evaporation. [91] This structural characteristic makes FAME more difficult to evaporate than non-polar hydrocarbons. [92] Furthermore, the viscosity of FAME is higher than that of pure diesel and HVO. [89] Higher viscosity leads to greater internal friction between liquid molecules, which increases resistance during evaporation, further reducing the evaporation rate. [91]

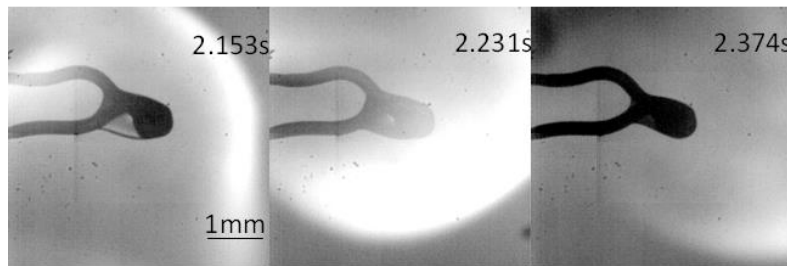


Figure 4.16 1.5 μL single D-HVO microdroplet combustion at HLPT, atm

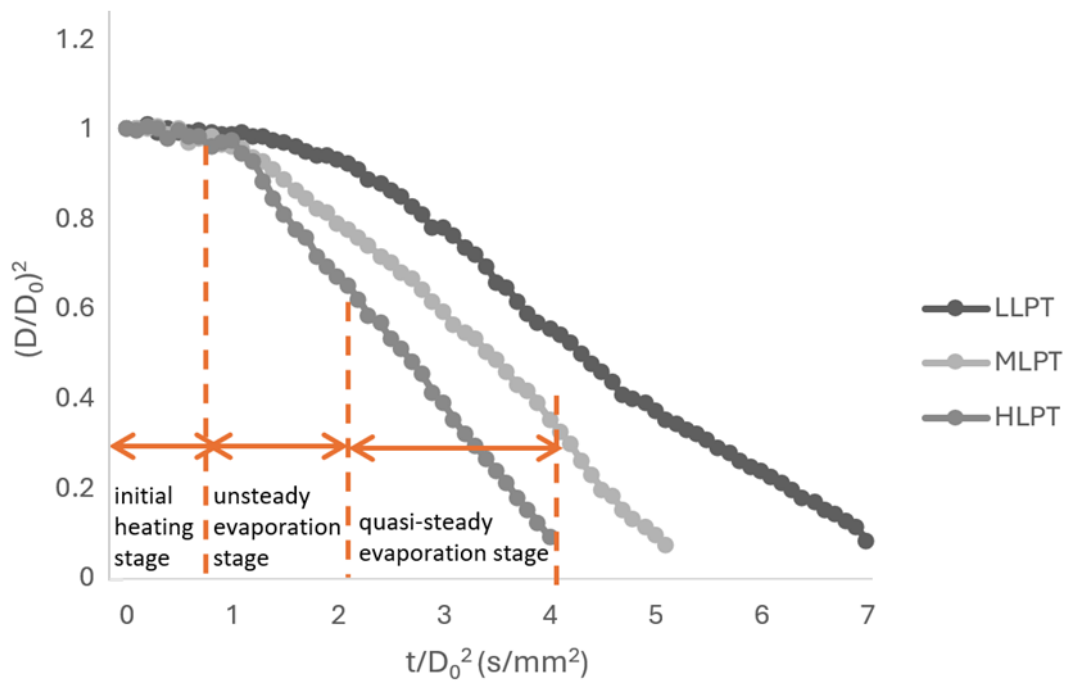


Figure 4.17 1.5 μL single diesel microdroplet normalized squared diameter at LLPT, MLPT, HLPT, atm

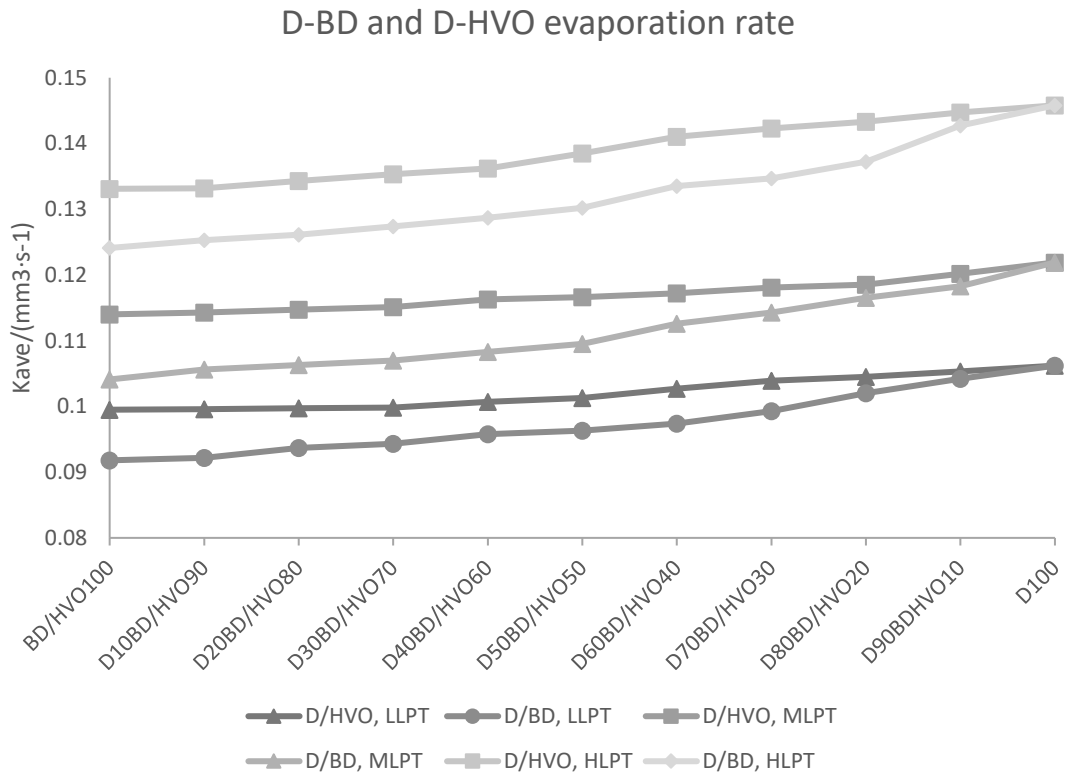


Figure 4.18 1.5 μL single D-BD and D-HVO microdroplet evaporation rate at LLPT, MLPT, HLPT, atm

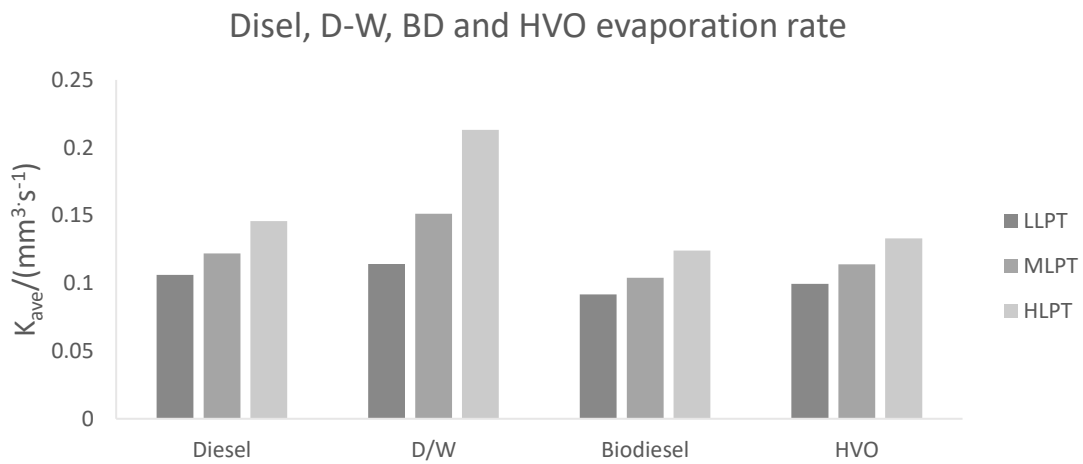


Figure 4.19 1.5 μL single diesel, D-W, biodiesel and HVO microdroplet evaporation rate at LLPT, MLPT HLPT, atm

4.5 Diesel with Gas Injection Droplet Behaviour at MLPT

The transient behaviour of diesel microdroplet under gas injection was investigated at MLPT. Gas injection durations were set at 1 hour, 3 hours, and 5 hours, denoted as D_{1h} , D_{3h} , and D_{5h} , respectively, to study the influence of gas bubble injection on fuel droplet dynamics. [224] Droplet behaviour was captured using the DBLMP method and the corresponding data is analysed and discussed in this section. Additionally, the effect of gas injection was compared with that of pure diesel.

Experimental findings revealed that single microdroplets experienced rapid evaporation under the given temperature conditions, which is consistent with research. [224] Further analysis focused on the evaporation rates of fuel samples exposed to different gas injection durations. D_{3h} exhibited a slightly shorter evaporation period compared to D_{1h} , while D_{5h} displayed the shortest evaporation time of all conditions. The evaporation rates followed the order: $D_{5h} > D_{3h} > D_{1h}$, as shown in Figure 4.20. Using the average evaporation rates of diesel with gas injection (derived from Figure 4.20), a fitting curve was generated to characterize the relationship.

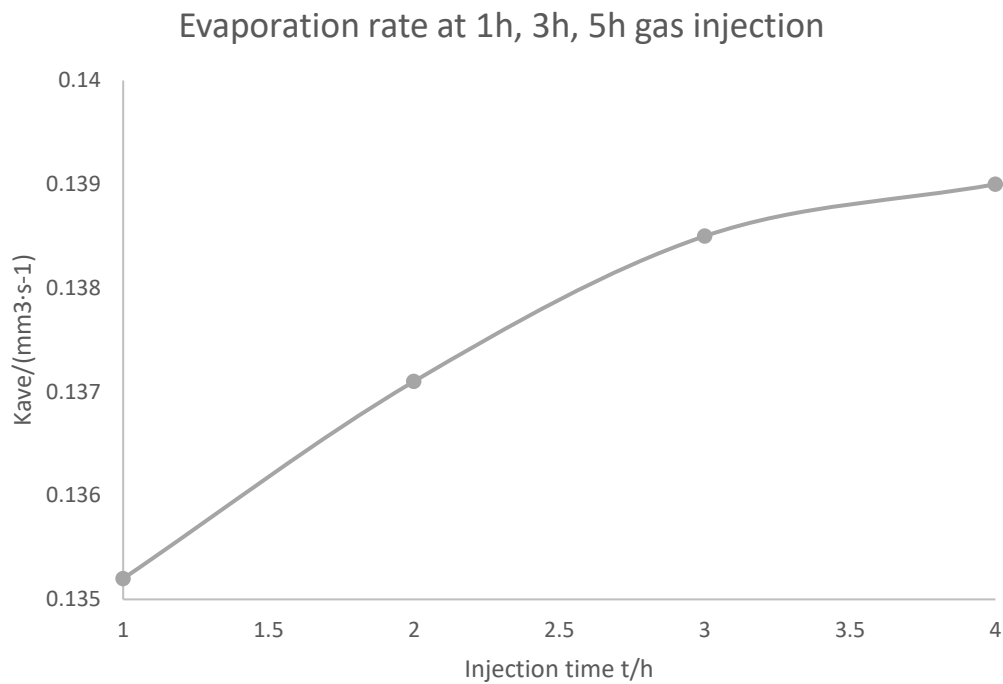


Figure 4.20 1.5 μ L single diesel microdroplet evaporation rate at of 1h,3h, 5h gas injection at MLPT, atm

The single diesel microdroplet evaporation rate in terms of the gas injection duration can be expressed as

$$K_{ave} = 0.0028 \ln(t) + 0.1352 \quad (4.1)$$

where K_{ave} is the average evaporation rate, t is the gas injection duration, the coefficient of determination R^2 is 0.9936.

As the relationship between the total gas injection volume and the gas injection duration can be described as follows: the total gas injection volume is directly proportional to the gas injection time, with the injection rate determining the volume over a specified time interval. This can be mathematically expressed as

$$V_{tg} = V_{ig}t = \int_0^t \dot{V}(t)dt \quad (4.2)$$

where V_{tg} is the total gas injection volume, V_{ig} is gas injection rate, as constant 4 L/min mentioned in § 3.2.2- (10) of this study.

Hence, theoretically the diesel microdroplet evaporation rate in terms of gas injection volume can be expressed as

$$K_{ave} = 0.0028 \ln \left(\frac{V_{tg}}{V_{ig}} \right) + 0.1352 = 0.0028 \ln V_{tg} + 0.1267 \quad (4.3)$$

Although, under practical conditions, the gas cannot completely dissolve in diesel, according to Henry's Law [225], the amount of gas dissolved in a liquid is directly proportional to the partial pressure of the gas above the liquid. In this case, for diesel, the dissolved gas concentration can be expressed as

$$C = k_H \cdot P \quad (4.4)$$

where C is the concentration of the dissolved gas, k_H is Henry's law constant for the gas-liquid pair (in this case, air-diesel), this constant varies with temperature, P is the partial pressure of the gas in contact with the liquid, as constant 16Kpa mentioned in § 3.2.2- (10) of this study, which is 0.16 atmospheres (since 1 atm \approx 101.3 KPa).

The diesel microdroplet evaporation rate in terms of gas injection volume can be expressed as

$$K_{ave} = 0.0028 \ln C \left(\frac{V_{tg}}{V_{ig}} \right) + 0.1267 \quad (4.5)$$

Hence, in this study, at MLPT environment, the diesel droplet evaporation rate as a function of the gas injection volume can be expressed as

$$K_{ave} = 0.0028 \ln(k_H \cdot V_{tg}) + 0.1216 \quad (4.6)$$

4.6 Conclusion

In this chapter, the behaviour of single diesel, D-W, D-BD and D-HVO microdroplets under varying high-temperature environments LLPT, MLPT and HLPT were investigated. The findings can be summarized as follows

Droplet behaviours

- Across all temperature environments, the microdroplets exhibited distinct evaporation and combustion behaviours. The evaporation rate increased with temperature, with the most rapid evaporation occurring under HLPT condition. D-W droplets consistently showed the highest evaporation rates compared to diesel, D-BD, and D-HVO blends.
- Combustion with visible flames was observed primarily under HLPT condition, with soot formation occurring more prominently in droplets with higher diesel content.

Fuel composition impact on droplet behaviours

- The D-W microdroplets exhibited complex behaviours with significant oscillation, deformation, and secondary breakup observed at higher temperatures, particularly under HLPT condition. The presence of water in the emulsion influenced the droplet's stability and evaporation rate, leading to a unique evaporation profile compared to diesel, D-BD, and D-HVO blends.
- For D-BD and D-HVO blends, the presence of FAME in biodiesel and the hydrotreated components in HVO were crucial in influencing evaporation and combustion behaviours. FAME's higher molecular weight, boiling point, and viscosity contributed to a lower evaporation rate compared to diesel and HVO, particularly at lower temperatures. HVO which lacks impurities such as sulphur and

aromatic compounds, contributes to its lower soot formation potential compared to pure diesel. The inclusion of HVO in the D-HVO blend reduces soot formation compared to both pure diesel and the D-BD blend, highlighting HVO's potential in reducing particulate emissions. Under HLPT condition, D-HVO also exhibited a shorter time to auto-ignition compared to the D-BD blend.

Temperature impact on droplet behaviours

- The temperature gradient between the droplet and the surrounding air was a key factor influencing evaporation and combustion. Higher temperature, such as the HLPT environment, accelerated evaporation and promoted combustion, often leading to visible flame formation and soot production.

Chapter 5 Diesel and Alcohol Blends Droplet Behaviour at Ambient Temperatures

5.1 Introduction

In this chapter, the behaviours of Diesel-Methanol-Octanol (D-M-O), Diesel-Biodiesel-Ethanol (B-BD-E), and Diesel-Methanol-UREA (D-M-U) blend microdroplets under varying high-temperature environments, LLPT, MLPT, and HLPT, were investigated. These tests aimed to analyse how different fuel compositions affect evaporation rates, occurrence and frequency of puffing and micro-explosion, auto-ignition, and soot formation under high-temperature conditions. To further explore the effect of water content on microdroplet behaviour, additional tests were conducted using D-M-O blends with varying water content proportions of 10%, 20%, and 50% under the HLPT environment. Their sub-droplets size distribution was quantitatively analysed and discussed.

5.2 D-M-O, D-BD-E, D-M-U Droplet Behaviour at LLPT

The various blending ratio D-M-O single microdroplets were tested in the LLPT air environment. In the LLPT air environment, the single D-M-O microdroplet undergoes evaporation and diffusion processes. [120] The high temperature accelerates the evaporation of D-M-O blends. The presence of methanol, which has a lower boiling point compared to diesel and octanol [108], intend to cause more rapid evaporation. Typical behaviours of D-M-O blends microdroplet at LLPT are as shown in Figure 5.1. Various blending ratio D-M-O single microdroplets observed behaviours at LLPT are outlined in Figure 5.2.

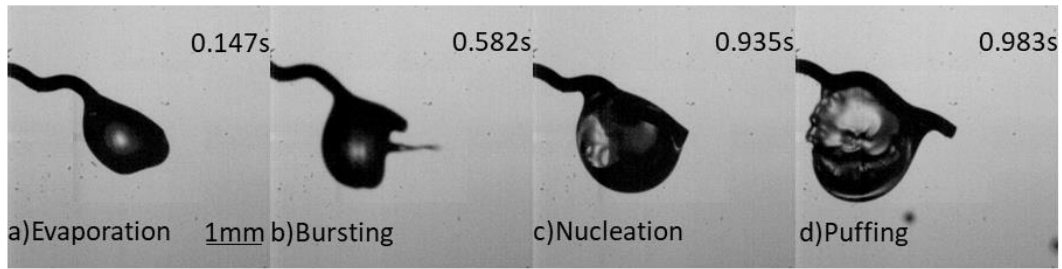


Figure 5.1 1.5 μL single D-M-O microdroplet behaviour, (a)evaporation, (b)bursting, (c)nucleation, (d)puffing at LLPT, atm

Figure 5.2 is a ternary phase diagram indicating the relationship between the proportions of diesel, methanol and octanol in a blend. The three corners of the triangle represent 100% of diesel (bottom-left), and 100% of methanol (top) and 100% of octanol (bottom-right). The percentages of each component are labelled on the sides of the triangle with different phenomena (marked by coloured dots) occurring depending on the blend's composition. The red points (pure evaporation) at lower methanol concentrations suggest that the lower volatility of diesel and octanol slows down the evaporation process [109] allowing it to proceed without nucleation or puffing. The green points (evaporation with nucleation) occur when methanol's faster evaporation induces localized pressure changes within the droplet, causing nucleation. Blue points (evaporation, nucleation and puffing) are observed at higher methanol concentrations, suggesting that methanol's volatile nature and its interaction with octanol and diesel lead to both nucleation and subsequent puffing due to rapid vaporization.

As methanol content increases, the propensity for more complex phenomena such as puffing increases. [135] Puffing is often associated with the rapid expansion of vapor bubbles formed during nucleation, causing the droplet to eject small portions of liquid or vapor suddenly. [138] The blue dots at the higher end of methanol content indicate the most intense vaporization, due to the dominance of methanol, which evaporates much more readily than diesel and octanol. Octanol, which has a higher boiling point than both methanol and diesel [120], may act as a stabilizer in the mixture. When combined with methanol, octanol slows down the rate of evaporation, which is why nucleation and puffing

only appear once methanol content is sufficiently high. [138] The intermediate green dots reflect the transition phase where octanol suppresses puffing but allows nucleation due to localized heating and methanol's lower boiling point. [139]

At this elevated temperature, the droplet dynamics would be influenced by how each component interacts with heat. Methanol, being the most volatile, would evaporate first, leaving behind a mixture richer in diesel and octanol, which would have different evaporation characteristics. [134] The nucleation and puffing are due to the rapid phase change in the droplet's core, where heat transfer creates volatile zones that drive these phenomena. [140]

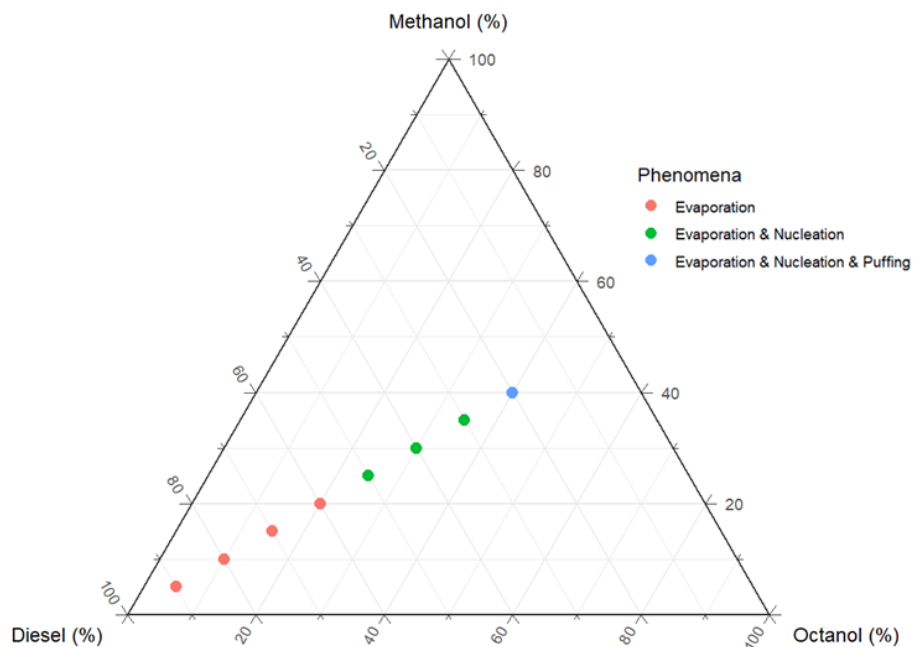


Figure 5.2 1.5 µL single D-M-O microdroplet behaviours at LLPT, atm

The microdroplet behaviours according to methanol content, can be expressed as

$$f(C_d, C_m, C_o) = \begin{cases} \text{Evaporation,} & \text{if } 0 < C_m \leq 20\% \\ \text{Evaporation + Nucleation,} & \text{if } 25\% \leq C_m \leq 35\% \\ \text{Evaporation + Nucleation + Puffing,} & \text{if } C_m \geq 40\% \end{cases} \quad (5.1)$$

where C_d represent the percentage of diesel, C_m represent the percentage of methanol, and C_o represent the percentage of octanol.

The various blending ratio D-BD-E single microdroplets were tested in the LLPT air environment. When the D-BD-E microdroplet was heated in the LLPT air environment, it undergoes volumetric expansion followed by steady evaporation with the droplet volume gradually decreasing. The overall evaporation time of the droplet decreases as the ethanol content increases.

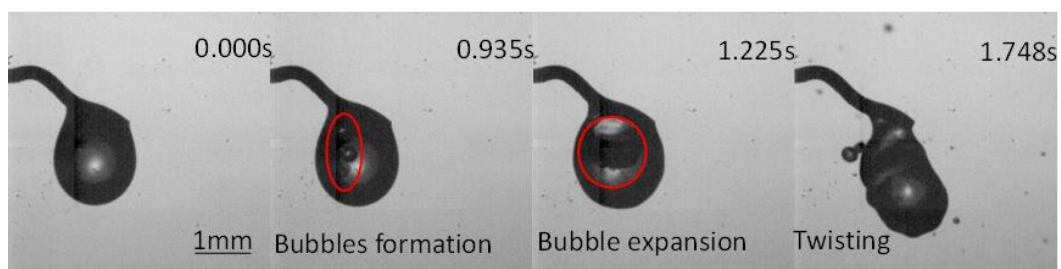


Figure 5.3 1.5 μL single D-BD-E microdroplet nucleation at LLPT, atm

This ternary phase diagram, as shown in Figure 5.4 represents the single microdroplet behaviour of blends of diesel, biodiesel, and ethanol in LLPT air. The red points are clustered toward the bottom left, indicating that at higher diesel content, the phenomenon is predominantly simple evaporation. [142] The cyan points, representing more complex behaviours with both evaporation and nucleation, appear when the concentration of ethanol increases to 35-40% ethanol. This suggests that the higher volatility of ethanol leads to nucleation in addition to evaporation. [144]

At lower ethanol content below 35%, droplets mainly show evaporation. The higher content of diesel and biodiesel slows down the evaporation process without triggering complex nucleation or puffing phenomena. [149] No obvious puffing or micro-explosions were observed during the test. This can be attributed to several factors: the low ethanol content in the blend, the relatively low temperature of the environment [142], and the high boiling points of diesel and biodiesel [152]. Although ethanol has a boiling point of 351K, at low

concentrations and in a low-temperature environment, it is less favourable to form vapor bubbles inside the D-BD-E blend. When ethanol content is above 35%, vapor bubble formation inside the microdroplet [153], as shown in Figure 5.3. The bubbles first present at the location near the thermocouples. This could be because the temperature at the location near the thermocouple is higher than other areas. [159] Another cause is the ethanol content is higher than other areas. Although the D-BD-E blends were prepared under 1 hour stirring mixing, the ethanol molecule cannot completely integrate with the other two compositions. The ethanol content in droplets vaporised to form bubbles and expanded. When the bubble shell was broken, small sub-droplets were ejected into the surrounding air. [135] This led to the parent droplet oscillating and twisting. Additionally, since the boiling points of diesel and biodiesel are higher than the temperature in the LLPT environment, the D-BD-E droplet is not prone to auto-ignition during the heating process. While the ethanol content within the droplet evaporates quickly, it did not lead to puffing, micro-explosions, auto-ignition or combustion during the test.

Compared to D-M-O blends, methanol's higher volatility causes more severe puffing, while ethanol, though also volatile, does not lead to the same degree of puffing. In both blends, methanol is more prone to triggering complex phenomena such as nucleation and puffing, while ethanol mostly causes nucleation without puffing. In short, in the D-M-O blend, the transition to complex phenomena such as nucleation and puffing happens at lower methanol content compared to the D-BD-E blend, where puffing is absent even at higher ethanol content. Both octanol and biodiesel contribute to stabilizing their respective blends. Biodiesel in the D-BD-E system suppresses drastic phase transitions, while octanol has a similar effect in the D-M-O system, though it is eventually overcome by methanol's volatility at higher concentrations.

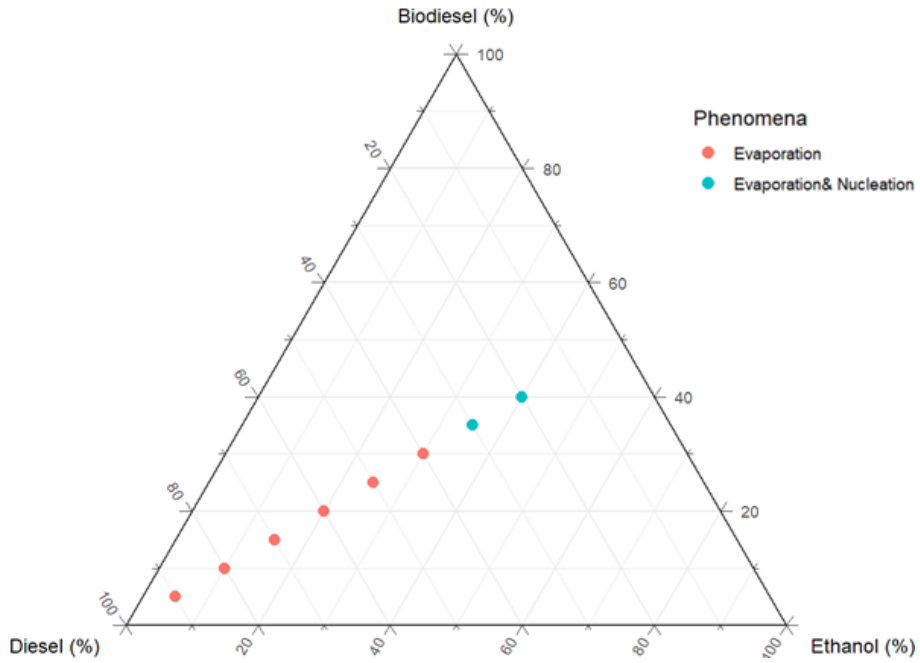


Figure 5.4 1.5 μL single D-BD-E microdroplet behaviours at LLPT, atm

The microdroplet behaviours according to ethanol content, can be expressed as

$$f(C_d C_{bd} C_e) = \begin{cases} \text{Evaporation, if } 0 < C_e \leq 30\% \\ \text{Evaporation + Nucleation, if } C_e \geq 35\% \end{cases} \quad (5.2)$$

where C_d represent the percentage of diesel, C_{bd} represent the percentage of biodiesel, and C_e represent the percentage of ethanol.

When the single D-M-U microdroplet is heated in a LLPT air environment, it undergoes evaporation and nucleation behaviours [145], consistent with the D-W droplet. Several bubbles form inside the droplet due to methanol's low boiling point, as shown in Figure 5.5.

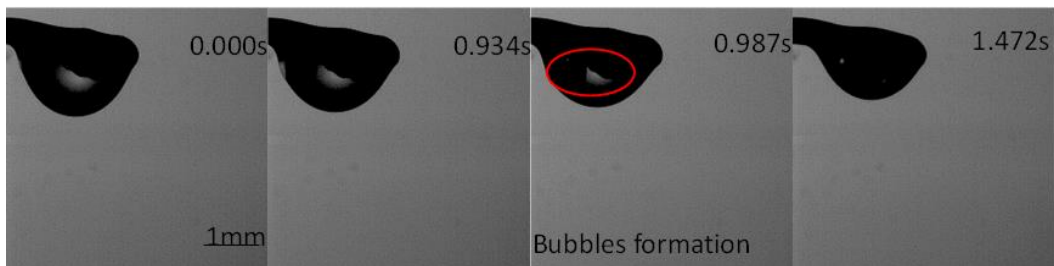


Figure 5.5 1.5 μL single D-M-U microdroplet behaviour at LLPT, atm

Compared to the D-W droplet, the D-M-U droplet tends to form vapor bubbles within the droplet rather than ejecting tiny sub-droplets from its surface. This difference is due to the surfactant's role in the mixture: while the diesel and water in the D-W droplet are more inclined to form a macroemulsion, allowing water molecules to escape more easily from the droplet surface when heated, the D-M-U mixture forms a microemulsion due to the addition of the surfactant. [121][162] As the droplet heats, methanol molecules inside the D-M-U droplet transform into gas, creating bubbles that gradually move to the surface and escape. Throughout the entire testing process, the single D-M-U microdroplet experiences steady evaporation until it completely disappears. No puffing, micro-explosions, boiling, or combustion reactions were detected during this heating test.

5.3 D-M-O, D-BD-E, D-M-U Droplet Behaviour at MLPT

As the air temperature increases to MLPT levels, the single D-M-O microdroplet undergoes faster evaporation during the higher temperature heating process. Typical behaviours of D-M-O blends microdroplet at MLPT are as shown in Figure 5.6.

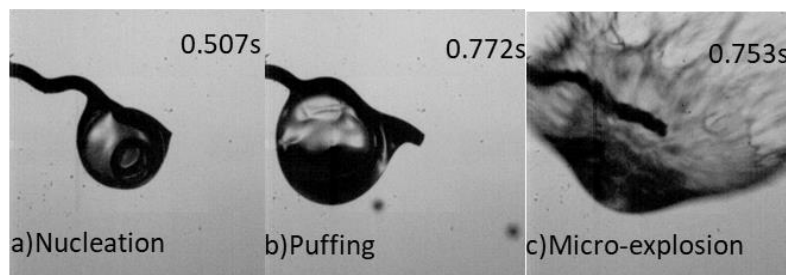


Figure 5.6 1.5 μL single D-M-O microdroplet behaviour, (a)nucleation, (b)puffing, (c)micro-explosion at MLPT, atm

Figure 5.7 represents the behaviours of D-M-O blends microdroplets in MLPT air, compared to the previous analysis at LLPT air. At lower methanol concentrations below 15%, the droplets primarily show simple evaporation, similar to what was observed at LLPT. However,

compared to the LLPT experiment, nucleation happens over a slightly wider range at higher temperatures, indicating that the increased energy provided by MLPT enhances evaporation rates for all components. [142] As methanol content increases to 20%-30%, the blend exhibits both evaporation and nucleation. The region of nucleation appears at slightly lower methanol concentrations in the MLPT air compared to LLPT. This suggests that nucleation is more easily triggered due to the higher temperature, which accelerates internal pressure buildup in the droplet, leading to nucleation. [153] At high methanol content above 35%, complex phenomena such as evaporation, nucleation, and puffing are observed. Puffing occurs earlier in terms of methanol concentration at MLPT compared to LLPT. The higher temperature increases the volatility of methanol, promoting more rapid internal vapor formation and leading to the puffing phenomenon at lower methanol concentrations than at LLPT. [159]

In both LLPT and MLPT air, evaporation is the dominant phenomenon at lower methanol concentrations. At MLPT, the increased temperature accelerates the evaporation process and slightly broadens the range where nucleation occurs. [149] At MLPT, nucleation occurs at lower methanol content than at LLPT. This is due to the increased temperature accelerating the formation of vapor bubbles inside the droplet, causing earlier nucleation. [138] Puffing happens at a lower methanol content above 35% at MLPT compared to the LLPT experiment, where puffing was observed above 40% methanol. The higher temperature increases the volatility of methanol, leading to more rapid vaporization and pressure changes within the droplet, causing puffing at a lower methanol content threshold. [159] The higher temperature significantly affects the internal phase change processes as nucleation and puffing due to the increased volatility of methanol, shifting the thresholds for more complex behaviours to lower methanol concentrations.

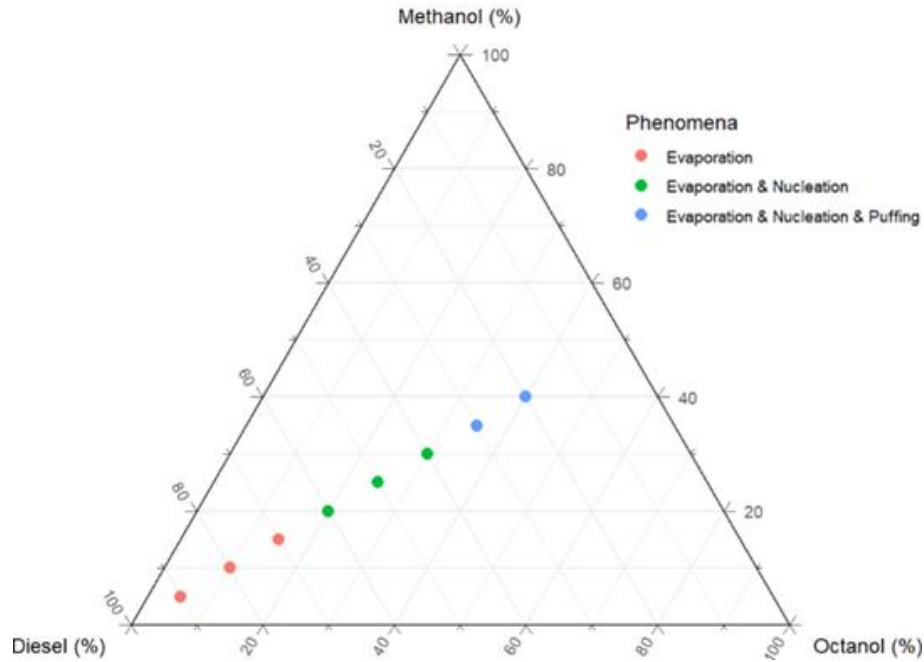


Figure 5.7 1.5 μ L single D-M-O microdroplet behaviours at MLPT, atm

The microdroplet behaviours according to methanol content, can be expressed as

$$f(C_d, C_m, C_o) = \begin{cases} \text{Evaporation,} & \text{if } 0 < C_m \leq 15\% \\ \text{Evaporation + Nucleation,} & \text{if } 20\% \leq C_m \leq 30\% \\ \text{Evaporation + Nucleation + Puffing,} & \text{if } C_m \geq 35\% \end{cases} \quad (5.3)$$

where C_d represent the percentage of diesel, C_m represent the percentage of methanol, and C_o represent the percentage of octanol.

When the air temperature increases to MLPT, which exceeds both the diesel and biodiesel boiling points, puffing was observed in blends with high ethanol content, as shown in Figure 5.8. [156] Specifically, when the ethanol content exceeds 40%, the single D-BD-E microdroplet is more favour to undergo puffing with the probability of these events increasing as the ethanol content rises. No combustion reactions were captured during this heating test at MLPT. Based on the current testing results, for a D-BD-E droplet to ignite and burn out, the heating temperature would need to exceed MLPT. [159] While the ethanol

content within the droplet evaporates quickly, it did not lead to micro-explosions and auto-ignition during the test.

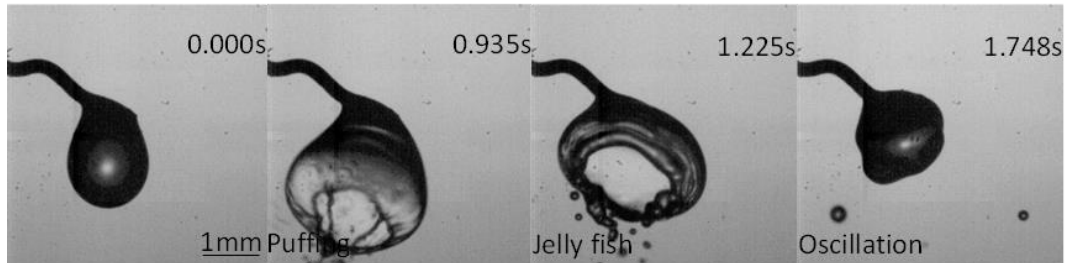


Figure 5.8 1.5 μL single D-BD-E microdroplet puffing at MLPT, atm

As Figure 5.9 shown, at lower ethanol concentrations below 25%, the droplets mainly exhibit evaporation. At MLPT, the nucleation range is slightly broader compared to LLPT, indicating that the increased temperature enhances the rate of evaporation for diesel and biodiesel. [142] As ethanol content increases to 30%-40%, droplets begin to show both evaporation and nucleation. Compared to the LLTP results, nucleation occurs at a slightly lower ethanol content, showing that the higher temperature promotes faster internal phase changes and bubble formation inside the droplets. [138] At high ethanol content above 40%, the phenomena observed include evaporation, nucleation, and puffing. The threshold for puffing has shifted to a slightly lower ethanol content compared to the LLTP experiment, where puffing was observed around 60% ethanol. This shift indicates that higher temperatures facilitate faster vapor formation inside the droplet, leading to puffing at lower ethanol content. [156]

In both the LLTP and MLPT experiments, the droplets exhibit simple evaporation at low ethanol concentrations. However, at MLPT, the evaporation process occurs more efficiently due to the higher temperature, slightly widening the region where nucleation occurs. [159] At MLPT, nucleation begins at lower ethanol content compared to LLPT. This is because the higher temperature provides more energy, causing vapor bubbles to form inside the droplets more easily. [162] At MLPT, puffing occurs at slightly lower ethanol content above

40% compared to the LLPT results where puffing is absent even at higher ethanol content 40%. The increased temperature facilitates the rapid vaporization of ethanol, leading to pressure changes within the droplets and causing puffing to happen earlier. [153]

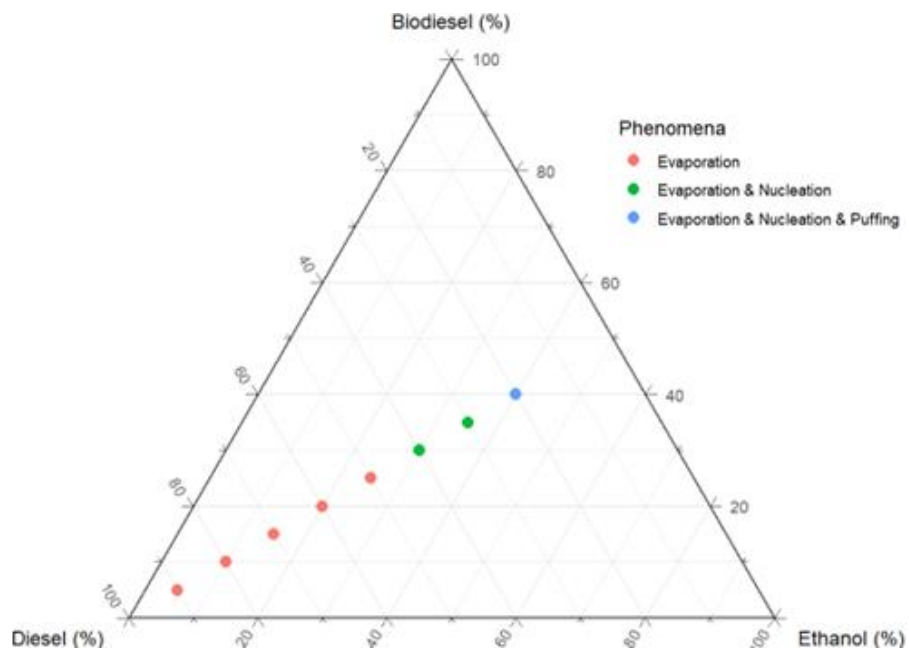


Figure 5.9 1.5 μL single D-BD-E microdroplet behaviours at MLPT, atm

The microdroplet behaviours according to ethanol content, can be expressed as

$$f(C_d, C_{bd}, C_e) = \begin{cases} \text{Evaporation,} & \text{if } 0 < C_e \leq 25\% \\ \text{Evaporation + Nucleation,} & \text{if } 30\% \leq C_e \leq 35\% \\ \text{Evaporation + Nucleation + Puffing,} & \text{if } C_e \geq 40\% \end{cases} \quad (5.4)$$

where C_d represent the percentage of diesel, C_{bd} represent the percentage of biodiesel, and C_e represent the percentage of ethanol.

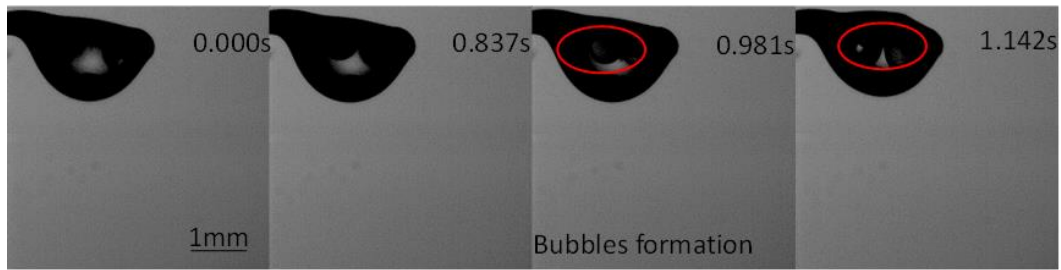


Figure 5.10 1.5 μL single D-M-U microdroplet behaviour at MLPT, atm

As the air temperature increases to MLPT, the single D-M-U microdroplet becomes more active. Methanol is the first component to transition from the liquid phase to the gas phase. The UREA content undergoes both evaporation and decomposition in the MLPT air environment, breaking down into biuret, ammonia, and cyanuric acid. [226] Larger bubbles form at the centre of the droplet, where methanol and UREA molecules coalesce into bubbles then move to the droplet's edge before escaping [144], as shown in Figure 5.10. This process is relatively stable and slow, attributed to the stability of the microemulsion. [165] No puffing or micro-explosions were observed during the test, due to the relatively low heating temperature and the low methanol content.

5.4 D-M-O, D-BD-E, D-M-U Droplet Behaviour at HLPT

In the HLPT air environment, the single D-M-O microdroplet was observed to evaporate faster than previous tests. Methanol vapor bubbles form more rapidly inside the droplet compared to the MLPT environment. The droplet becomes unstable, shaking and vibrating violently. The vapor bubbles move quickly within the droplet and are rapidly ejected into the surrounding air, resembling a boiling state. As large quantities of methanol evaporate from the D-M-O droplet, its mass decreases while its volume expands, eventually forming a thin membrane-like shape. When the kinetic energy surpasses the surface tension, the droplet bursts into hundreds of tiny particles, a phenomenon known as a strong micro-explosion during the heating process. [153] Typical behaviours of D-M-O blends microdroplet at HLPT are as shown in Figure 5.11. Among the tested blends, D20M40O40

remains the most active and prone to puffing and micro-explosions during heating, while D70M15O15 continues to be the most stable, undergoing steady evaporation. The probability of puffing and micro-explosion increases as the diesel content decreases and the methanol content increases. Combustion reaction with visible flames is observed at high diesel content blends, accompanied by soot formation in the surrounding air. The high-temperature combustion reaction accelerates the evaporation of the droplet, causing it to burn out quickly at the end of its lifetime.

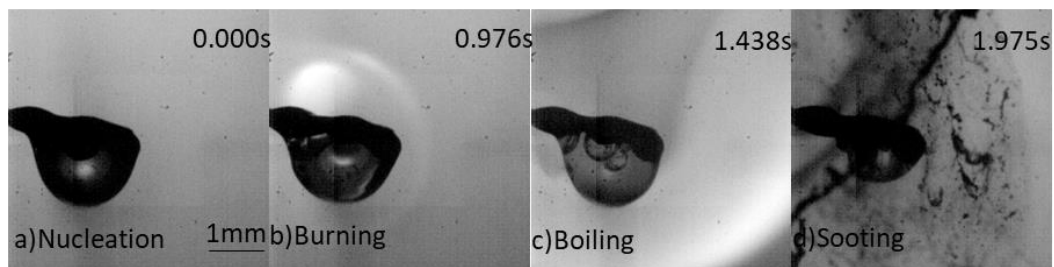


Figure 5.11 1.5 μL single D-M-O microdroplet behaviour, (a) nucleation, (b) burning, (c) boiling, (d)sooting at HLPT, atm

Various blending ratio D-M-O single microdroplets behaviours are outlined in Figure 5.12. This ternary phase diagram represents the single droplet phenomena for diesel, methanol, and octanol blends in HLPT air, and it shows several different phenomena. At lower methanol concentrations below 10%, droplets undergo evaporation and burning. The higher temperature of HLPT causes burning in addition to more rapid evaporation. [159] Compared to LLPT and MLPT, burning becomes a significant phenomenon due to the elevated energy input, which is sufficient to ignite the fuel blend. [162] As the methanol content increases to 15%-20%, the droplets exhibit evaporation and nucleation. This is similar to the behaviours at lower temperatures, but the nucleation occurs earlier and more intensely due to the higher temperature, which enhances vapor bubble formation inside the droplets. [157] At methanol concentrations of 25%-30%, evaporation, nucleation, and puffing occur. Compared to LLPT and MLPT, puffing happens more readily at HLPT due to faster vaporization and internal pressure changes. [156] At higher methanol content above 35%,

complex phenomena involving micro-explosions are observed. The higher temperature at HLPT causes rapid vaporization and intense pressure buildup, leading to micro-explosions alongside puffing. [135] This is a new phenomenon not observed at the lower temperatures of LLPT or MLPT, highlighting the extreme volatility of methanol at HLPT.

At HLPT, burning becomes a significant phenomenon at lower methanol content, which was not observed at LLPT or MLPT. This is due to the higher temperature providing enough energy to ignite the fuel components [138], particularly diesel and octanol. Nucleation occurs earlier (at lower methanol concentrations) as the temperature increases from LLPT to HLPT. The higher temperatures enhance the formation of vapor bubbles inside the droplet. [142] Puffing occurs at lower methanol concentrations as the temperature increases, with puffing occurring as early as 25% methanol at HLPT, compared to 40% and 35% at LLPT and MLPT respectively. This phenomenon is unique to the HLPT experiment, where the rapid vaporization at high methanol content above 35% leads to violent internal pressure changes, resulting in micro-explosions. [153] This was not observed at lower temperatures.

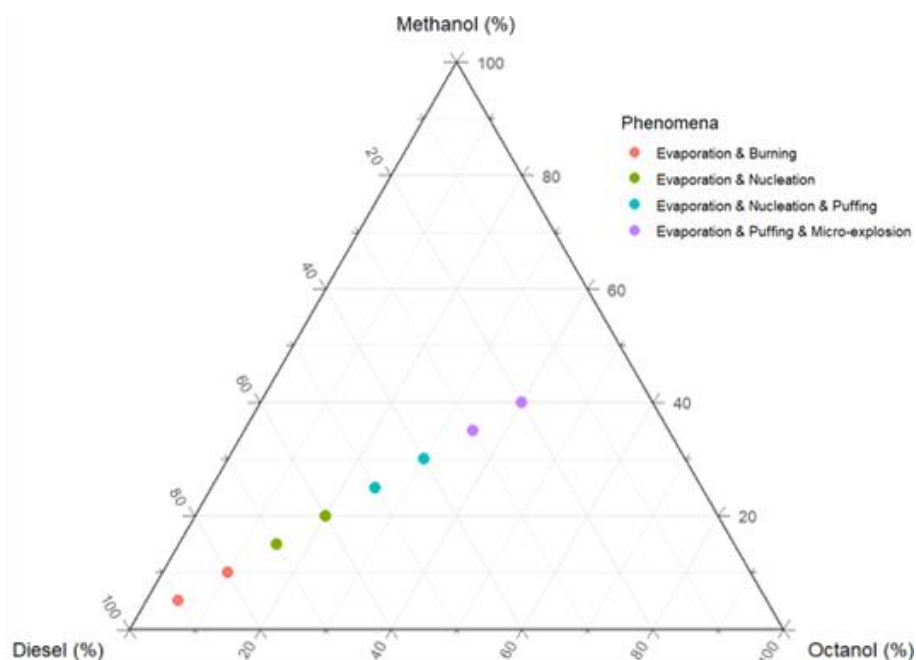


Figure 5.12 1.5 µL single D-M-O microdroplet behaviours at HLPT, atm

The microdroplet behaviours according to methanol content, can be expressed as

$$f(C_d, C_m, C_o) = \begin{cases} \text{Evaporation + Burning,} & \text{if } 0 < C_m \leq 10\% \\ \text{Evaporation + Nucleation,} & \text{if } 15\% \leq C_m \leq 20\% \\ \text{Evaporation + Nucleation + Puffing,} & \text{if } 25\% \leq C_m \leq 30\% \\ \text{Evaporation + Nucleation + Puffing + Micro - explosion,} & \text{if } C_m \geq 35\% \end{cases} \quad (5.5)$$

where C_d represent the percentage of diesel, C_m represent the percentage of methanol, and C_o represent the percentage of octanol.

When the heating temperature reaches HLPT, and with sufficient oxygen supply, combustion reaction accompanied by evaporation is observed [157], particularly when the ethanol content below 10%. Ethanol evaporates more rapidly than diesel and biodiesel, forming vapor bubbles inside the droplet that subsequently escape. The movement of ethanol vapor bubbles increases the droplet's kinetic energy and combined with the non-uniform temperature gradient, causes the droplet to oscillate. [143] This oscillation leads to deformation, making the droplet irregular in shape. [155] Despite the violent oscillation and deformation, the droplet does not disintegrate like D-W or D-M-O droplets, due to the higher viscosity of diesel and biodiesel. [149] The weak micro-explosion was observed as shown in Figure 5.13.

Combustion reactions typically occur after the evaporation, puffing, and micro-explosions, particularly when the droplet's volume has significantly decreased. [157] No puffing or micro-explosion is observed in the relatively larger sub-droplets. However, secondary breakup is captured in the smaller, highly mobile sub-droplets. These tiny droplets often break up into a series of smaller, aligned droplets that move in the same direction, or they rapidly vaporize and disappear into the surrounding air due to their small mass and volume. [137] While the ethanol content within the droplet evaporates quickly, it does not lead to puffing, micro-explosions, auto-ignition, or combustion during the test. [157]

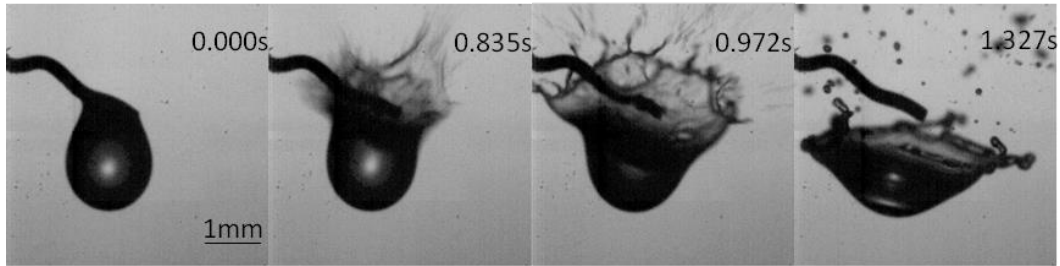


Figure 5.13 1.5 μL single D-BD-E microdroplet micro-explosion at HLPT, atm

Various blending ratio D-BD-E single microdroplets behaviours are outlined in Figure 5.14. This ternary phase diagram represents the single droplet behaviour of diesel, biodiesel, and ethanol blends in HLPT air. The phenomena observed are categorized as follows. At lower ethanol concentrations below 10%, the droplets primarily undergo simple evaporation. [139] The higher temperature of HLPT accelerates the evaporation rate [142], as seen in both diesel- and biodiesel-rich regions. As the heating process and evaporation undergoing, the droplet behaviour transitions to burning. [157] This phenomenon is more common at HLPT due to the increased energy causing the fuel blend to ignite more easily. At ethanol concentrations between 20% and 25%, the droplets exhibit evaporation and nucleation. The higher temperature increases internal pressure, leading to bubble formation inside the droplets. [144] Between 25% and 30% ethanol content, the droplets show signs of evaporation, nucleation, and puffing. The volatile nature of ethanol at HLPT leads to rapid vaporization, which increases internal pressure and causes puffing. At higher ethanol content above 35%, the droplets experience evaporation, puffing, and micro-explosion. This is due to the rapid phase change and pressure buildup at HLPT, where the highly volatile ethanol leads to more extreme phenomena such as micro-explosions. [155]

In both LLPT and MLPT experiments, the droplets predominantly showed simple evaporation at lower ethanol content. However, at HLPT, the evaporation process happens more quickly due to the increased energy input. Burning was not observed at LLPT or MLPT, but it becomes significant at HLPT, starting at 5% - 10% ethanol content. The higher temperature provides enough energy for the mixture to ignite, with diesel or biodiesel

present. [157] At HLPT, nucleation begins earlier compared to LLPT and MLPT, where it occurred at slightly higher ethanol content. The higher temperature increases the probability of bubble formation within the droplets. [142] Puffing occurs at lower ethanol content, starting around 30% at HLPT compared to the 40% threshold at LLPT and MLPT, indicating that higher temperatures promote faster and more intense phase transitions. [149] Micro-explosions are unique to the HLPT experiment and occur at high ethanol content above 35%. These were not observed at LLPT or MLPT, highlighting the more extreme internal pressure changes at HLPT.

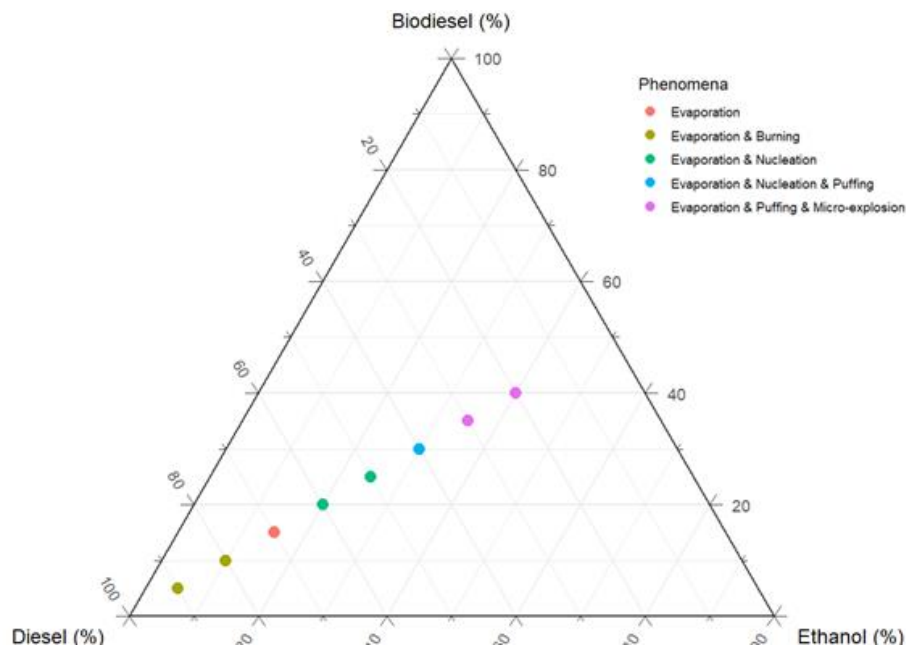


Figure 5.14 1.5 μ L single D-BD-E microdroplet behaviours at HLPT, atm

The microdroplet behaviours according to ethanol content, can be expressed as

$$f(C_d, C_{bd}, C_e) = \begin{cases} \text{Evaporation + Burning,} & \text{if } 0 < C_e \leq 10\% \\ \text{Evaporation,} & \text{if } 10\% < C_e \leq 15\% \\ \text{Evaporation + Nucleation,} & \text{if } 20\% \leq C_e \leq 25\% \\ \text{Evaporation + Nucleation + Puffing,} & \text{if } 25\% < C_e \leq 30\% \\ \text{Evaporation + Puffing + Micro - explosion,} & \text{if } C_e \geq 35\% \end{cases} \quad (5.6)$$

where C_d represent the percentage of diesel, C_{bd} represent the percentage of biodiesel, and C_e represent the percentage of ethanol.

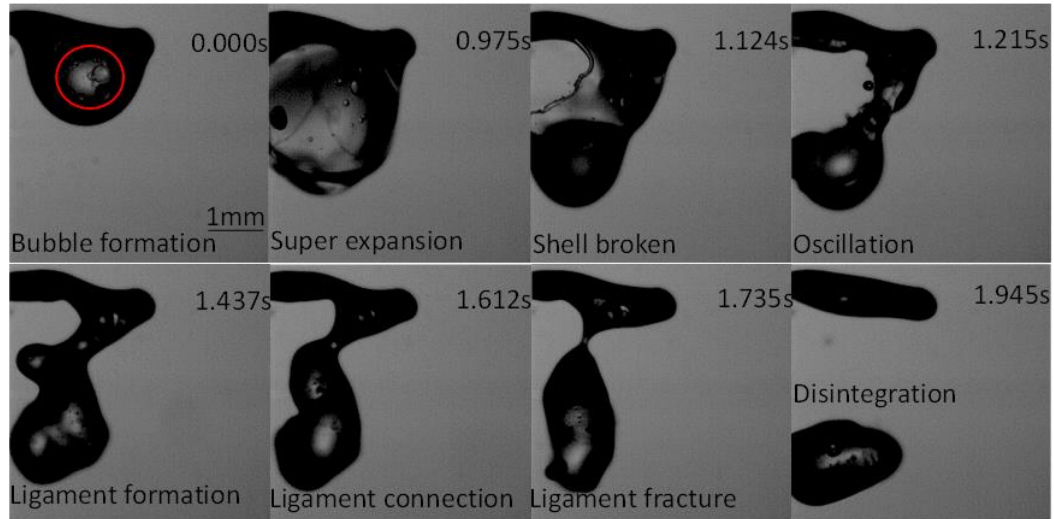


Figure 5.15 1.5 μ L single D-M-U- microdroplet behaviour at HLPT, atm

The D-M-U microdroplet was tested in the TLPT air environment, where it underwent evaporation, expansion, and eventual splitting. Vapor bubbles formed inside the droplet, moving around within it. The droplet expanded to twice its original size before breaking up at its thinnest edge, as shown in Figure 5.15. The droplet split into two parts, with heat from the surrounding air and the droplet's own kinetic energy causing it to oscillate. [144] Due to the high surface tension of the blend, the droplet did not break up further and eventually restored a spherical shape. [153] Bubbles continued to form inside the broken sub-droplets. [154]

5.5 Temperature and Blending Ratio Impact on Puffing and Micro-explosion

This section provides comparative analysis of how temperature and blending ratio interact to influence fuel droplet behaviours, such as nucleation, puffing, and micro-explosion. The study conducts a quantitative assessment of the intensity of these phenomena across

different temperature ranges and blending ratios. By examining the impact of these factors on fuel droplet dynamics, this analysis aims to offer a deeper understanding of the underlying mechanisms driving droplet breakup.

This section also presents the probability heatmap that indicates the occurrence of various behaviours of fuel microdroplets, including nucleation, puffing, and micro-explosion, as influenced by heating temperature. This heatmap is used to investigate how different temperatures affect the transient behaviours of microdroplets, providing a visual representation of the probability of each phenomenon under varying conditions.

In addition, a detailed analysis of the puffing change rate is conducted to explore the transition between puffing and micro-explosion. This analysis aims to identify the specific temperature thresholds and conditions that lead to these different behaviours. By examining these dynamics, the study seeks to enhance the understanding of the underlying mechanisms governing fuel droplet breakup behaviour and to contribute to the optimization of fuel atomization strategies for improved combustion efficiency and performance.

5.5.1 D-M-O blend

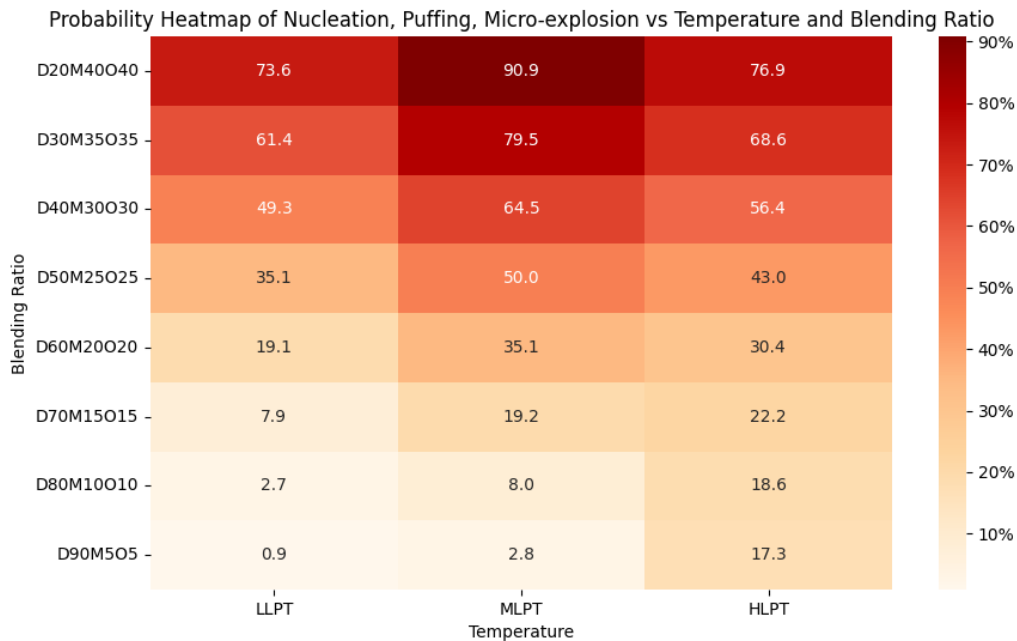


Figure 5.16 Probability heatmap of nucleation, puffing and micro-explosion under varying temperature and D-M-O ratio

Figure 5.16 visualizes the probability of nucleation, puffing and micro-explosion under various temperature conditions LLPT, MLPT, HLPT across a range of D-M-O ratios. As Figure 5.16 shown, across all blending ratios, as temperature increases from LLPT to HLPT, the probability of nucleation, puffing and micro-explosion increases. At lower temperatures (LLPT), higher blending ratios (D20M40O40) show a higher probability of nucleation and micro-explosion, indicating that more intense physical reaction and phase changing occur under these conditions.

Higher blending ratios (D20M40O40 and D30M35O35) show significantly higher probabilities of nucleation, puffing and micro-explosion across all temperatures, particularly in medium to high temperatures (MLPT and HLPT), where the probability approaches or exceeds 80%. Lower blending ratios (D80M10O10 and D90M5O5) exhibit low probabilities

of nucleation, puffing and micro-explosion across all temperatures, indicating that these blends can be more stable.

D20M40O40 exhibits the highest probability of nucleation, puffing and micro-explosion across all temperatures, under MLPT and HLPT conditions, with probabilities exceeding 90%, indicating that this blend is less stable at high temperatures and more prone to intense micro-explosions. D90M5O5 shows the lowest probability of nucleation, puffing and micro-explosion, with only 17.3% even at high temperatures (HLPT), suggesting that this blend is relatively stable across various temperature conditions.

Overall, temperature and blending ratio are crucial factors influencing the probability of nucleation, puffing and micro-explosions. Higher blending ratios and temperatures tend to result in higher probabilities of nucleation, puffing and micro-explosions. For practical applications, D20M40O40 is tending to undergo explosive phenomena in high-temperature environments, whereas D90M5O5 is relatively stable and require adjustment of fuel atomization strategy.

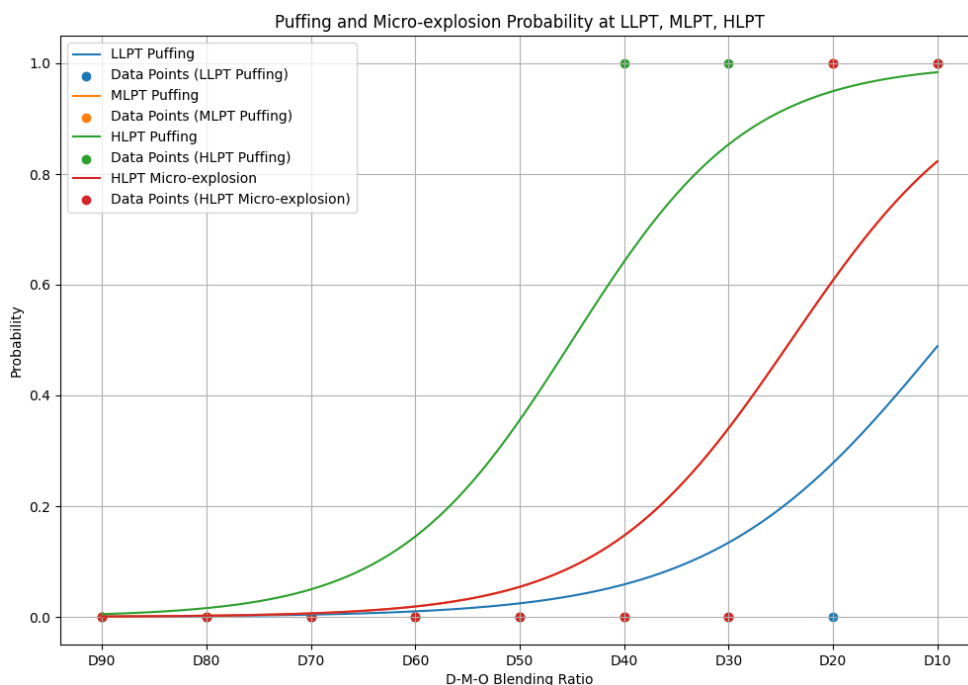


Figure 5.17 Probability of puffing and micro-explosion under varying temperature and D-M-O ratio

Figure 5.17 shows the probability of puffing and micro-explosion phenomena across different D-M-O blending ratios under three temperature conditions LLPT, MLPT, and HLPT. The probability of puffing increases as the D-M-O blending ratio increases (high alcohol content). This trend is observed consistently across all three temperature conditions LLPT, MLPT, HLPT. At the lower diesel content, the probability of puffing is relatively high for all temperatures. This indicates that puffing is to occur at high blending ratios (high alcohol content). As the blending ratio decreases, the puffing probability rapidly decreases, reaching near zero at lower blending ratios (low alcohol content).

HLPT conditions exhibit a higher probability of puffing at low blending ratios compared to MLPT and LLPT. The MLPT curve (overlap with HLPT micro-explosion curve) sits between the HLPT and LLPT curves, indicating that puffing is less likely under medium temperature conditions than at high temperatures but more likely than at low temperatures. LLPT shows the lowest puffing probability among the three, particularly noticeable as the blending ratio decreases.

The red curve represents the probability of micro-explosions under HLPT conditions. The micro-explosion probability is highest at low diesel content and decreases as the blending ratio decreases. Micro-explosion events have a significant probability at lower diesel content, but this probability increases slowly compared to puffing as the blending ratio increases.

In summary, both puffing and micro-explosion probabilities are highly dependent on the blending ratio, with higher blending ratios being more prone to these phenomena. Higher temperatures (HLPT) significantly increase the probability of both puffing and micro-explosions at lower blending ratios. As the D-M-O blending ratio decreases, the system

becomes more stable, with significantly reduced probabilities for both puffing and micro-explosions across all temperature conditions.

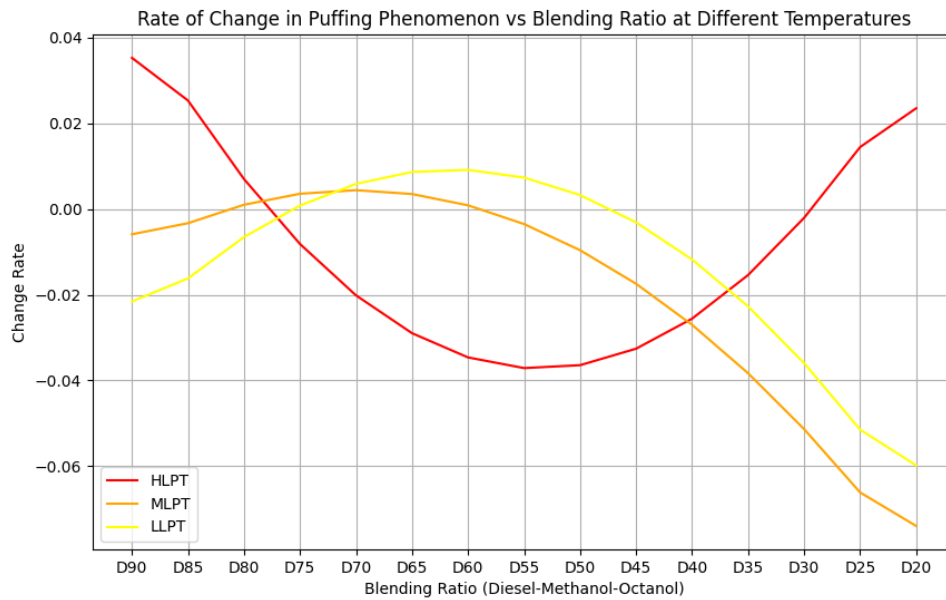


Figure 5.18 Puffing change rate under varying temperature and D-M-O ratio

Figure 5.18 illustrates the rate of change in the puffing phenomenon as a function of the D-M-O blending ratio at different temperature conditions LLPT, MLPT and HLPT. The red curve (HLPT) represents the rate of change in puffing under high-temperature conditions. At lower blending ratios (D90 to D75), the rate of change decrease although it is positive, indicating a decreasing probability of puffing as the blending ratio increases. Between D75 and D45, the rate of change turns negative, with a steep decline, suggesting that puffing becomes less likely as the blending ratio continues to decrease. As the blending ratio further increases (D45 to D20), the rate of change becomes positive again, indicating a resurgence in the probability of puffing at high blending ratios.

The orange curve (MLPT) shows the rate of change in puffing at medium temperatures. Initially, the curve is relatively flat, indicating a stable rate of change between D90 and D70. From D70 to D55, the curve slightly rises, showing a small increase in the rate of puffing, but it remains close to zero, suggesting minimal impact on puffing probability. After D55, the

rate of change turns negative, with a gradually increased absolute value, indicating that puffing becomes more probable as the blending ratio increases further.

The yellow curve (LLPT) represents the rate of change in puffing at low temperatures. At the lowest blending ratios (D90 to D80), the rate of change is positive but low, showing a modest increase in puffing probability. As the blending ratio increases from D80 to D55, the rate of change is mostly flat or slightly positive, suggesting a stable probability of puffing in this range. From D55 onward, the rate of change becomes negative, with a steep increased absolute value, indicating a rapid increase in puffing probability as the blending ratio increases further.

The HLPT condition shows significant variability in the rate of change of puffing across different blending ratios, with sharp increases and decreases, suggesting that puffing is highly sensitive to changes in the blending ratio at high temperatures. The MLPT curve is more stable, with minor fluctuations around zero, indicating that the rate of puffing change is less sensitive to blending ratio variations at medium temperatures. The LLPT curve shows a relatively stable rate of change at lower blending ratios, but a sharp increased absolute value at higher blending ratios, indicating that puffing becomes significantly more likely as the blending ratio increases under low-temperature conditions. The puffing change rate analysis provides insights into how temperature and blending ratio interact to influence the puffing phenomenon, which can be critical for optimizing fuel blends for stability and performance under different operating conditions.

5.5.2 D-BD-E blend

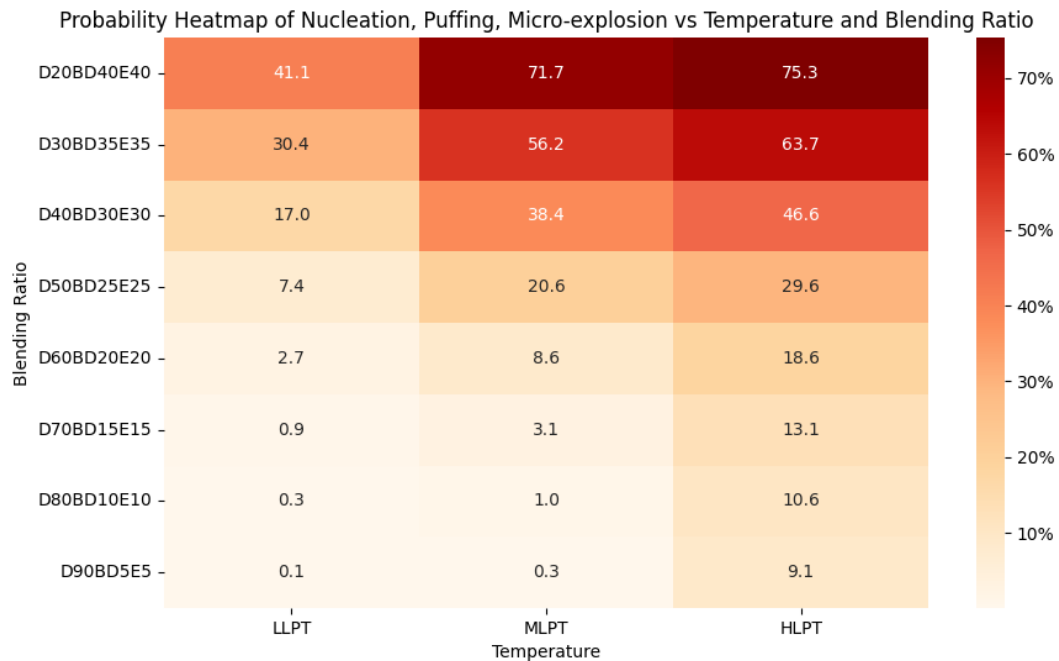


Figure 5.19 Probability heatmap of nucleation, puffing and micro-explosion under varying temperature and D-BD-E ratio

Figure 5.19 illustrates the probability of nucleation, puffing, and micro-explosion phenomena across different temperatures LLPT, MLPT, HLPT and varying D-BD-E blending ratio. As the temperature increases from LLPT to HLPT, the probability of these phenomena generally increases across all blending ratios. At HLPT, the highest probabilities are observed, particularly for the blending ratios D20BD40E40 and D30BD35E35, with probabilities reaching 75.3% and 63.7% respectively. The blending ratio D20BD40E40 shows the highest probability of nucleation, puffing, and micro-explosion across all temperature ranges, with a significant increase in probability as the temperature rises.

Conversely, lower blending ratios, such as D90BD5E5 and D80BD10E10, exhibit much lower probabilities across all temperature conditions, indicating that these blends are more stable and less prone to these phenomena.

At LLPT, the probabilities are relatively low across all blending ratios, with D20BD40E40 showing the highest probability at 41.1%, indicating that these phenomena are less likely at lower temperatures. At MLPT, the probabilities increase significantly for higher blending ratios, with D20BD40E40 reaching 71.7% and D30BD35E35 reaching 56.2%. At HLPT, the probability peaks, for D20BD40E40, where it reaches 75.3%, indicating a high probability of nucleation, puffing, and micro-explosion under these conditions.

Overall, blends with higher amounts of biodiesel and ethanol, such as D20BD40E40, are more susceptible to nucleation, puffing, and micro-explosion, at higher temperatures. Lower blending ratios, such as D90BD5E5 and D80BD10E10, show a much lower probability of these phenomena, even at higher temperatures, indicating greater stability. Temperature is a critical factor, significantly increasing the probability of these phenomena as it rises, particularly in blends with higher concentrations of biodiesel and ethanol. This analysis suggests that ingenious utilize of both blending ratios and operating temperatures is vertical for enhancing the intensity of nucleation, puffing, and micro-explosion in fuel atomization.

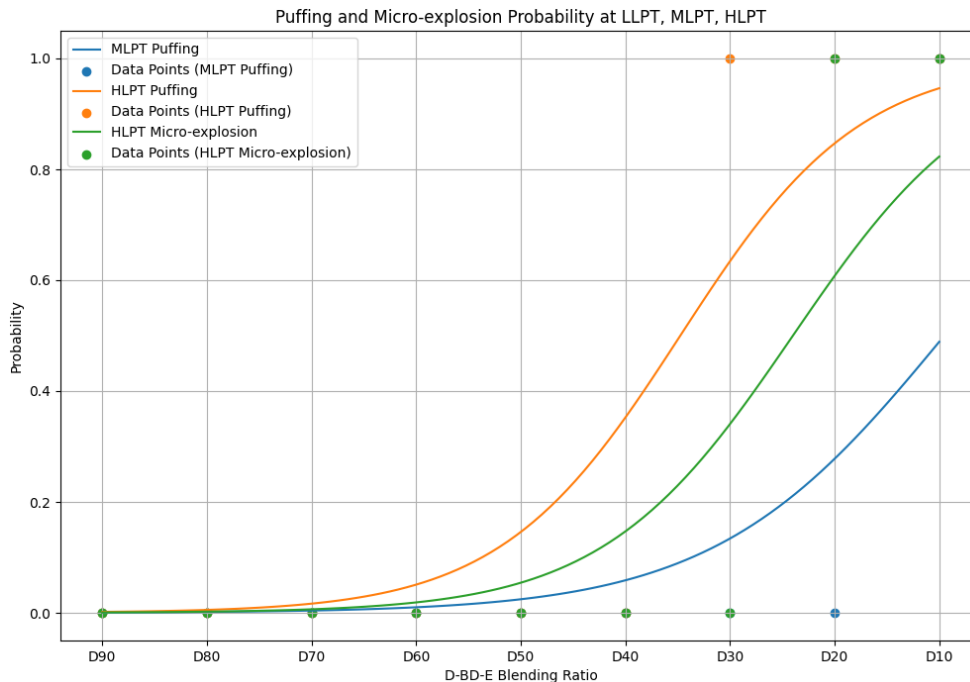


Figure 5.20 Probability of puffing and micro-explosion under varying temperature and D-BD-E ratio

Figure 5.20 indicates the probability of puffing and micro-explosion events across different D-BD-E blending ratios under three temperature conditions LLPT, MLPT, and HLPT. The probability of puffing increases as the D-BD-E blending ratio increases. This trend is consistent across all three temperature conditions. At high blending ratios, the probability of puffing is almost certain for higher temperature conditions, approaching 1.0 for MLPT and HLPT. This indicates a high probability of puffing when the blending ratio is maximum. As the blending ratio decreases, the puffing probability rapidly decreases and approaches zero, at blending ratios D7015O15.

HLPT conditions exhibit a higher probability of puffing at low blending ratios compared to MLPT and LLPT. The MLPT curve sits between the HLPT and LLPT curves, indicating that puffing is less likely under medium temperature conditions than at high temperatures but more likely than at low temperatures. LLPT shows the lowest puffing probability among the three, at lower blending ratios, where the probability is near zero.

The green curve represents the probability of micro-explosion under HLPT conditions. Similar to puffing, the micro-explosion probability is highest at very low diesel content and increases as the blending ratio increases. The micro-explosion probability shows a steep decline at lower blending ratios, indicating that micro-explosions are most likely to occur when the D-BD-E blending ratio is high.

Both puffing and micro-explosion probabilities are highly dependent on the D-BD-E blending ratio, with higher blending ratios being more prone to these phenomena. Higher temperatures (HLPT) significantly increase the probability of both puffing and micro-explosions at lower blending ratios. As the D-BD-E blending ratio decreases, the system becomes more stable, with significantly reduced probabilities for both puffing and micro-explosions across all temperature conditions.

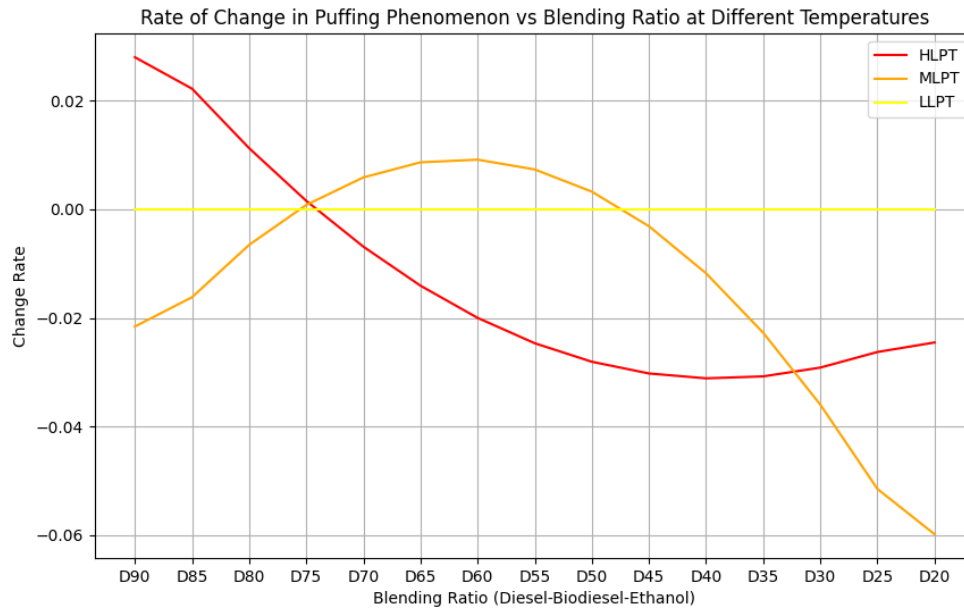


Figure 5.21 Puffing change rate under varying temperature and D-BD-E ratio

Figure 5.21 illustrates the rate of change in the puffing phenomenon as a function of the D-BD-E blending ratio at different temperature conditions LLPT, MLPT, and HLPT. The red curve (HLPT) represents the rate of change in puffing under high-temperature conditions. At lower blending ratios (D90 to D75), the rate of change is positive, indicating that the probability of puffing is increasing as the blending ratio increases. From D75 to D45, the curve dips into the negative region with an increased absolute value, showing that the rate of puffing increases as the blending ratio further increases. The most significant decrease occurs between D65 and D45. Beyond D45, the curve starts to rise again slightly although remains in the negative region, indicating that the rate of change in puffing is still increasing, but at a slower rate.

The orange curve (MLPT) shows the rate of change in puffing at medium temperatures. Initially, the curve is slightly negative, indicating a small decrease in the probability of puffing as the blending ratio increases from D90 to D75. The curve then rises into the positive region from D75 to D55, suggesting an increase in the rate of puffing in this range.

After D55, the curve declines steadily, moving back into the negative region, indicating a rapid increase in the puffing rate as the blending ratio continues to increase.

The yellow curve (LLPT) represents the rate of change in puffing at low temperatures. The curve is mostly flat and close to zero, indicating that the puffing rate remains relatively constant and is minimally affected by changes in the blending ratio under low-temperature conditions.

In summary, the HLPT condition shows significant variability in the rate of change of puffing across different blending ratios, with both positive and negative trends, indicating that puffing is highly sensitive to blending ratio changes at high temperatures. The MLPT curve shows a moderate sensitivity to blending ratio changes, with a positive rate of change at mid-range blending ratios, suggesting that puffing may increase in this range but decreases significantly at both lower and high blending ratios. The LLPT curve remains nearly flat, suggesting that puffing is not significantly influenced by blending ratio changes at low temperatures, indicating stability in the puffing rate under these conditions. The puffing change rate analysis highlights how temperature and blending ratio interact to affect the rate of change in puffing. Understanding these interactions can help in optimizing fuel mixtures to boost puffing behaviour under various operating conditions.

5.6 D-M-O(with 10%, 20%, 50% water) Droplet Behaviour at HLPT

Compared to previous experiment results, puffing and micro-explosions are more easily triggered at high methanol content and high temperature environment. Hence, the water as additives is introduced to D-M-O blends to investigate its impact on these two phenomena. Three blending ratio blends were selected to produce the droplet transient behaviour observation test, D70M15O15, D50M25O25, and D20M40O40 with three different water addition amounts, 10%, 20% and 50% respectively.

Puffing and micro-explosion were observed in all three fuel blends with 50% water content addition. The addition of water in the D-M-O blend shows a positive correlation with the occurrence of puffing and micro-explosions. Notably, D20M40O40 with 50% water is more prone to puffing and micro-explosions, at higher methanol content. By increasing the water content in the D-M-O blend to 20%, more intense puffing, and micro-explosions are observed during the droplet heating process. These strong puffing and micro-explosion events cause smaller sub-droplets to disintegrate and be ejected with high motion into the surrounding air, thereby enhancing fuel and air mixing. The size distribution of sub-droplet sizes was analysed, as shown in Figure 5.22, Figure 5.23 and Figure 5.24. The increased water content in the fuel blend significantly boosts the occurrence of puffing and micro-explosions and shortens the trigger time for these phenomena.

5.6.1 D70M15O15 with 10%, 20%, 50% water

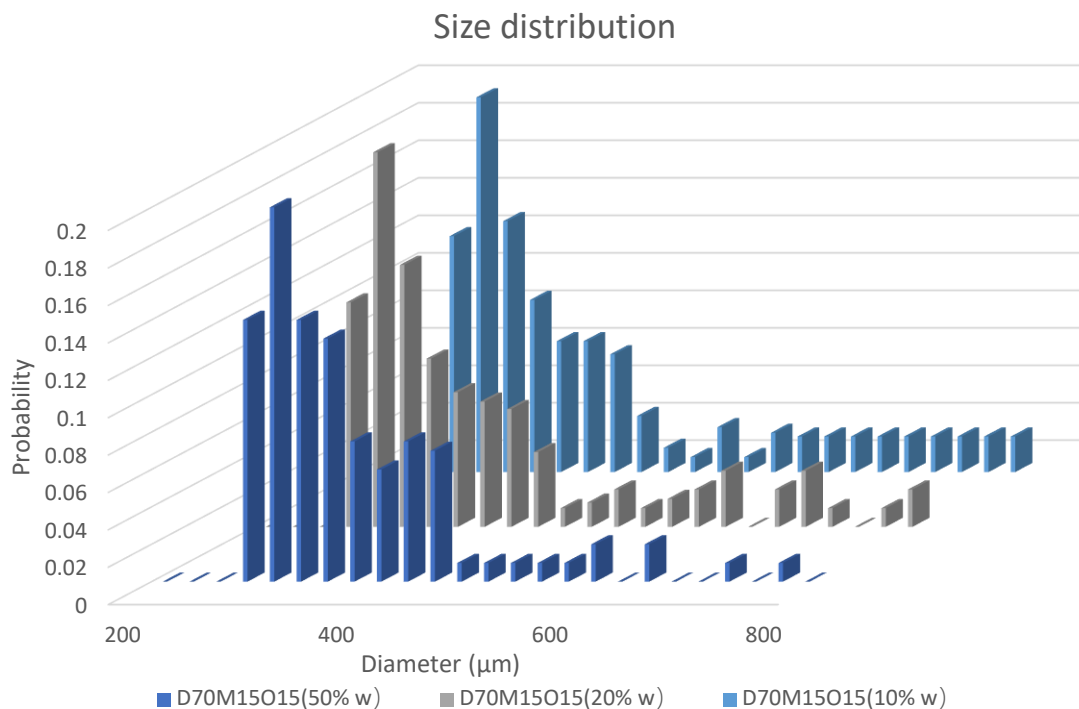


Figure 5.22 D70M15O15 with 10%, 20%, 50% water sub-droplet size distribution at TLPT, atm

Figure 5.22 shows the size distribution of sub-droplets formed after the micro-explosion of a D70M15O15 blend with the addition of 10%, 20%, and 50% water. The chart details the probability distribution of sub-droplet diameters in μm .

1. 50% water Case

Figure 5.22 (first row) presents the size distribution of sub-droplets generated from a blend of D70M15O15 with 50% water. The most frequent sub-droplet size is $300\ \mu\text{m}$, with a peak probability of 0.2, indicating that most sub-droplets are concentrated in this size range. The $200\text{--}250\ \mu\text{m}$ range is also significant, with probabilities of 0.14 and 0.13.

A noticeable presence of mid-sized droplets in the $400\text{--}500\ \mu\text{m}$ range is observed, with probabilities between 0.06 and 0.07. The size distribution extends to droplets up to $600\ \mu\text{m}$, but the probabilities for sizes larger than $500\ \mu\text{m}$ are relatively low.

The higher diesel content (70%) reduces the intensity of the micro-explosion compared to blends with higher methanol or octanol content, resulting in a broader distribution of droplet sizes. Diesel's lower volatility limits the energy available for fragmentation, resulting in a higher proportion of mid- and larger-sized droplets.

2. 20% water Case

Figure 5.22 (second row) shows the size distribution of sub-droplets of D70M15O15 blend formed with 20% water. Similar to the 50% water case, the most common size is $300\ \mu\text{m}$, with a peak probability of 0.2. Other significant sizes include $200\text{--}300\ \mu\text{m}$, with probabilities ranging from 0.12 to 0.14.

A higher proportion of mid-sized droplets ($400\text{--}500\ \mu\text{m}$) is observed compared to the 50% water case. The probabilities for this range decline from 0.07 to 0.04, but larger droplets are more common, with sizes extending to $700\text{--}800\ \mu\text{m}$, albeit at low probabilities.

The reduced water content (20%) weakens the micro-explosion, resulting in less efficient droplet fragmentation. This leads to a broader distribution with a noticeable increase in the number of larger droplets compared to the 50% water case, where smaller droplets were more predominant.

3. 10% water Case

Figure 5.22 (third row) illustrates the size distribution for the 10% water case. The most frequent sub-droplet size remains at 300 μm , with a peak probability of 0.2. Other sizes within the 200–250 μm range show probabilities between 0.126 and 0.134.

In this case, the distribution is broader and extends further into the larger droplet range. The 350–500 μm range is more pronounced, with probabilities gradually decreasing from 0.07 at 350 μm to 0.03 at 400 μm . Larger droplets, in the 500–600 μm and 700–800 μm ranges, have non-negligible probabilities, indicating a less intense micro-explosion compared to higher water content blends.

Comparative analysis

In all cases, 300 μm is the most frequent droplet size, irrespective of the water content. However, the efficiency of the micro-explosion and the resulting size distribution are highly dependent on the water concentration:

- 50% water case shows the most efficient fragmentation, with a sharp decline in probability beyond 400 μm and minimal presence of larger droplets. The higher water content creates a stronger explosion, leading to a more concentrated distribution of smaller droplets.
- 20% water case size distribution is broader than in the 50% water case, with more droplets in the 400–600 μm range and a higher presence of larger droplets. The

lower water content generates less explosive pressure, leading to less intense fragmentation and a wider size distribution.

- 10% water case shows the weakest micro-explosion effect, resulting in the broadest size distribution. A higher proportion of larger droplets, in the 500–800 μm range, indicates that the explosion was less efficient at breaking down the initial droplets.

Conclusion

The D70M15O15 blend with decreasing water content (50%, 20%, and 10%) results in progressively less efficient droplet fragmentation. The 50% water blend generates primarily smaller droplets due to a more intense micro-explosion, while the 20% water blend produces a wider size range with more mid-sized droplets. The 10% water blend demonstrates the least efficient fragmentation, resulting in the broadest distribution and the highest proportion of larger droplets. The water content is a key factor in influencing the intensity of the micro-explosion and the resulting droplet size distribution.

5.6.2 D50M25O25 with 10%, 20%, 50% water

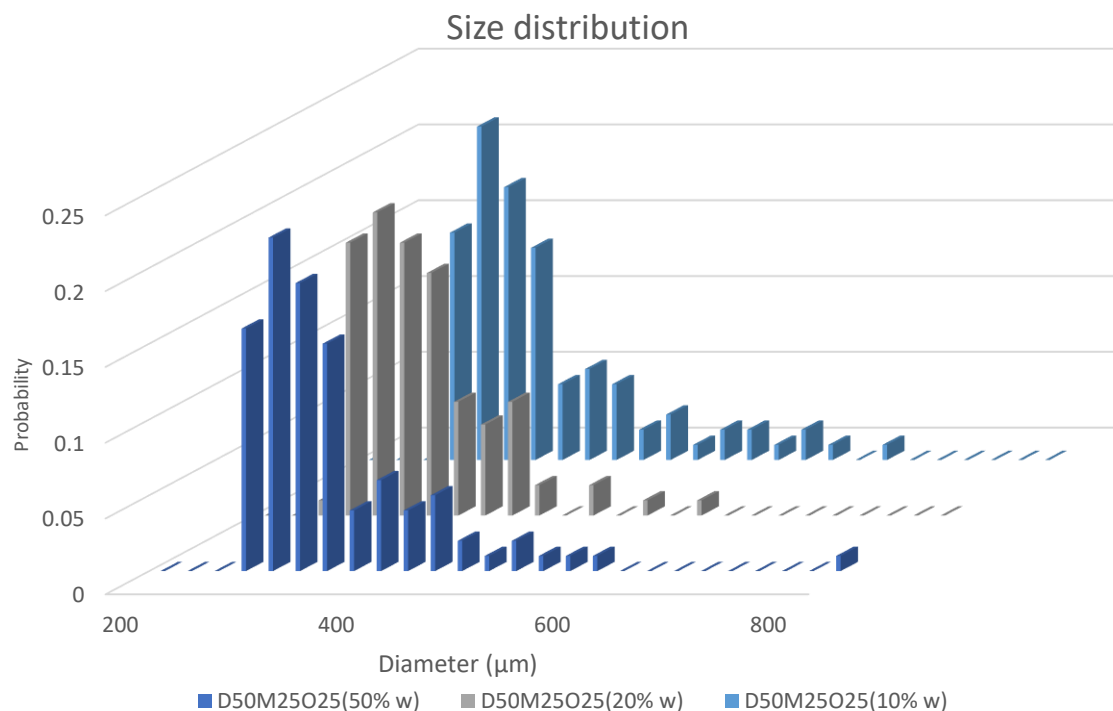


Figure 5.23 D50M25O25 with 10%, 20%, 50% water sub-droplet size distribution at TLPT, atm

Figure 5.23 shows the size distribution of sub-droplets formed after the micro-explosion of a D50M25O25 blend with the addition of 10%, 20%, and 50% water. The chart details the probability distribution of sub-droplet diameters in μm .

1. 50% water Case

Figure 5.23 (first row) presents the size distribution of sub-droplets generated after a micro-explosion of a blend of D50M25O25 with 50% water content. The most frequent sub-droplet size is 300 μm , with a peak probability of 0.22. This indicates that a significant portion of sub-droplets produced by the micro-explosion fall into this size range. There is also a substantial probability of droplets between 200 μm and 300 μm , with values ranging from 0.16 to 0.19.

The probability decreases rapidly as the droplet size increases beyond 400 μm , dropping from 0.06 at 400 μm to very low values beyond 500 μm . The probability of sub-droplets larger than 600 μm is negligible, with probabilities close to zero. The sharp decline in the distribution indicates that the micro-explosion predominantly results in smaller sub-droplets, with only a few large droplets remaining. The presence of water and volatile components like methanol likely drives this fragmentation, making the micro-explosion quite efficient in breaking the original droplet into smaller sizes.

2. 20% water Case

Figure 5.23 (second row) shows the size distribution of sub-droplets generated after a micro-explosion of D50M25O25 blend with 20% water. The most frequent sub-droplet sizes are between 200 μm and 400 μm , with peak probabilities at 300 μm (0.2), 250 μm (0.18), and 350 μm (0.18).

Compared to the 50% water case, the distribution here is slightly broader, extending into the 400–500 μm range with non-negligible probabilities. There are still small probabilities for droplets larger than 500 μm , but the probability of droplets beyond 600 μm remains low. With 20% water, the intensity of the micro-explosion is lower than with 50% water, leading to a less aggressive breakup of the parent droplets. Consequently, larger droplets are more prevalent and the distribution is wider.

3. 10% water Case

Figure 5.23 (third row) presents the size distribution of sub-droplets generated after a micro-explosion of D50M25O25 blend with 10% water. The most common sub-droplet size is 300 μm , with a peak probability of 0.22.

The distribution is broader compared to the 50% and 20% water cases, with more droplets in the 400–500 μm range. Probabilities at 400 μm and 450 μm are 0.06 and 0.05,

respectively. The probabilities for droplets larger than 500 μm are low but not negligible, with some droplets extending up to 600 μm , though the probabilities are very small. The lower water content (10%) results in a less intense micro-explosion, leading to a broader size distribution with more larger droplets compared to higher water content cases.

Comparative analysis

- The most efficient fragmentation occurs in the 50% water case, where the distribution is concentrated in the 200–300 μm range. There is a rapid decline in probability beyond 400 μm , with very few large droplets remaining. The higher water content generates a stronger micro-explosion, leading to more efficient fragmentation and smaller droplets.
- The size distribution is slightly broader in the 20% water case, with more droplets in the 400–500 μm range. The reduced water content leads to a less intense micro-explosion, and as a result, the distribution extends to more mid-sized droplets. There is a more gradual tapering of the distribution compared to the 50% water case, and larger droplets are more prevalent.
- The 10% water case shows the broadest size distribution, with the presence of more large droplets extending up to 600 μm . The weaker micro-explosion, caused by the lower water content, results in less efficient fragmentation and a higher proportion of larger droplets. The peak probability remains at 300 μm , but the overall size distribution is more varied compared to the higher water content cases.

Conclusion

The D50M25O25 blend with 10%, 20%, and 50% water shows clear differences in the efficiency of the micro-explosion process based on water content. The 50% water blend produces a high proportion of small sub-droplets, with a concentrated size distribution in the 200–300 μm range. As water content decreases to 20% and 10%, the micro-explosion becomes less efficient, leading to a broader size distribution and a higher proportion of

larger sub-droplets. The 10% water blend results in the broadest distribution, with a significant number of larger droplets, in the 300–500 μm range. The water content is crucial in determining the size distribution of sub-droplets following a micro-explosion, higher water content results in finer fragmentation and a greater proportion of smaller droplets.

5.6.3 D20M40O40 with 10%, 20%, 50% water

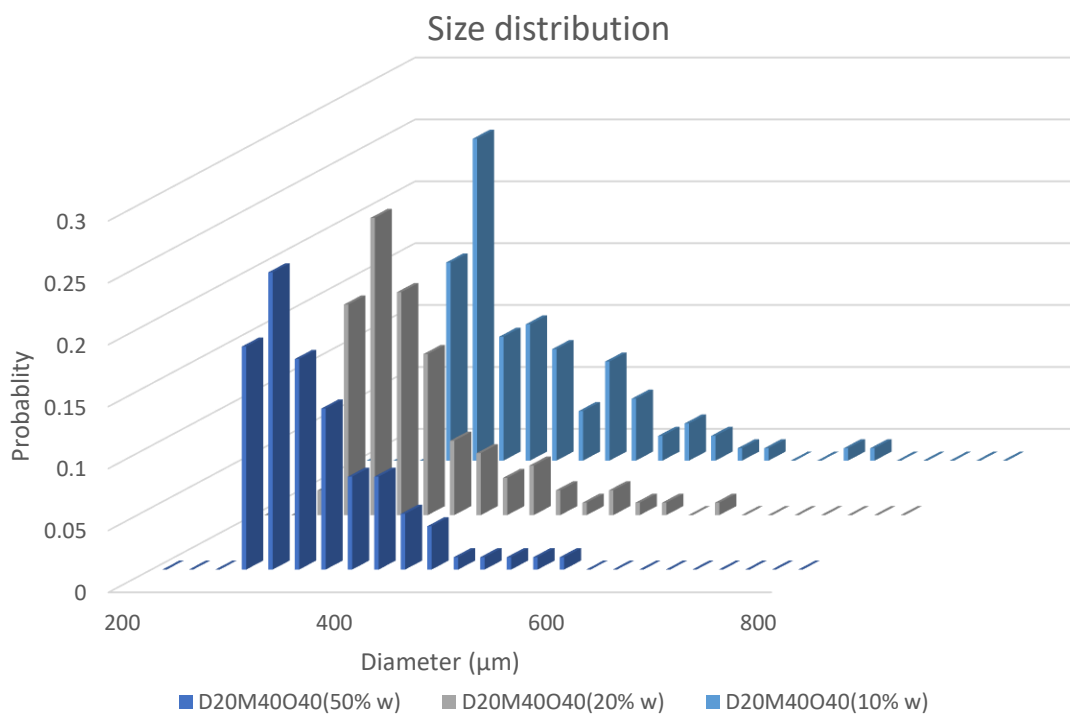


Figure 5.24 D20M40O40 with 10%, 20%, 50% water sub-droplet size distribution at TLPT, atm

Figure 5.24 shows the size distribution of sub-droplets formed after the micro-explosion of a D20M40O40 blend with the addition of 10%, 20%, and 50% water. The chart details the probability distribution of sub-droplet diameters in μm .

1. 50% water Case

Figure 5.24 (first row) presents the size distribution of sub-droplets generated after a micro-explosion of a blend of D20M40O40 with 50% water content. The most frequent sub-

droplet diameters fall between 200 μm and 300 μm , with probabilities peaking at 0.24 for droplets in the 300 μm range. This indicates that a significant portion of sub-droplets produced by the micro-explosion fall into this size range.

The distribution is skewed towards smaller sub-droplets, typical of micro-explosion phenomena, where larger droplets break into smaller fragments. The probability decreases rapidly as the droplet size increases beyond 400 μm , with very low values for droplets exceeding 600 μm . The presence of methanol and water, which evaporate faster than octanol, contributes to the high-pressure buildup inside the droplet, leading to fragmentation into smaller sub-droplets. The probability of droplets larger than 500 μm forming is negligible, indicating that the micro-explosion process efficiently generates smaller droplets.

2. 20% water Case

Figure 5.24 (second row) shows the size distribution of sub-droplets generated after a micro-explosion of a D20M40O40 blend with 20% water added. The most common sub-droplet size remains between 200 μm and 300 μm , similar to the 50% water case, with a peak probability of 0.24 at around 300 μm . However, the distribution of smaller droplets (200–300 μm) is slightly more prominent in the 50% water case than in the 20% water blend.

The 20% water blend shows a broader size distribution, with more sub-droplets in the 400 μm and above range compared to the 50% water case. Small but non-zero probabilities of sub-droplets extending up to 600 μm are observed. Although the 300 μm sub-droplet size remains dominant, the fraction of smaller droplets is lower compared to the 50% water case. This suggests that the 50% water blend promotes more efficient fragmentation, producing smaller sub-droplets more effectively.

3. 10% water Case

Figure 5.24 (third row) shows the size distribution of sub-droplets formed after a micro-explosion of a D20M40O40 blend with 10% water added. The most frequent droplet size is in the 300 μm range, where the probability peaks at 0.26, slightly higher than the previous cases with 20% and 50% water content. There is also a substantial proportion of droplets in the 200–300 μm range, with a probability of 0.16.

The 10% water case shows a relatively broad distribution, with a greater number of sub-droplets in the 400–500 μm range. The probability of droplets in the 400 μm range is 0.08. However, the probability of larger droplets above 500 μm is lower than in the 20% water case. With less water (10%), the micro-explosion process appears to be less efficient at fragmenting droplets into smaller sizes, leading to a broader distribution and more mid-sized droplets. The lower water content generates less internal pressure during evaporation, causing a less intense breakup.

Comparative analysis

- The highest concentration of smaller droplets (200–300 μm) is observed in the 50% water case. This blend promotes the most efficient micro-explosion, generating predominantly smaller sub-droplets and showing a rapid decline in probability for larger droplets.
- The 20% water blend has a broader size distribution, with a higher number of sub-droplets in the 400–500 μm range. The fragmentation process is less effective compared to the 50% water case, as seen by the presence of more large droplets.
- The 10% water blend shows the broadest distribution of droplet sizes, with more large sub-droplets in the 400–500 μm range. The lower water content results in less efficient fragmentation, with more droplets in the mid-size range. This blend generates fewer smaller droplets than the 50% water blend.

Conclusion

The D20M40O40 blend with decreasing water content (50%, 20%, and 10%) results in progressively less efficient droplet fragmentation. The 50% water blend produces a high proportion of smaller sub-droplets, concentrated in the 200–300 μm range. As water content decreases to 20% and 10%, the size distribution becomes broader, with more larger sub-droplets. The 10% water case leads to a wider size distribution and more mid-sized droplets. The water content is essential in determining the intensity of the micro-explosion and the resulting size distribution, with higher levels leading to more efficient fragmentation and smaller droplets.

5.7 Conclusion

In this chapter, the behaviours of D-M-O, D-BD-E and D-M-U blend microdroplets under varying high-temperature environments LLPT, MLPT, and HLPT, were investigated. To further explore the effect of water content on microdroplet behaviour, additional tests were conducted using D-M-O blends with varying water content proportions of 10%, 20%, and 50% under the HLPT environment. The findings can be summarized as follows:

Evaporation and combustion

- The evaporation rates of D-M-O, D-BD-E, and D-M-U blends showed significant variation across the LLPT, MLPT, and HLPT environments, with higher evaporation rates observed at HLPT due to the higher surrounding air temperature.
- Combustion reactions, including flame ignition and soot formation, were more prevalent in diesel-rich blends, particularly in D-M-O and D-BD-E, while D-M-U showed reduced soot production due to the presence of UREA.

Soot formation

- The propensity for soot formation increased with higher diesel content. The presence of alcohols such as methanol and ethanol, along with biodiesel, reduced soot formation, particularly in the D-M-O and D-BD-E blends.

Puffing and micro-explosion

- In blends with high water content, in the D-M-O blend, puffing and micro-explosions were more commonly observed. This behaviour was due to the rapid vaporization of water at the high temperatures of the HLPT environment, which caused internal pressure buildup and subsequent droplet breakup.

Comparison between blends

- D-M-O blends generally showed faster evaporation and more aggressive droplet dynamics compared to D-BD-E and D-M-U. The presence of methanol and octanol contributed to more volatile behaviour, while biodiesel and UREA slowed down evaporation.

Water content impact

- The inclusion of water in the D-M-O blend significantly affected droplet behaviour. As the water content increased, the microdroplets exhibited more pronounced expansion, oscillation, and droplet breakup due to the rapid vaporization of water at high temperatures.
- At 50% water content, microdroplet was highly unstable, with puffing and strong micro-explosion of the droplet and secondary breakup of sub-droplets.

Chapter 6 Biodiesel/HVO and Alcohol Blends

Droplet Behaviour at Ambient Temperatures

6.1 Introduction

In this chapter, the behaviours of BD-E and HVO-M-O microdroplets were investigated under varying high-temperature environments LLPT, MLPT, and HLPT. The effects of temperature and multi-fuel blend blending ratios on these phenomena were quantitatively analysed and comparatively discussed. The microdroplet behaviours were accurately classified into several distinct categories based on temperature and component ratio.

6.2 BD-E, HVO-M-O Droplet Behaviour at LLPT

The BD-E blend droplets were tested in the LLPT air environment. Among all the BD-E blends, due to ethanol's low boiling point, the droplet exhibited faster evaporation compared to D-BD. Puffing and strong micro-explosion were observed during the test when the ethanol content exceeded 80%. During the heating process, tiny sub-droplets ejected from the surface of the BD-E droplet, as shown in Figure 6.1. No combustion was observed during this temperature test. As the ethanol content increased, the overall evaporation time decreased. The BD90E10 blend had the longest evaporation time, while BD10E90 was the most prone to puffing and micro-explosions.

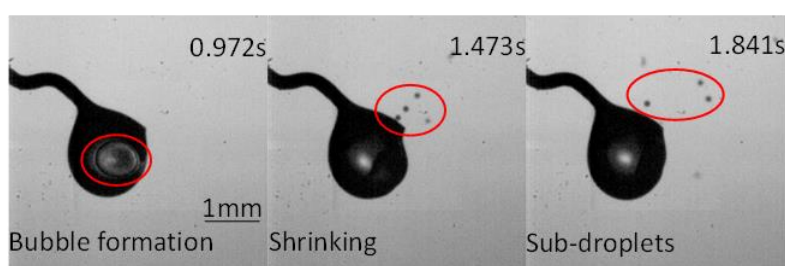


Figure 6.1 1.5 μ L single BD-E microdroplet nucleation at LLPT, atm

Various blending ratio BD-E single microdroplets behaviours are outlined in Figure 6.2. In fuel blends with a high biodiesel content exceeding 80%, evaporation is the predominant phenomenon. This is primarily due to the higher boiling point and lower volatility of biodiesel compared to ethanol, which act to suppress more complex droplet behaviours. nucleation is observed in intermediate blends, where biodiesel and ethanol concentrations range between 30% and 60%. In these cases, ethanol's volatility begins to exert greater influence, yet the stabilizing properties of biodiesel moderate the intensity of the phase transitions, preventing more severe outcomes. Explosive behaviour becomes prevalent in ethanol-rich mixtures, particularly when ethanol concentrations exceed 60%. [159] In these blends, ethanol's high volatility drives rapid phase transitions, resulting in droplet puffing and micro-explosion, which are prominent in blends containing approximately 70% ethanol.

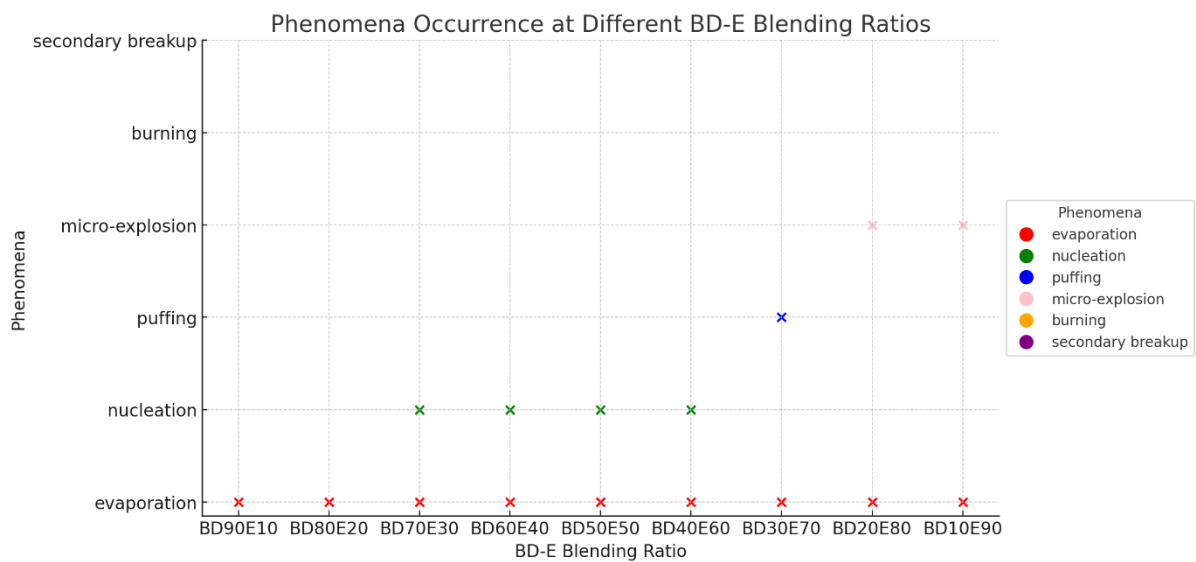


Figure 6.2 1.5 μL single BD-E microdroplet behaviours at LLPT, atm

The microdroplet behaviours according to ethanol content, can be expressed as

$$f(C_{bd}C_e) = \begin{cases} \text{Evaporation, if } 0 < C_e < 0\% \\ \text{Evaporation + Puffing, if } 50\% \leq C_e \leq 60\% \\ \text{Evaporation + Puffing + Micro - explosion, if } C_e \geq 70\% \end{cases} \quad (6.1)$$

where C_{bd} represent the percentage of biodiesel, and C_e represent the percentage of ethanol.

The HVO-M-O microdroplet exhibited volumetric expansion and steady evaporation when heated in the LLPT air environment. The overall evaporation time was slightly shorter than that of the D-M-O blend at the same mixing ratio. At this temperature, no puffing or micro-explosions were observed, as shown in Figure 6.3. This could be due to the relatively low heating temperature and the low methanol content in the blend.

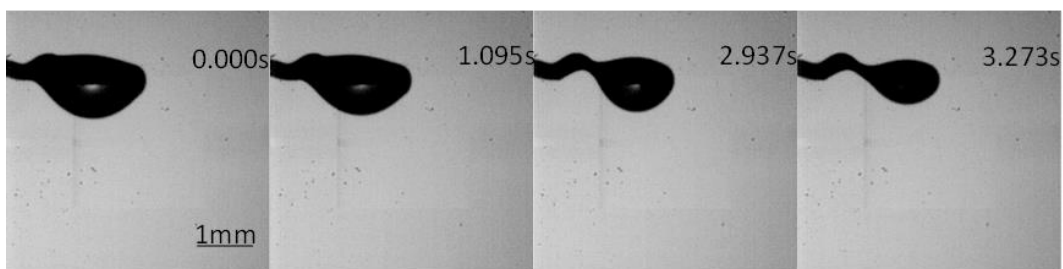


Figure 6.3 1.5 μ L single HVO-M-O microdroplet evaporation at LLPT, atm

Various blending ratio D-M-O single microdroplets behaviours are outlined in Figure 6.4. This ternary phase diagram illustrates the single droplet behaviour of HVO, methanol, and octanol mixtures in LLPT air. At lower methanol content below 25%, the droplets mainly exhibit evaporation. This indicates that in blends with a higher proportion of HVO or octanol, the droplets evaporate without the onset of nucleation. This behaviour is similar to the D-M-O blend at LLPT, where simple evaporation also occurs at low methanol concentrations. As methanol content increases to 30%-40%, droplets begin to experience both evaporation and nucleation. This is marked by the formation of vapor bubbles within the droplet as the more volatile methanol evaporates. The transition from simple evaporation to nucleation occurs at a similar methanol content range as in the D-M-O blend at LLPT.

In both blends (HVO-M-O and D-M-O), simple evaporation occurs at low methanol content below 30%. This indicates that the replacement of diesel with HVO does not significantly

change the threshold for evaporation in this temperature range. HVO behaves similarly to diesel in this regard, as both fuels have relatively low volatility compared to methanol. In both blends, nucleation starts at around 30% methanol content. The onset of nucleation at this threshold is primarily driven by the methanol, which is more volatile and evaporates faster than either HVO or octanol.

No significant difference in the nucleation behaviour is observed between the two blends, indicating that the substitution of diesel with HVO has little effect on the phase change processes at LLPT.

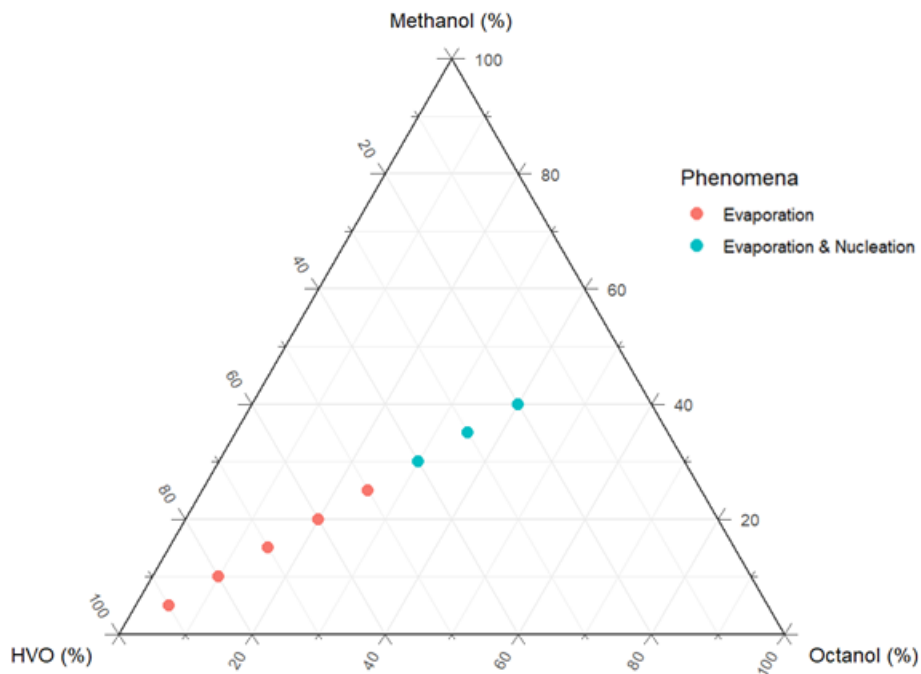


Figure 6.4 1.5 µL single HVO-M-O microdroplet behaviour at LLPT, atm

The microdroplet behaviours according to methanol content, can be expressed as

$$f(C_{HVO}, C_m, C_o) = \begin{cases} \text{Evaporation}, & \text{if } 0 < C_m \leq 25\% \\ \text{Evaporation + Nucleation}, & \text{if } 30\% \leq C_m \leq 40\% \end{cases} \quad (6.2)$$

where C_{HVO} represent the percentage of HVO, C_m represent the percentage of methanol, and C_o represent the percentage of octanol.

6.3 BD-E, HVO-M-O Droplet Behaviour at MLPT

The BD-E droplet becomes more active and unstable at MLPT compared to LLPT. It tends to form vapor bubbles inside, and the surrounding high-temperature air increases internal pressure, causing the vapor bubbles to swell. Under the influence of surface tension, the entire droplet oscillates and shakes in multiple directions until gravity and inertia cause it to break. [153] Due to ethanol's low density and viscosity, the BD-E droplet undergoes significant deformation, including expansion and elongation, before ultimately returning to its droplet shape under the action of surface tension. [155] The overall evaporation time decreases as the ethanol content increases and is shorter than the evaporation time at LLPT. The shrinking, oscillation and ligament disintegration phenomena are presented as shown in Figure 6.5.

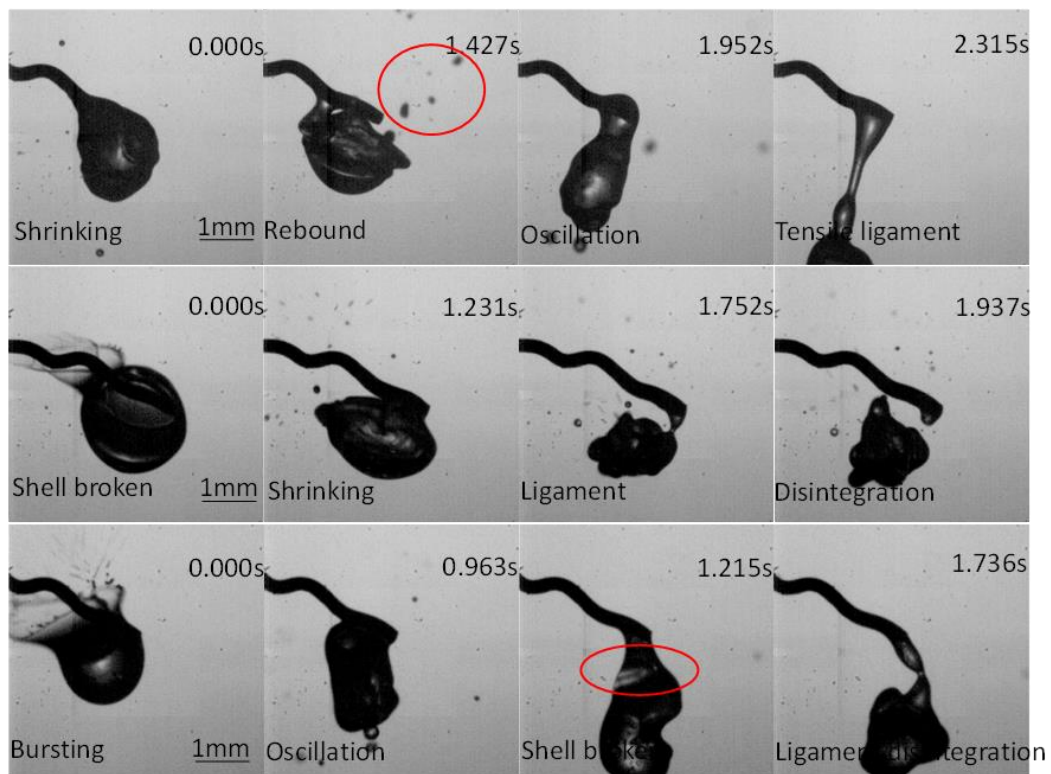


Figure 6.5 1.5 μL single BD-E microdroplet behaviour at MLPT, atm

Various blending ratio BD-E single microdroplets behaviours are outlined in Figure 6.6. In blends where biodiesel content exceeds 80%, evaporation is the predominant phenomenon, reflecting the stabilizing effect of biodiesel due to its lower volatility. [149] Puffing is commonly observed in intermediate compositions, with biodiesel concentrations ranging between 30% and 50%. In these blends, ethanol's higher volatility begins to exert significant influence, yet biodiesel's stabilizing properties moderate the overall behaviour, preventing more extreme transitions. At ethanol concentrations above 50%, explosive behaviour becomes prominent. Ethanol's high volatility and low boiling point induce rapid phase transitions, culminating in droplet explosions. [144]

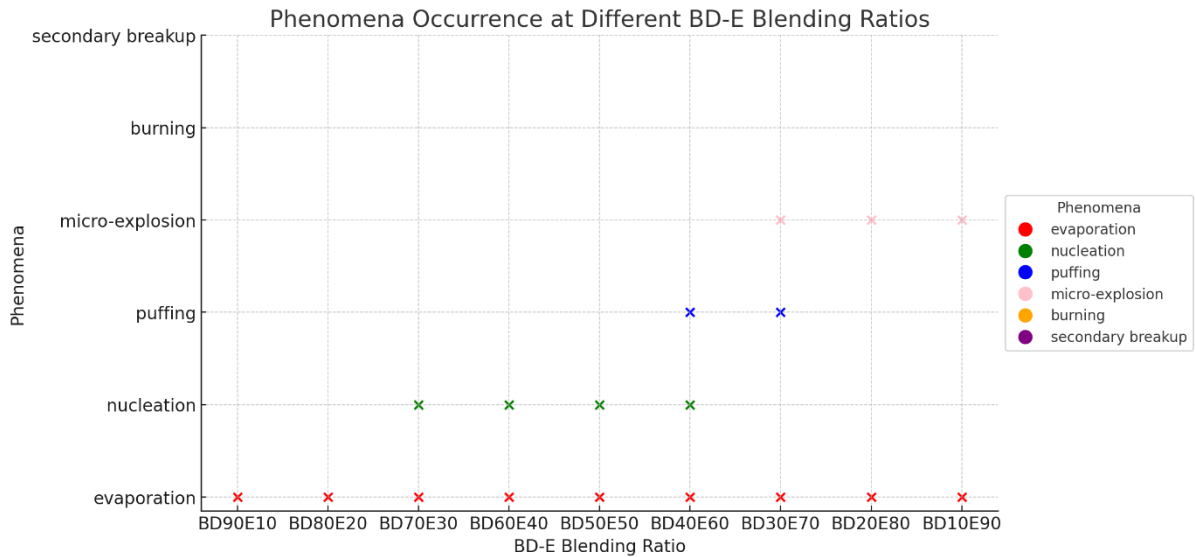


Figure 6.6 1.5 μL single BD-E microdroplet behaviours at MLPT, atm

The microdroplet behaviours according to ethanol content, can be expressed as

$$f(C_{bd}, C_e) = \begin{cases} \text{Evaporation}, & \text{if } 0 < C_e \leq 20\% \\ \text{Evaporation} + \text{Puffing}, & \text{if } 30\% \leq C_e \leq 40\% \\ \text{Evaporation} + \text{Puffing} + \text{Micro-explosion}, & \text{if } C_e \geq 50\% \end{cases} \quad (6.3)$$

where C_{bd} represent the percentage of biodiesel, and C_e represent the percentage of ethanol.

In the MLPT air environment, the HVO-M-O droplet exhibits a shorter evaporation time due to the increased temperature. The methanol content makes the droplet more active and unstable, causing it to move up and down. However, no vapor bubbles form due to the low methanol content, and no significant deformation is observed during the heating process, as shown in Figure 6.7. The HVO-M-O droplet tends to follow a similar evaporation process as observed in LLPT.

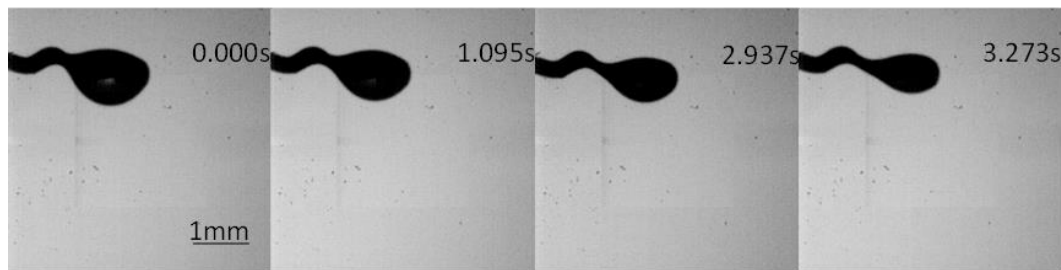


Figure 6.7 1.5 μ L single HVO-M-O microdroplet evaporation at MLPT, atm

Various blending ratio HVO-M-O single microdroplets behaviours are outlined in Figure 6.8. This ternary phase diagram represents the single droplet phenomena for HVO, methanol, and octanol mixtures in MLPT air. At low ethanol concentrations below 20%, the droplets primarily exhibit simple evaporation. This suggests that when methanol content is low, the higher boiling points of HVO and octanol limit nucleation and puffing. At methanol concentrations between 25% and 35%, droplets begin to experience both evaporation and nucleation. The increased temperature of MLPT facilitates the internal vapor bubble formation necessary for nucleation. [142] At methanol concentrations greater than 40%, the droplets experience more complex behaviour, including evaporation, nucleation, and puffing. Puffing at higher methanol content occurs due to the rapid vaporization and internal pressure build-up caused by ethanol's high volatility at elevated temperatures. [144]

In both the LLPT and MLPT experiments, evaporation occurs at low methanol concentrations. However, at MLPT, evaporation happens faster, and the blend transitions to more complex behaviour at a slightly lower methanol content. At MLPT, nucleation begins at 25% methanol content, which is the earlier than LLPT. The intensity and speed of nucleation are likely greater at the higher temperature. [138] Puffing is observed only at MLPT, starting at 40% methanol, which is not present at LLPT. The higher temperature facilitates more rapid vaporization and internal pressure build-up, leading to puffing. [159]

The behaviour in both HVO-M-O and D-M-O blends at MLPT is quite similar. Both blends show evaporation at low methanol content, followed by nucleation and puffing at higher methanol content. This suggests that the replacement of diesel with HVO does not significantly change the fundamental droplet behaviour in these blends at MLPT.

In the D-BD-E blends at MLPT, evaporation also occurs at lower ethanol content. This is comparable to the behaviour seen in both HVO-M-O and D-M-O systems at low methanol content. Nucleation and puffing in the D-BD-E blends also start at around 40% ethanol. This is similar to the behaviour seen with methanol in both HVO and diesel blends, indicating that both methanol and ethanol have similar effects on droplet behaviour at higher concentrations in these temperature ranges.

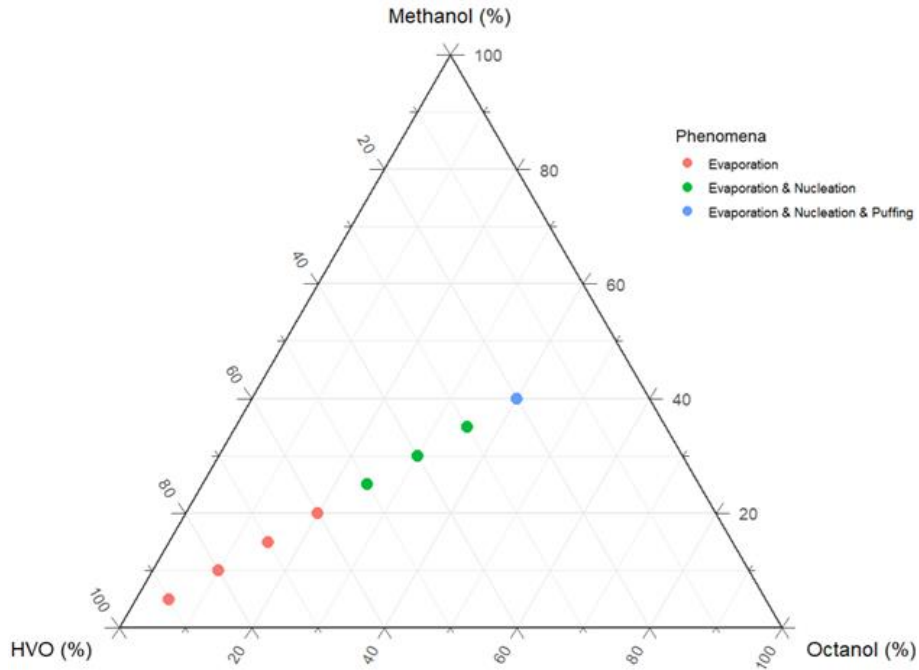


Figure 6.8 1.5 µL single HVO-M-O microdroplet behaviour at MLPT, atm

The microdroplet behaviours according to methanol content, can be expressed as

$$f(C_{HVO}, C_m, C_o) = \begin{cases} \text{Evaporation,} & \text{if } 0 < C_m \leq 20\% \\ \text{Evaporation + Nucleation,} & \text{if } 25\% \leq C_m \leq 35\% \\ \text{Evaporation + Nucleation + Puffing,} & \text{if } C_m \geq 40\% \end{cases} \quad (6.4)$$

where C_{HVO} represent the percentage of HVO, C_m represent the percentage of methanol, and C_o represent the percentage of octanol.

6.4 BD-E, HVO-M-O Droplet Behaviour at HLPT

Due to the high heating temperature, the BD-E droplet becomes unstable and highly active. The droplet's activity increases as the ethanol content rises, with the BD10E90 blend experiencing the fastest evaporation when exposed to the furnace, while BD90E10 has the longest overall evaporation time. Bubbles form and flow within the droplet, as shown in Figure 6.9 (a) and tiny sub-droplets burst into the surrounding air. Both weak and strong

micro-explosions were observed during the heating process, as shown in Figure 6.9 (b) & (c), along with a visible combustion reaction with flames.

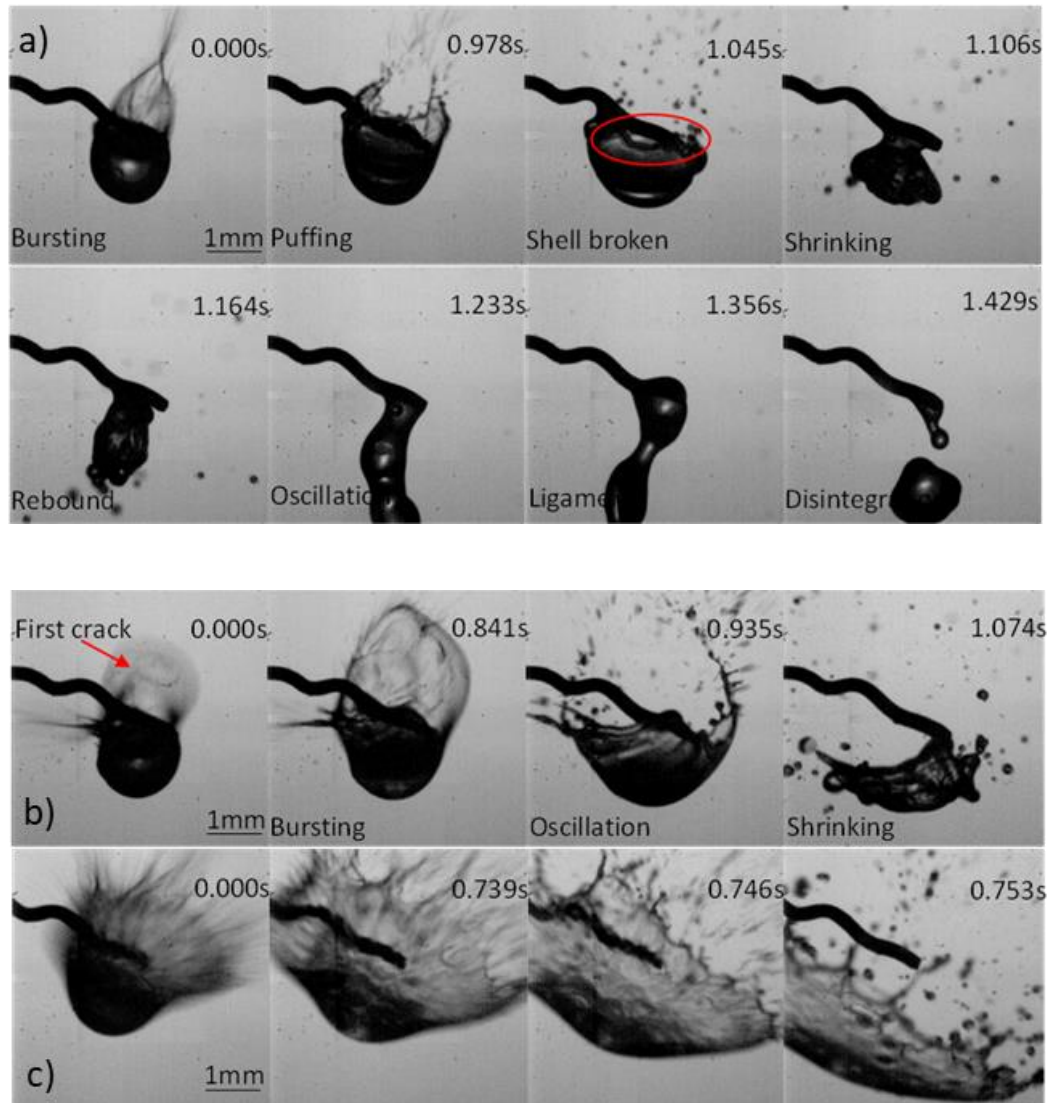


Figure 6.9 1.5 μL single BD-E microdroplet behaviour (a)puffing, (b)weak micro-explosion, (c)strong micro-explosion at HLPT, atm

Compared to D-BD, puffing, micro-explosions, and secondary breakup were more prominent in the BD-E blend, indicating that the addition of ethanol enhances and improves the fuel-air mixing process. [159]

Various blending ratio BD-E single microdroplets behaviours are outlined in Figure 6.10. Evaporation is most prevalent in biodiesel-rich blends above 80%, as biodiesel stabilizes the droplet and suppresses more intense behaviours. Puffing and burning dominate in intermediate blends 30%-40% biodiesel, with ethanol's volatility driving vaporization and combustion. Micro-explosion occurs at higher ethanol content (above 50%), where ethanol's low boiling point and high volatility lead to rapid phase transitions and eventual droplet explosion.

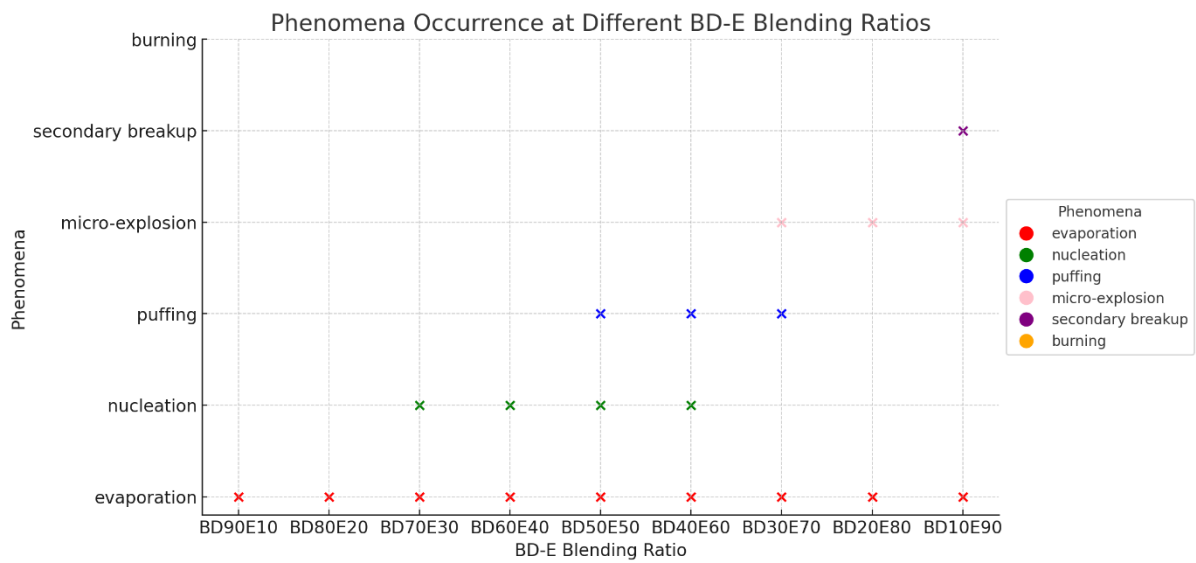


Figure 6.10 1.5 μL single BD-E microdroplet behaviours at HLPT, atm

The microdroplet behaviours according to ethanol content, can be expressed as

$$f(C_{bd}, C_e) = \begin{cases} \text{Evaporation, if } 10\% < C_e \leq 20\% \\ \text{Evaporation} + \text{Burning, if } 30\% < C_e \leq 40\% \\ \text{Evaporation} + \text{Puffing} + \text{Micro-explosion, if } C_e \geq 50\% \end{cases} \quad (6.5)$$

where C_{bd} represent the percentage of biodiesel, and C_e represent the percentage of ethanol.

When HVO-M-O droplet exposed and heated up at HLPT air environment, puffing and micro-explosion were observed during the process, as shown in Figure 6.11. Vapor bubbles

form and move around inside the droplet. The HVO-M-O droplet expand twice as large than original area. Small bumps burst into the surrounding air. The droplet vibrates up and down and become irregular. After this, it undergoes a rapid evaporation. At this temperature, methanol vapor bubble is easier to form than MLPT.

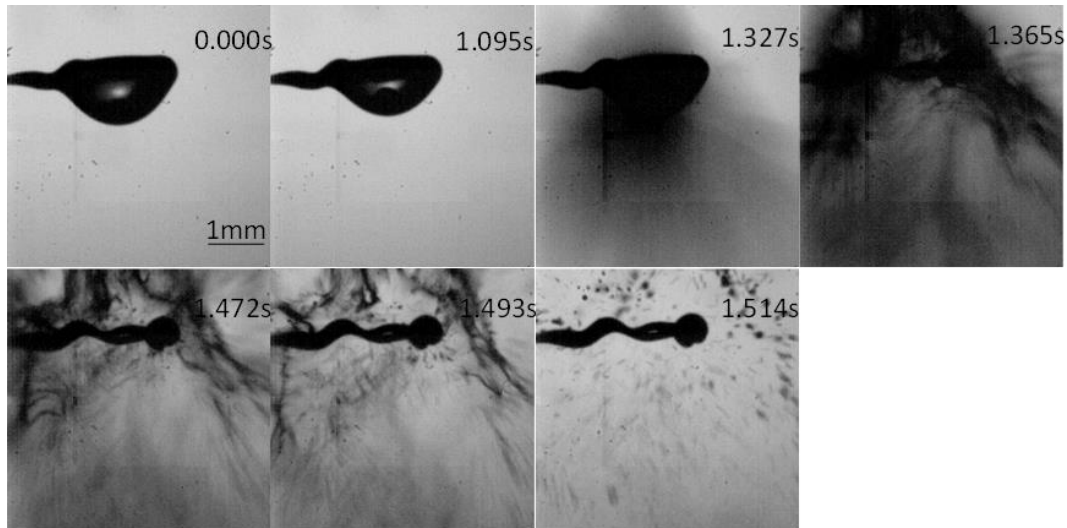


Figure 6.11 1.5 μ L single HVO-M-O microdroplet micro-explosion at HLPT, atm

Various blending ratio HVO-M-O single microdroplets behaviours are outlined in Figure 6.12. This ternary phase diagram represents the single droplet phenomena for HVO, methanol, and octanol blends in HLPT air. The phenomena observed are categorized as follows. At low methanol content below 20%, the droplets primarily undergo simple evaporation. The high temperature of HLPT accelerates evaporation in the mixture of HVO and octanol, both of which have higher boiling points compared to methanol. Burning is observed at 5% methanol content blend. At HLPT, the increased energy input promotes the ignition of the fuel blend, with the presence of methanol. For methanol concentrations between 20% and 25%, evaporation occurs alongside nucleation. This is due to rapid internal vapor bubble formation within the droplet, driven by methanol's volatility at HLPT. Between 30% and 40% methanol content, puffing is observed in addition to micro-explosion. The rapid vaporization of methanol leads to pressure buildup inside the droplet, causing puffing. At high methanol content above 35%, more intense behaviour such as micro-explosion occurs. The elevated

temperature and high methanol volatility cause rapid phase changes, leading to violent internal pressure increases and eventual micro-explosion.

Similar to the D-M-O blends, the HVO-M-O blends at HLPT also exhibits evaporation and burning at low methanol content between 5%-10%. In both the HVO and diesel blends, micro-explosions occur above 40% methanol content. The presence of methanol and the high temperature drive this behaviour.

The HVO-M-O blends at HLPT also shows evaporation at low ethanol content below 10%, accompanied by burning and more complex phenomena at higher concentrations. Puffing and micro-explosion occur in both blends (HVO-M-O and D-BD-E) at higher alcohol content above 35%, showing that both methanol and ethanol have similar effects on phase transitions at HLPT.

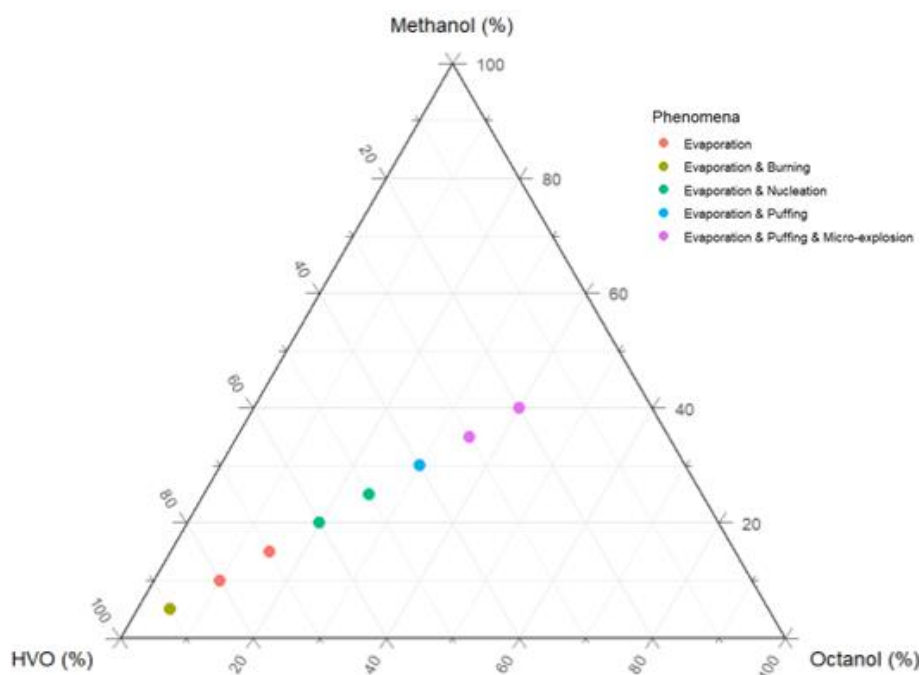


Figure 6.12 1.5 µL single HVO-M-O microdroplet behaviour at HLPT, atm

The microdroplet behaviours according to methanol content, can be expressed as

$$f(C_{HVO}, C_m, C_o) = \begin{cases} \text{Evaporation + Burning,} & \text{if } 0 < C_m \leq 5\% \\ \text{Evaporation,} & \text{if } 10\% \leq C_m \leq 15\% \\ \text{Evaporation + Nucleation,} & \text{if } 20\% \leq C_m \leq 25\% \\ \text{Evaporation + Nucleation + Puffing,} & \text{if } 25\% < C_m \leq 30\% \\ \text{Evaporation + Puffing + Micro - explosion,} & \text{if } C_m \geq 35\% \end{cases} \quad (6.6)$$

where C_{HVO} represent the percentage of HVO, C_m represent the percentage of methanol, and C_o represent the percentage of octanol.

6.5 Temperature and Blending Ratio Impact on Puffing and Micro-explosion

6.5.1 BD-E blend

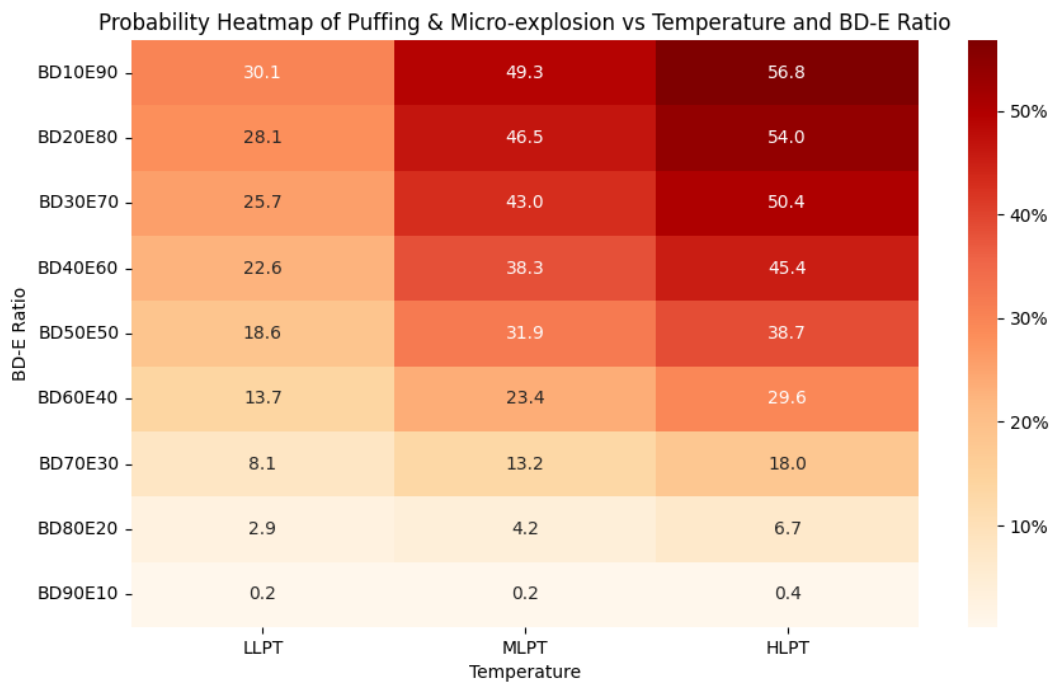


Figure 6.13 Probability heatmap of puffing and micro-explosion under varying temperature and BD-E ratio

Figure 6.13 visualizes the probability of puffing and micro-explosion under various temperature conditions LLPT, MLPT, HLPT across a range of BD-E ratios. The vertical axis

represents the BD-E ratio, moving from BD90E10 at the bottom to BD10E90 at the top, indicating increasing ethanol content as moving up the axis. The horizontal axis indicates temperature levels LLPT, MLPT, and HLPT. The colour intensity corresponds to the probability of puffing and micro-explosion occurring under the given conditions. Lighter shades (pale yellow) indicate lower probabilities, while darker shades (deep red) indicate higher probabilities. As the vertical axis (increasing ethanol content) moving up, the probability of explosive phenomena such as puffing and micro-explosion generally increases, particularly at higher temperatures MLPT and HLPT.

At LLPT, the probability of puffing and micro-explosion remains low across most BD-E ratios. The colour is pale, reflecting minimal explosive phenomena. For example, at a BD90E10 ratio, the probability is nearly zero (0.2%). As the ethanol content increases (BD30E70, BD20E80, and BD10E90 ratios), the probability begins to rise, although it remains modest. At BD10E90 (highest ethanol content), the probability reaches 30.1%, indicating that LLPT can induce some degree of puffing and micro-explosion, but it is still limited compared to higher temperatures. At MLPT, the probability of puffing and micro-explosion is notably higher compared to LLPT. As the BD-E ratio decreases (more ethanol content), the probability increases steadily, with values ranging from 0.2% at BD90E10 to 49.3% at BD10E90. Significant probabilities appear around the BD50E50 and BD40E60 ratios, with values reaching around 31.9% and 38.3%, respectively. This indicates that MLPT is effective in initiating puffing and micro-explosion, as the ethanol content increases. At HLPT, the heatmap shows the highest probabilities of puffing and micro-explosion across all BD-E ratios. Even at higher BD ratios such as BD90E10 and BD80E20, there are noticeable probabilities (0.4% and 6.7%, respectively), reflecting the strong influence of high temperature on these phenomena. As the BD-E ratio decreases further (BD10E90, BD20E80), the probability reaches its peak (56.8% and 54.0%), indicating that HLPT not only accelerates puffing and micro-explosion but also makes them almost inevitable at high ethanol contents. The presence of secondary breakup at these conditions further intensifies the observed phenomena.

The heatmap clearly demonstrates that temperature plays a crucial role in accelerating the probability of puffing and micro-explosion. Higher temperatures correspond to higher probabilities, at BD-E ratios where ethanol content is dominant. The heatmap also suggests the presence of threshold effects where certain BD-E ratios, particularly those with higher ethanol content, act as triggers for puffing and micro-explosion, at MLPT and HLPT. The influence of the BD-E ratio on these phenomena is evident, with the most significant changes occurring as the ratio approaches BD10E90. This suggests that fuel composition plays a critical role in the probability of these phenomena, under higher temperature conditions.

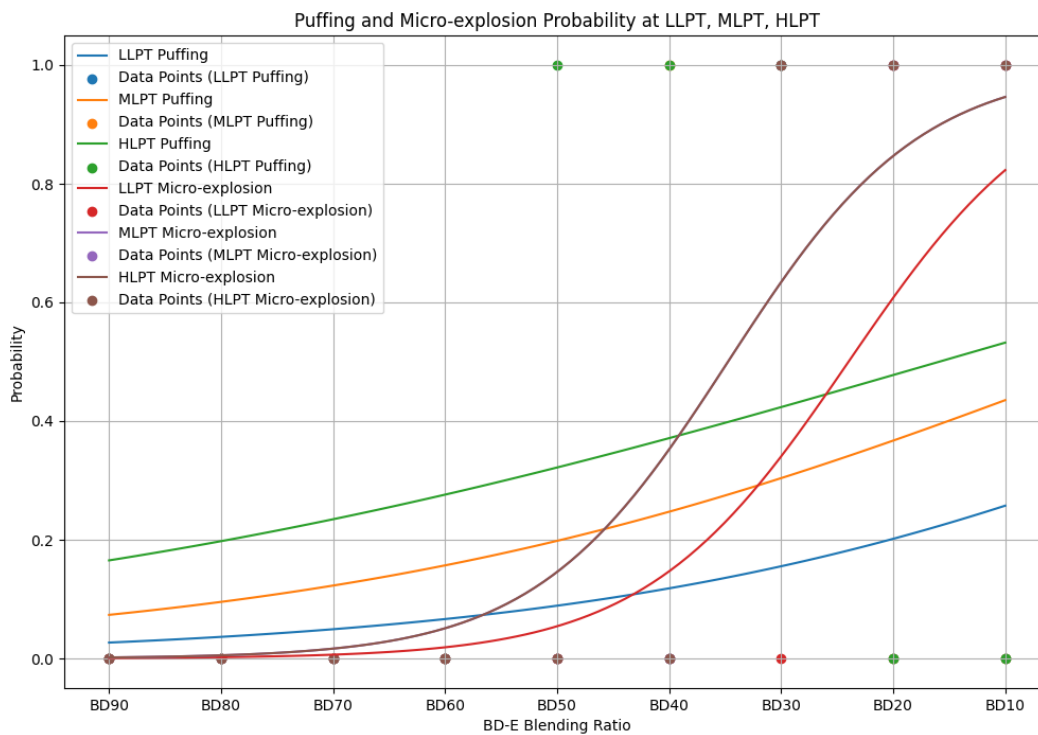


Figure 6.14 Probability of puffing and micro-explosion under varying temperature and BD-E ratio

Figure 6.14 illustrates the probability of puffing and micro-explosion under different temperature conditions LLPT, MLPT, HLPT as the BD-E ratio changes. The horizontal axis

represents the BD-E ratio. As the BD-E ratio increases, the biodiesel content decreases. The vertical axis represents the probability of these phenomena occurring.

At higher BD-E ratios (BD90E10, BD80E20), evaporation is the predominant phenomenon. The graph shows low probabilities of puffing and micro-explosion at these ratios, indicating that at LLPT, the fuel mainly undergoes evaporation without significant explosion. The first noticeable increase in the probability of puffing occurs around the BD30E70 ratio, where puffing begins to accompany evaporation and nucleation. However, even at this stage, the overall probability remains low, indicating that puffing is not a dominant phenomenon at this temperature. Micro-explosion starts to appear at BD80E20 and BD10E90 ratios, but the probabilities remain relatively low, reflecting the fact that LLPT is not conducive to the rapid onset of explosive phenomena such as puffing or micro-explosion. As the temperature increases to MLPT, the probability of puffing increases earlier in the BD-E ratio range. Puffing becomes more probable around the BD40E60 ratio, where it starts to occur alongside evaporation and nucleation. By the time the ratio reaches BD30E70, the probability of puffing increases substantially, accompanied by the onset of micro-explosion. This trend continues as the ratio decreases further, with puffing and micro-explosion becoming more likely at BD20E80 and BD10E90 ratios. The graph reflects a noticeable acceleration in the probability of puffing and micro-explosion at MLPT, indicating that this temperature is more conducive to these phenomena than LLPT but less so than HLPT. At HLPT, the probability of puffing increases significantly earlier in the BD-E ratio range. Puffing starts to become likely around the BD50E50 and BD4E60 ratios, where it occurs alongside evaporation and nucleation. The high temperature accelerates the onset of these phenomena. As the BD-E ratio decreases further to BD30E70 and below, puffing and micro-explosion become dominant, with the highest probabilities seen in the BD20E80 and BD10E90 ratios. At this stage, secondary breakup is also observed, particularly at BD10E90. The high temperature has facilitated the rapid vaporization of fuel, leading to frequent and intense disruptions. The graph shows a steep increase in the probability of these phenomena, indicating that HLPT strongly accelerates the occurrence of puffing, micro-explosion, and secondary breakup, at lower BD-E ratios where ethanol content is higher.

The graph clearly demonstrates that as temperature increases, the probability of both puffing and micro-explosion increases across the BD-E ratio spectrum. HLPT conditions show the earliest and most significant onset of these phenomena, followed by MLPT, with LLPT showing the least probability. The onset of puffing occurs progressively earlier as the temperature increases from LLPT to HLPT. At HLPT, explosive phenomena dominate much of the BD-E ratio spectrum, while at LLPT, these phenomena are only noticeable at the lowest BD-E ratios.

In summary, the probability of puffing and micro-explosion is highly dependent on temperature and BD-E ratio. Higher temperatures accelerate the onset of these phenomena and increase their probability, at ratios where ethanol content is higher. Understanding these trends is crucial for optimizing fuel performance in practical ICEs. At higher temperatures, fuel mixtures with higher ethanol content are more likely to experience explosive phenomena, which could affect combustion efficiency.

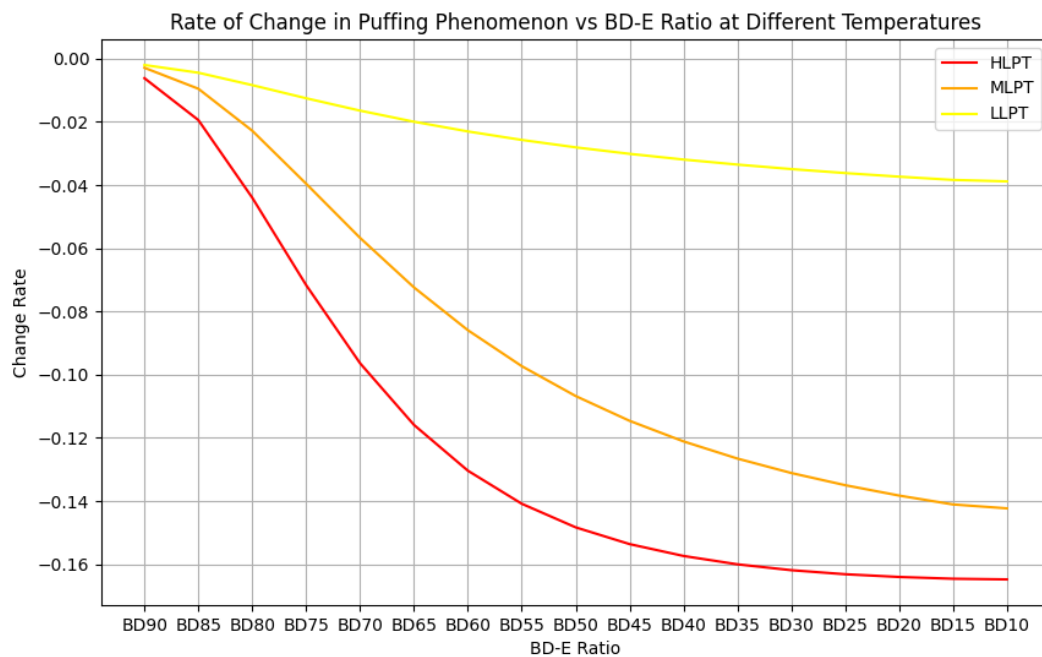


Figure 6.15 Puffing change rate under varying temperature and BD-E ratio

This section explores the acceleration or suppression effects of temperature on the puffing phenomenon by analysing the rate of change in the probability of occurrence under different temperature conditions. To quantitatively evaluate the impact of temperature on the puffing phenomenon, the rate of change in puffing probability with varying BD-E ratios at three temperature levels LLPT, MLPT, and HLPT were calculated, as shown in Figure 6.15.

Figure 6.15 illustrates the rate of change in puffing occurrence probability as a function of BD-E ratio under different temperature conditions. The horizontal axis represents the BD-E ratio, the biodiesel content ranges from 90% to 10%, indicating a transition from low ethanol content to high ethanol content. The vertical axis shows the rate of change, which reflects how quickly the probability of puffing occurrence changes with respect to the BD-E ratio. The yellow, orange, and red lines represent temperature conditions of LLPT, MLPT, and HLPT, respectively. The negative values indicate that the puffing probability initially increases slowly, and then accelerates as the BD-E ratio increases. Higher absolute values of the rate of change suggest a faster increase in puffing probability as the ratio shifts towards higher ethanol content.

The graph in Figure 6.15 clearly shows distinct trends in puffing occurrence probabilities across different temperature conditions. The yellow curve has the flattest slope, with the rate of change remaining closer to zero across all BD-E ratios. This indicates that LLPT has the weakest effect on puffing, and the puffing probability increases more slowly, even as the ethanol content rises. At this lower temperature, the fuel evaporation and molecular motion are slower, resulting in less frequent puffing occurrences. The orange curve exhibits a moderate rate of change. The slope is not as steep as the HLPT curve but still shows a significant increase in puffing probability as the ratio increases. The results suggest that LLPT is also capable of accelerating the puffing phenomenon, but to a lesser extent than HLPT. The red curve shows the steepest rate of change, particularly for ratios below BD50E50. The curve rapidly dips, indicating that puffing accelerates significantly as the BD-E ratio increases towards higher ethanol content. This suggests that HLTP has the most pronounced impact on puffing, which aligns with expectations that higher temperatures facilitate fuel

vaporization, leading to more rapid puffing. From the analysis above, it's evident that increasing temperature accelerates the occurrence of the puffing phenomenon. Specifically, at HLPT, the puffing phenomenon occurs more frequently, and the rate of change is the largest.

At LLPT, puffing is a much slower process, with minimal acceleration observed until the BD-E ratio reaches BD30E70, where puffing becomes evident. The phenomenon is even slower compared to the higher temperature conditions. Micro-explosion only starts to occur at BD20E80 and BD10E90, with the rate of change remaining relatively flat overall. At this temperature, the overall rate of change is minimal, indicating that LLPT has the least impact on accelerating the puffing phenomenon. At MLPT, puffing occurs later compared to HLPT but is still significant. The first noticeable increase in puffing happens at ratios such as BD40E60, where puffing accompanies nucleation. At BD30E70, both puffing and micro-explosion are present, contributing to the moderate rate of increase. This suggests that MLPT is capable of inducing puffing but to a lesser extent than HLPT. As the BD-E ratio reaches BD20E80 and BD10E90, the phenomenon continues to accelerate, although at a slower rate compared to HLPT. At HLPT, puffing accelerates early and significantly, as shown by the steep slope of the red curve. The phenomenon becomes noticeable at ratios such as BD50E50 and BD40E60, where puffing occurs alongside evaporation and nucleation. This steep acceleration continues at BD30E70 with the onset of puffing and micro-explosion, and the steepest increase happens at BD20E80 and BD10E90, where secondary breakup is introduced. The acceleration is most pronounced in this condition, as high temperatures enable faster fuel vaporization, leading to frequent puffing occurrences.

The rate of change analysis in this section further quantifies this phenomenon, revealing how temperature accelerates or suppresses puffing as the BD-E ratio changes. A notable feature of the graph is that the curves are not linear. This non-linearity suggests the presence of threshold effects, where the puffing phenomenon remains suppressed at certain BD-E ratios and then suddenly accelerates as the ratio crosses a threshold. For example, in the HLPT and MLPT curves, the rate of change is relatively small for higher BD

ratios (BD90E10, BD80E20), where evaporation dominates. This suggests that at lower ethanol content, the temperature has a less pronounced accelerating effect on puffing. However, once the ratio shifts towards higher ethanol content (BD50E50, BD40E60), puffing and later micro-explosion significantly contribute to the steep increase in the rate of change.

The steep increase in the rate of change at higher temperatures and BD-E ratios can be attributed to several factors:

- Faster fuel vaporization at high temperatures. At HLPT, fuel components vaporize more quickly, leading to a more rapid buildup of internal droplet pressure, which triggers puffing and micro-explosion.
- Increased molecular motion. At higher temperatures, the fuel molecules inside the droplets move more energetically, which facilitates the transition from liquid to vapor and contributes to the rapid onset of puffing.
- Thermodynamic threshold. As the BD-E ratio increases, the balance between biodiesel and ethanol components may cross a thermodynamic threshold that triggers faster vaporization and more frequent puffing events, particularly at high ethanol content and higher temperatures.

In summary, the analysis of Figure 6.15 shows that temperature has a significant accelerating effect on the puffing phenomenon, with the most pronounced impact observed at HLPT. The rate of change in puffing occurrence increases with the BD-E ratio, particularly at ratios involving higher ethanol content. The results suggest that understanding the interaction between temperature and fuel composition is crucial for optimizing fuel spray performance.

6.5.2 HVO-M-O blend

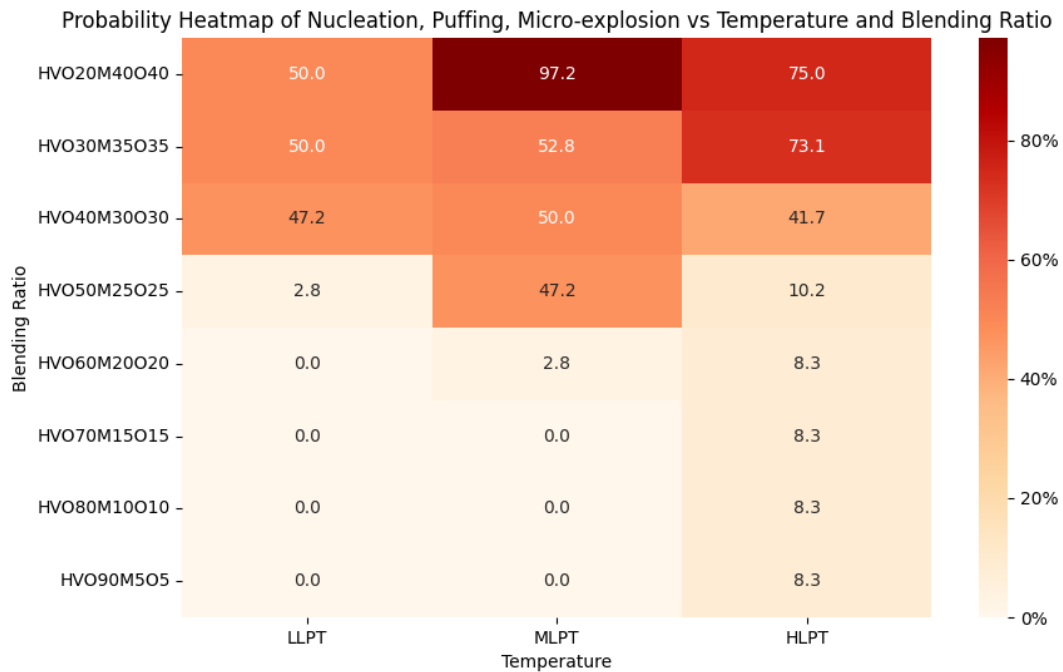


Figure 6.16 Probability heatmap of puffing and micro-explosion under varying temperature and HVO-M-O ratio

Figure 6.16 heatmap shows the probability of nucleation, puffing, and micro-explosion across different temperatures LLPT, MLPT, HLPT and blending ratios ranging from HVO20M40O40 to HVO90M5O5.

As the temperature increases from LLPT to HLPT, there is a general increase in the probability of nucleation, puffing, and micro-explosion, in the higher blending ratios. MLPT conditions show a particularly high probability of these phenomena for the HVO20M40O40 blend, with a peak probability of 97.2%, indicating extreme instability at this temperature for this specific blending ratio.

The highest probabilities are observed in the blends with higher percentages of methanol and octanol such as, HVO20M40O40, HVO30M35O35, and HVO40M30O30. These blends show significant probabilities across all temperature ranges, at MLPT and HLPT. Lower

blending ratios, such as HVO70M15O15, HVO80M10O10, and HVO90M5O5, demonstrate much lower probabilities, with many cases showing non-probability across all temperatures, suggesting these mixtures are more stable. HVO30M35O35 and HVO40M30O30 also show high probabilities, particularly at higher temperatures, with HLPT values reaching 73.1% and 41.7%, respectively. In contrast, blends with higher percentages of HVO, such as HVO50M25O25 and higher, show much lower probabilities, indicating that increasing the HVO content generally leads to more stable mixtures with reduced risk of these phenomena.

In summary, blends with higher concentrations of methanol and octanol are more prone to nucleation, puffing, and micro-explosion, particularly at medium to high temperatures. Lower blending ratios with higher HVO content blends are more stable, with significantly lower probabilities of the analysed phenomena, even at higher temperatures. The MLPT range appears to be particularly critical for the onset of these phenomena, for blends such as HVO20M40O40, which shows a very high probability of instability at this temperature. This heatmap provides valuable insights into how temperature and blending ratios interact to affect the probability of nucleation, puffing, and micro-explosion, which can inform the design and optimization of fuel blends for fuel atomization in ICEs.

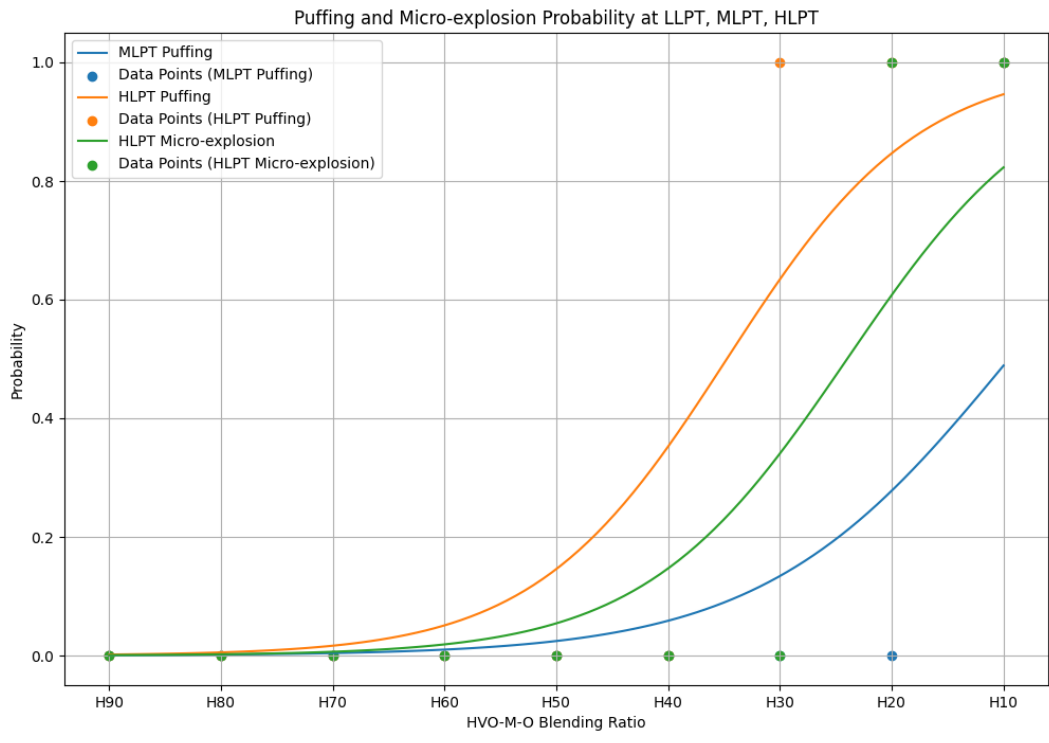


Figure 6.17 Probability of puffing and micro-explosion under varying temperature and HVO-M-O ratio

Figure 6.17 illustrates the probability of puffing and micro-explosion events across different HVO-M-O blending ratios under three temperature conditions LLPT, MLPT, and HLPT.

The probability of puffing increases as the HVO content decreases across all three temperature conditions. At very high blending ratios, the probability of puffing is near 1.0 for both MLPT and HLPT, indicating that puffing is almost certain to occur at these temperatures with high blending ratios. As the blending ratio decreases, the probability of puffing drops sharply, reaching near zero at lower blending ratios HVO70M15O15.

HLPT conditions show the highest probability of puffing at high blending ratios, with a more significant increase as the ratio increases. The MLPT curve is situated between the HLPT and LLPT curves, suggesting that puffing is less likely at medium temperatures than at high temperatures, but still more likely than at low temperatures. LLPT shows the lowest

probability of puffing among the three temperature conditions, at lower blending ratios where the probability is negligible.

The green curve represents the probability of micro-explosion under HLPT conditions. Similar to puffing, the probability of micro-explosion is highest at very low HVO content and decreases as the HVO content increases. Micro-explosion probabilities are particularly low at higher HVO content, indicating that these events are less likely as the HVO-M-O blending ratio decreases.

Both puffing and micro-explosion probabilities are highly dependent on the HVO-M-O blending ratio, with lower HVO content being more susceptible to these phenomena. Higher temperatures significantly increase the probability of puffing and micro-explosions at lower blending ratios, emphasizing the importance of controlling temperature in these systems. As the HVO-M-O blending ratio increases, the system becomes more unstable, with a significant increasing in the probabilities for both puffing and micro-explosions across all temperature conditions.

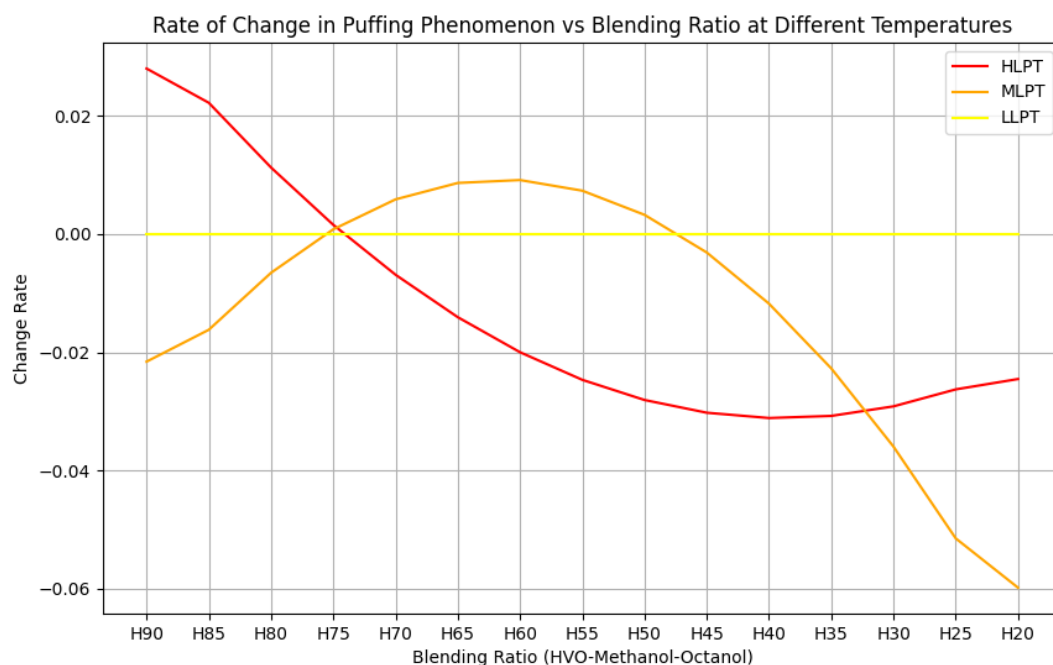


Figure 6.18 Puffing change rate under varying temperature and HVO-M-O ratio

Figure 6.18 illustrates the rate of change in the puffing phenomenon as a function of the HVO-M-O blending ratio at different temperature conditions LLPT, MLPT and HLPT. The red curve (HLPT) represents the rate of change in puffing under high-temperature conditions. At lower blending ratios (H90 to H75), the rate of change is positive, indicating that the probability of puffing increases as the blending ratio increases. From H75 to H55, the curve dips into the negative region, the steep decline showing that the rate of change in puffing increases as the blending ratio continues to increase. The most significant decrease occurs between H65 and H55. Beyond H55, the curve starts to rise again slightly but remains negative, indicating that while the rate of puffing increase slows down, puffing is becoming less likely due to micro-explosion is the dominate phenomena that droplet experiencing.

The orange curve (MLPT) shows the rate of change in puffing at medium temperatures. Initially, the curve is slightly negative but increase, indicating a small increase in puffing probability as the HVO content decreases from H90 to H75. The curve then rises into the positive region from H75 to H60, suggesting a slowly increase in the rate of puffing in this range. After H60, the curve declines sharply, moving back into the negative region, indicating an increase rate of change in puffing as the HVO content continues to decrease.

The yellow curve (LLPT) represents the rate of change in puffing at low temperatures. The curve remains flat and close to zero throughout the range, indicates that LLPT has the weakest effect on puffing, and the puffing probability increases more slowly, even as the methanol content rises.

In conclusion, the HLPT condition shows significant variability in the rate of change of puffing across different blending ratios, with both positive and negative trends. This suggests that puffing is highly sensitive to blending ratio changes at high temperatures. The MLPT curve shows moderate sensitivity to blending ratio changes, with a positive rate of change at mid-range blending ratios, indicating that puffing might increase in this range but decreases significantly at higher blending ratios. The LLPT curve remains nearly flat,

suggesting that puffing is not significantly influenced by blending ratio changes at low temperatures, indicating stability in puffing behaviour under these conditions.

6.6 Conclusion

In this chapter, the behaviour of BD-E and HVO-M-O microdroplets under varying high-temperature environments LLPT, MLPT and HLPT were investigated. The findings can be summarized as follows:

Evaporation

- The evaporation rates of BD-E and HVO-M-O microdroplets were significantly influenced by the testing environment. At HLPT, the highest evaporation rates were observed due to elevated temperatures, with BD-E showing the fastest evaporation rates due to ethanol's high volatility.

Puffing and micro-explosion

- Puffing and micro-explosions were observed more frequently in the BD-E and HVO-M-O blends, particularly at HLPT. This behaviour is attributed to the lower boiling points of ethanol and methanol, which rapidly vaporized and caused internal pressure buildup in the droplets, leading to droplet disintegration.

Comparison between blends

- BD-E exhibited the fastest evaporation rates due to the high volatility of ethanol, but with minimal soot formation during combustion.
- HVO-M-O showed steady evaporation and combustion, with methanol and octanol contributing to rapid initial evaporation and HVO ensuring clean combustion with minimal soot.

Fuel composition impact

- The addition of ethanol in the BD-E blend significantly enhanced evaporation due to ethanol's lower boiling point. However, ethanol also contributed to less soot formation, leading to a cleaner combustion profile.
- The HVO-M-O blend exhibited slower evaporation rates compared to BD-E but faster than D-BD. The presence of methanol and octanol accelerated the initial evaporation phase, while HVO's low impurity content contributed to minimal soot formation.

Chapter 7 Numerical Modelling of Droplet Behaviour

7.1 Introduction

A numerical model was developed to elucidate the relationship between the thermodynamic system and microdroplet behaviours, including evaporation, puffing, micro-explosion, and combustion. This model investigates how high environmental temperatures, fuel composition, and multi-fuel blending ratios affect microdroplet dynamics. By precisely controlling microdroplet and nanoscale droplet behaviour, the model aims to enhance fuel efficiency and reduce emissions. This study experiment heating system can be established as following two sections, a thermodynamic field which providing the heat for microdroplet evaporation, breakup and combustion, a being heated droplet suspended inside of it at a certain temperature position.

7.2 Thermodynamic System

The heating element is $\emptyset 50 \times L70$ mm cylinder, the volume of it is 0.137cm^3 , slightly smaller than a combustion chamber cylinder in an ICEs. In the mathematical model building process, the heating furnace is assumed as a constant volume combustor (CVC), according to § 2.2.1. [132] Thus, the thermodynamics field is established as follows,

7.2.1 Conduction heat

Heat conduction is the transfer of heat due to temperature gradients within the material, from regions of higher temperature to lower temperature. [46][132] The model uses the heat conduction equation to describe the temperature field as

$$\rho c_p \frac{\partial T(r, z, t)}{\partial t} = k(T) \left(\frac{1}{r} \frac{\partial}{\partial r} \left(r \frac{\partial T}{\partial r} + \frac{\partial^2 T}{\partial z^2} \right) \right) \quad (7.1)$$

where ρ represents the density of the material, $T(r,z,t)$ the temperature field, which is a function of the radial coordinate r , the axial coordinate z , and time t , $k(T)$ represents the thermal conductivity of the material, r is the radial coordinate in cylindrical coordinates.

7.2.2 Convection heat

Convection is the heat transfer mechanism involving the movement of fluid (such as air in this study) that carries heat with it. In high-temperature environments, both natural convection and forced convection can occur. Convection effects can be incorporated into the heat conduction equation by adding convective terms. [46][132] The convection-modified energy equation in cylindrical coordinates as

$$\rho c_p \left(\frac{\partial T}{\partial t} + u \frac{\partial T}{\partial r} + w \frac{\partial T}{\partial z} \right) = k \left(\frac{1}{r} \frac{\partial}{\partial r} \left(r \frac{\partial T}{\partial r} \right) + \frac{\partial^2 T}{\partial z^2} \right) \quad (7.2)$$

where u and w are the velocity components of the gas in the r and z directions, respectively. There are two types of convection existing in this system, natural convection and radiation convection. Natural convection is typically caused by density differences due to temperature variations within the fluid. Forced convection is generally caused by external forces such as fans or pumps that induce fluid motion.

7.2.3 Radiation heat

Radiation is the transfer of heat through electromagnetic waves, and it becomes significant at high temperatures. [46][132] The radiative heat flux can be described using the Stefan-Boltzmann law

$$q_{rad} = \sigma \epsilon (T^4 - T_{surrounding}^4) \quad (7.3)$$

where σ is the Stefan-Boltzmann constant, ϵ is the emissivity of the material, $T_{surrounding}$ is the temperature of the surroundings.

7.2.4 Complex coupled thermodynamic system

By combining heat conduction, convection, and radiation, the complete thermodynamic field equation can be expressed as

$$\rho c_p \left(\frac{\partial T}{\partial t} + v \times \Delta T \right) = k \nabla^2 T + \frac{\partial q_{rad}}{\partial t} \quad (7.4)$$

where $v=(u,w)$ is the velocity vector field accounting for convection effects. $\frac{\partial q_{rad}}{\partial t}$ represents the change in radiative heat flux over time.

7.2.5 Conclusion

To accurately model a thermodynamic field that includes heat conduction, convection, and radiation, these mechanisms need to be incorporated into the energy equation and solved using appropriate numerical methods. While heat conduction forms the basis of heat transfer, convection and radiation become crucial in high-temperature environments. All these mechanisms together provide a more comprehensive simulation of complex thermodynamic systems.

7.3 Droplet Behaviour

According to § 2.2 research work and this study massive experiment results, a droplet behaviour under high temperature environment can be catalogued into three phase, evaporation phase, combustion phase and breakup phase. These three phases can be theoretically represented as following.

7.3.1 Evaporation phase

In the initial stage, the droplet primarily undergoes evaporation. The evaporation process is controlled by the difference in temperature between the droplet surface and the surrounding environment, and the evaporation follows the D² law. [132]

Conditions:

- Time $t < t_{combustion}$, i.e., before the combustion starts.
- The droplet's diameter gradually decreases due to evaporation, but no combustion has occurred yet.

Evaporation equation can be expressed as

$$r(t)^2 = r_0^2 - kt \quad (7.5)$$

where $r(t)$ is the droplet radius at time (t), r_0 is the initial droplet radius, k is the evaporation constant, which depends on air temperature, fuel properties, and other factors. The evaporation phase continues until the droplet reaches a temperature where combustion can occur, or evaporation stops when the vapor pressure at the droplet surface equals the surrounding vapor pressure.

7.3.2 Combustion phase

Once the droplet reaches the ignition temperature, it starts to burn. In this phase, both evaporation and combustion occur simultaneously. The combustion process is described by the combustion rate equation. [132]

Conditions:

- Time $t_{combustion} \leq t < t_{breakup}$, i.e., the droplet has ignited but not yet reached the breakup point.

- The droplet radius continues to decrease, and combustion accelerates evaporation.

Combustion equation can be expressed as

$$\dot{m}_{combustion} = 4\pi r^2 B \rho_{\infty} Y_{oxygen} \quad (7.6)$$

where $\dot{m}_{combustion}$ is the combustion rate, r is the droplet radius, B is the combustion constant, ρ_{∞} is the air density, Y_{oxygen} is the mass fraction of oxygen.

In this phase, energy conservation is also important,

$$Q_{combustion} = \dot{m}_{combustion} \Delta H \quad (7.7)$$

where $Q_{combustion}$ is the heat released during combustion, H is the heat of combustion.

7.3.3 Breakup phase

As combustion continues, the droplet may experience breakup due to either surface tension forces or internal pressure caused by rapid heating. The Weber number or Rayleigh-Taylor instability describes the breakup phenomenon. [132]

Conditions:

- Time $t \geq t_{breakup}$, i.e., when the Weber number exceeds the critical value or when pressure instability occurs.
- $We > We_{critical}$ meaning that the droplet undergoes breakup.

Breakup equation can be expressed as

Weber number equation

$$W_e = \frac{\rho u^2 d}{\sigma} \quad (7.8)$$

where ρ is the gas density, u is the relative velocity between the droplet and the surrounding gas, d is the droplet diameter, σ is the surface tension. When the Weber number exceeds a critical value, the droplet will undergo breakup. $W_{e,critical}$ is around 10–20 under this study conditions.

Or Rayleigh-Taylor instability equation:

$$P_{drop} = P_{\infty} + \frac{2\sigma}{r} \quad (7.9)$$

where P_{drop} is the internal pressure of the droplet, P is the surrounding pressure, r is the droplet radius, σ is the surface tension.

When the internal pressure exceeds the critical value, the droplet breaks up. Hence, the droplet evaporation, combustion, and breakup process can be expressed as follows:

$$f(t) = \begin{cases} r(t)^2 = r_0^2 - kt, 0 \leq t < t_{combustion}, \\ \dot{m}_{combustion} = 4\pi r^2 B \rho_{\infty} Y_{oxygen}, t_{combustion} \leq t \leq t_{breakup} \\ W_e = \frac{\rho u^2 d}{\sigma}, t \geq t_{breakup} \end{cases} \quad (7.10)$$

- When $0 < t < t_{combustion}$, the droplet is in the evaporation phase, governed by the D^2 law.
- When $t_{combustion} < t < t_{breakup}$, the droplet is undergoing both evaporation and combustion, following the combustion rate equation.
- When $t < t_{breakup}$ the droplet may break up, governed by the Weber number or Rayleigh-Taylor instability.

7.3.4 Conclusion

These equations outline the different phases and conditions, and the specific numerical results can be determined through numerical simulations based on the physical properties of the droplet and the environment.

This study experiment results indicate that at the first stage, the droplet undergoes an evaporation process. Then after the initial evaporation follows a faster evaporation. This always happens under a lower temperature environment. This study also found the velocity and intensity of the evaporation rate is the key point for droplet whether undergo evaporation, breakup or combustion based on thousands single droplet test during the research. The evaporation rate is responding to surrounding environment temperature, fuel composition (high volatility or low boiling point).

According to this study and other research works, droplet breakup such as micro-explosion is happening instantly when the droplet enters the high temperature environment, typically in microseconds while combustion need an ignition delay time when the fuel-air ratio and temperature is appropriate.

Hence, the piecewise function can be adjusted as

$$f(t) = \begin{cases} r(t)^2 = r_0^2 - kt, 0 \leq t < t_{breakup}, \\ We = \frac{\rho u^2 d}{\sigma}, t_{breakup} \leq t < t_{combustion} \\ \dot{m}_{combustion} = 4\pi r^2 B \rho_{\infty} Y_{oxygen}, t > t_{combustion} \end{cases} \quad (7.11)$$

The evaporation constant k can be represented as a function of the evaporation rate and material properties:

$$k = \frac{8\rho_l}{\rho_g c_p T_{\infty}} \quad (7.12)$$

where λ is the latent heat of vaporization, ρ_l is the liquid density, ρ_g is the gas density, c_p is the specific heat capacity of the gas, T_∞ is the surrounding air temperature.

The piecewise function can be expressed as

$$f(t) = \begin{cases} r(t)^2 = r_0^2 - \left(\frac{8\rho_l}{\rho_g c_p T_\infty} \right) t, & 0 \leq t < t_{breakup}, \\ W_e = \frac{\rho u^2 d}{\sigma}, & t_{breakup} \leq t < t_{combustion} \\ \dot{m}_{combustion} = 4\pi r^2 B \rho_\infty Y_{oxygen}, & t > t_{combustion} \end{cases} \quad (7.13)$$

- When $0 < t < t_{breakup}$, the droplet is in the evaporation phase, governed by the D²-law.
- When $t_{breakup} < t < t_{combustion}$, the droplet may break up, governed by the Weber number or Rayleigh-Taylor instability.
- When $t < t_{combustion}$, the droplet is undergoing both evaporation and combustion, following the combustion rate equation.

7.4 Droplet Behaviour in Thermodynamic System

To link the thermodynamic system with the behaviour of a droplet suspended at a specific temperature within the system, an effective approach is by solving the governing equations for both the temperature field and the droplet's behaviour simultaneously.

7.4.1 Temperature field

The temperature field in the cylindrical system is governed by the heat conduction, convection and radiation equations, the equation describes how the temperature T evolves over time within the system, which can be present as

$$f(t) = \begin{cases} \rho c_p \left(\frac{\partial T}{\partial t} + u \frac{\partial T}{\partial r} + w \frac{\partial T}{\partial z} \right) = k \left(\frac{1}{r} \frac{\partial}{\partial r} \left(r \frac{\partial T}{\partial r} \right) + \frac{\partial^2 T}{\partial z^2} \right) \\ q_{rad} = \sigma \epsilon (T^4 - T_{surrounding}^4) \\ \rho c_p \left(\frac{\partial T}{\partial t} + v \times \Delta T \right) = k \nabla^2 T + \frac{\partial q_{rad}}{\partial t} \end{cases} \quad (7.14)$$

where $k(T)$ is the temperature-dependent thermal conductivity.

7.4.2 Droplet behaviour

The behaviour of the droplet such as evaporation, breakup and combustion are influenced by the local temperature at the droplet's position. The droplet's radius decreases over time due to evaporation, governed by

$$f(t) = \begin{cases} r(t)^2 = r_0^2 - \left(\frac{8\rho_l}{\rho_g c_p T_\infty} \right) t, 0 \leq t < t_{breakup}, \\ We = \frac{\rho u^2 d}{\sigma}, t_{breakup} \leq t < t_{combustion} \\ \dot{m}_{combustion} = 4\pi r^2 B \rho_\infty Y_{oxygen}, t > t_{combustion} \end{cases} \quad (7.15)$$

7.4.3 Droplet in thermodynamic system

To couple the thermodynamic system with the droplet's piecewise equations, integrate the droplet's heat transfer equations with the temperature field equations of the thermodynamic system. The specific steps are as follows:

7.4.3.1 Temperature at droplet's location

Within the thermodynamic system, determine the temperature T_d at the droplet's location (r_d, z_d) and at time t

$$T_d = T(r_d, z_d, t) \quad (7.16)$$

7.4.3.2 Droplet's state

Use the temperature T_d to update the droplet's evaporation, combustion, and breakup states. Specifically, substitute T_d into the droplet's evaporation equation:

$$f(t) = \begin{cases} r(t)^2 = r_0^2 - \left(\frac{8\rho_l}{\rho_g c_p T_d}\right) t, 0 \leq t < t_{breakup}, \\ W_e = \frac{\rho u^2 d}{\sigma}, t_{breakup} \leq t < t_{combustion} \\ \dot{m}_{combustion} = 4\pi r^2 B \rho_\infty Y_{oxygen}, t > t_{combustion} \end{cases} \quad (7.17)$$

7.4.3.3 Temperature field

Use the energy released from the droplet's breakup or combustion to update the temperature field $T(r, z, t)$ in the thermodynamic system. Then, iterate to calculate the temperature field and droplet state at the next time step.

7.4.4 Numerical method for coupled solution

Since the equations involved are nonlinear partial differential equations, numerical methods are typically employed to solve them simultaneously. The numerical method adopted in this study is using Python to program and calculate the simulation result then compared with the experiment results of this study and others work. Due to Python's superior open-source capabilities, it offers a more flexible and convenient platform for integration with other software such as MATLAB and Open FOAM. This allows for easier development and computational expansion in future analyses. The initial numerical model code and results are presented in Appendix C and D.

The main procedure to simulate and calculate the droplet radius include:

- Discretize the temperature field. Use finite difference or finite element methods to discretize the temperature field $T(r, z, t)$. This involves dividing the spatial domain into a grid and calculating the temperature at each grid point over time.
- Update droplet radius and state. At each time step, update the droplet's evaporation, combustion, and breakup state based on the current temperature T_d at the droplet's location.
- Solve for the next time step. Use numerical methods to solve for the temperature field $T(r, z, t)$ and the droplet state $r(t)$ at the next time step.
- Iterative loop. Repeat these steps iteratively until the desired simulation time is reached.

7.5 Conclusion

A numerical model was established to simulate the experimental conditions of this study. This model describes the thermodynamic system in which a single microdroplet is situated and the behaviours it undergoes. It incorporates factors such as environmental temperature and droplet heating time. By specifying fuel type, heating temperature and heating duration, the model can predict transient droplet behaviour.

Based on the experimental results, the current model is limited to the specific fuel types and temperature conditions tested. To develop a more accurate model with additional parameters, further experiments should be conducted across a range of temperatures and fuel mixtures.

Chapter 8 Conclusions and Recommendations

8.1 Summary of Findings

This study investigated alternative biofuels and multi-biofuel blends evaporation, breakup and combustion characteristics with a focus on single microdroplet in high temperature environment. The experiments using BDIMP technique to capture the microdroplet transient behaviour through LDBOS. The test fuels included standard diesel, biodiesel, HVO, and bio-alcohols such as methanol, ethanol, and octanol. These fuels and multi-fuel blends were tested at high temperatures ranging from LLPT to HLPT. Various phenomena such as evaporation, nucleation, puffing, micro-explosion, secondary breakup and combustion were observed and analysed. The influence of droplet composition and temperature gradient between fuel and high temperature air on the behaviours were comparatively analysed and discussed in Chapter 4, Chapter 5 and Chapter 6. Fuel and multi-fuel blends droplet behaviours at experiment temperature were classified as shown in Figure 8.1.

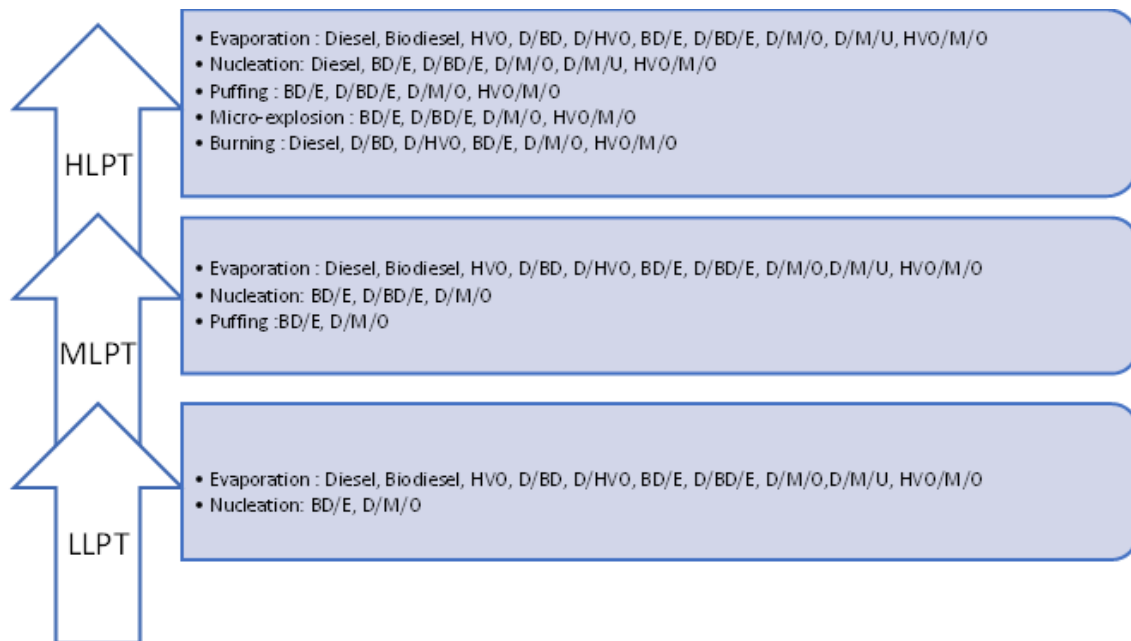


Figure 8.1 Fuel and multi-fuel blend droplet behaviours at LLPT, MLPT and HLPT, atm

The findings can be summarized as follows

- Diesel-biodiesel/HVO blends: The evaporation rate of diesel-biodiesel/HVO blends at a constant temperature was slightly lower than that of pure diesel. Diesel-biodiesel blends showed an evaporation rate similar to diesel alone, while diesel-HVO blends exhibited a slightly faster evaporation rate than the diesel-biodiesel blend. The addition of biodiesel and HVO resulted in less soot formation during combustion in the high-temperature HLPT environment compared to pure diesel.
- Diesel-water emulsions: In tests with diesel-water emulsion droplets under the same temperature conditions, the emulsions were more reactive than pure diesel droplets. The emulsions displayed significant expansion and intense deformation during high-temperature tests.
- Diesel-methanol-octanol blends: Droplets of diesel blended with methanol and octanol evaporated faster than pure diesel. At high temperatures, these droplets were prone to puffing and micro-explosions, breaking into smaller droplets and enhancing fuel-air mixing. Even in blends with a high diesel content, significant puffing and micro-explosions occurred, indicating that the addition of alcohols promoted these effects. Incorporating varying proportions of water into the alcohols further increased the frequency and intensity of puffing and micro-explosions.
- Diesel-biodiesel-ethanol blends: Puffing and micro-explosions were observed at high temperatures in blends of diesel, biodiesel, and ethanol, particularly with higher ethanol content. As both air temperature and ethanol concentration increased, the frequency and intensity of these effects also increased. At HLPT, when the ethanol content exceeded 35%, the droplets became more prone to puffing and micro-explosions.
- Diesel-methanol-UREA blends: In blends of diesel, methanol, and UREA, puffing and intense expansion were observed at HLPT, leading to the disintegration of the droplets under high temperatures.

- Biodiesel-ethanol blend and HVO-methanol-octanol blends: Puffing and micro-explosions were observed in these blends under high-temperature conditions. As both the temperature and alcohol content increased, the frequency and intensity of these phenomena also rose.
- Aerated diesel: In comparative high-temperature experiments between standard diesel and aerated diesel, the diesel with the longest aeration time exhibited the shortest evaporation time, with evaporation time decreasing as aeration duration increased.

From the test results, it was concluded that heating temperature had a greater impact on fuel evaporation, puffing, and micro-explosion than fuel composition, which in turn had a greater influence than the fuel blending ratio.

For practical ICEs fuel application, considering the diverse consumer needs for specific applications, adding methanol and ethanol to conventional diesel helps achieve faster fuel atomization, reaching the optimal fuel-air mixing ratio required for fast combustion. This results in a more rapid and efficient combustion process. Additionally, the simultaneous addition of biodiesel and alcohols to diesel can enhance fuel atomization and counteract the issues of incomplete atomization and ignition delay caused by the biodiesel component, making it more viable for the commercial market and better suited to meet the increasingly strict regulations on emissions and fuel efficiency.

Through detailed physical experiments and analysis of the extensive analysis of the experimental data, this study offers valuable insights into the application of multi-component biofuel blends with various compositions and mixing ratios in internal combustion engines (ICEs). The research emphasizes how these customized fuel formulations can be optimized to meet the specific demands of different scenarios, particularly by enhancing fuel volatility, fragmentation, and flammability, which collectively lead to an overall improvement in fuel performance. These findings contribute significantly to the development of more sustainable and high-performance fuel technologies, which are

essential for the continued viability of ICEs in meeting stringent environmental and efficiency standards

8.2 Recommendations for Future Work

Based on the findings from the current study, the following recommendations are proposed for future research.

Experimental investigation

- Expansion of test fuel matrix. It's advisable to broaden the test fuel matrix to encompass long carbon chain alcohols, esters, ketones, aldehydes, and ethers, such as C8 oxygenates. These compounds ought to be heated at a high temperature of 773K to facilitate a comparative analysis with the short carbon chain chemicals used in the present study.
- Increased test temperature. Consider increasing the experiment's test temperature to 1073K This adjustment would emulate a high-air temperature diesel combustion chamber, offering insights into droplet behaviours in harsher conditions.
- Increased Test Pressure: In subsequent experiments, consider elevating the pressure to match the injection system's pressure. This enhancement would pave the way for understanding droplet behaviours under intensified temperature and pressure settings, rendering a holistic comprehension.
- Test equipment automation. The testing methodology could benefit from the integration of fully automated equipment for droplet generation and delivery. Such automation could expedite droplet delivery, enabling swift temperature variations and heat adjustments within the droplets.
- Engine chamber wall test. Investigate the droplets under conditions that replicate the collision with the chamber wall of a diesel engine to understand their behaviour in actual engine conditions.

- In engine test. Consider combusting the test fuel used in this study within a constant volume chamber or a single-cylinder engine. This would provide insights into fuel spray atomization, structural examination, and the assessment of combustion performance. It would also facilitate the evaluation of emissions (exhaust gas, soot, and particulate matter) across varying load conditions.

Numerical investigation

- Molecular thermodynamic analysis of droplet behaviour under high pressure. Investigate the effects of increased pressure on the evaporation, combustion, and breakup of fuel droplets, simulating conditions similar to high-pressure fuel injection system. Model different pressures, ranging from standard atmospheric pressure to the high pressures found in fuel injection systems (up to 2000 bar). Include variations in fuel type, droplet size, and pressure. Analyse droplet, evaporation rates, breakup mechanism, combustion characteristics.

Reference

- [1] European Commission. Report from the Commission to the European Parliament, the Council, the European Economic and Social Committee and the Committee of the Regions on the implementation of the Circular Economy Action Plan. COM(2019) 190 final. Available from: <https://eur-lex.europa.eu/legal-content/EN/TXT/PDF/?uri=CELEX:52019DC0190&from=EN>
- [2] Wang K, Xue Y, Xu H, Huang L, Ma R, Zhang P, Jiang X, Yuan Y, Negenborn RR, Sun P. Joint energy consumption optimization method for wing-diesel engine-powered hybrid ships towards a more energy-efficient shipping. *Energy*. 2022 Apr 15;245:123155.
- [3] Hosseinzadeh-Bandbafha H, Tabatabaei M, Aghbashlo M, Khanali M, Demirbas A. A comprehensive review on the environmental impacts of diesel/biodiesel additives. *Energy Conversion and Management*. 2018 Oct 15;174:579-614.
- [4] Mwangi JK, Lee WJ, Chang YC, Chen CY, Wang LC. An overview: Energy saving and pollution reduction by using green fuel blends in diesel engines. *Applied Energy*. 2015 Dec 1;159:214-36.
- [5] Fayyazbakhsh A, Pirouzfard V. Comprehensive overview on diesel additives to reduce emissions, enhance fuel properties and improve engine performance. *Renewable and Sustainable Energy Reviews*. 2017 Jul 1;74:891-901.
- [6] International Council on Clean Transportation. Briefing: Euro 6/VI – Benefits of adopting world-class standards for heavy-duty vehicles in Brazil. Washington, D.C.: ICCT; 2016 Jun. Available from: https://theicct.org/sites/default/files/publications/ICCT_Euro6-VI_briefing_jun2016.pdf
- [7] Lv Y, Yang X, Li Y, Liu J, Li S. Fault detection and diagnosis of marine diesel engines: A systematic review. *Ocean Engineering*. 2024 Feb 15;294:116798.
- [8] Hiroyasu H, Arai M. Structures of fuel sprays in diesel engines. *SAE transactions*. 1990 Jan 1:1050-61.
- [9] Shibata G, Nishiuchi S, Xie P, Takai S, Ogawa H, Kobashi Y. Measurements of fuel adhesion on cylinder walls and fuel wall-flow behavior with post diesel fuel injections. *International journal of engine research*. 2020 Feb;21(2):352-66.
- [10] Ashraful AM, Masjuki HH, Kalam MA, Rashedul HK, Sajjad H, Abedin MJ. Influence of anti-corrosion additive on the performance, emission and engine component wear characteristics of an IDI diesel engine fueled with palm biodiesel. *Energy Conversion and Management*. 2014 Nov 1;87:48-57.
- [11] Sjögren M, Li H, Rannug U, Westerholm R. A multivariate statistical analysis of chemical composition and physical characteristics of ten diesel fuels. *Fuel*. 1995 Jul 1;74(7):983-9.
- [12] Gatts T, Liu S, Liew C, Ralston B, Bell C, Li H. An experimental investigation of incomplete combustion of gaseous fuels of a heavy-duty diesel engine supplemented with hydrogen and natural gas. *International Journal of Hydrogen Energy*. 2012 May 1;37(9):7848-59.

- [13] Ekoto IW, Colban WF, Miles PC, Park S, Foster DE, Reitz RD. Sources of UHC emissions from a light-duty diesel engine operating in a partially premixed combustion regime. *SAE International Journal of Engines*. 2009 Jan 1;2(1):1265-89.
- [14] Johnson TV. Diesel emission control in review. *SAE international journal of fuels and lubricants*. 2009 Jan 1;1(1):68-81.
- [15] Simoneit BR. Biomass burning—a review of organic tracers for smoke from incomplete combustion. *Applied Geochemistry*. 2002 Mar 1;17(3):129-62.
- [16] Miravete EJ, Moral MJ, Thurk J. Fuel taxation, emissions policy, and competitive advantage in the diffusion of European diesel automobiles. *The RAND Journal of Economics*. 2018 Sep;49(3):504-40.
- [17] Ni P, Wang X, Li H. A review on regulations, current status, effects and reduction strategies of emissions for marine diesel engines. *Fuel*. 2020 Nov 1;279:118477.
- [18] Krivoshto IN, Richards JR, Albertson TE, Derlet RW. The toxicity of diesel exhaust: implications for primary care. *The Journal of the American Board of Family Medicine*. 2008 Jan 1;21(1):55-62.
- [19] Walker AP. Controlling particulate emissions from diesel vehicles. *Topics in catalysis*. 2004 Apr;28:165-70.
- [20] Wadud Z. Diesel demand in the road freight sector in the UK: Estimates for different vehicle types. *Applied Energy*. 2016 Mar 1;165:849-57.
- [21] Murugesan A, Umarani C, Subramanian R, Nedunchezian N. Bio-diesel as an alternative fuel for diesel engines—a review. *Renewable and sustainable energy reviews*. 2009 Apr 1;13(3):653-62.
- [22] Jaichandar S, Annamalai K. The status of biodiesel as an alternative fuel for diesel engine—an overview. *Journal of Sustainable Energy & Environment*. 2011;2(2):71-5.
- [23] Othman MF, Adam A, Najafi G, Mamat R. Green fuel as alternative fuel for diesel engine: A review. *Renewable and Sustainable Energy Reviews*. 2017 Dec 1;80:694-709.
- [24] Demirbas A. Alternatives to petroleum diesel fuel. *Energy Sources, Part B*. 2007 Oct 24;2(4):343-51.
- [25] Karthikeyan S, Prathima AJ. Characteristics analysis of carbon nanowires in diesel: *Neochloris oleoabundans* algae oil biodiesel–ethanol blends in a CI engine. *Energy Sources, Part A: Recovery, Utilization, and Environmental Effects*. 2016 Oct 17;38(20):3089-94.
- [26] Lapuerta M, Hernández JJ, Fernández-Rodríguez D, Cova-Bonillo A. Autoignition of blends of n-butanol and ethanol with diesel or biodiesel fuels in a constant-volume combustion chamber. *Energy*. 2017 Jan 1;118:613-21.
- [27] Thanigaivelan V, Loganathan M, Vikneswaran M, Venkatramanan S, Manickam M. Effect of hydrogen and ethanol addition in cashew nut shell liquid biodiesel operated direct injection (DI) diesel engine. *International Journal of Hydrogen Energy*. 2022 Jan 26;47(8):5111-29.
- [28] Chigier NA. The atomization and burning of liquid fuel sprays. In *Energy and Combustion Science* 1979 Jan 1 (pp. 183-200). Pergamon.

- [29] Pandey RK, Rehman A, Sarviya RM. Impact of alternative fuel properties on fuel spray behavior and atomization. *Renewable and Sustainable Energy Reviews*. 2012 Apr 1;16(3):1762-78
- [30] Corral-Gómez L, Rubio-Gómez G, Martínez-Martínez S, Sánchez-Cruz FA. Effect of diesel-biodiesel-ethanol blends on the spray macroscopic parameters in a common-rail diesel injection system. *Fuel*. 2019 Apr 1;241:876-83.
- [31] Kalvāns J. The efficiency of photodissociation for molecules in interstellar ices. *Monthly Notices of the Royal Astronomical Society*. 2018 Aug;478(2):2753-65.
- [32] Cheeseman PC. A new efficient combustion method for ICEs. SAE Technical Paper; 2020 Apr 14.
- [33] Vaja I, Gambarotta A. Internal combustion engine (ICE) bottoming with organic Rankine cycles (ORCs). *Energy*. 2010 Feb 1;35(2):1084-93.
- [34] Chatzopoulou MA, Markides CN. Thermodynamic optimisation of a high-electrical efficiency integrated internal combustion engine–Organic Rankine cycle combined heat and power system. *Applied Energy*. 2018 Sep 15;226:1229-51.
- [35] Awad OI, Mamat R, Noor MM, Ibrahim TK, Yusri IM, Yusop AF. The impacts of compression ratio on the performance and emissions of ice powered by oxygenated fuels: A review. *Journal of the Energy Institute*. 2018 Feb 1;91(1):19-32.
- [36] Friedl H, Fraidl G, Kapus P. Highest efficiency and ultra low emission-internal combustion engine 4.0. *Combustion Engines*. 2020;59.
- [37] Yusof SN, Sidik NA, Asako Y, Japar WM, Mohamed SB, Muhammad NM. A comprehensive review of the influences of nanoparticles as a fuel additive in an internal combustion engine (ICE). *Nanotechnology Reviews*. 2020 Dec 24;9(1):1326-49.
- [38] Heywood JB, Weiss MA, Schafer A, Bassene SA, Natarajan VK. The performance of future ICE and fuel cell powered vehicles and their potential fleet impact. SAE Technical Paper; 2004 Mar 8.
- [39] Çay Y, Çiçek A, Kara F, Sağıroğlu S. Prediction of engine performance for an alternative fuel using artificial neural network. *Applied Thermal Engineering*. 2012 May 1;37:217-25.
- [40] Pourkhesalian AM, Shamekhi AH, Salimi F. Alternative fuel and gasoline in an SI engine: A comparative study of performance and emissions characteristics. *Fuel*. 2010 May 1;89(5):1056-63.
- [41] Yadav P, Kumar N, Gautam R. Improvement in performance of CI engine using various techniques with alternative fuel. *Energy Sources, Part A: Recovery, Utilization, and Environmental Effects*. 2021 Jan 14:1-27.
- [42] Rao KV, Kurbet SN, Kuppast VV. A review on performance of the IC engine using alternative fuels. *Materials Today: Proceedings*. 2018 Jan 1;5(1):1989-96.
- [43] Gülüm M. Effects of compression ratio, blending ratio and engine speed on fuel cost, performance and exhaust emissions of a diesel engine fueled with bio-derived alternative fuels. *Sustainable Energy Technologies and Assessments*. 2022 Oct 1;53:102464.

- [44] Bandyopadhyay D, Sutar PS, Sonawane SB, Rairikar S, Thipse SS, Jadhav A. Hydrogen as a Carbon Neutral ICE Fuel for Future India. SAE Technical Paper; 2024 Jan 16.
- [45] Simsek S, Uslu S, Simsek H. Evaluation of the effect of a new alternative fuel containing boron and hydrogen on gasoline engine performance and emission responses. International Journal of Environmental Science and Technology. 2022 Jun;19(6):4913-22.
- [46] Heywood, John B. Internal Combustion Engine Fundamentals. New York :McGraw-Hill, 1988
- [47] Algayyim SJ, Saleh K, Wandel AP, Fattah IM, Yusaf T, Alrazen HA. Influence of natural gas and hydrogen properties on internal combustion engine performance, combustion, and emissions: A review. Fuel. 2024 Apr 15;362:130844.
- [48] Benjamin MA. FUEL ATOMIZATION FOR NEXT-GENERATION GAS TURBINE COMBUSTION-IS. Atomization and Sprays. 2000;10:427-38.
- [49] Suh HK, Park SW, Lee CS. Atomization characteristics of dimethyl ether fuel as an alternative fuel injected through a common-rail injection system. Energy & fuels. 2006 Jul 19;20(4):1471-81.
- [50] Jankowski A. Laser research of fuel atomization and combustion processes in the aspect of exhaust gases emission. Journal of KONES. 2008;15:119-26.
- [51] Shatrov MG, Malchuk I, Dunin AY. A laboratory investigation into the fuel atomization process in a diesel engine for different configurations of the injector nozzles and flow conditions. Fluid Dynamics & Materials Processing. 2020;16(4):747-60.
- [52] Takeuchi K, Senda J, Shikuya M. Transient characteristics of fuel atomization and droplet size distribution in diesel fuel spray. SAE Technical Paper; 1983 Feb 1.
- [53] Ra Y, Reitz RD. A vaporization model for discrete multi-component fuel sprays. International Journal of Multiphase Flow. 2009 Feb 1;35(2):101-17.
- [54] Heldmann M, Knorsch T, Wensing M. Investigation of fuel atomization and evaporation of a DISI injector spray under homogeneous charge conditions. SAE International Journal of Engines. 2013 Jun 1;6(2):1213-21.
- [55] Liu R, Huang K, Qiao Y, Ji H, Zhong L, Wu H. Effects of Low Pressure Injection on Fuel Atomization and Mixture Formation for Heavy Fuel Engines. Processes. 2022 Nov 3;10(11):2276.
- [56] Mukhtar MN, Hagos FY, Noor MM, Mamat R, Abdullah AA. Tri-fuel emulsion with secondary atomization attributes for greener diesel engine—A critical review. Renewable and Sustainable Energy Reviews. 2019 Sep 1;111:490-506.
- [57] Myers GD, Lefebvre AH. Flame propagation in heterogeneous mixtures of fuel drops and air. Combustion and Flame. 1986 Nov 1;66(2):193-210.
- [58] Chen W, Pan J, Fan B, Liu Y, Peter O. Effect of injection strategy on fuel-air mixing and combustion process in a direct injection diesel rotary engine (DI-DRE). Energy Conversion and Management. 2017 Dec 15;154:68-80.
- [59] Bression G, Soleri D, Savy S, Dehoux S, Azoulay D, Hamouda HB, Doradoux L, Guerrassi N, Lawrence N. A study of methods to lower HC and CO emissions in diesel HCCI. SAE International Journal of Fuels and Lubricants. 2009 Jan 1;1(1):37-49.

- [60] Guarieiro LL, de Souza AF, Torres EA, de Andrade JB. Emission profile of 18 carbonyl compounds, CO, CO₂, and NO_x emitted by a diesel engine fuelled with diesel and ternary blends containing diesel, ethanol and biodiesel or vegetable oils. *Atmospheric Environment*. 2009 Jun 1;43(17):2754-61.
- [61] Schemme S, Samsun RC, Peters R, Stolten D. Power-to-fuel as a key to sustainable transport systems—An analysis of diesel fuels produced from CO₂ and renewable electricity. *Fuel*. 2017 Oct 1;205:198-221.
- [62] Fonseca N, Casanova J, Valdés M. Influence of the stop/start system on CO₂ emissions of a diesel vehicle in urban traffic. *Transportation Research Part D: Transport and Environment*. 2011 Mar 1;16(2):194-200.
- [63] Plee SL, Ahmad T, Myers JP, Faeth GM. Diesel NO_x emissions—A simple correlation technique for intake air effects. In *Symposium (International) on Combustion* 1982 Jan 1 (Vol. 19, No. 1, pp. 1495-1502). Elsevier.
- [64] Guan B, Zhan R, Lin H, Huang Z. Review of state of the art technologies of selective catalytic reduction of NO_x from diesel engine exhaust. *Applied Thermal Engineering*. 2014 May 1;66(1-2):395-414.
- [65] Wang YQ, Zhang XY, Sun JY, Zhang XC, Che HZ, Li YJ. Spatial and temporal variations of the concentrations of PM₁₀, PM_{2.5} and PM₁ in China. *Atmospheric Chemistry and Physics*. 2015 Dec 9;15(23):13585-98.
- [66] Ristovski ZD, Miljevic B, Surawski NC, Morawska L, Fong KM, Goh F, Yang IA. Respiratory health effects of diesel particulate matter. *Respirology*. 2012 Feb;17(2):201-12.
- [67] Wang X, Li H, Li G, Fan J, Bai H, Gao Y, Huo H. Effect of injection pressure on low-temperature fuel atomization characteristics of diesel engines under cold start conditions. *International Journal of Multiphase Flow*. 2024 Feb 1;172:104712.
- [68] Mehra KS, Pal J, Goel V. A comprehensive review on the atomization and spray characteristics of renewable biofuels. *Sustainable Energy Technologies and Assessments*. 2023 Mar 1;56:103106.
- [69] Arunkumar G, Dhavare P, Alharbi SA, Nasif O, Strunecky O, Subramani N. Effect of injection pressure on spray cone and penetration angle for enhanced fuel atomization of various blended viscous fluid: a numerical modeling. *Journal of Energy Resources Technology*. 2023 Jan 1;145(1):012303.
- [70] Li X, Wang S, Yang S, Qiu S, Sun Z, Hung DL, Xu M. A review on the recent advances of flash boiling atomization and combustion applications. *Progress in Energy and Combustion Science*. 2024 Jan 1;100:101119.
- [71] Kuznetsov GV, Volokitin DI, Volkov RS, Podgornaya ER, Strizhak PA. Atomization of composite liquid fuels in experimental setup with varied gas temperature and pressure. *Fuel*. 2024 Feb 15;358:130213.
- [72] Shahnazari S, Astaraki MA, Sobati MA, Ghassemi H. Atomization characteristics of different water/heavy fuel oil emulsions in a pressure-swirl injector. *Journal of the Energy Institute*. 2023 Jun 1;108:101204.
- [73] Postrioti L, Battistoni M, Zempi J, Brizi G, La Sana M, Brignone M, Napoli F, Pizza S, Milani E. Experimental and Numerical Analysis of a Swirled Fuel Atomizer for an Aftertreatment Diesel Burner. *SAE Technical Paper*; 2023 Aug 28.

- [74] Ibrahim IA, Elzallat AM, Elsakka MM, Farag TM, Gad HM. Effect of atomizing gas type on kerosene spray combustion using gas-blast atomizer: A comparative numerical study. *Applied Thermal Engineering*. 2024 Feb 15;239:121996.
- [75] Islamova A, Tkachenko P, Shlegel N, Kuznetsov G. Secondary atomization of fuel oil and fuel oil/water emulsion through droplet-droplet collisions and impingement on a solid wall. *Energies*. 2023 Jan 16;16(2):1008.
- [76] Liu R, Huang K, Qiao Y, Ji H, Wu H. Atomization characteristics of low-volatility heavy fuel for low-pressure direct injection aviation piston engines. *Journal of Energy Resources Technology*. 2023 Apr 1;145(4):042304.
- [77] Qingsong BA, Yang WU, Li HO. Atomization characteristics analysis and structure optimization of an aviation fuel nozzle. *Journal of Shanghai Jiaotong University*. 2023 Jan 28;57(1):84.
- [78] Britannica, The Editors of Encyclopaedia. "diesel fuel". *Encyclopedia Britannica*, Available from: <https://www.britannica.com/technology/diesel-fuel>.
- [79] Hsu CS. Diesel fuel analysis. *Encyclopedia of Analytical Chemistry*. 2000:6613-22
- [80] Environment Pollution (Prevention & Control) Authority for NCR. Comprehensive Action Plan for air pollution control in Delhi & NCR. Available from: <http://www.epca.org.in>
- [81] Sharma S, Maréchal F. Carbon dioxide capture from internal combustion engine exhaust using temperature swing adsorption. *Frontiers in Energy Research*. 2019 Dec 16;7:143.
- [82] Lim MC, Ayoko GA, Morawska L, Ristovski ZD, Jayaratne ER. The effects of fuel characteristics and engine operating conditions on the elemental composition of emissions from heavy duty diesel buses. *Fuel*. 2007 Aug 1;86(12-13):1831-9.
- [83] Jansma H, Fino D, Uitz R, Makkee M. Influence of diesel fuel characteristics on soot oxidation properties. *Industrial & engineering chemistry research*. 2012 Jun 6;51(22):7559-64.
- [84] Wang G, Yu W, Yu Z, Li X. Study on Characteristics Optimization of Combustion and Fuel Injection of Marine Diesel Engine. *Atmosphere [Internet]* 2022;13(8):1301. Available from: <http://dx.doi.org/10.3390/atmos13081301>.
- [85] IEA (2021), Biofuel demand growth and share of total demand by fuel, 2021-2026, IEA, Paris <https://www.iea.org/data-and-statistics/charts/biofuel-demand-growth-and-share-of-total-demand-by-fuel-2021-2026>, Licence: CC BY 4.0
- [86] <https://www.iea.org/data-and-statistics/data-tools/greenhouse-gas-emissions-from-energy-data-explorer>
- [87] U.S. Energy Information Administration. Monthly Biodiesel Production Report. Available from: <https://www.eia.gov/biofuels/biodiesel/production/>
- [88] Farm Energy. Commercial and Large Scale Biodiesel Production Systems. Available from: <https://farm-energy.extension.org>
- [89] Mishra VK, Goswami R. A review of production, properties and advantages of biodiesel. *Biofuels*. 2018 Mar 4;9(2):273-89.
- [90] Park SH, Kim HJ, Suh HK, Lee CS. Experimental and numerical analysis of spray-atomization characteristics of biodiesel fuel in various fuel and ambient

- temperatures conditions. International journal of heat and fluid flow. 2009 Oct 1;30(5):960-70.
- [91] Choi SH, Oh YT. Spray Behavior and Atomization Characteristics of Biodiesel. In International Journal of Modern Physics: Conference Series 2012 (Vol. 6, pp. 419-424). World Scientific Publishing Company.
- [92] Kim H, Kim Y, Lee K. An experimental study on the spray, combustion, and emission characteristics of two types of biodiesel fuel. Energy & fuels. 2013 Sep 19;27(9):5182-91.
- [93] Tinprabath P, Hespel C, Chanchaona S, Foucher F. Influence of biodiesel and diesel fuel blends on the injection rate and spray injection under cold conditions. In ILASS–Europe 2014, 26th Annual Conference on Liquid Atomization and Spray System 2014 Sep 8.
- [94] Taghizadeh-Alisaraei A, Ghobadian B, Tavakoli-Hashjin T, Mohtasebi SS, Rezaei-asl A, Azadbakht M. Characterization of engine's combustion-vibration using diesel and biodiesel fuel blends by time-frequency methods: A case study. Renewable Energy. 2016 Sep 1;95:422-32.
- [95] Vinoth Kanna I, Arulprakasajothi M, Eliyas S. A detailed study of IC engines and a novel discussion with comprehensive view of alternative fuels used in petrol and diesel engines. International Journal of Ambient Energy. 2021 Nov 18;42(15):1794-802.
- [96] Hunicz J, Krzaczek P, Gęca M, Rybak A, Mikulski M. Comparative study of combustion and emissions of diesel engine fuelled with FAME and HVO. Combustion Engines. 2021;60.
- [97] ETIP Bioenergy. EVC2: Hydrotreatment to HVO. Available from: <https://www.etipbioenergy.eu>
- [98] Gehrler M, Seyfried H, Staudacher S. Life cycle assessment of BtL as compared to HVO paths in alternative aviation fuel production. Deutsche Gesellschaft für Luft- und Raumfahrt-Lilienthal-Oberth eV; 2015 Feb 6.
- [99] Lorenzi G, Mignini L, Venezia B, Silva C, Santarelli M. Integration of high-temperature electrolysis in an HVO production process using waste vegetable oil. Energy Procedia. 2019 Feb 1;158:2005-11.
- [100] Johnson E. A carbon footprint of HVO biopropane. Biofuels, Bioproducts and Biorefining. 2017 Sep;11(5):887-96.
- [101] Kuronen M, Mikkonen S, Aakko P, Murtonen T. Hydrotreated vegetable oil as fuel for heavy duty diesel engines. SAE Technical Paper; 2007 Oct 29.
- [102] Kim D, Kim S, Oh S, No SY. Engine performance and emission characteristics of hydrotreated vegetable oil in light duty diesel engines. Fuel. 2014 Jun 1;125:36-43.
- [103] Dimitriadis A, Natsios I, Dimaratos A, Katsaounis D, Samaras Z, Bezergianni S, Lehto K. Evaluation of a hydrotreated vegetable oil (HVO) and effects on emissions of a passenger car diesel engine. Frontiers in Mechanical Engineering. 2018 Jul 31;4:7. 7.
- [104] Sonthalia A, Kumar N. Comparison of fuel characteristics of hydrotreated waste cooking oil with its biodiesel and fossil diesel. Environmental Science and Pollution Research. 2021 Mar;28(10):11824-34.

- [105] Zhai C, Li K, Dong P, Jin Y, Luo H, Zhou B, Liu Y. Experimental Study on the Spray Characteristics of Diesel and Hydrotreated Vegetable Oil (HVO) Fuels under Different Injection Pressures. *Processes*. 2024 Aug 14;12(8):1697.
- [106] Nakagawa H, Sakai M, Harada T, Ichinose T, Takeno K, Matsumoto S, Kobayashi M, Matsumoto K, Yakushido K. Biomethanol production from forage grasses, trees, and crop residues. In *Biofuel's Engineering Process Technology 2011* Aug 1. IntechOpen.
- [107] Shamsul NS, Kamarudin SK, Rahman NA, Kofli NT. An overview on the production of bio-methanol as potential renewable energy. *Renewable and Sustainable Energy Reviews*. 2014 May 1;33:578-88.
- [108] Udayakumar R, Sundaram S, Sivakumar K. Engine performance and exhaust characteristics of dual fuel operation in DI diesel engine with methanol. *SAE Technical Paper*; 2004 Mar 8.
- [109] Yao C, Cheung CS, Cheng C, Wang Y, Chan TL, Lee SC. Effect of diesel/methanol compound combustion on diesel engine combustion and emissions. *Energy conversion and management*. 2008 Jun 1;49(6):1696-704.
- [110] Valera H, Agarwal AK. Methanol as an alternative fuel for diesel engines. *Methanol and the alternate fuel economy*. 2019:9-33.
- [111] Verhelst S, Turner JW, Sileghem L, Vancoillie J. Methanol as a fuel for internal combustion engines. *Progress in Energy and Combustion Science*. 2019 Jan 1;70:43-88.
- [112] Gardiner M. Energy requirements for hydrogen gas compression and liquefaction as related to vehicle storage needs. url: https://www.hydrogen.energy.gov/pdfs/9013_energy_requirements_for_hydrogen_gas_compression.pdf; 2009.
- [113] Zabed H, Sahu JN, Suely A, Boyce AN, Faruq G. Bioethanol production from renewable sources: Current perspectives and technological progress. *Renewable and Sustainable Energy Reviews*. 2017 May 1;71:475-501.
- [114] Zabochnicka-Świątek M, Sławik L. Bioethanol-production and utilization. *Archivum Combustionis*. 2010;30(3):237-46.
- [115] Bilgin A, Durgun O, Sahin Z. The effects of diesel-ethanol blends on diesel engine performance. *Energy sources*. 2002 May 1;24(5):431-40.
- [116] He BQ, Shuai SJ, Wang JX, He H. The effect of ethanol blended diesel fuels on emissions from a diesel engine. *Atmospheric Environment*. 2003 Nov 1;37(35):4965-71.
- [117] Rakopoulos CD, Antonopoulos KA, Rakopoulos DC. Experimental heat release analysis and emissions of a HSDI diesel engine fueled with ethanol–diesel fuel blends. *Energy*. 2007 Oct 1;32(10):1791-808.
- [118] Vergel OA, Cárdenas D, García-Contreras R, Mata C. Bioethanol-Diesel Blends Used in Diesel Engines and Vehicles under Transient Operation. *Bioethanol Technologies*. 2020 Nov 3.
- [119] Barua S, Sahu D, Sultana F, Baruah S, Mahapatra S. Bioethanol, internal combustion engines and the development of zero-waste biorefineries: an approach towards sustainable motor spirit. *RSC Sustainability*. 2023;1(5):1065-84.

- [120] Zhang CP, Zhai XM, Li YJ, Sun ZG. Research on combustion characteristics and emissions of methanol-diesel fuel with different additives. *Advanced Materials Research*. 2012 Jan 12;354:462-7.
- [121] El-Seesy AI, Waly MS, He Z, El-Batsh HM, Nasser A, El-Zoheiry RM. Enhancement of the combustion and stability aspects of diesel-methanol-hydrous methanol blends utilizing n-octanol, diethyl ether, and nanoparticle additives. *Journal of Cleaner Production*. 2022 Oct 15;371:133673.
- [122] Fernando S, Hanna M. Phase behavior of the ethanol-biodiesel-diesel micro-emulsion system. *Transactions of the ASAE*. 2005;48(3):903-8.
- [123] Hulwan DB, Joshi SV. Performance, emission and combustion characteristic of a multicylinder DI diesel engine running on diesel–ethanol–biodiesel blends of high ethanol content. *Applied Energy*. 2011 Dec 1;88(12):5042-55.
- [124] How HG, Masjuki HH, Kalam MA, Teoh YH. Engine performance, emission and combustion characteristics of a common-rail diesel engine fuelled with bioethanol as a fuel additive in coconut oil biodiesel blends. *Energy Procedia*. 2014 Jan 1;61:1655-9.
- [125] Paul G, Datta A, Mandal B. Numerical investigation of the performance and emission characteristics of a CI engine using diesel and its blends with ethanol and *Jatropha* biodiesel. *Int. J. Curr. Eng. Technol*. 2014;3:5-9.
- [126] Datta A, Mandal BK. Numerical investigation of the performance and emission parameters of a diesel engine fuelled with diesel-biodiesel-methanol blends. *Journal of Mechanical Science and Technology*. 2016 Apr;30:1923-9.
- [127] Park SH, Yoon SH, Suh HK, Lee CS. Effect of the temperature variation on properties of biodiesel and biodiesel-ethanol blends fuels. *Oil & Gas Science and Technology-Revue de l'IFP*. 2008 Nov 1;63(6):737-45.
- [128] Yilmaz N, Sanchez TM. Analysis of operating a diesel engine on biodiesel-ethanol and biodiesel-methanol blends. *Energy*. 2012 Oct 1;46(1):126-9.
- [129] El-seesy AI, Waly MS, He Z, El-Batsh HM, Nasser A, El-Zoheiry RM. Influence of quaternary combinations of biodiesel/methanol/n-octanol/diethyl ether from waste cooking oil on combustion, emission, and stability aspects of a diesel engine. *Energy Conversion and Management*. 2021 Jul 15;240:114268.
- [130] Xuan T, Sun Z, EL-Seesy AI, Mi Y, Zhong W, He Z, Wang Q, Sun J, El-Batsh HM, Cao J. An optical study on spray and combustion characteristics of ternary hydrogenated catalytic biodiesel/methanol/n-octanol blends; part II: Liquid length and in-flame soot. *Energy*. 2021 Jul 15;227:120543.
- [131] Lakshminarayanan PA, Aghav YV, Lakshminarayanan PA, Aghav YV. Turbulent Structure of the Diesel Spray. *Modelling Diesel Combustion*. 2010:39-58.
- [132] Baumgarten C. Mixture formation in internal combustion engines. *Springer Science & Business Media*; 2006 Sep 28.
- [133] Lamanna G, Sun H, Schüler M, Weigand B, Magatti D, Ferri F. Comparative Study of Equilibrium and Nonequilibrium Evaporation Models for Vaporizing Droplet Arrays at High-Pressure. In *Advanced Combustion and Aerothermal Technologies: Environmental Protection and Pollution Reductions 2007* (pp. 445-455). Springer Netherlands.

- [134] Chauveau C, Halter F, Lalonde A, Gökalp I. An experimental study on the droplet vaporization: effects of heat conduction through the support fiber. In 22nd Annual Conference on Liquid Atomization and Spray Systems (ILASS Europe 2008) 2008.
- [135] Antonov DV, Fedorenko RM, Strizhak PA, Nissar Z, Sazhin SS. Puffing/micro-explosion in composite fuel/water droplets heated in flames. *Combustion and Flame*. 2021 Nov 1;233:111599.
- [136] Ismael, M.A.; Heikal, M.R.; Aziz, A.R.A.; Crua, C. The Effect of Fuel Injection Equipment of Water-in-Diesel Emulsions on Micro-Explosion Behaviour. *Energies* 2018, 11, 1650.
- [137] Zhao, H.; Liu, H.-F.; Xu, J.-L.; Li, W.-F.; Lin, K.-F. Temporal Properties of Secondary Drop Breakup in the Bag-Stamen Breakup Regime. *Phys. Fluids* 2013, 25, 54102 Barabás I, Todoruț IA. Utilization of biodiesel-diesel-ethanol blends in CI engine. Biodiesel-quality, emissions and by-products, InTech. 2011 Nov 16:215-34.
- [138] Kuznetsov, G.V.; Piskunov, M.V.; Strizhak, P.A. Evaporation, Boiling and Explosive Breakup of Heterogeneous Droplet in a High-Temperature Gas. *Int. J. Heat Mass Transf.* 2016, 92, 360–369.
- [139] Antonov, D.V.; Kuznetsov, G.V.; Sazhin, S.S.; Strizhak, P.A. Puffing/Micro-Explosion in Droplets of Rapeseed Oil with Coal Micro-Particles and Water. *Fuel* 2022, 316, 123009.
- [140] Price C, Hamzehloo A, Aleiferis P, Richardson D. Numerical modelling of droplet breakup for flash-boiling fuel spray predictions. *International Journal of Multiphase Flow*. 2020 Apr 1;125:103183.
- [141] Nyashina GS, Vershinina KY, Strizhak PA. Impact of micro-explosive atomization of fuel droplets on relative performance indicators of their combustion. *Fuel Processing Technology*. 2020 May 1;201:106334.
- [142] Zhang Y, Huang R, Huang Y, Huang S, Ma Y, Xu S, Zhou P. Effect of ambient temperature on the puffing characteristics of single butanol-hexadecane droplet. *Energy*. 2018 Feb 15;145:430-41.
- [143] Kropotova S, Strizhak P. Collisions of liquid droplets in a gaseous medium under conditions of intense phase transformations. *Energies*. 2021 Sep 27;14(19):6150.
- [144] Antonov DV, Fedorenko RM, Strizhak PA. Micro-explosion and puffing of a group of two-component droplets. *Applied Thermal Engineering*. 2020 Nov 25;181:116023.
- [145] Ithnin AM, Yahya WJ. A review on micro-explosion phenomena in water-in-diesel emulsion fuel. *Journal of Advanced Vehicle System*. 2019;7(1):11-8.
- [146] Kozak P, Asztalos K. Effects of Liquid Droplet-Droplet Interactions in a Pressure Swirl Spray.
- [147] Arcoumanis C, Gavaises M, French B. Effect of fuel injection processes on the structure of diesel sprays. *SAE transactions*. 1997 Jan 1:1025-64.
- [148] Fedorenko, R.M.; Antonov, D.V.; Strizhak, P.A.; Sazhin, S.S. Time Evolution of Composite Fuel/Water Droplet Radii before the Start of Puffing/Micro-Explosion. *Int. J. Heat Mass Transf.* 2022, 191, 122838.

- [149] Antonov DV, Fedorenko RM, Strizhak PA. Micro-explosion phenomenon: Conditions and benefits. *Energies*. 2022 Oct 18;15(20):7670.
- [150] Fostiropoulos, S.; Strotos, G.; Nikolopoulos, N.; Gavaises, M. A Simple Model for Breakup Time Prediction of Water-Heavy Fuel Oil Emulsion Droplets. *Int. J. Heat Mass Transf.* 2021, 164, 120581.
- [151] Meng, K.; Wu, Y.; Lin, Q.; Shan, F.; Fu, W.; Zhou, K.; Liu, T.; Song, L.; Li, F. Microexplosion and Ignition of Biodiesel/Ethanol Blends Droplets in Oxygenated Hot Co-Flow. *J. Energy Inst.* 2019, 92, 1527–1536.
- [152] Rosli, M.A.F.; Aziz, A.R.A.; Ismael, M.A.; Elbashir, N.O.; Zainal A., E.Z.; Baharom, M.; Mohammed, S.E. Experimental Study of Micro-Explosion and Puffing of Gas-to-Liquid (GTL) Fuel Blends by Suspended Droplet Method. *Energy* 2021, 218, 119462.
- [153] Tarlet, D.; Allouis, C.; Bellettre, J. The Balance between Surface and Kinetic Energies within an Optimal Micro-Explosion. *Int. J. Therm. Sci.* 2016, 107, 179–183.
- [154] Antonov, D.; Strizhak, P. Explosive Disintegration of Two-Component Droplets in a Gas-Flow at Its Turbulization. *Therm. Sci.* 2019, 23, 2983–2993.
- [155] Antonov, D.V.; Kuznetsov, G.V.; Strizhak, P.A. The Micro-Explosive Fragmentation Criteria of Two-Liquid Droplets. *Int. J. Heat Mass Transf.* 2022, 196, 123293.
- [156] Antonov, D.V.; Strizhak, P.A. Heating, Evaporation, Fragmentation, and Breakup of Multi-Component Liquid Droplets When Heated in Air Flow. *Chem. Eng. Res. Des.* 2019, 146, 22–35.
- [157] Hou, S.S.; Rizal, F.M.; Lin, T.H.; Yang, T.Y.; Wan, H.P. Microexplosion and Ignition of Droplets of Fuel Oil/Bio-Oil (Derived from Lauan Wood) Blends. *Fuel* 2013, 113, 31–42.
- [158] Antonov, D.V.; Shlegel, N.E.; Strizhak, P.A.; Tarlet, D.; Bellettre, J. Energy Analysis of Secondary Droplet Atomization Schemes. *Int. Commun. Heat Mass Transf.* 2020, 117, 104666.
- [159] Pamuluri VK, Avulapati MM. Effect of composition and temperature on the puffing and microexplosion of diesel-ethanol-jatropha oil ternary fuel blend droplets. *Energy*. 2024 Aug 8:132755.
- [160] Huang J, Xia J, He Y, Wang ZH, Cen KF. Direct Puffing Simulation of Miscible and Emulsified Multicomponent Single Droplets. *Atomization and Sprays*. 2024;34(7).
- [161] Kapadia, H.; Brahmabhatt, H.; Dabhi, Y.; Chourasia, S. Investigation of Emulsion and Effect on Emission in CI Engine by Using Diesel and Bio-Diesel Fuel: A Review. *Egypt. J. Pet.* 2019, 28, 323–337.
- [162] Antonov DV, Voitkov IS, Volkov RS, Vysokomornaya OV. Explosion breakdown of drops of emulsions of water with petroleum products as a result of their intensive heating. *Journal of Engineering Physics and Thermophysics*. 2019 Mar 15;92:398-408.
- [163] Wang Z, Yuan B, Cao J, Huang Y, Cheng X, Wang Y, Zhang X, Liu H. A new shift mechanism for micro-explosion of water-diesel emulsion droplets at different ambient temperatures. *Applied Energy*. 2022 Oct 1;323:119448.

- [164] Yahaya Khan M, Abdul Karim ZA, Hagos FY, Aziz AR, Tan IM. Current trends in water-in-diesel emulsion as a fuel. *The Scientific world journal*. 2014;2014(1):527472.
- [165] Preetika R, Mehta PS, Kaisare NS, Basavaraj MG. Kinetic stability of surfactant stabilized water-in-diesel emulsion fuels. *Fuel*. 2019 Jan 15;236:1415-22. Duan M, Zhu X, Shan X, Wang H, Chen S, Liu J. Responsive liquid metal droplets: from bulk to nano. *Nanomaterials*. 2022 Apr 10;12(8):1289.
- [166] Alias EA, Hagos FY, Ishak MI, Dzaharudin F, Abdullah AA, Asyraf A. Performance and Emission characteristics of microbubble-enhanced fuels in a diesel engine. *Energy & Fuels*. 2021 Jan 19;35(3):2630-8.
- [167] Oh SH, Han JG, Kim JM. Long-term stability of hydrogen nanobubble fuel. *Fuel*. 2015 Oct 15;158:399-404.
- [168] Xuan R, Guo L, Cai N, Sun W, Yan Y, Zhang H, Chen Y, Wang H, Zhang J, Ge Y. Study on spray characteristics of micro-nano bubble premixed fuel. *Fuel*. 2024 May 1;363:131035.
- [169] Oh SH, Yoon SH, Song H, Han JG, Kim JM. Effect of hydrogen nanobubble addition on combustion characteristics of gasoline engine. *International journal of hydrogen energy*. 2013 Nov 13;38(34):14849-53.
- [170] Gan Y, Qiao L. Combustion characteristics of fuel droplets with addition of nano and micron-sized aluminum particles. *Combustion and Flame*. 2011 Feb 1;158(2):354-68.
- [171] Westlye FR, Penney K, Ivarsson A, Pickett LM, Manin J, Skeen SA. Diffuse back-illumination setup for high temporally resolved extinction imaging. *Applied optics*. 2017 Jun 10;56(17):5028-38.
- [172] Hinrichs J, Shastry V, Junk M, Hemberger Y, Pitsch H. An experimental and computational study on multicomponent evaporation of diesel fuel droplets. *Fuel*. 2020 Sep 1;275:117727.
- [173] Gun'ko VM, Nasiri R, Sazhin SS, Lemoine F, Grisch F. A quantum chemical study of the processes during the evaporation of real-life Diesel fuel droplets. *Fluid Phase Equilibria*. 2013 Oct 25;356:146-56.
- [174] Zhou L, Liang Y. Study of the combustion process inside an ethanol-diesel dual direct injection engine based on a non-uniform injection approach. *Fluid Dyn. Mater. Process*. 2021;17:159-70.
- [175] Cheng C, Hu Y, Jiang Y. Investigation of evaporation and combustion characteristics of diesel and fatty acid methyl esters emulsified fuel droplets. *Fuel*. 2024 Mar 15;360:130609.
- [176] de Souza WF, Guimarães IR, Guerreiro MC, Oliveira LC. Catalytic oxidation of sulfur and nitrogen compounds from diesel fuel. *Applied Catalysis A: General*. 2009 Jun 1;360(2):205-9.
- [177] Chang Z, Chen X, Peng Y. The interaction between diesel and surfactant Triton X-100 and their adsorption on coal surfaces with different degrees of oxidation. *Powder Technology*. 2019 Jan 15;342:840-7.

- [178] Sazhin SS, Krutitskii PA, Abdelghaffar WA, Sazhina EM, Mikhalovsky SV, Meikle ST, Heikal MR. Transient heating of diesel fuel droplets. *International Journal of Heat and Mass Transfer*. 2004 Jul 1;47(14-16):3327-40.
- [179] Ochowiak M, Bielecki Z, Bielecki M, Włodarczak S, Krupińska A, Matuszak M, Choiński D, Lewtak R, Pavlenko I. The D₂-Law of Droplet Evaporation When Calculating the Droplet Evaporation Process of Liquid Containing Solid State Catalyst Particles. *Energies*. 2022 Oct 16;15(20):7642.
- [180] Kryukov AP, Levashov VY, Sazhin SS. Evaporation of diesel fuel droplets: kinetic versus hydrodynamic models. *International journal of heat and mass transfer*. 2004 Jun 1;47(12-13):2541-9.
- [181] Sazhin SS, Al Qubeissi M, Kolodnytska R, Elwardany AE, Nasiri R, Heikal MR. Modelling of biodiesel fuel droplet heating and evaporation. *Fuel*. 2014 Jan 1;115:559-72.
- [182] Song C. Introduction to chemistry of diesel fuels. In *Chemistry of diesel fuels* 2020 Aug 8 (pp. 1-60). CRC Press.
- [183] Sazhin SS, Gun'ko VM, Nasiri R. Quantum-chemical analysis of the processes at the surfaces of Diesel fuel droplets. *Fuel*. 2016 Feb 1;165:405-12.
- [184] Hardalupas Y, Taylor AM, Whitelaw JH. Mass flux, mass fraction and concentration of liquid fuel in a swirl-stabilized flame. *International journal of multiphase flow*. 1994 Aug 1;20:233-59.
- [185] Bruneaux G. A study of mixture formation in direct injection diesel like conditions using quantitative fuel concentration visualizations in a gaseous fuel jet. *SAE Technical Paper*; 2002 May 6.
- [186] Chen H, Cheng Y, He Q, Wang X. Experimental study on combustion and unregulated emission characteristics of a diesel engine fueled with light hydrocarbon/diesel blends. *Fuel*. 2022 May 1;315:123075.
- [187] Krupčík J, Gorovenko R, Špánik I, Bočková I, Sandra P, Armstrong DW. On the use of ionic liquid capillary columns for analysis of aromatic hydrocarbons in low-boiling petrochemical products by one-dimensional and comprehensive two-dimensional gas chromatography. *Journal of Chromatography A*. 2013 Aug 2;1301:225-36.
- [188] Van Buuren AR, Marrink SJ, Berendsen HJ. A molecular dynamics study of the decane/water interface. *The Journal of Physical Chemistry*. 1993 Sep;97(36):9206-12.
- [189] Choi D, Kang W, Park T. Anti-allergic and anti-inflammatory effects of undecane on mast cells and keratinocytes. *Molecules*. 2020 Mar 28;25(7):1554.
- [190] Lemmon EW, Huber ML. Thermodynamic properties of n-dodecane. *Energy & fuels*. 2004 Jul 21;18(4):960-7.
- [191] Muhammad F, Monteiro-Riviere NA, Riviere JE. Comparative in vivo toxicity of topical JP-8 jet fuel and its individual hydrocarbon components: identification of tridecane and tetradecane as key constituents responsible for dermal irritation. *Toxicologic Pathology*. 2005 Feb;33(2):258-66.
- [192] Duong TH, Beniddir MA, Genta-Jouve G, Aree T, Chollet-Krugler M, Boustie J, Ferron S, Sauvager A, Nguyen HH, Chavasiri W, Le Pogam P. Tsavoenones A–C: unprecedented polyketides with a 1, 7-dioxadispiro [4.0. 4.4] tetradecane core from

- the lichen *Parmotrema tsavoense*. *Organic & Biomolecular Chemistry*. 2018;16(32):5913-9.
- [193] Lawal AT. Polycyclic aromatic hydrocarbons. A review. *Cogent Environmental Science*. 2017 Jan 1;3(1):1339841.
- [194] Lima DG, Soares VC, Ribeiro EB, Carvalho DA, Cardoso EC, Rassi FC, Mundim KC, Rubim JC, Suarez PA. Diesel-like fuel obtained by pyrolysis of vegetable oils. *Journal of Analytical and Applied Pyrolysis*. 2004 Jun 1;71(2):987-96.
- [195] Imron MF, Kurniawan SB, Ismail NI, Abdullah SR. Future challenges in diesel biodegradation by bacteria isolates: a review. *Journal of Cleaner Production*. 2020 Apr 1;251:119716.
- [196] Wu M, Zhao Z, Zhang P, Wan M, Lei J, Pan B, Xing B. Environmental persistent free radicals in diesel engine exhaust particles at different altitudes and engine speeds. *Science of the Total Environment*. 2021 Nov 20;796:148963.
- [197] Hsu CS, Dechert GJ, Abbott DJ, Genowitz MW, Barbour R. Molecular characterization of diesel fuels using modern analytical techniques. In *Chemistry of Diesel Fuels 2020 Aug 8 (pp. 61-76)*. CRC Press.
- [198] Mosonik BC, Kibet JK, Ngari SM, Nyamori VO. Environmentally persistent free radicals and particulate emissions from the thermal degradation of Croton megalocarpus biodiesel. *Environmental Science and Pollution Research*. 2018 Sep;25:24807-17.
- [199] Hernández JJ, Cova-Bonillo A, Wu H, Barba J, Rodríguez-Fernández J. Low temperature autoignition of diesel fuel under dual operation with hydrogen and hydrogen-carriers. *Energy Conversion and Management*. 2022 Apr 15;258:115516.
- [200] Blank DA. Hydrogen Lean-Combustion Studies in a Four-Stroke DI Radical-Ignition Diesel Engine with EGR. *SAE Technical Paper*; 2007 Jul 23.
- [201] Talibi M, Hellier P, Ladommatos N. Impact of increasing methyl branches in aromatic hydrocarbons on diesel engine combustion and emissions. *Fuel*. 2018 Mar 15;216:579-88.
- [202] Clothier PQ, Pritchard HO, Poirier M. Synergy between additives in stimulating diesel-fuel ignition. *Combustion and flame*. 1993 Dec 1;95(4):427-9.
- [203] Dadi RK, Daya R, Reddy GK, Kumar A, Srinivasan A, An H, Cunningham MJ, Joshi SY, Currier NW, Yezerets A. Modeling and experimental insights on oxidation of heavy chain HCs on diesel oxidation catalysts. *Chemical Engineering Journal*. 2022 May 1;435:134996.
- [204] Zhou L, Liang Y. Study of the combustion process inside an ethanol-diesel dual direct injection engine based on a non-uniform injection approach. *Fluid Dyn. Mater. Process*. 2021;17:159-70.
- [205] Calabria R, Chiariello F, Massoli P. Thermal behavior of pyrolysis oil-diesel oil emulsion in evaporating micronic droplets. *Combustion Science and Technology*. 2022 Jan 25;194(2):397-416.
- [206] Arcoumanis C, Cutter P, Whitelaw DS. Heat transfer processes in diesel engines. *Chemical Engineering Research and Design*. 1998 Feb 1;76(2):124-32.
- [207] Fardad D, Ladommatos N. Evaporation of hydrocarbon compounds, including gasoline and diesel fuel, on heated metal surfaces. *Proceedings of the Institution of*

- Mechanical Engineers, Part D: Journal of Automobile Engineering. 1999 Jun 1;213(6):625-45.
- [208] Men Y, Haskara I, Zhu G. Multi-zone reaction-based modeling of combustion for multiple-injection diesel engines. *International Journal of Engine Research*. 2020 Aug;21(6):1012-25.
- [209] Tao F, Chomiak J. Numerical investigation of reaction zone structure and flame liftoff of DI diesel sprays with complex chemistry. *SAE Transactions*. 2002 Jan 1:1836-54.
- [210] Welch AB, Wallace JS. Performance characteristics of a hydrogen-fueled diesel engine with ignition assist. *Alternative Diesel Fuels*. 1990 Dec:227.
- [211] Yesilyurt MK. A detailed investigation on the performance, combustion, and exhaust emission characteristics of a diesel engine running on the blend of diesel fuel, biodiesel and 1-heptanol (C7 alcohol) as a next-generation higher alcohol. *Fuel*. 2020 Sep 1;275:117893.
- [212] El Wakil MM, Myers PS, Uyehara OA. Fuel Vaporization and Ignition Las in Diesel Combustion. *SAE Technical Paper*; 1956 Jan 1.
- [213] Edenhofer R, Lucka K, Köhne H. Low temperature oxidation of diesel–air mixtures at atmospheric pressure. *Proceedings of the Combustion Institute*. 2007 Jan 1;31(2):2947-54.
- [214] Gao J, Wang Y, Li X, Wang S, Ma C, Wang X. Catalytic effect of diesel PM derived ash on PM oxidation activity. *Chemosphere*. 2022 Jul 1;299:134445.
- [215] Rajamohan S, Kasimani R. Analytical characterization of products obtained from slow pyrolysis of *Calophyllum inophyllum* seed cake: study on performance and emission characteristics of direct injection diesel engine fuelled with bio-oil blends. *Environmental Science and Pollution Research*. 2018 Apr;25:9523-38.
- [216] Russell A, Epling WS. Diesel oxidation catalysts. *Catalysis Reviews*. 2011 Oct 1;53(4):337-423.
- [217] Dobbins RA, Fletcher RA, Benner Jr BA, Hoefft S. Polycyclic aromatic hydrocarbons in flames, in diesel fuels, and in diesel emissions. *Combustion and flame*. 2006 Mar 1;144(4):773-81.
- [218] Farrell-Jones J. *Petroleum hydrocarbons and polyaromatic hydrocarbons*. Blackwell publishing crc press: New york; 2003.
- [219] Ottikkutti P. *Multizone modeling of a fumigated diesel engine*. Iowa State University; 1989.
- [220] Hagos FY, Aziz AR, Tan IM. Water-in-diesel emulsion and its micro-explosion phenomenon-review. In 2011 IEEE 3rd international conference on communication software and networks 2011 May 27 (pp. 314-318). Ieee.
- [221] Wang L, Wang J, Qiao X, Ju D, Lin Z. Effect of ambient temperature on the micro-explosion characteristics of soybean oil droplet: The phenomenon of evaporation induced vapor cloud. *International Journal of Heat and Mass Transfer*. 2019 Aug 1;139:736-46.
- [222] Prasad S, Narayanan S, Mandal DK. Bicomponent Drop's Evaporation: Effect of Acoustics and Hot Surrounding. *Heat Transfer Engineering*. 2024 Mar 1:1-4.

- [223] Khuong LS, Hashimoto N, Konno Y, Suganuma Y, Nomura H, Fujita O. Droplet evaporation characteristics of hydrotreated vegetable oil (HVO) under high temperature and pressure conditions. *Fuel*. 2024 Jul 15;368:131604.
- [224] Xuan R, Guo L, Cai N, Sun W, Yan Y, Zhang H, Chen Y, Wang H, Zhang J, Ge Y. Study on spray characteristics of micro-nano bubble premixed fuel. *Fuel*. 2024 May 1;363:131035.
- [225] Huang D, Chen Z. Reinvestigation of the Henry's law constant for hydrogen peroxide with temperature and acidity variation. *Journal of Environmental Sciences*. 2010 Jan 1;22(4):570-4.
- [226] Eldredge T, Medina H, Hertzler N. Predicting the evaporation and decomposition of aqueous urea droplets in hot gas streams for SCR system design: A critical review. *Thermal Science and Engineering Progress*. 2024 Apr 1:102565.

Appendix A MATLAB image processing code

1:	% Image Loading and Display
2:	
3:	% Create an image datastore object specifying the folder "testimages"
4:	ds = imageDatastore("testimages");
5:	% Get the list of image filenames
6:	datafilenames = (ds.Files);
7:	% Get the number of image files
8:	nFiles = numel(datafilenames);
9:	% Read the first image from the datastore
10:	img = read(ds);
11:	% Display the image
12:	imshow(img)
13:	
14:	% Read and Classify the First Image
15:	
16:	% Create an image datastore object specifying the folder "testimages"
17:	ds = imageDatastore("testimages");
18:	% Read the first image from the datastore
19:	I = readimage(ds, 1);
20:	% Display the image
21:	imshow(I)
22:	% Call the classifyImage function to classify the image
23:	isReceipt = classifyImage(I);
24:	
25:	% Function Definition to Classify Image
26:	
27:	function isReceipt = classifyImage(I)
28:	% This function processes an image using the algorithm developed in
29:	% previous chapters and classifies the image as receipt or non-receipt
30:	
31:	% Convert the image to grayscale
32:	gs = im2gray(I);
33:	% Adjust the grayscale image
34:	gs = imadjust(gs);
35:	
36:	% Create an average filter mask
37:	mask = fspecial("average", 3);
38:	% Smooth the grayscale image using the filter
39:	gsSmooth = imfilter(gs, mask, "replicate");
40:	
41:	% Create a structuring element
42:	SE = strel("disk", 8);
43:	% Use morphological closing to remove the background
44:	lbg = imclose(gsSmooth, SE);

45:	% Subtract the smoothed image to remove the background
46:	lbgsb = lbg - gsSmooth;
47:	% Binarize the image
48:	lbw = ~imbinarize(lbgsb);
49:	
50:	% Use a rectangular structuring element for morphological opening
51:	SE = strel("rectangle", [3 25]);
52:	stripes = imopen(lbw, SE);
53:	
54:	% Sum the binary image rows
55:	signal = sum(stripes, 2);
56:	
57:	% Classify by finding local minima
58:	minIndices = islocalmin(signal, "MinProminence", 70, "ProminenceWindow", 25);
59:	Nmin = nnz(minIndices);
60:	% If the number of local minima is greater than or equal to 9, classify as a receipt
61:	isReceipt = Nmin >= 9;
62:	end
63:	
64:	% Load and Display Images
65:	
66:	% Read the image file "IMG_File.jpg"
67:	I = imread("IMG_File.jpg");
68:	% Display the image
69:	imshow(I)
70:	% Read the same image file again
71:	I2 = imread("IMG_File.jpg");
72:	% Display the image
73:	imshow(I2)
74:	% Display the two images side by side
75:	imshowpair(I, I2, "montage")
76:	% Save the image as "myImage.png"
77:	imwrite(I, "myImage.png")
78:	% Read the saved image
79:	Inew = imread("myImage.png")
80:	% Display the new image
81:	imshow(Inew)
82:	
83:	% Comparison and Histogram Adjustment
84:	
85:	% Read two image files
86:	I = imread("IMG_001.jpg");
87:	I2 = imread("IMG_002.jpg");
88:	% Convert the images to grayscale
89:	gs = im2gray(I);
90:	gs2 = im2gray(I2);

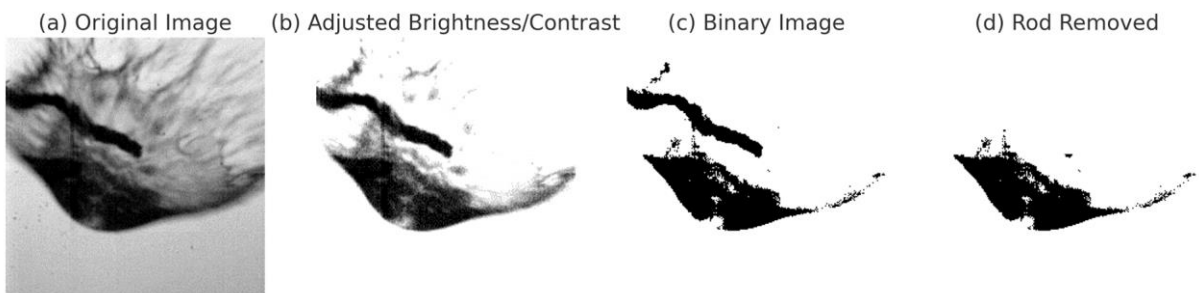
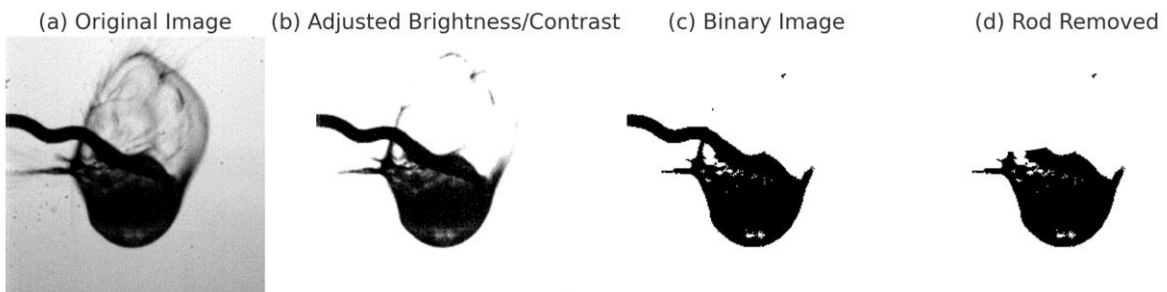
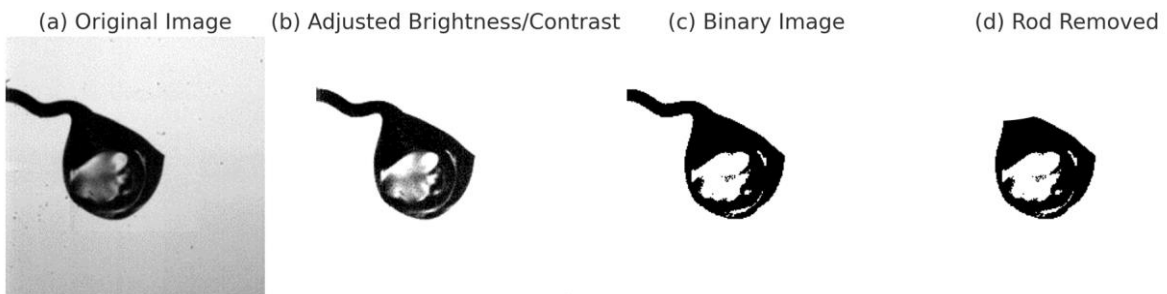
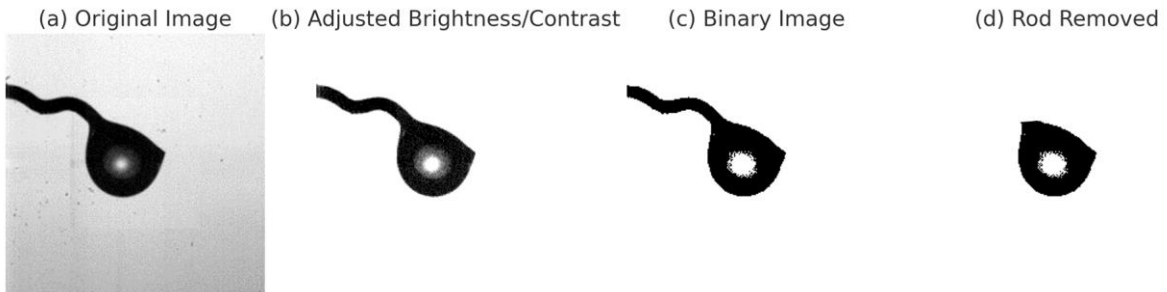
91:	% Display the two grayscale images side by side
92:	imshowpair(gs, gs2, "montage")
93:	% Display the histogram of the first grayscale image
94:	imhist(gs)
95:	% Display the histogram of the second grayscale image
96:	imhist(gs2)
97:	% Adjust the grayscale values of the second image
98:	gs2Adj = imadjust(gs2);
99:	% Display the original and adjusted second grayscale image side by side
100:	imshowpair(gs, gs2Adj, "montage")
101:	% Display the histogram of the adjusted second grayscale image
102:	imhist(gs2Adj)
103:	% Adjust the second image using local brightness enhancement
104:	I2adj = imlocalbrighten(I2);
105:	
106:	% Adaptive Binarization
107:	
108:	% Read the image file "IMG_006.jpg"
109:	I = imread("IMG_006.jpg");
110:	% Convert the image to grayscale
111:	gs = im2gray(I);
112:	% Adjust the grayscale values
113:	gsAdj = imadjust(gs);
114:	% Perform adaptive binarization on the adjusted grayscale image with dark foreground
115:	BW = imbinarize(gsAdj, "adaptive", "ForegroundPolarity", "dark");
116:	% Display the original and binarized images side by side
117:	imshowpair(I, BW, "montage")
118:	
119:	% Filtering and Binarization
120:	
121:	% Read the image file "IMG_005.jpg"
122:	I2 = imread("IMG_005.jpg");
123:	% Convert the image to grayscale
124:	gs2 = im2gray(I2);
125:	% Adjust the grayscale values
126:	gs2Adj = imadjust(gs2);
127:	% Perform binarization on the adjusted grayscale image
128:	BW2 = imbinarize(gs2Adj);
129:	% Display the original and binarized images side by side
130:	imshowpair(I2, BW2, "montage")
131:	% Sum the binary image rows and plot the result
132:	s = sum(BW, 2);
133:	plot(s)
134:	% Sum the binary image rows for the second binary image and plot the result
135:	S2 = sum(BW2, 2);
136:	plot(S2)

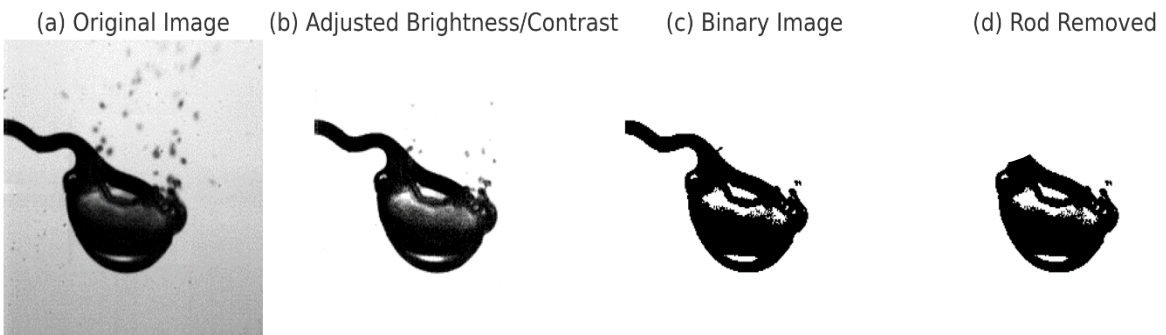
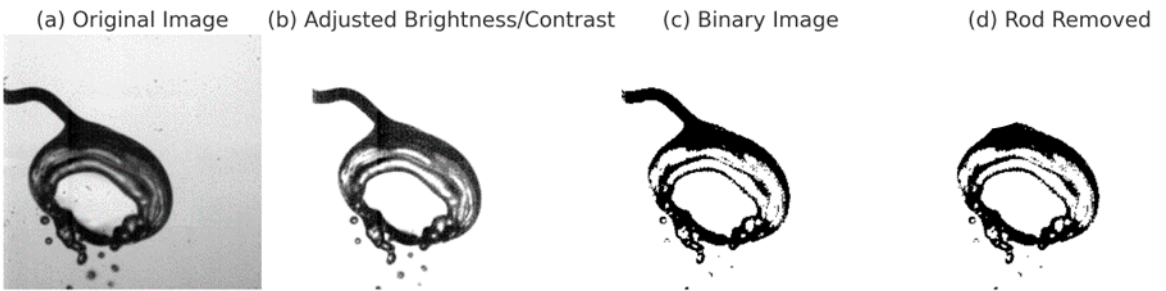
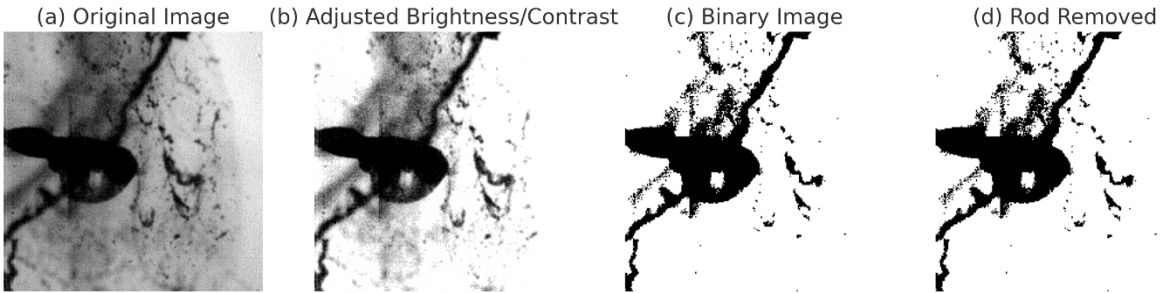
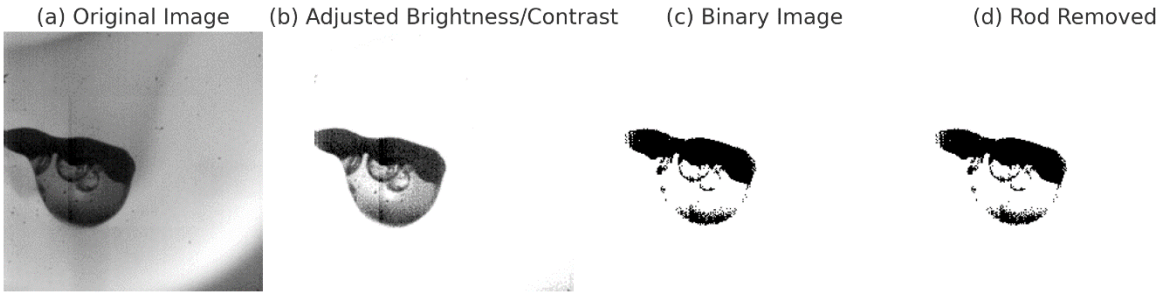
137:	
138:	% Image Smoothing and Binarization
139:	
140:	% Read the image file "IMG_007.jpg"
141:	I = imread("IMG_007.jpg");
142:	% Convert the image to grayscale
143:	gs = im2gray(I);
144:	% Adjust the grayscale values
145:	gs = imadjust(gs);
146:	% Perform adaptive binarization on the adjusted grayscale image with dark foreground
147:	BW = imbinarize(gs, "adaptive", "ForegroundPolarity", "dark");
148:	% Display the original and binarized images side by side
149:	imshowpair(I, BW, "montage")
150:	% Create an average filter
151:	H = fspecial("average", 3);
152:	% Smooth the grayscale image using the filter
153:	gsSmooth = imfilter(gs, H);
154:	% Perform adaptive binarization on the smoothed grayscale image
155:	BWsmooth = imbinarize(gsSmooth, "adaptive", "ForegroundPolarity", "dark");
156:	% Display the smoothed binarized image
157:	imshow(BWsmooth)
158:	% Smooth the grayscale image using the filter with replicated borders
159:	gsSmooth = imfilter(gs, H, "replicate");
160:	% Perform adaptive binarization on the smoothed grayscale image
161:	BWsmooth = imbinarize(gsSmooth, "adaptive", "ForegroundPolarity", "dark");
162:	% Display the smoothed binarized image
163:	imshow(BWsmooth)
164:	
165:	% Morphological Operations
166:	
167:	% Read the image file "IMG_001.jpg"
168:	I = imread("IMG_001.jpg");
169:	% Convert the image to grayscale
170:	gs = im2gray(I);
171:	% Adjust the grayscale values
172:	gs = imadjust(gs);
173:	% Create an average filter
174:	H = fspecial("average", 3);
175:	% Smooth the grayscale image using the filter with replicated borders
176:	gs = imfilter(gs, H, "replicate");
177:	% Perform adaptive binarization on the smoothed grayscale image with dark foreground
178:	BW = imbinarize(gs, "adaptive", "ForegroundPolarity", "dark");
179:	% Display the smoothed grayscale and binarized images side by side
180:	imshowpair(gs, BW, "montage")
181:	% Create a disk-shaped structuring element
182:	SE = strel("disk", 8);

183:	% Use morphological closing to remove the background
184:	lbg = imclose(gs, SE);
185:	% Display the background-removed image
186:	imshow(lbg)
187:	% Subtract the smoothed grayscale image from the background-removed image
188:	gsSub = lbg - gs;
189:	% Perform binarization on the subtracted image
190:	BWsub = ~imbinarize(gsSub);
191:	% Display the binarized subtracted image
192:	imshow(BWsub)
193:	% Use bottom-hat transformation to remove the background
194:	BW = imbothat(gs, SE);

Appendix B Image processing

Binary thresholding image processing





Appendix C Droplet behaviour numerical calculation code

1:	<code>import numpy as np</code>
2:	<code>import matplotlib.pyplot as plt</code>
3:	
4:	<code># Initial conditions</code>
5:	<code>r0 = 1.5e-6 # Initial droplet radius (m)</code>
6:	<code>T_inf = 573 # Ambient temperature (K)</code>
7:	<code>T0 = 293 # Initial droplet temperature (K)</code>
8:	<code>rho_inf = 1.225 # Air density (kg/m^3)</code>
9:	<code>sigma = 0.072 # Droplet surface tension (N/m)</code>
10:	<code>u = 0.1 # Droplet relative velocity to air (m/s)</code>
11:	
12:	<code># Evaporation constant (based on experimental data or assumptions)</code>
13:	<code>k = 1e-12 # Evaporation constant</code>
14:	
15:	<code># Combustion parameters (based on fuel properties)</code>
16:	<code>B = 1e-5 # Combustion constant</code>
17:	<code>Y_oxygen = 0.21 # Oxygen mass fraction</code>
18:	<code>delta_H = 44e6 # Heat of combustion (J/kg)</code>
19:	
20:	<code># Critical Weber number (assumed value)</code>
21:	<code>We_critical = 10</code>
22:	
23:	<code># Time step and total time</code>
24:	<code>dt = 1e-6 # Time step (s)</code>
25:	<code>total_time = 1e-3 # Total simulation time (s)</code>
26:	
27:	<code># Define the evaporation model</code>
28:	<code>def evaporate(r, k, dt):</code>
29:	<code> return np.sqrt(max(r**2 - k * dt, 0))</code>
30:	
31:	<code># Define the combustion rate model</code>
32:	<code>def combustion_rate(r, B, rho_inf, Y_oxygen):</code>
33:	<code> return 4 * np.pi * r**2 * B * rho_inf * Y_oxygen</code>
34:	
35:	<code># Define the Weber number calculation</code>
36:	<code>def weber_number(r, u, rho_inf, sigma):</code>
37:	<code> return rho_inf * u**2 * 2 * r / sigma</code>
38:	
39:	<code># Time-stepping simulation</code>
40:	
41:	<code># Initialize variables</code>
42:	<code>r = r0</code>

43:	time = 0
44:	r_values = [r0]
45:	time_values = [0]
46:	phase = "evaporation" # Current phase
47:	
48:	while time < total_time and r > 0:
49:	# Evaporation process
50:	if phase == "evaporation":
51:	r = evaporate(r, k, dt)
52:	# Check if combustion condition is met (adjust based on actual conditions)
53:	if r < 0.8 * r0:
54:	# Assume combustion starts when the radius is reduced to 80% of the initial value
55:	phase = "combustion"
56:	
57:	# Combustion process
58:	elif phase == "combustion":
59:	m_combustion = combustion_rate(r, B, rho_inf, Y_oxygen)
60:	r = r - (m_combustion * delta_H * dt) / (4 * np.pi * r**2)
61:	# Assume combustion heat mainly acts on the droplet surface
62:	# Check if breakup condition is met
63:	We = weber_number(r, u, rho_inf, sigma)
64:	if We > We_critical:
65:	phase = "breakup"
66:	
67:	# Record results
68:	r_values.append(r)
69:	time_values.append(time)
70:	time += dt
71:	
72:	# Check if breakup occurred
73:	if phase == "breakup":
74:	print("Droplet breakup occurred at time:", time, "s")
75:	else:
76:	print("Simulation ended without breakup.")
77:	
78:	# Plot droplet radius over time
79:	plt.plot(time_values, r_values)
80:	plt.xlabel('Time (s)')
81:	plt.ylabel('Droplet Radius (m)')
82:	plt.title('Droplet Evolution Over Time')
83:	plt.show()
84:	

Appendix D Numerical calculations of evaporation, breakup and combustion

a) 1.5 μL diesel, biodiesel, HVO microdroplet radius change over time at LLPT, atm

